IAEA Quality Control Atlas for Scintillation Camera Systems

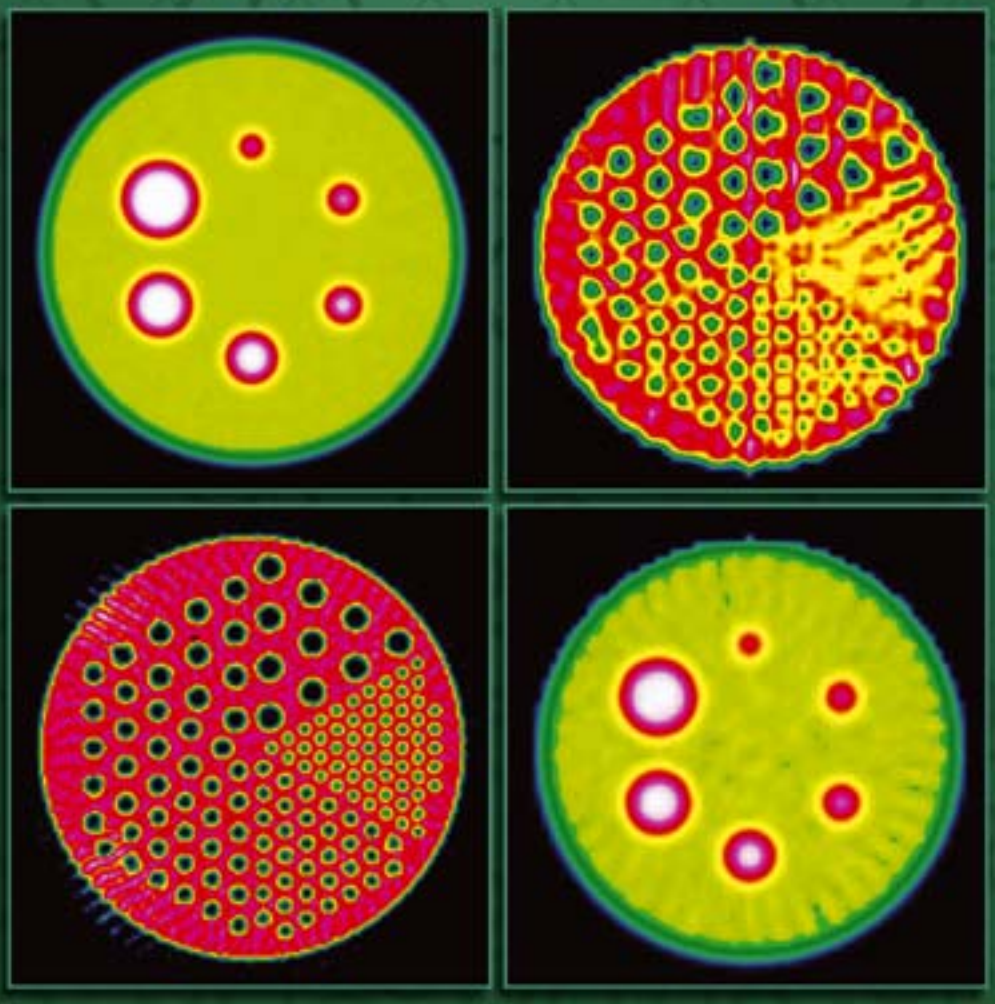

International Atomic Energy Agency

IAEA QUALITY CONTROL ATLAS FOR SCINTILLATION CAMERA SYSTEMS

Please note: This is a downsampled version for the Internet and does not show the full resolution of the images.

If you need the images in electronic form in full resolution, please order STI/PUB/1141 as CD-ROM.

The following States are Members of the International Atomic Energy Agency:

AFGHANISTAN
ALBANIA
ALGERIA
ANGOLA
ARGENTINA
ARMENIA
AUSTRALIA
AUSTRIA
AZERBAIJAN
BANGLADESH
BELARUS
BELGIUM
BENIN
BOLIVIA
BOSNIA AND HERZEGOVINA
BOTSWANA
BRAZIL
BULGARIA
BURKINA FASO
CAMBODIA
CAMEROON
CANADA
CENTRAL AFRICAN REPUBLIC
CHILE
CHINA
COLOMBIA
COSTA RICA
CÔTE D'IVOIRE
CROATIA
CUBA
CYPRUS
CZECH REPUBLIC
DEMOCRATIC REPUBLIC OF THE CONGO
DENMARK
DOMINICAN REPUBLIC
ECUADOR
EGYPT
EL SALVADOR
ESTONIA
ETHIOPIA
FINLAND
FRANCE
GABON
GEORGIA
GERMANY
GHANA
GREECE
GUATEMALA
HAITI
HOLY SEE
HONDURAS
HUNGARY
ICELAND
INDIA
INDONESIA
IRAN, ISLAMIC REPUBLIC OF
IRAQ
IRELAND
ISRAEL
ITALY
JAMAICA
JAPAN
JORDAN
KAZAKHSTAN
KENYA
KOREA, REPUBLIC OF
KUWAIT
LATVIA
LEBANON
LIBERIA
LIBYAN ARAB JAMAHIRIYA
LIECHTENSTEIN
LITHUANIA
LUXEMBOURG
MADAGASCAR
MALAYSIA
MALI
MALTA
MARSHALL ISLANDS
MAURITIUS
MEXICO
MONACO
MONGOLIA
MOROCCO
MYANMAR
NAMIBIA
NETHERLANDS
NEW ZEALAND
NICARAGUA
NIGER
NIGERIA
NORWAY
PAKISTAN
PANAMA
PARAGUAY
PERU
PHILIPPINES
POLAND
PORTUGAL
QATAR
REPUBLIC OF MOLDOVA
ROMANIA
RUSSIAN FEDERATION
SAUDI ARABIA
SENEGAL
SERBIA AND MONTENEGRO
SIERRA LEONE
SINGAPORE
SLOVAKIA
SLOVENIA
SOUTH AFRICA
SPAIN
SRI LANKA
SUDAN
SWEDEN
SWITZERLAND
SYRIAN ARAB REPUBLIC
TAJIKISTAN
THAILAND
THE FORMER YUGOSLAV REPUBLIC OF MACEDONIA
TUNISIA
TURKEY
UGANDA
UKRAINE
UNITED ARAB EMIRATES
UNITED KINGDOM OF GREAT BRITAIN AND NORTHERN IRELAND
UNITED REPUBLIC OF TANZANIA
UNITED STATES OF AMERICA
URUGUAY
UZBEKISTAN
VENEZUELA
VIETNAM
YEMEN
ZAMBIA
ZIMBABWE

The Agency's Statute was approved on 23 October 1956 by the Conference on the Statute of the IAEA held at United Nations Headquarters, New York; it entered into force on 29 July 1957. The Headquarters of the Agency are situated in Vienna. Its principal objective is "to accelerate and enlarge the contribution of atomic energy to peace, health and prosperity throughout the world''.

Printed by the IAEA in Austria
April 2003
STI/PUB/1141

IAEA QUALITY CONTROL ATLAS FOR SCINTILLATION CAMERA SYSTEMS

INTERNATIONAL ATOMIC ENERGY AGENCY
VIENNA, 2003

IAEA Library Cataloguing in Publication Data

IAEA quality control atlas for scintillation camera systems / [compiled by E. Busemann Sokole]. — Vienna : International Atomic Energy Agency, 2003.
p. ; 24 cm.
STI/PUB/1141
ISBN 92–0–101303–5
Includes bibliographical references.

1. Nuclear medicine — Equipment and supplies — Quality control. 2. Scintillation cameras. 3. Imaging systems in medicine. I. Busemann Sokole, E. II. International Atomic Energy Agency.

IAEAL 03–00312

EDITORIAL NOTE

FOREWORD

Nuclear medicine professionals deal with various medical images almost daily. Often, however, they may not be aware — as a result of the limited information available to them or of a lack of experience — of possible image problems, among them abnormalities in the image and various artefacts. At times, even when it is eventually seen that an image is incorrect, it is already too late to take any remedial action, for example in the case of images with crystal hydration at various stages. To provide nuclear medicine professionals with an assortment of examples of possible image errors and problems, this Quality Control Atlas has been produced under the auspices of the IAEA, through technical co-operation projects and research and technical contracts. About 250 typical nuclear scintillation camera images — normal images as well as those showing abnormalities and various artefacts — have been collected in this volume, all catalogued and provided with explanations as to the causes of and solutions to each individual image problem. This atlas is intended to be used as a guide on how to take proper quality control measures, on performing situation and problem analysis, and on problem prevention.

It is hoped that the atlas will be especially useful to physicists, physicians, technologists and service engineers in the nuclear medicine field. It is available in CD-ROM, Internet and hard copy versions.

The IAEA is grateful to the compiler/author of this atlas, E. Busemann Sokole, of the Academic Medical Centre, Amsterdam, as well as to the contributors and reviewers.

The IAEA technical officers responsible for the preparation of this publication are Y. Xie and A.K. Padhy of the Division of Human Health.

ACKNOWLEDGEMENTS

This Quality Control Atlas for Scintillation Camera Systems has been developed under the auspices of the IAEA. The content has been established from the contributions of many persons and represents a wide range of situations from around the world and from scintillation camera systems produced by different manufacturers.

The major contributors to this atlas are: L.S. Graham, United States of America, who, in particular, supplied many images and much of the text; A. Todd-Pokropek, United Kingdom, who supplied all the SPECT simulations; E. Busemann Sokole, Netherlands; and A. Wegst, USA.

Considerable contributions were also made by: C. Chow Robilotta, Brazil (especially for SPECT), and Anchali Krisanachinda, Thailand.

Further contributions were made by: J.S. AlSuwaidi, United Arab Emirates; A.J. Arends, Netherlands; H. Bergmann, Austria; J. Camps, Netherlands; D. Coiro da Silva, Brazil; T.D. Cradduck, Canada; A. Dias Neto, Brazil; V. Fidler, Slovenia; B. Hutton, Australia; M. Marengo, Italy; G.M. Oberladstaetter, Austria; H.Y. Oei, Netherlands; G.S. Pant, India; R. Puchal-Ane, Spain; A.H.J. Renders, Netherlands; R.L. Romijn, Netherlands; G. Sayed, USA; V.E. Soroa, Argentina; A. Teresinska, Poland; and R.E. Zimmerman, USA.

In April 1999, an IAEA workshop was convened in Amsterdam to review the images submitted up until that time and to assess the atlas content. The workshop included the following members: E. Busemann Sokole, Netherlands; L.S. Graham, USA; A. Krisanachinda, Thailand; A. Todd-Pokropek, UK; A. Wegst, USA; and Y. Xie, IAEA. Following this workshop, many more images were submitted for inclusion. Most of the images were in some form of hard copy — prints, X ray film, 35 mm slides, some original images and some copies — and only a few in digital format. During 2000 it became clear that all images required digitization so that they could be directly added to the text. Once digitization was completed, it became possible to produce a final manuscript with images, which, in files of about 2 Mbytes, could be sent for review. The following persons contributed to this final review: H. Bergmann, Austria; J. Camps, Netherlands; L.S. Graham, USA; M.K. O'Connor, USA; R. Puchal-Ane, Spain; C. Chow Robilotta, Brazil; A. Todd-Pokropek, UK; A. Wegst, USA; E.D. Williams, UK; and R.E. Zimmerman, USA.

The compiler/author, E. Busemann Sokole, is indebted to the members of the Department of Nuclear Medicine, Academic Medical Centre, Amsterdam, for their support and understanding during the final stages of the preparation of the manuscript, which involved digitizing images, the final writing and revision of the text, and acquiring additional illustrative images. Particular thanks are due to B.L.F. van Eck-Smit (Department Head), R. Mirhossini, J.N.N. Visser, I. Lingg and J. Habraken. The cover design was provided by R.J.J. Knol, Department of Nuclear Medicine, Academic Medical Centre, Amsterdam.

CONTENTS

1. INTRODUCTION

Accurate interpretation of nuclear medicine image data depends upon an understanding of image patterns and quantitative results. This holds true both for quality control tests and for clinical studies. Such an understanding is gained by learning from many different examples, in addition to having a thorough knowledge of the underlying principles and how to achieve optimum results. This publication is intended to assist with the learning process of interpreting quality control tests and recognizing artefacts. The examples are not limited to the quality control tests, but include clinical images obtained from unsuspected malfunctioning of the scintillation camera and/or computer system, suboptimal use of the system or operator error. It is as important to recognize deteriorating quality and artefacts in clinical images as it is in routine monitoring of system performance with quality control checks.

Gradual deterioration of image quality may be difficult to determine in clinical images of a particular investigation type, because of the variations in the patient population. However, a review of clinical studies and clinical procedures performed over a period of time can assist in determining reproducibility and consistency, and can reveal gradual changes. Although instrument performance should be monitored by routine and periodic quality control tests, instrumentation can malfunction unexpectedly and at any time. Continuous daily observance and alertness on the part of all persons involved are vital. When any abnormal situation or deterioration is suspected or encountered, immediate action is essential. This atlas gives some guidelines regarding possible procedures to follow for troubleshooting and problem solving.

The images and data presented in this atlas show normal results, abnormal results that occur if the imaging system is not adjusted or used properly, and artefacts due to defects in the system. Some image patterns are generic to any scintillation camera system, while others may be specific to a particular vendor system and depend on system design and corrections applied in image formation. New developments in imaging instrumentation and clinical procedures will introduce other variants.

The user should learn what to expect from his/her particular instrument. Communication with others using the same vendor and type of system, and exchange of experience (possibly through users' groups), make an excellent starting point. The examples in this atlas cover a wide range of different situations and represent just some of the variants that may be observed. Where possible, data acquisition and analysis parameters, and other relevant conditions, such as environmental conditions, are included.

For definitions of terms and details of quality control tests, the reader is referred to:

INTERNATIONAL ATOMIC ENERGY AGENCY, Quality Control of Nuclear Medicine Instruments, IAEA-TECDOC-602, Vienna (1991).

A copy may be obtained from the Nuclear Medicine Section, IAEA, Wagramer Strasse 5, P.O. Box 100, A-1400 Vienna, Austria.

In order to assist the users of this atlas, all examples are presented in a consistent style as follows:

- Image;
- Brief description of the acquisition technique, radionuclide/radiopharmaceutical and any specific circumstances necessary to the understanding of the example image;
- Results: what is seen and what conclusions are drawn;
- Comments: advice regarding the results, follow-up strategies, etc.
- Specific literature reference (if appropriate).

In order to maintain and update this Quality Control Atlas, further well documented examples are required. Readers are encouraged to contribute to this process by submitting material that could assist others. Data should preferably be submitted in digital form, or otherwise as a hard copy or a 35 mm slide, with an accompanying description following the style used in this atlas. The digital data should be appropriate for viewing on a high resolution computer monitor (which implies digitization

to about 1500 pixels in width), and should preferably be stored in JPEG (with a high quality factor) or PCX format. The file size should then be about 200 kB.

Examples, with their associated images as attachments, may be sent by e-mail to the following address:

E.SOKOLE@AMC.UVA.NL

or mailed to:

E. Busemann Sokole, PhD,
Department of Nuclear Medicine,
Academic Medical Centre,
Meibergdreef 9,
1105 AZ Amsterdam, Netherlands

Tel: +31 20 566 4550
Fax: +31 20 566 9092

1.1. DEFINITIONS

For definitions of terms and information on quality control testing see:

INTERNATIONAL ATOMIC ENERGY AGENCY, Quality Control of Nuclear Medicine Instruments, IAEA-TECDOC-602, Vienna (1991), a copy of which may be obtained as indicated above.

NATIONAL ELECTRICAL MANUFACTURERS ASSOCIATION, Performance Measurements of Scintillation Cameras, NEMA Standards Publication No. NU1, Washington, DC (1994).

1.2. ABBREVIATIONS

Images

T	top
M	middle
B	bottom
R	right
L	left
TR, TL	top right, top left
MR, ML	middle right, middle left
BR, BL	bottom right, bottom left

Text

ADC	analogue to digital converter
CFOV	centre field of view
COR	centre of rotation
CRT	cathode ray tube
DTPA	diethylenetriaminepentaacetic acid
ECG	electrocardiogram
ECT	emission computed tomography
FBP	filtered back-projection
FOV	field of view
FWHM	full width at half-maximum

HIDA	hepatoiminodiacetic acid
HMPAO	hexamethylpropylenamine oxime
IMP	isopropyliodoamphetamine
LEAP	low energy all purpose
LEHR	low energy high resolution
LEUHR	low energy ultra-high resolution
MAA	macroaggregated albumin
MDP	methylene diphosphonate
MIBG	meta-iodobenzylguanidine
MWSR	multiple window spatial registration
NEMA	National Electrical Manufacturers Association
OHP	orthogonal hole phantom
PHA	pulse height analyser
PLES	parallel line equal spacing
PM	photomultiplier
QC	quality control
SPECT	single photon emission computed tomography
UFOV	useful field of view

2. PLANAR

2.1. PULSE HEIGHT ANALYSER

2.1.1. Example: Wrong energy setting — uniformity

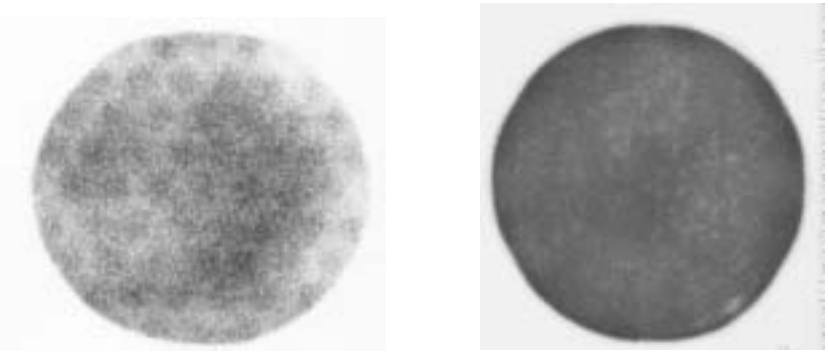

A B

Two examples, from different departments and different cameras, of a routine QC check of extrinsic flood field uniformity made with a ^{57}Co sheet source and low energy collimator. In both instances the energy window had not been set for ^{57}Co but remained at the energy window setting of ^{99m}Tc, which had been used in the previous clinical study.

Results: Both images show non-uniformity because the ^{57}Co source was imaged with a ^{99m}Tc energy window.

A shows poor tuning and visible PM tubes.
B shows discrete small cold spots (the white on the grey) due to crystal hydration.

Comments: When performing any study, it is imperative to visually check the energy window in the spectral display mode with the nuclide to be imaged prior to data acquisition. This is even more important in a modern scintillation camera in which the energy window setting is defined electronically as one field in the set of data acquisition parameters.

In this example, the ^{99m}Tc energy window (set over 140 keV) is equivalent to an asymmetric energy window set on the high side of the ^{57}Co photopeak (122 keV). This incorrect energy window still produces a reasonable count rate so that an image can be made. However, the time taken for collection of the image is much longer than is usual, and this should be taken as a signal that something is wrong with the set-up of the study.

Note that if the reverse situation existed, and ^{99m}Tc were imaged in a ^{57}Co energy window, then the cold spots seen in image B would become hot spots (the ^{57}Co window is equivalent to an asymmetric window on the low side of the ^{99m}Tc photopeak).

See Sections 2.2.2 and 2.2.7.4 for more information about crystal hydration.

2.1.2A. Example: QC tests — unstable energy window setting (1)

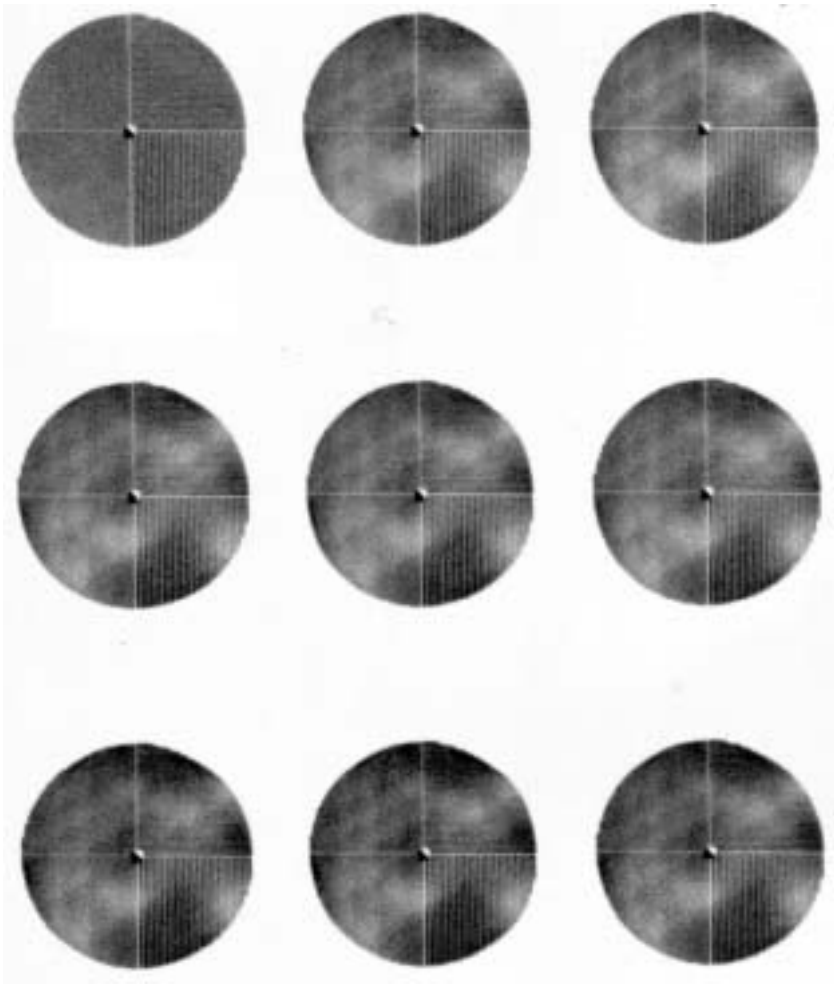

A dynamic series of analogue consecutive intrinsic spatial resolution images using ^{99m}Tc were made to check the consistency of the image formatter. The energy window had been centred over the photopeak of ^{99m}Tc prior to the check.

Results: The top left image shows the spatial resolution image as expected. All other images appear patchy because the energy window over the photopeak had shifted.

Comments: The correct energy window setting and a stable energy window are crucial for good data acquisition. The centre line should be monitored and action taken if drift occurs or if instability is suspected or found.

2.1.2B. Example: Clinical study — unstable energy window setting (2)

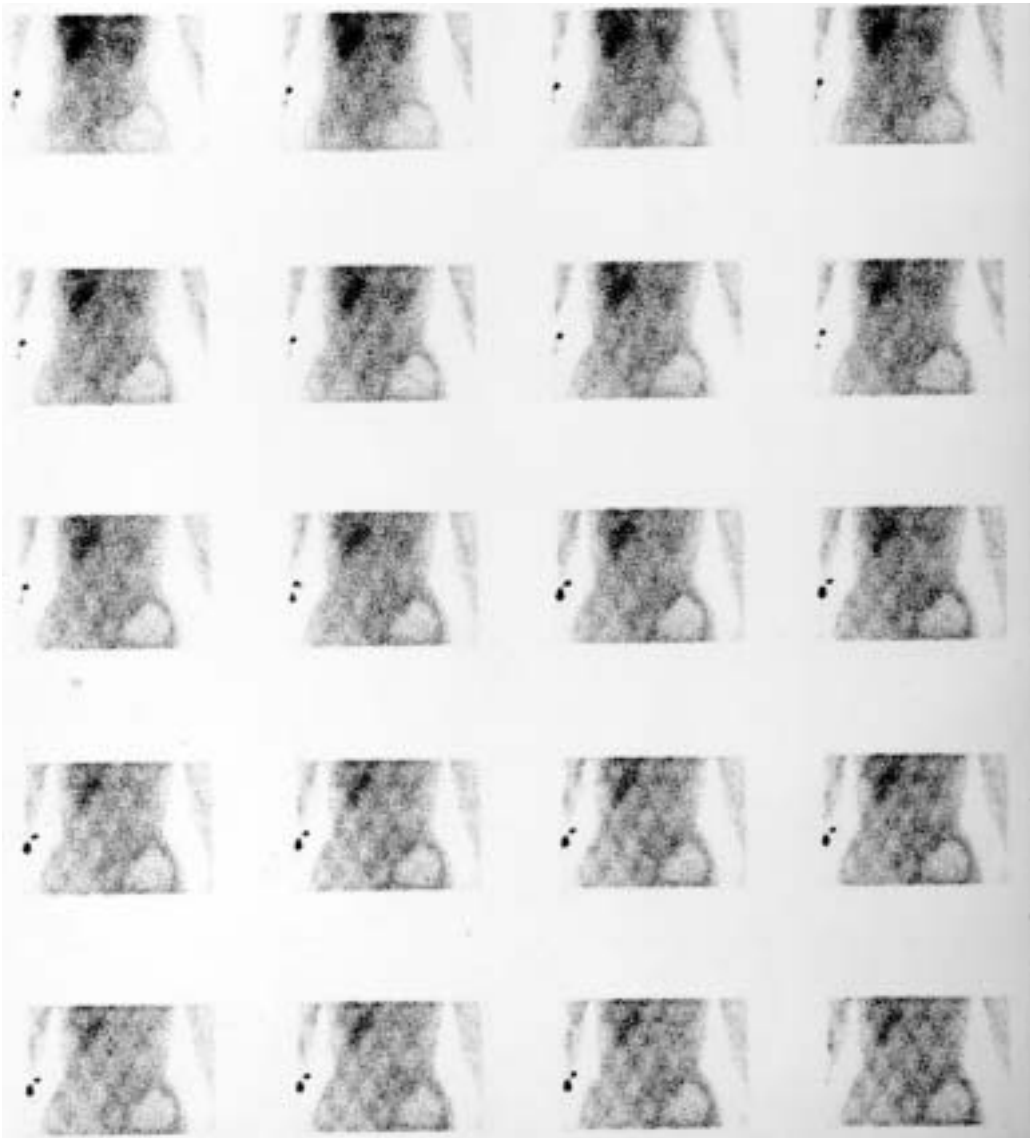

Clinical study of a patient who underwent a dynamic ^{99m}Tc DTPA study of the kidneys. The 20 consecutive images (30 s each) shown here were obtained in the posterior view starting at 1 min (top left) after intravenous injection of 110 MBq of ^{99m}Tc DTPA. The 20% energy window had been set over the photopeak of ^{99m}Tc before the study was started.

Results: During the study the energy window position in relation to the ^{99m}Tc photopeak slowly changed, producing images of increasingly poorer uniformity. All PM tubes became visible. This is especially evident about halfway through this series of images but is also seen in the first image.

The problem was an unstable high voltage, causing a change in PM tube gain and thus a drift of the energy peak out of the PHA window. Service was required.

Note: The large, circular cold area in the lower right hand part of the FOV was an artefact from the patient and not the camera.

2.1.2C. Example: Dynamic clinical study — unstable energy window (3)

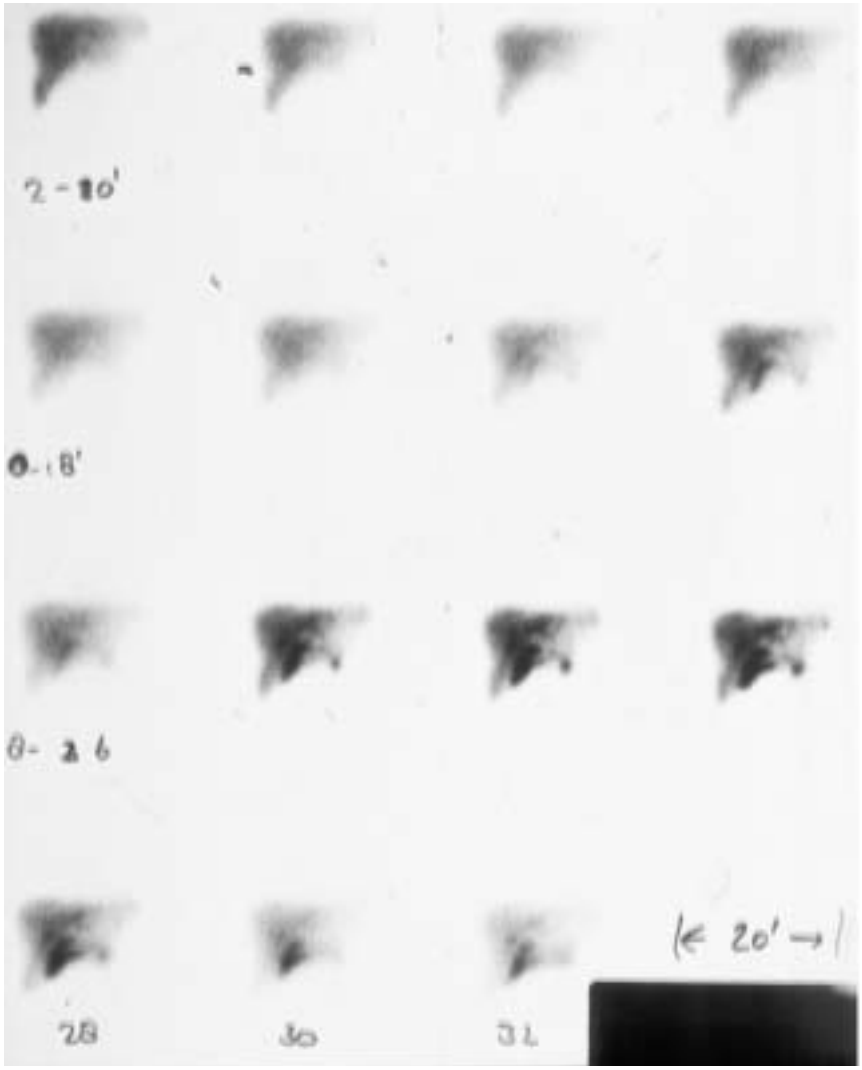

Dynamic clinical study of hepatobiliary function using ^{99m}Tc HIDA. 15% energy window. Each image is of 2 min duration starting at 2 min (top left).

Results: The 15 consecutive images show fading in image intensity and changes in contrast between images that are unrelated to the physiological change in activity distribution in the liver and gall bladder. This was caused by an unstable energy window position, so that the counts within the energy window fluctuated between the consecutive images of the dynamic study.

Comments: This problem was due to instability within the scintillation camera. It was not a problem of the formatter giving a non-uniform response in different parts of the film.

2.1.2D. Example: Dynamic clinical study — energy peak shift — electrical grounding problem

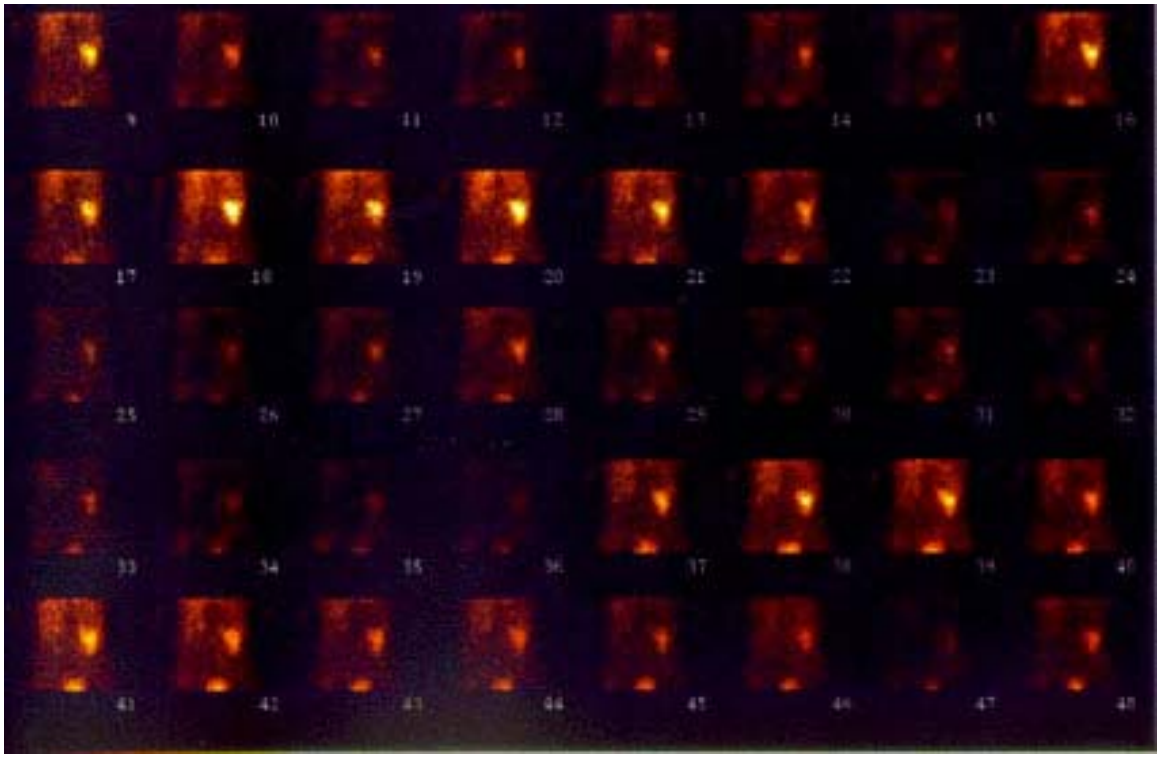

Dynamic clinical study of kidney function using a ^{99m}Tc radiopharmaceutical. 15% energy window.

Results: The intensity varied considerably between the images. The problem was a missing ground connection in the power supply to the detector head.

Comments: This problem first became evident during dynamic studies about six months after the installation of a new digital camera. These studies sometimes showed images of varying intensities within the dynamic group. The group of images given here is a drastic example of this. The routine QC uniformity studies gave normal results, with non-uniformity of less than 2%.

The technologist who was responsible for QC observed that the energy peak sometimes shifted between 90 and 160 keV, the effect seemingly connected to the position of the detector head or the movement of the head. The local service personnel spent several weeks trying to locate the problem, concentrating mainly on the detector head, but without success. The hospital finally insisted that the local service personnel consult the main service office, where in fact the problem and solution were known: a missing ground connection to the power supply for the head, located in the gantry (and not the detector head). Two points on potential zero required to be connected, a simple procedure.

This example illustrates not only the difficulty in finding problems, but also the usefulness of consulting a wider network of service resources and the error logs that manufacturers maintain. This could reduce the time required to solve problems as well as reduce the possibility of erroneous patient studies and of repeat studies involving an extra radiation burden to the patient.

2.1.2E. Example: Static clinical study — energy peak shift — electrical grounding problem

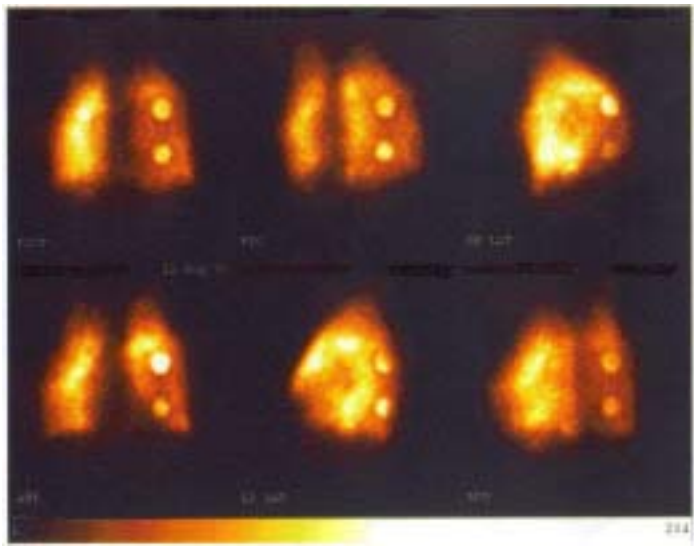

A

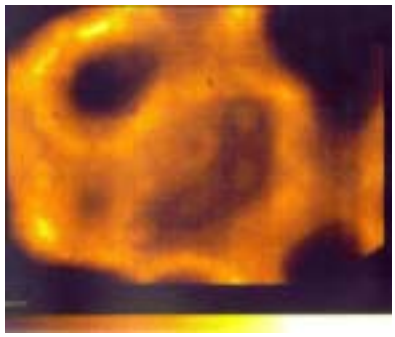

B

This static clinical lung perfusion study using ^{99m}Tc macroaggregates was obtained with the same scintillation camera as for the previous example, 2.1.2D. The camera was a relatively new digital camera with a rectangular FOV.

A: Six static images (400 000 counts each image) forming a clinical lung perfusion study in six different views.
B: Flood field image obtained after the lung study.

Results: In the left set of images of the lungs, two intense hot spots are seen in the same location in the right half of the FOV in each image. The right image of the uniformity of the camera obtained after the clinical study shows gross non-uniformity.

Before the study was started, the energy window position over the ^{99m}Tc photopeak had been checked and was satisfactory.

The artefacts were observed at a time when the camera was known to have an unstable photopeak position with respect to the energy window. The changes in energy peak position were dynamic processes and were caused by a fault in the electrical grounding of the digital camera, which had one ADC per PM tube. Significant changes could be found within minutes. The flood image above therefore does not necessarily show the situation at the time of the clinical study and does not exactly explain the lung images in detail. It only shows a rough overview of the status which could develop within minutes.

Comments: See example 2.1.2D for further information.

2.1.3. Example: Energy window autopeak not functioning properly

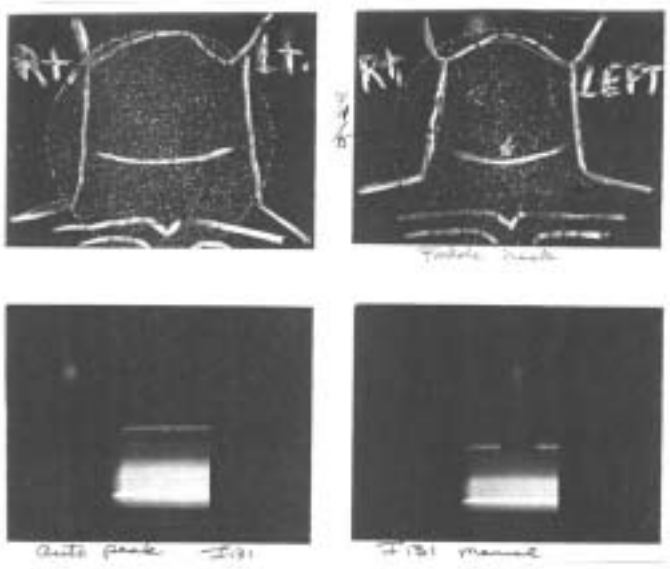

Images of the thyroid region were obtained with a pinhole collimator following administration of ^{131}I in order to ascertain the remaining thyroid function. The preset energy window of the scintillation camera had been set without first checking the accuracy of this setting.

TL: Thyroid image using the preset energy window.
BL: Energy spectrum after automatically peaking the energy window (as depicted from an old analogue camera). The energy window is not positioned over the photopeak of ^{131}I.
TR: Thyroid image using manually adjusted energy window.
BR: Energy spectrum from manually adjusted energy window. The window is now set symmetrically over the photopeak of ^{131}I (seen as a narrow black band on the upper narrow white stripe which represents the photopeak).

Results: The thyroid image using the autopeaked energy window shows a diffuse pattern corresponding to background and no discernible foci of ^{131}I. This was due to the energy window not being centred on the 364 keV photopeak of ^{131}I. When the energy window was manually adjusted, the thyroid image did indeed show localized foci of ^{131}I uptake in the neck.

Comments: Although this example is a historic one from a very old camera, it nevertheless holds a message, namely that a properly adjusted energy window is essential. In this example the patient would have had a misdiagnosis. It is imperative that any preset window settings be checked prior to scintigraphy.

2.2. UNIFORMITY

2.2.1. Symmetric energy window — ^{99m}Tc

A symmetric energy window is one where the photopeak energy is at the centre of the window.

For ^{99m}Tc:

A 20% energy window set symmetrically over the ^{99m}Tc photopeak is equivalent to 140 ± 10% keV or a window spanning 126–154 keV.

A 15% energy window set symmetrically over the ^{99m}Tc photopeak is equivalent to 140 ± 7.5% keV or a window spanning 130–151 keV.

A 10% energy window set symmetrically over the ^{99m}Tc photopeak is equivalent to 140 ± 5% keV or a window spanning 133–147 keV.

2.2.1A. Example: Symmetric 20% energy window

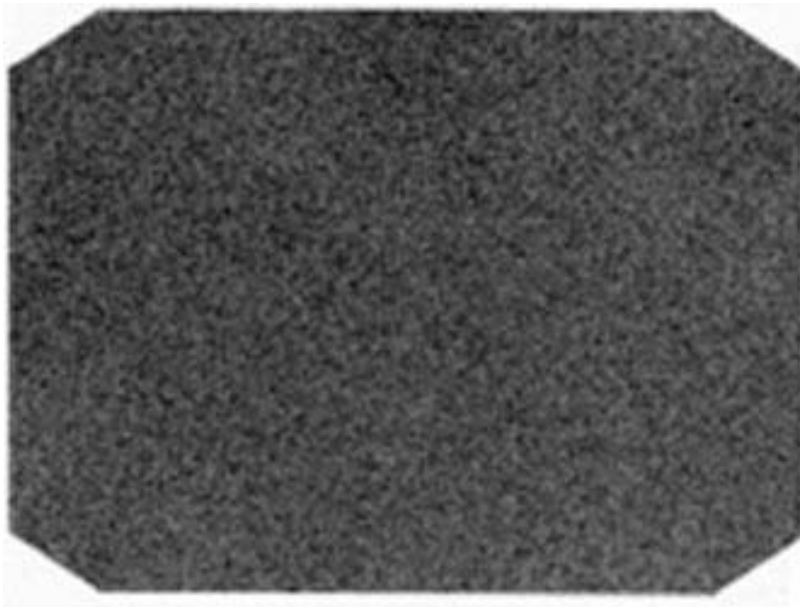

Routine intrinsic uniformity image, ^{99m}Tc, 3 million counts, 20% energy window set symmetrically over the 140 keV photopeak of ^{99m}Tc.

Results: The image shows good uniformity.

Comments: The most basic and sensitive routine QC test of a gamma camera is that of uniformity. This must be performed carefully (preferably daily before using the camera for clinical studies), it must be critically evaluated and any necessary action must be undertaken before further imaging takes place.

See also Section 2.2.4.

2.2.1B. Example: Symmetric 10%, 15% and 20% energy windows (1)

10% energy window

15% energy window

20% energy window

Intrinsic uniformity, ^{99m}Tc, 30 million counts each image, no contrast enhancement of images, acceptance testing.

TL: 10% symmetric energy window.
TR: 15% symmetric energy window.
B: 20% symmetric energy window.

Results: Comparison of the three images shows a degradation in uniformity as the window width is decreased. At a 10% energy window, a pattern of PM tubes is seen in the right half of the uniformity image. The scintillation camera was retuned.

Comments: This test assesses the state of tuning of the PM tubes. Uniformity can be slightly degraded as the energy window width is decreased. It is not unusual to obtain non-uniformity at a 10% energy window, but the asymmetry in non-uniformity observed in this example indicates a problem. Periodic performance of this test is important to assess the state of tuning of PM tubes and when narrow energy windows are clinically used (e.g. when performing dual isotope studies).

2.2.1C. Example: Symmetric 10%, 15% and 20% energy windows (2)

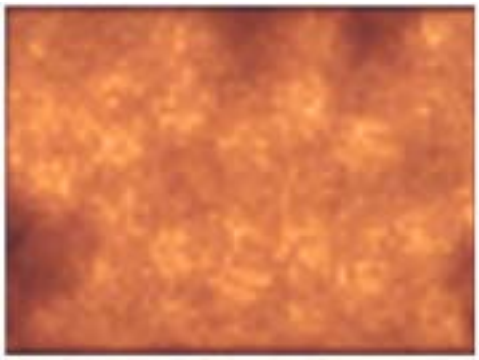

10% energy window

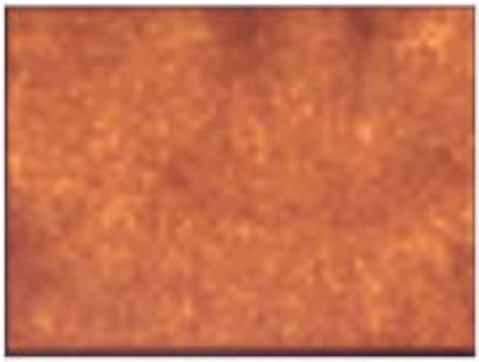

15% energy window

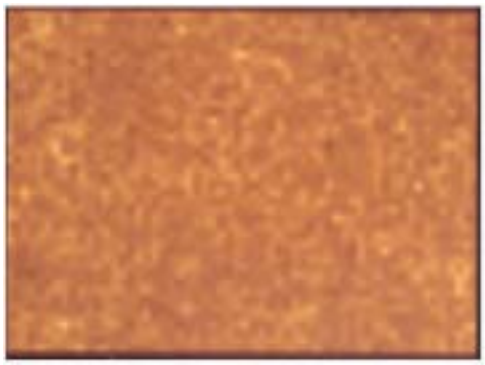

20% energy window

Intrinsic uniformity, ^{99m}Tc, 30 million counts each image, no contrast enhancement of images, modern scintillation camera, images obtained at acceptance testing.

TL: 10% symmetric energy window.
TR: 15% symmetric energy window.
B: 20% symmetric energy window.

Results: Comparison of the three images shows an overall degradation in uniformity as the window width is decreased. Non-uniformity is already quite evident in the 15% energy window image. At 10% the poor tuning is obvious. These results are unacceptable. The scintillation camera was retuned.

Comments: Uniformity can be slightly degraded as the energy window width is decreased, but there should not be non-uniformity to such a degree as in this example. Since the energy resolution of modern cameras is <10%, a 15% energy window is recommended for clinical imaging (in order to avoid loss of contrast due to scatter). The image obtained with a 15% symmetric energy window must therefore be uniform. This example clearly shows a state of poor tuning of the PM tubes.

This test is one of the first tests that should be done at acceptance testing. If an unsatisfactory result is obtained, servicing and retuning must be performed before further acceptance tests are carried out. Furthermore, periodic performance of this test is important when narrow energy windows are clinically used (e.g. when performing dual isotope studies).

2.2.1D. Example: Symmetric energy window — defective linearity map

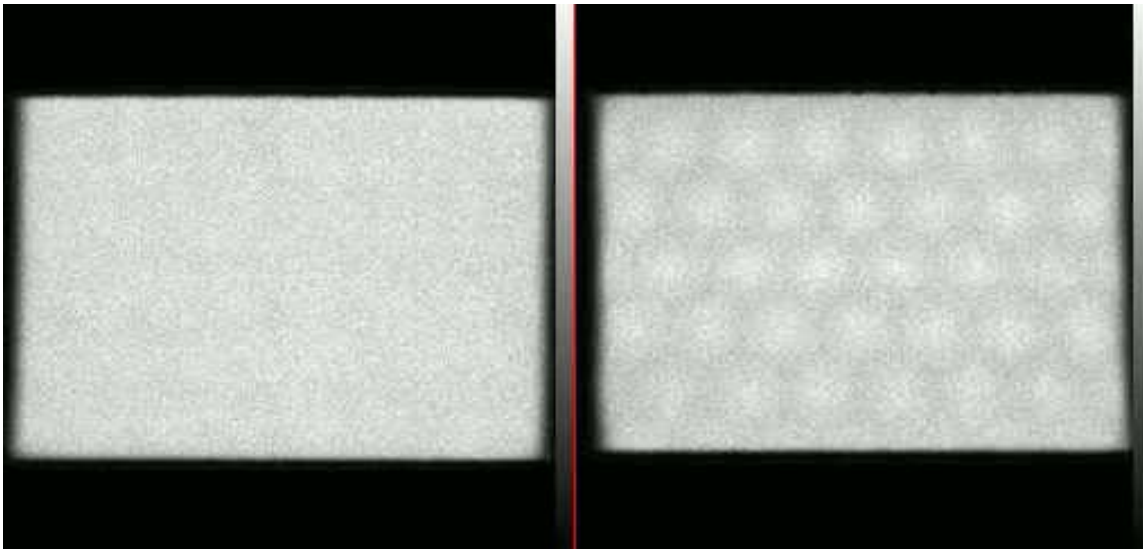

Dual head scintillation camera, routine extrinsic flood images from each detector using ^{57}Co sheet source placed centrally between the detectors with the detectors at their maximum distance apart, 20% symmetric energy window, 30 million counts each image.

Results: The image on the left, from detector 1, shows good uniformity. A new linearity correction had just been performed. The image on the right, from detector 2, shows poor uniformity. All PM tubes are clearly visible as a homogeneous pattern of hot areas. The PM tube pattern is uniform, indicating that this detector is well tuned. However, the linearity maps need to be renewed. This level of deterioration is unacceptable.

Comments: Following the recreation of the linearity maps, the uniformity of detector 2 was similar to that of detector 1.

2.2.1E. Example: Symmetric energy window — source too close to detector in intrinsic uniformity measurement

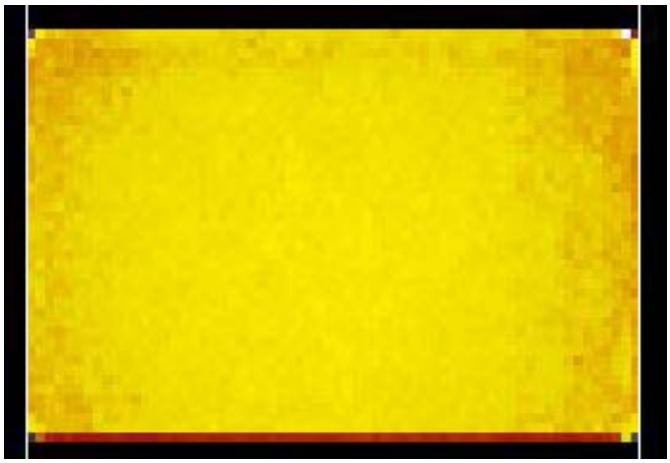

Intrinsic uniformity image, ^{99m}Tc point source, detector to source distance of about 3 FOV, 30 million counts, 20% symmetric energy window.

Results: The image shows increased counts towards the centre (more uniformly intense yellow in this colour table) and a fall-off in counts towards the edge of the FOV. This convex response (dome effect) is the result of the point source being too close to the detector. Apart from this dome effect, the general appearance of the image shows no obvious uniformity defects. However, for a proper assessment of more subtle non-uniformities, a software inverse square correction should be applied. Alternatively, if the detector configuration permits, the source should be placed at more than 5 FOV distance from the detector.

Comments: In some cameras, the software correction is based on the source being at a fixed distance and configuration (the manufacturer supplies a jig and source holder). In other cameras, the source can be at a variable distance, and a least squares fit is used to correct for the inverse square effect of the image pattern obtained. In the case of a variable distance, a reference distance, or minimum distance, should be specified and used.

This problem of an intrinsic measurement of uniformity being made with a source placed too close to the detector is to be avoided, but it may be inevitable owing to the architecture of the scintillation camera or room configuration.

2.2.1F. Example: Uniformity with and without a uniformity correction map

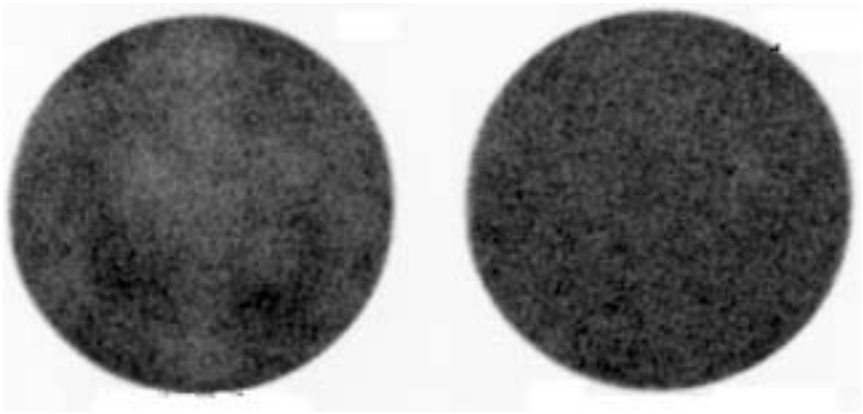

Two extrinsic uniformity images from the same scintillation camera without and with a uniformity correction map applied, ^{57}Co, 20% energy window set symmetrically over the photopeak, 2 million counts each image.

L: Image obtained without application of the uniformity correction map.
R: Image obtained with the appropriate uniformity correction map.

Results: The left image shows the state of tuning of the camera and is unevenly non-uniform. This is concealed by the application of the uniformity correction map (right image).

Comments: A uniformity correction map can conceal severe non-uniformity problems. Scintillation camera systems that require the use of a uniformity correction map should be periodically tested without application of this map in order to assess the state of tuning of the camera.

2.2.2. Asymmetric energy windows

Schematic representation of asymmetric energy windows

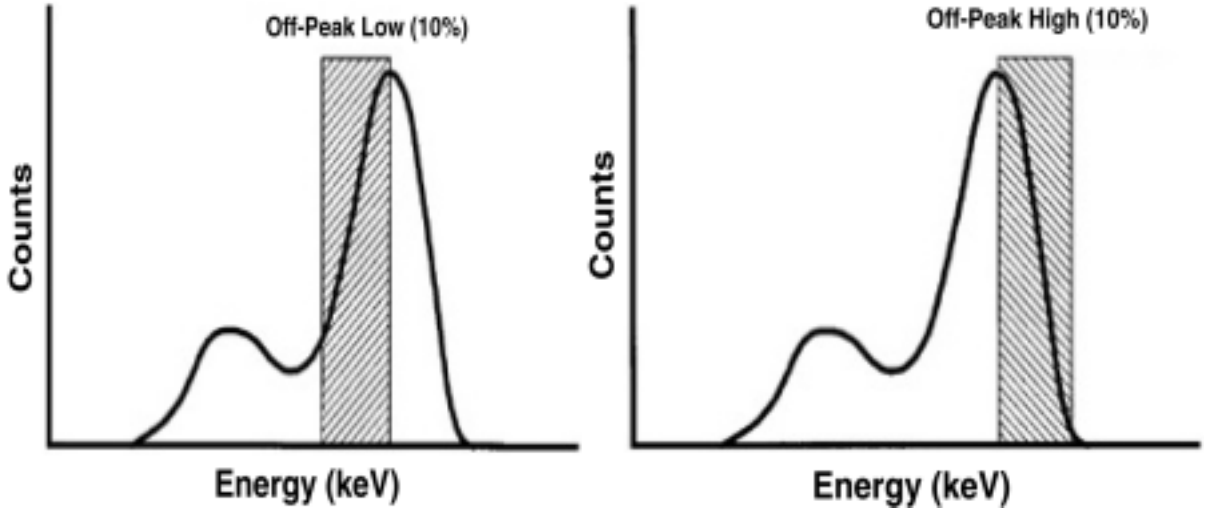

Asymmetric energy windows are produced when the photopeak is not centred within the pulse height analyser window. The diagrams illustrate the position of an asymmetric high and an asymmetric low energy window.

L: 10% energy window set asymmetrically over the lower half of the photopeak (126–140 keV) (asymmetric low, sometimes also referred to as off-peak low).
R: 10% energy window set asymmetrically over the upper half of the photopeak (140–154 keV) (asymmetric high, sometimes also referred to as off-peak high).

Comments: Asymmetric energy windows are used to check the NaI(Tl) detector for effects of possible hydration, sometimes called measles (because the crystal is hygroscopic), to evaluate the balance or tuning of PM tubes and to reveal electronic problems. Some scintillation cameras are more sensitive to off-peak windows than others, even when the same amount of asymmetric shift is used.

For more information on crystal hydration, see Section 2.2.7.4.

2.2.2A. Example: Asymmetric energy window — good result

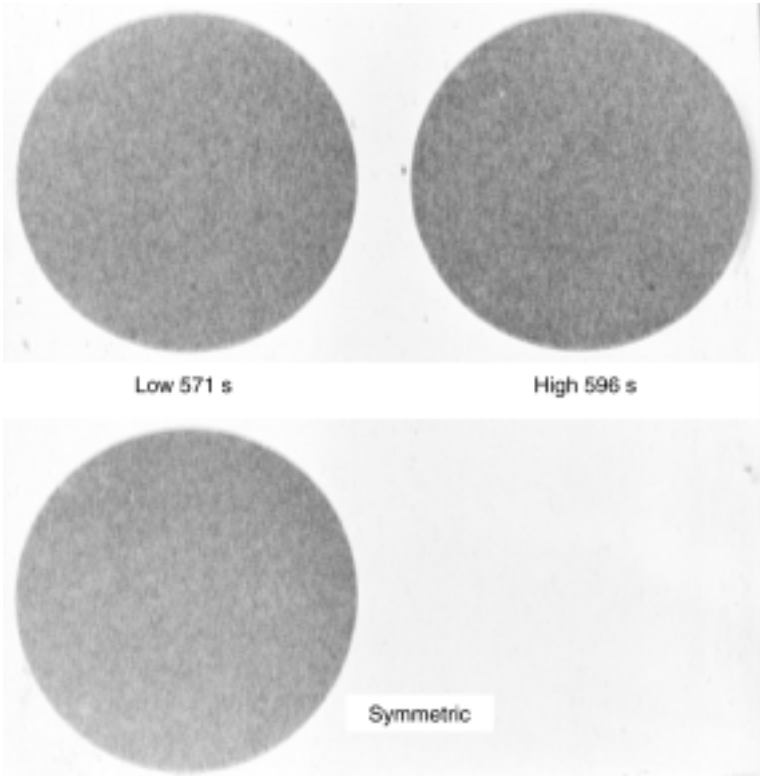

Intrinsic uniformity, ^{99m}Tc, 20% energy window, 3 million counts each image.

L: 10% asymmetric low energy window.
R: 10% asymmetric high energy window.
BL: 20% symmetric energy window.

Results: For this scintillation camera, the images all show good uniformity and tuning in all energy windows. This indicates that the linearity and energy corrections are working well, and that the camera is well tuned.

2.2.2B1. Example: Symmetric and asymmetric energy windows — poor PM tube balance and crystal hydration

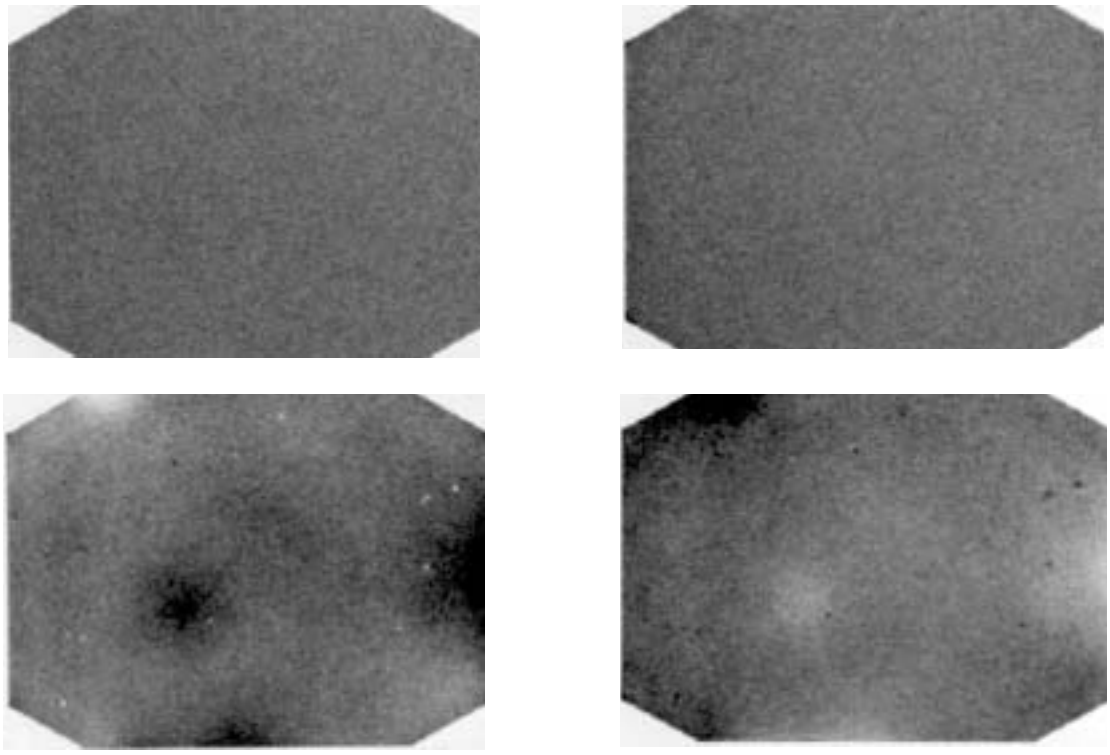

Four million counts were acquired in each of the four intrinsic (collimator removed) QC images. Images with asymmetric windows were acquired in order to check PM tube balance and whether there was any hydration of the crystal.

TL: 20% symmetric energy window, approximately 30 000 counts/s.
TR: 20% symmetric energy window, approximately 75 000 counts/s.
BL: 10% asymmetric high energy window.
BR: 10% asymmetric low energy window.

Results: The TL and TR images show that intrinsic uniformity with symmetric windows at moderate and high count rates is generally satisfactory. The images obtained with asymmetric energy windows reveal that both problems are present. Some PM tubes are out of balance and the detector is hydrated. The latter condition is sometimes called measles.

In the asymmetric high image, there are some regions with higher counts that appear darker, indicating that some tubes have higher gain than others. Tubes with lower gain appear as regions of reduced intensity. The small areas of hydration appear as cold spots.

In the asymmetric low image, the tubes that are hot or cold in the asymmetric high window image appear as cold or hot, respectively. Crystal hydration now appears as hot spots.

Comments: At this point in time this crystal does not need to be replaced, but it will probably deteriorate with time and the measles will eventually appear in the standard symmetric (on-peak) window images.

The fact that off-peak images reveal hydration before it affects clinical images makes it possible to select an appropriate time at which the detector will be replaced, or a decision can be made to replace the camera if funds are available.

For more information on crystal hydration, see Section 2.2.7.4.

2.2.2B2. Example: Asymmetric energy windows — comparison of images from cameras manufactured by two different vendors

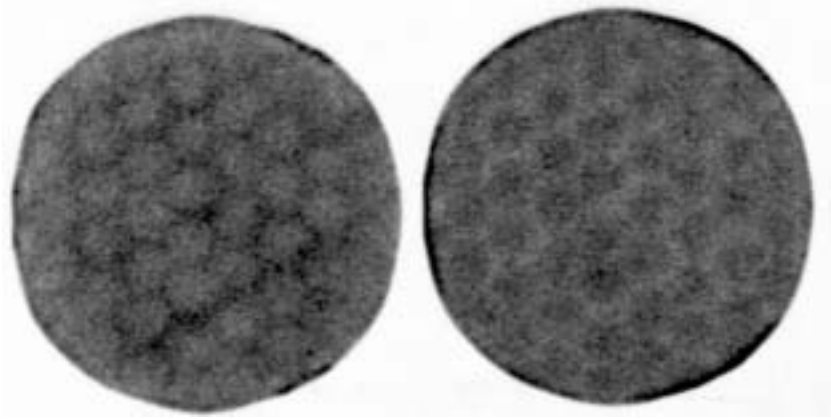

Manufacturer A

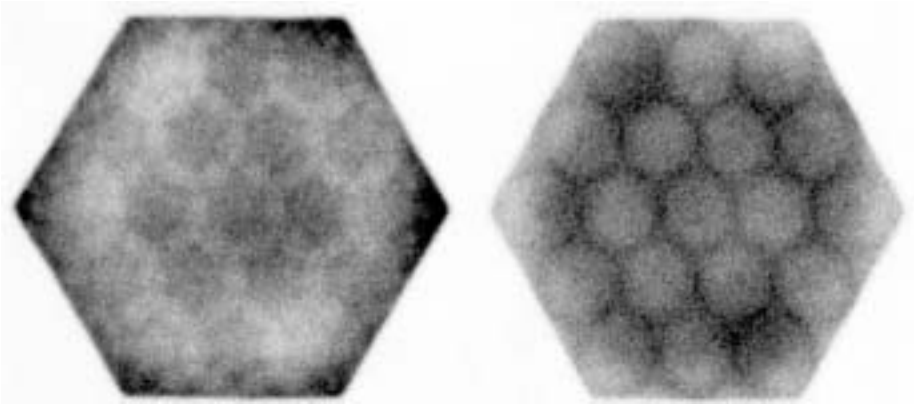

Manufacturer B

Two scintillation cameras from different manufacturers. Intrinsic uniformity, ^{99m}Tc, 2.5 million counts each image. (The asymmetric energy windows were shifted from the symmetric position by 10%.)

Top row: Camera from manufacturer A:
L: 20% asymmetric low energy window.
R: 20% asymmetric high energy window.

Bottom row: Camera from manufacturer B:
L: 20% asymmetric low energy window.
R: 20% asymmetric high energy window.

Results: On camera A the asymmetric low window shows the individual tubes as cold. On camera B the asymmetric low window shows the tubes as warm. With the asymmetric high windows this situation is reversed.

In addition, camera A shows a pattern of PM tubes that is uniformly intense throughout the FOV, indicating good tuning, whereas camera B shows considerable variation in intensity in the PM tube pattern, indicating poor tuning.

Comments: The difference in images between these two cameras is due to their design. Camera A uses a light pipe to produce a uniform image. Camera B does not have a light pipe and uses non-linear preamplifiers and a skimming technique to produce a uniform image. Both cameras utilize energy and linearity correction circuits.

This example indicates that not all scintillation cameras show the same patterns.

2.2.2C1. Example: Asymmetric energy window — poor PM tube adjustment

Intrinsic uniformity, ^{99m}Tc, 3 million counts each image.

L: 10% asymmetric low energy window.
R: 10% asymmetric high energy window.

Results: The extremely irregular non-uniformity in the images shows very poor adjustment or tuning of the PM tubes. The images complement each other: hot areas on the asymmetric low window setting correspond to cold areas on the asymmetric high window setting. These images were obtained at acceptance testing. The vertical and horizontal stripes also seen indicate a problem with the linearity correction. The scintillation camera requires servicing before further acceptance tests are performed.

Comments: This extremely poor test result indicates an unacceptable situation. It is not to be expected at acceptance testing. Before further tests are performed on this camera, the camera should be tuned and all corrections reloaded.

2.2.2C2. Example: Asymmetric energy window — out of balance PM tubes

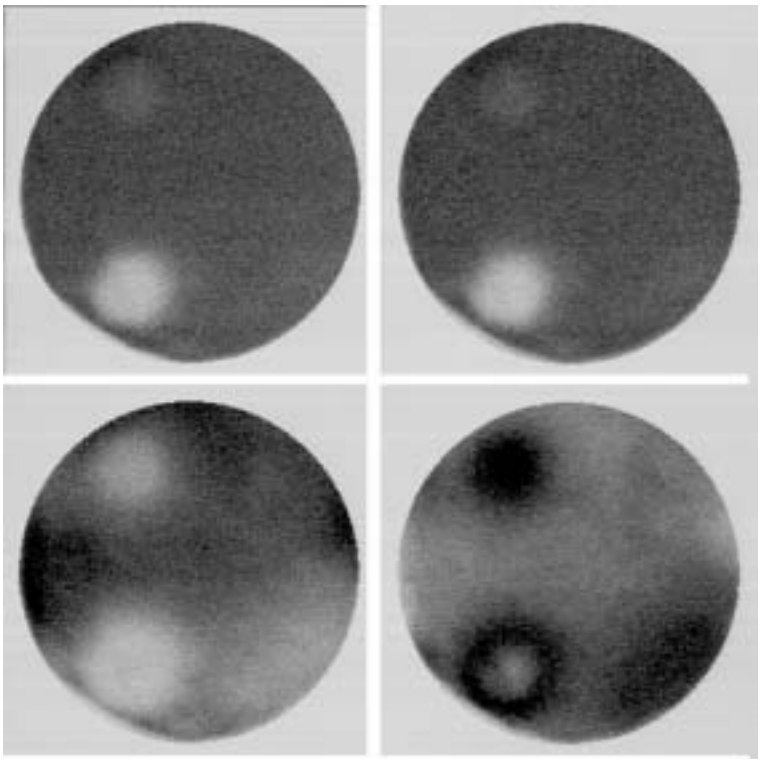

Intrinsic uniformity images were acquired with 2.5 million counts for each image using a 20% energy window.

TL: Symmetric energy window, ~30 000 counts/s.
TR: Symmetric energy window, ~75 000 counts/s.
BL: Asymmetric high energy window.
BR: Asymmetric low energy window.

Results: The symmetric energy window images (upper row) reveal one PM tube that is slightly out of tune (in the upper left quadrant) and a second tube that is markedly out of tune (in the lower left quadrant). The two PM tubes appear as cold areas in the asymmetric high energy image (BL), which indicates that both tubes have low gain/voltage. The asymmetric low energy image (BR) confirms that the gain/voltage for both tubes is low by showing the same tubes as hot areas. Moreover, the more intense of these two tubes (in the lower left quadrant of the image) has an unusual cold spot in the centre. The reason for this cold centre is that some light from events close to the PM tube is not measured, and the system interprets this as photons of lower energy than their true value. If the asymmetric energy window were set even lower, both the hot ring and the central cold area would appear smaller. These PM tubes need to be adjusted or replaced.

2.2.2C3. Example: Asymmetric energy window — poor tuning

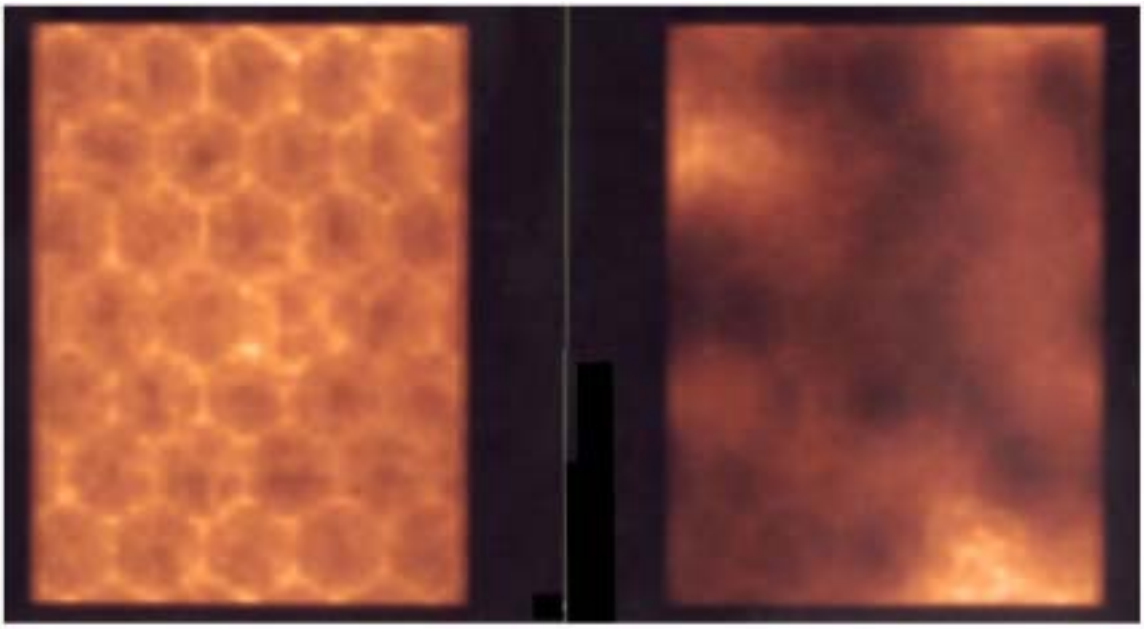

Dual head scintillation camera, intrinsic uniformity, ^{99m}Tc, 10% energy window set asymmetrically low over the photopeak. The images were obtained at acceptance testing of the camera.

L: Image from detector 1.
R: Image from detector 2.

Results: The left image shows a reasonably uniform hexagonal pattern of PM tubes. The right image shows very patchy uniformity. The wide variation in response is indicative of very poor tuning. This detector requires retuning before further acceptance tests are performed.

2.2.2D1. Example: Asymmetric energy window — crystal hydration (1)

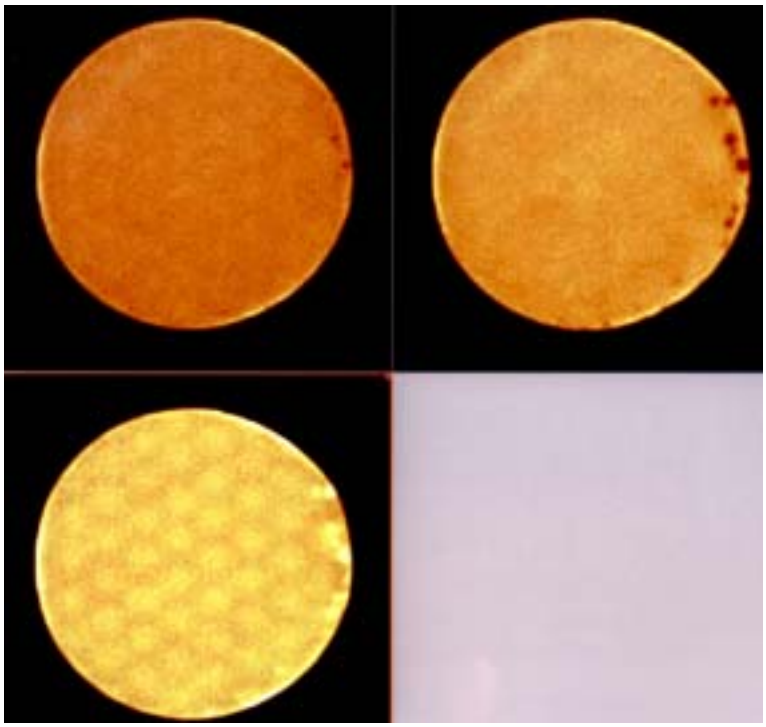

Intrinsic uniformity, ^{99m}Tc, 30 million counts each image, 512 × 512 matrix.

TL: 20% symmetric energy window.
TR: 10% asymmetric high energy window.
BL: 10% asymmetric low energy window.

Results: The effect of hydration is clearly visible on the right border of the FOV. It is seen as discrete cold spots on the offset high image (TR) and as complementary hot spots on the offset low image (BL). An indication of the presence of hydration is also visible on the symmetric window image (TL).

Comments: This is a sensitive test of the condition of hydration of a crystal. A high number of total counts is required. When obtaining a digital image, a large matrix size (small pixel size) must be used, because larger pixel sizes could cause small scale defects to be concealed.

The example given here shows a severe condition, since it is already visible in the symmetric energy window image. However, the hydration is at the edge of the FOV, and when the collimator is mounted, it will not give artefacts in clinical images. This situation needs to be carefully monitored in order to assess the progress of hydration as it spreads and covers more of the FOV. The crystal will eventually need to be replaced.

2.2.2D2. Example: Asymmetric energy window — crystal hydration (2)

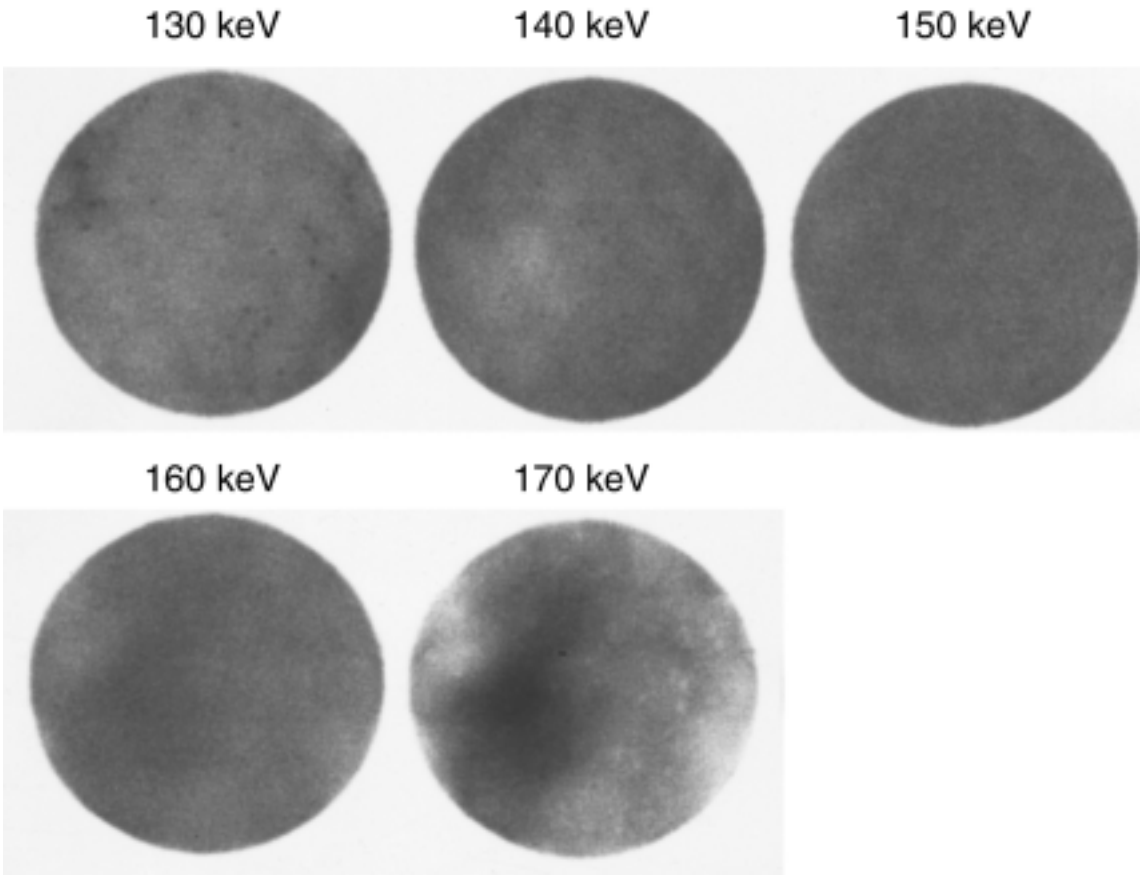

A series of intrinsic images of ^{99m}Tc obtained with a 20% energy window. For each image, the centre of the window was shifted by 10 keV, to give images from 130 to 170 keV.

Results: The images show crystal hydration: small discrete hot spots in the 130 keV image and small discrete cold spots in the same location in the 170 keV image. Also, PM tubes are out of tune. Those giving a cold pattern on the 130 and 140 keV images give a hot pattern on the 160 and 170 keV images. Interestingly, the best uniformity is at 150 keV and not at 140 keV.

This camera needs tuning and careful monitoring of crystal hydration.

2.2.2D3. Example: Asymmetric energy window — crystal hydration (3) — acceptance testing

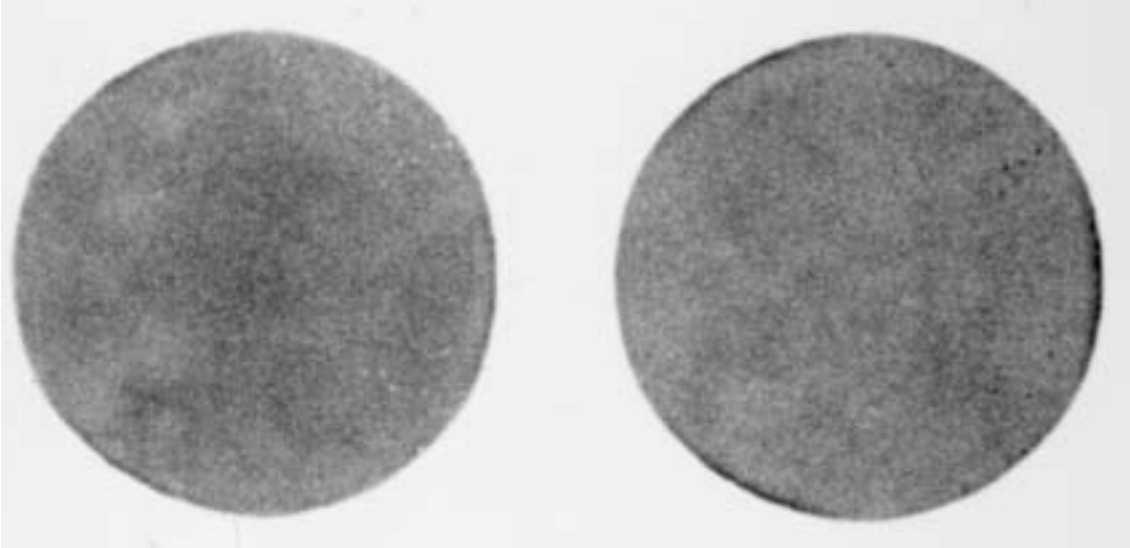

New scintillation camera, intrinsic uniformity, ^{99m}Tc, images obtained with 20% asymmetric energy windows, 2.5 million counts each image.

L: Asymmetric high energy window.
R: Asymmetric low energy window.

Results: Crystal hydration (measles) is present along the upper right quadrant of the images. The asymmetric high window image (L) shows discrete cold spots, and the asymmetric low window image (R) shows discrete hot spots. The image obtained with the symmetric energy window setting (not given here) showed satisfactory uniformity.

Comments: The camera was new, and the hydration was discovered during acceptance tests. This example stresses the importance of checking the detector thoroughly at acceptance testing, and of being prepared for unexpected results.

2.2.2E. Example: Asymmetric energy window — malfunction of energy calibration

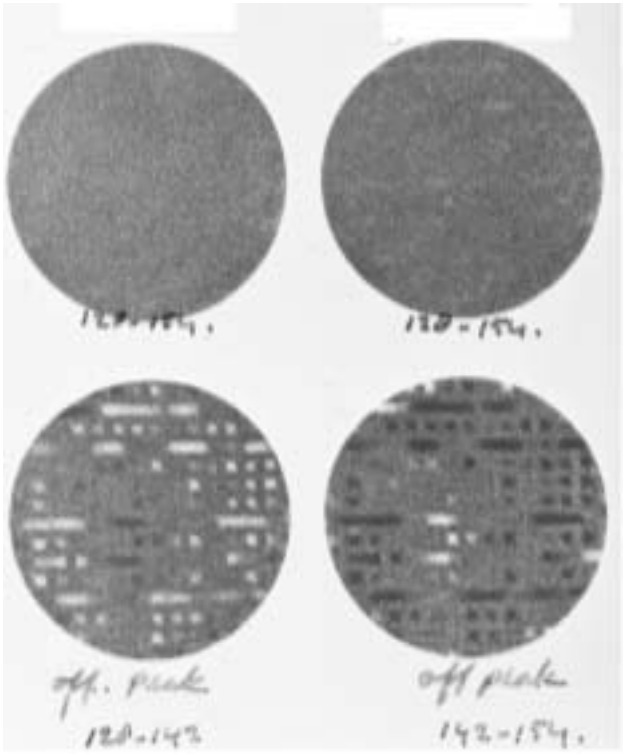

Intrinsic uniformity, ^{99m}Tc, 3 million counts each image.

TL: Before energy calibration, 20% energy window symmetric.
TR: After energy calibration performed by user, 20% energy window symmetric.
BL: After calibration, 10% energy window asymmetric low (off-peak low).
BR: After calibration, 10% energy window asymmetric high (off-peak high).

Results: The irregular striped patches in the symmetric window image obtained after energy calibration (TR) indicate that a problem exists with the energy correction map. A comparison of the offset images (BL and BR) clearly demonstrates the problem. Note the complementary cold and hot areas. Because the uniformity was checked prior to the energy calibration and did not demonstrate these artefacts (TL), the problem was attributed to the new energy correction map. The artefacts disappeared in images obtained after a repeat calibration.

Comments: These images relate to an older camera that required routine (e.g. monthly) hardware energy calibration.

A comparison of the uniformity obtained with asymmetric low and high energy windows is a sensitive test of whether an energy calibration or PM tuning is successful. This test was therefore part of the routine QC procedure carried out following each energy calibration.

2.2.2F. Example: Asymmetric energy window — fault in energy correction map

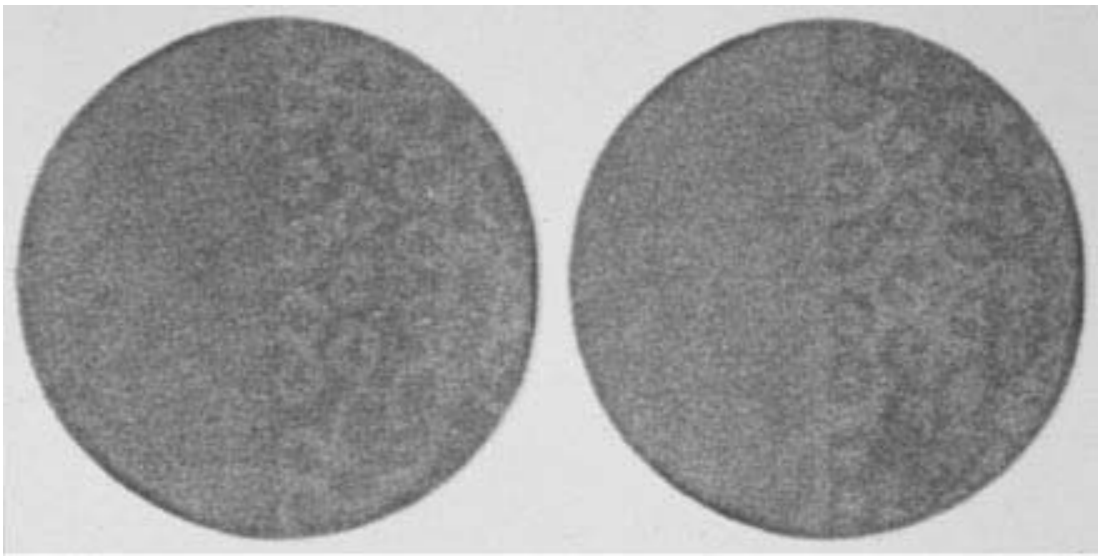

Intrinsic uniformity, ^{99m}Tc, 3 million counts each image.

TL: 10% energy window asymmetric high (offset high).
TR: 10% energy window asymmetric low (offset low).

Results: The right half of each image shows irregularity due to a fault in the memory chip of the energy correction map.

Comments: A comparison of the uniformity obtained in offset low and offset high energy windows is a sensitive test of whether the electronic energy correction (Z map) is functioning correctly.

2.2.2G. Example: Asymmetric energy window — non-uniformity

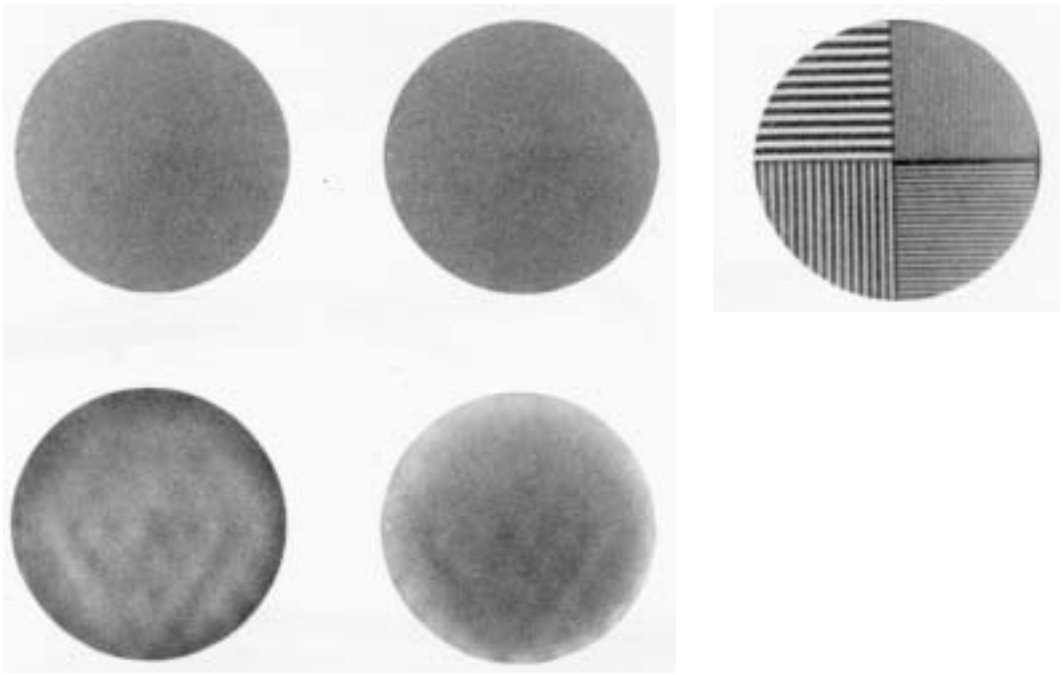

Intrinsic uniformity at low and high count rates, ^{99m}Tc, 3 million counts each image.

TL: 20% symmetric energy window at 20 000 counts/s.
TM: 20% symmetric energy window at 75 000 counts/s.
TR: Spatial resolution using a quadrant bar pattern at 20 000 counts/s.
BL: 10% energy window set asymmetric high.
BR: 10% energy window set asymmetric low.

Results: The uniformity and resolution images obtained with a symmetric energy window are satisfactory. The asymmetric uniformity images show a non-uniformity pattern particularly in the lower half of each image. This is seen less obviously in the asymmetric low image. The non-uniformity in the lower half of the image is due to a problem in the memory chip of the energy correction map.

The camera is usable until the problem is corrected by service personnel, unless asymmetric energy windows are used.

2.2.2H. Example: Asymmetric energy window — 70 000 counts/s

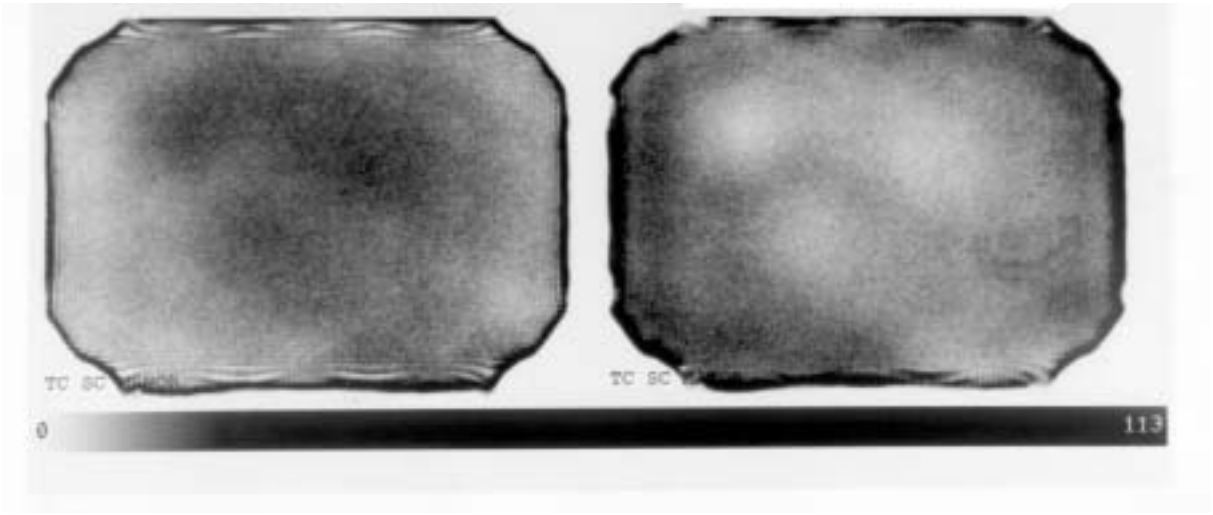

Intrinsic uniformity images, 10% asymmetric energy windows, ^{99m}Tc, 5 million counts each image.

TL: Asymmetric energy window set low.
TR: Asymmetric energy window set high.

Results: The images show gross non-uniformity from poor tuning. The hot areas on the asymmetric low image appear as equivalent cold areas on the asymmetric high image. The vertical and horizontal wavy lines, seen particularly at the edges, are indicative of a problem with the linearity correction map.

Note that the electronic mask has been deactivated. The hot border is due to edge packing. Service is required.

2.2.2I. Example: Asymmetric energy window — ADC problem related to internal corrections (1)

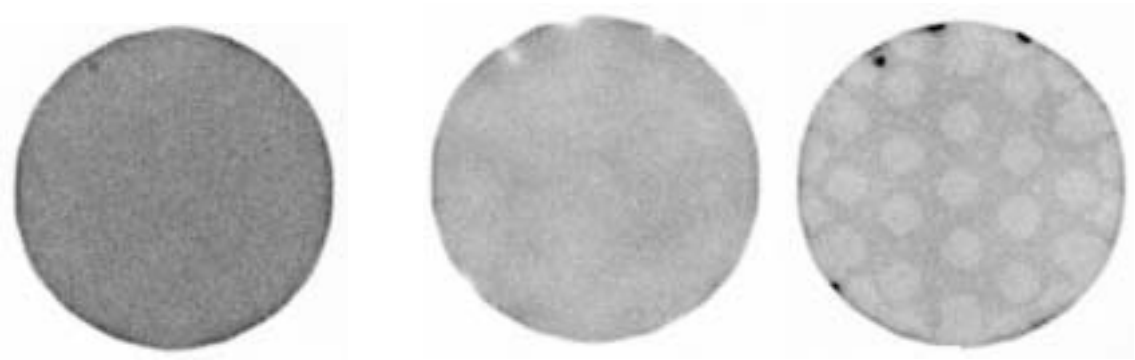

Intrinsic uniformity, ^{99m}Tc, 3 million counts each image.

L: 20% symmetric energy window.
M: 10% energy window set asymmetric high.
R: 10% energy window set asymmetric low.

Results: Diffuse non-uniformity is seen in the asymmetric high image (M). In addition, there are several cold spots at the top and the lower left edge of the circular FOV. The asymmetric low image (R) shows a very distinct symmetric pattern of cold PM tubes with cold spots interspersed. This was due to a problem in the conversion processes in the internal ADC corrections.

The intense hot spots at the top and the lower left edge of the FOV correspond to the same location as the cold spots on the off-peak high image and are due to crystal hydration. The uniformity obtained with the energy window set symmetrically over the photopeak was normal.

Comments: The images obtained with the asymmetric energy windows uncovered both of the problems shown here.

2.2.2J. Example: Asymmetric energy window — ADC problem related to internal corrections (2)

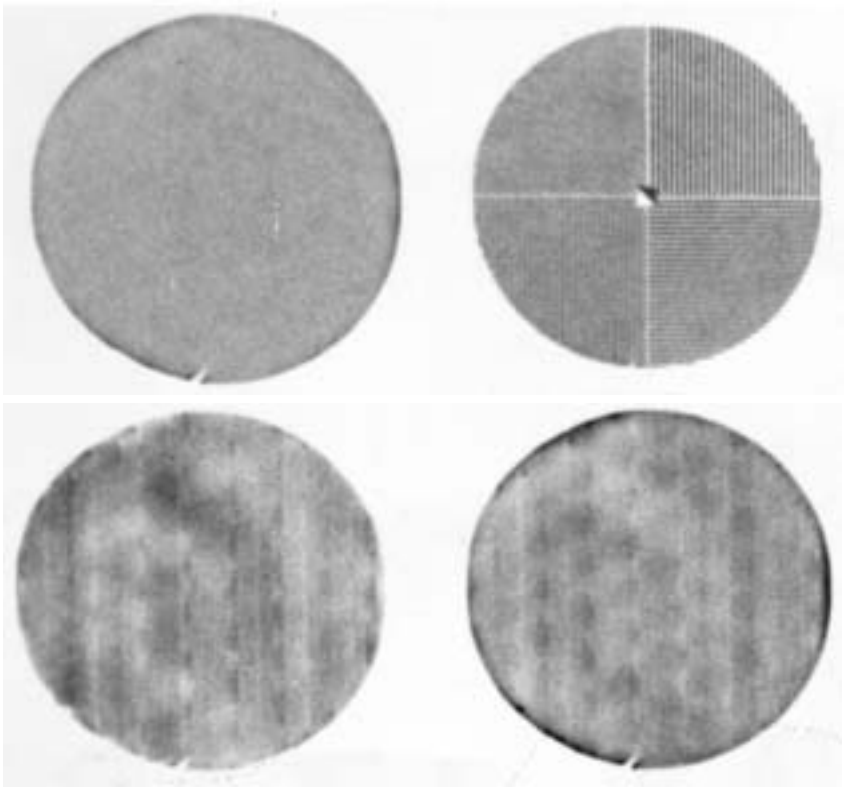

Intrinsic measurements, ^{99m}Tc, 20% energy window, 2.5 million counts each image.

TL: Uniformity with symmetric energy window.
TR: Spatial resolution using quadrant bar pattern with symmetric energy window.
BL: Uniformity with energy window set asymmetric high.
BR: Uniformity with energy window set asymmetric low.

Results: The uniformity and resolution images obtained with symmetric energy windows show reasonable results. The uniformity images obtained with asymmetric energy windows show vertical striped patterns, which are abnormal. The problem was caused by a faulty ADC board that digitizes events in the horizontal direction. This ADC problem relates to internal corrections for the detector. After the ADC board was replaced, the problem disappeared.

Comments: The white vertical fleck in the middle of the TL image was due to dirt on the image formatter. The small cold indentation at the bottom of the FOV is a crack in the crystal. In this situation the collimator covers most of the crack and the crystal does not need to be replaced.

2.2.2K. Example: Asymmetric energy window — ADC problem related to internal corrections (3)

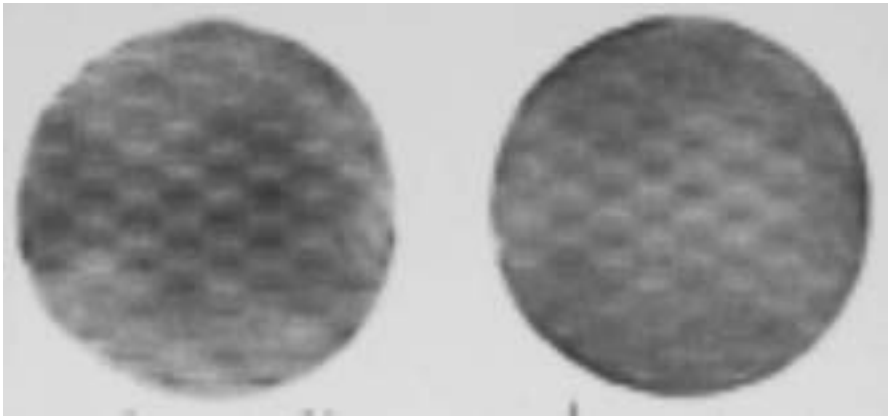

^{99m}Tc, 2.5 million counts each image, 20% energy window.

L: Asymmetric energy window high.
R: Asymmetric energy window low.

Results: A distinct non-uniform pattern is seen in both images. This is due to a non-functioning bit in the internal ADC of the camera. In addition, the darker areas in the asymmetric high image correspond to the lighter areas in the asymmetric low image, indicating poor PM tuning. Both problems need attention by service personnel.

2.2.2L. Example: Asymmetric energy window — ADC problem related to internal corrections (4)

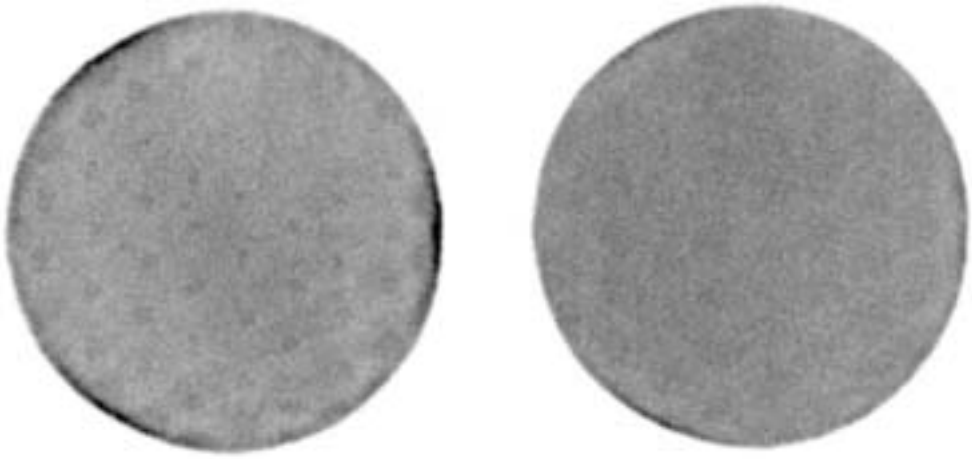

Intrinsic uniformity, 2.5 million counts each image, ^{99m}Tc, 20% energy window.

L: Asymmetric high energy window.
R: Asymmetric low energy window.

Results: The asymmetric high image (L) shows a pattern of discrete flecks of hot spots corresponding to the centre of PM tubes, whereas the asymmetric low image shows only a typical pattern of diffuse PM tubes. The flecks are artefacts due to a problem with the ADCs of the detector.

2.2.2M. Example: Asymmetric energy window — clinical example with ^{123}I and ^{99m}Tc

A: first series

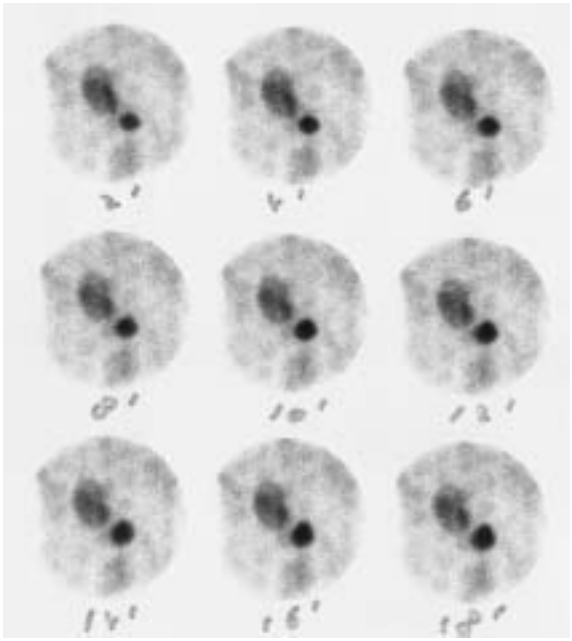

B: second series after the ^{99m}Tc study

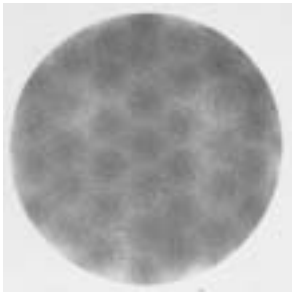

C: ^{99m}Tc flood in ^{123}I energy window

Clinical example of a patient with a kidney transplant, suffering from post-transplant oliguria because of an acute tubular necrosis. A 20 min renal study was performed using 10 MBq of ^{123}I hippuran followed by a 90 s flow study using 175 MBq of ^{99m}Tc DTPA. The first series of kidney images showed ^{123}I activity in the pelvis of the kidney but there was no visualization of the bladder. In order to rule out obstructive uropathy, the patient was then injected with the diuretic frusemide, and imaging of the ^{123}I hippuran was continued for a further 20 min. All images shown here were acquired with a 20% symmetric ^{123}I energy window.

A: First series of kidney studies after intravenous injection of ^{123}I hippuran.
B: Second series of kidney studies after a short 90 s perfusion study using ^{99m}Tc DTPA (not shown here) and intravenous administration of frusemide.
C: ^{99m}Tc flood source imaged in the ^{123}I energy window.

Results: The second series of ^{123}I images showed multiple hot areas over the whole FOV that had not been present in the first series of images. These were recognized as artefacts from the ^{99m}Tc flow study performed between the first and second series of ^{123}I images. The relatively high amount of

^{99m}Tc activity administered in comparison with the ^{123}I activity produced a considerable contribution to the ^{123}I images, since the ^{123}I energy window (20% over 159 keV) acts as an asymmetric high energy window for ^{99m}Tc. The artefacts seen are due to non-uniformity from ^{99m}Tc imaged in the asymmetric window (C).

Comments: The energy spectra of ^{99m}Tc and ^{123}I partially overlap, with photopeaks at 140 and 159 keV, respectively (see schema of spectra below). This means that the ^{123}I symmetric energy window appeared as an asymmetric high energy window for ^{99m}Tc. The ^{99m}Tc symmetric energy window appeared as an asymmetric low energy window for ^{123}I. Since the amount of ^{99m}Tc administered was relatively much higher than the amount of ^{123}I, the contribution of ^{99m}Tc imaged in the ^{123}I energy window was also relatively high and hence gave the intense artefacts shown here.

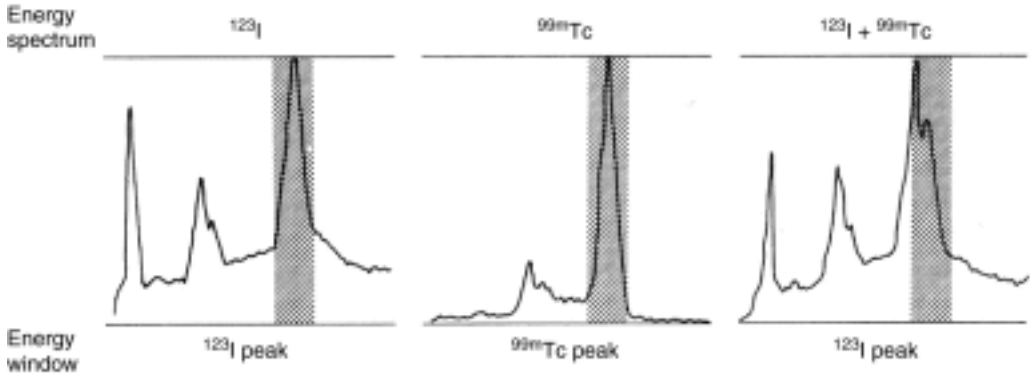

In this study, using this camera, the hot artefacts were caused by the asymmetry of the ^{123}I energy window over the ^{99m}Tc photopeak in the presence of ^{99m}Tc.

Note: Extreme care is required to ensure that correction circuits are properly functioning, that corrections are properly applied, and that the uniformity of the scintillation camera for any asymmetric energy window or overlapping energy window, as in this example, does not adversely influence the quality of the images.

2.2.2N. Example: Asymmetric energy window — clinical example with ^{123}I and ^{99m}Tc

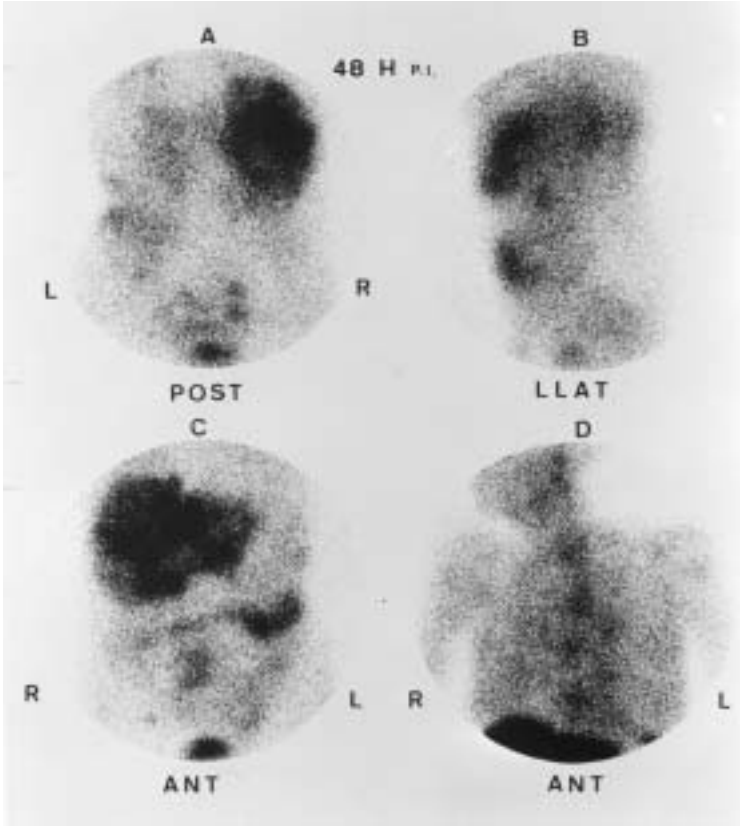

This example was obtained with the same scintillation camera as in the previous example (2.2.2M), and the same problem existed.

Clinical study of ^{123}I MIBG, 20% energy window centred over the 159 keV photopeak.

TL (A): Abdomen posterior.
TR (B): Abdomen left lateral.
BL (C): Abdomen anterior showing the liver in the upper half of the image.
BR (D): Thorax anterior showing a border of liver activity (at the bottom of the image).

Images A–C were made consecutively; ^{99m}Tc colloid was then administered for visualization of the liver. D was a final ^{123}I MIBG image taken as follow-up but not part of the usual study protocol.

Results: At first analysis, the increased count areas of ^{123}I in the lung area of image D were reported as abnormalities. On reconstruction of the clinical procedure, which diverged from the standard protocol, these abnormalities were attributed to the contribution of ^{99m}Tc photons included in the lower half of the energy window. (Note the differences between activity in the liver and cranial to the liver in images A–D, due to the administration of ^{99m}Tc colloid between C and D.) This was subsequently confirmed by a ^{99m}Tc uniformity image obtained with an asymmetric high energy window (140–170 keV). The ^{99m}Tc photons measured in the ^{123}I energy window (143–175 keV) essentially contributed an asymmetric high ^{99m}Tc image superimposed on the ^{123}I photon image, and introduced non-uniformity artefacts.

Comments: In any situation where an asymmetric energy window may be encountered in clinical studies (as in this example), extra care is required to ensure a uniform response for the energy window selected and the radionuclides used.

See also the comments on example 2.2.2M.

2.2.3. Different radionuclides and photon energies

2.2.3.1A. Example: Comparison of intrinsic uniformity for ^{99m}Tc, ^{201}Tl, ^{67}Ga and ^{131}I on the same scintillation camera

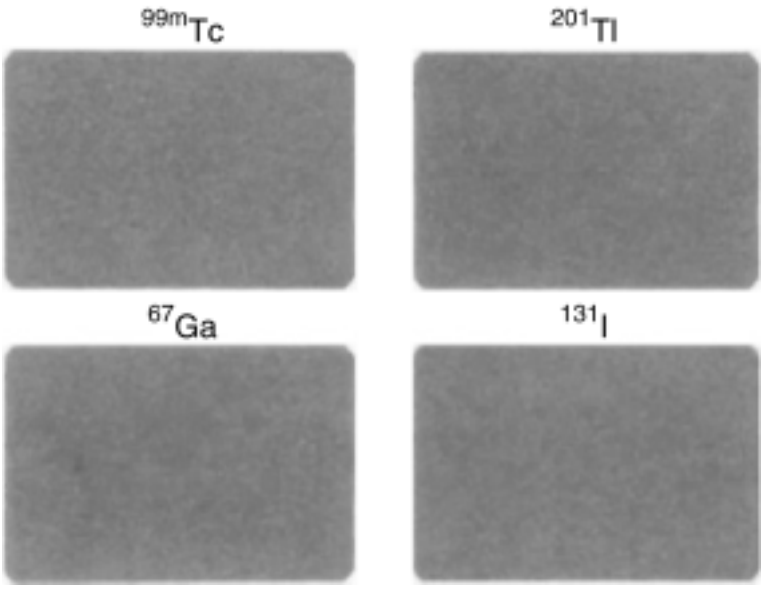

High count density images were acquired to evaluate the effect of photon energy on intrinsic uniformity. The images were acquired as follows:

TL: ^{99m}Tc with an energy window of 15% at 140 keV.
TR: ^{201}Tl with two energy windows: 15% at 72 keV and 20% at 167 keV.
BL: ^{67}Ga with three energy windows: 20% at 93 keV, 15% at 184 keV and 15% at 300 keV.
BR: ^{131}I with an energy window of 20% at 364 keV.

Results: No significant differences in intrinsic uniformity were observed for the four different radionuclides.

Comments: These images were acquired on a digital camera (an ADC digitizes the signal from each PM tube) with a digital light pipe (software used to reshape the distribution of light at the PM tube in the same way as a Perspex (Lucite) light pipe was used in older analogue cameras). No intrinsic uniformity correction maps were applied.

2.2.3.1B. Example: Comparison of intrinsic uniformity for ^{201}Tl, ^{67}Ga, ^{123}I, ^{111}In and ^{131}I on the same scintillation camera — ^{99m}Tc uniformity correction map

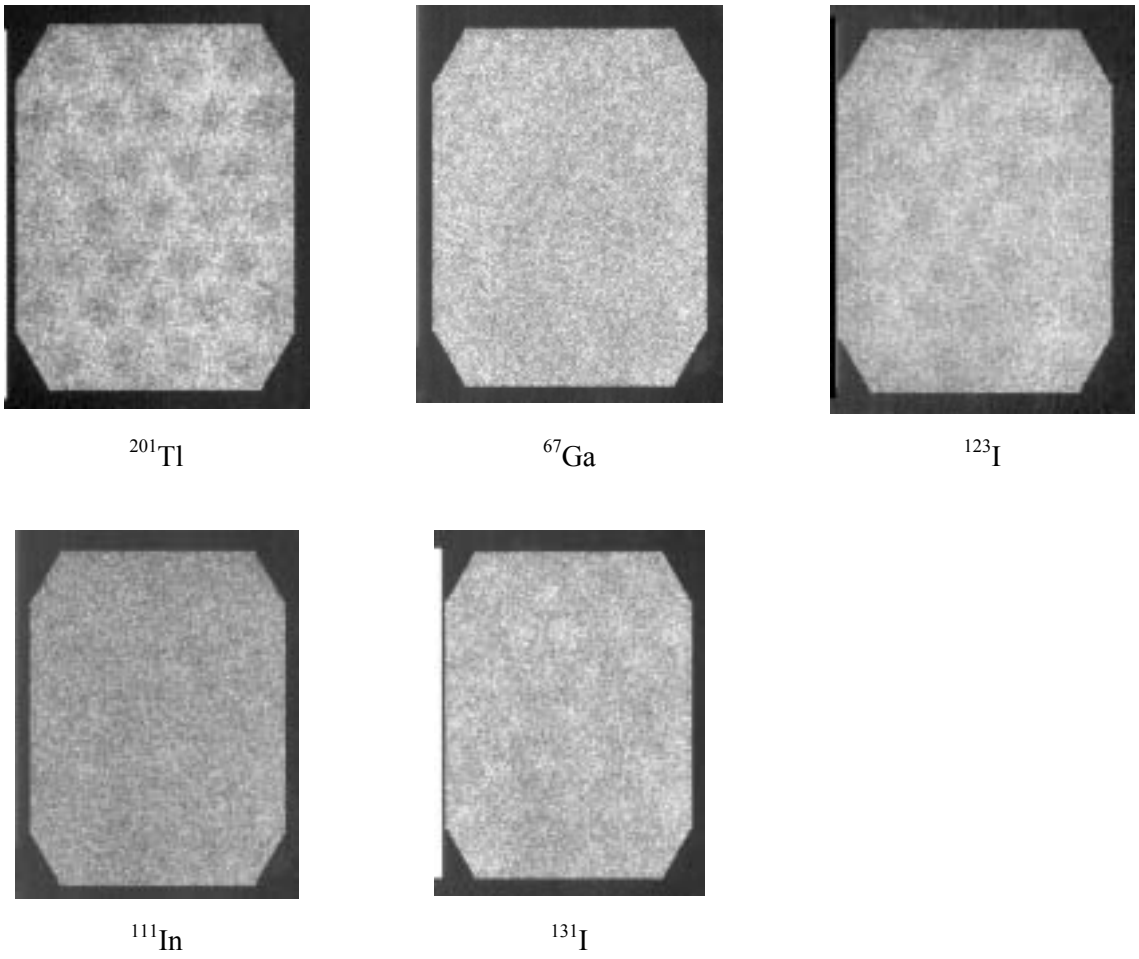

^{201}Tl ^{67}Ga ^{123}I

^{111}In ^{131}I

Intrinsic flood images obtained at the preset energy window settings for various radionuclides as part of the acceptance testing programme. Each image contains 3 million counts. A ^{99m}Tc uniformity correction map was applied to each radionuclide.

TL: ^{201}Tl with a 20% energy window at 72 keV.
TM: ^{67}Ga, a summed image from 20% energy windows at 93, 184 and 300 keV.
TR: ^{123}I with a 20% energy window at 159 keV.
BL: ^{111}In, a summed image from 20% energy windows at 171 and 247 keV.
BR: ^{131}I with a 20% energy window at 364 keV.

Results: The images show loss of uniformity, especially at low photon energies (^{201}Tl, ^{67}Ga).

Comments: The uniformity obtained at different photon energies without a radionuclide specific uniformity correction is unpredictable. For this scintillation camera system, an energy specific uniformity correction is needed for each radionuclide used.

2.2.3.1C. Example: Comparison of intrinsic uniformity for ^{201}Tl and ^{67}Ga on the same scintillation camera — radionuclide specific uniformity correction map

Intrinsic uniformity, 30 million counts each image, radionuclide specific uniformity correction, 20% energy windows.

L: ^{201}Tl with a 20% energy window at 72 keV.
R: ^{67}Ga, a summed image from 20% energy windows at 93, 184 and 300 keV.

Results: The images for both radionuclides show good uniformity.

2.2.3.2A. Example: Uniformity — ^{201}Tl

Intrinsic uniformity, ^{201}Tl, energy windows of 15% at 72 keV and 20% at 167 keV, 3 million counts, no correction map.

Results: Slightly degraded uniformity compared with the uniformity of ^{99m}Tc (not given here). Acceptable.

2.2.3.2B. Example: Uniformity — ^{201}Tl, defective linearity correction — clinical images and uniformity

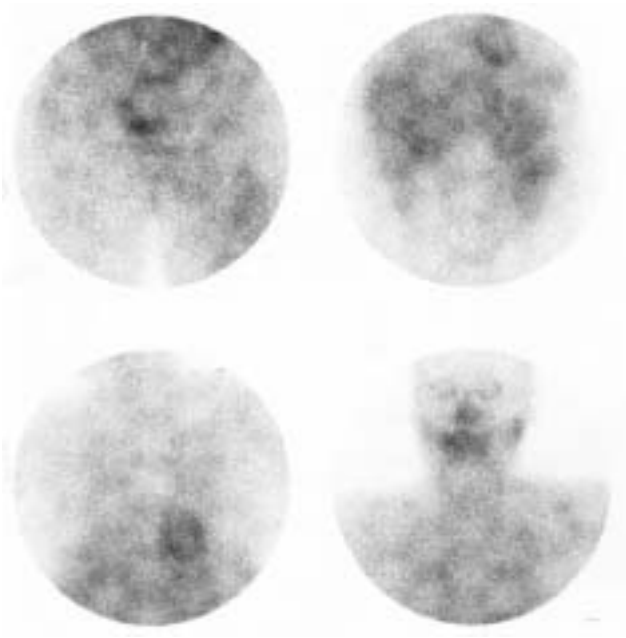

A: Clinical study
^{201}Tl, 20% energy window at 69–80 keV, 300 000 counts each image, anterior.

TL: Lower abdomen.
TR Mid-abdomen — liver/spleen; myocardium is seen in the upper part of the image.
BL: Thorax; myocardium is seen in the lower part of the image.
BR: Head and neck.

Results: Severe artefacts from visible PM tubes are seen in all the clinical images.

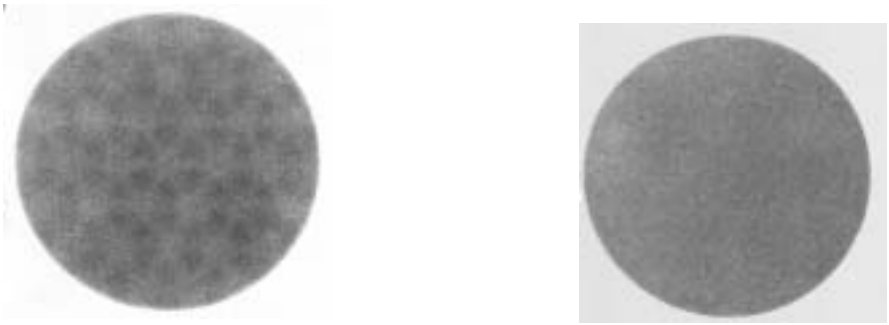

^{201}Tl ^{99m}Tc

B: Uniformity QC
^{201}Tl uniformity check was made following the clinical study and was compared with the daily uniformity check for ^{99m}Tc.

L: ^{201}Tl, 20% energy window at 72 keV, 3 million counts.
R: ^{99m}Tc, 20% energy window at 140 keV, 3 million counts.

Results: In the ^{201}Tl image all PM tubes are visible as hot areas, whereas the ^{99m}Tc image was normal and acceptable. The linearity correction map that functioned for ^{99m}Tc was malfunctioning at the lower ^{201}Tl energy.

Comments: The clinical result using ^{201}Tl was unexpected because the routine QC check using ^{99m}Tc showed good uniformity and no artefacts. This camera had never been tested with ^{201}Tl. At acceptance testing it was not considered necessary to check the uniformity for ^{201}Tl because it was not expected that ^{201}Tl would be used with this particular camera.

The uniformity QC check for ^{201}Tl was made only after the clinical study was obtained and confirmed that a major problem was present with images obtained at the low energy, even though the routine daily uniformity QC test with ^{99m}Tc was uniform and acceptable.

It is essential to check the camera at acceptance testing with the full range of photon energies and radionuclides used clinically within the department. If a new radionuclide is introduced into the department, especially one which has a photon energy that falls outside the range of energies already in use, then the uniformity should be checked with this radionuclide before clinical studies are made, in order to avoid the possible occurrence of a clinical artefact as presented here.

In this example, a satisfactory study could still be performed on another scintillation camera system in the department. Thus there was a satisfactory outcome for the patient, and an unnecessary repeat study with its associated extra radiation burden was avoided.

The problem was due to a faulty linearity correction map. The scintillation camera could not be used with ^{201}Tl until a new linearity map was acquired.

2.2.3.3A. Example: Uniformity — ^{67}Ga — separate and sum of energy windows (1)

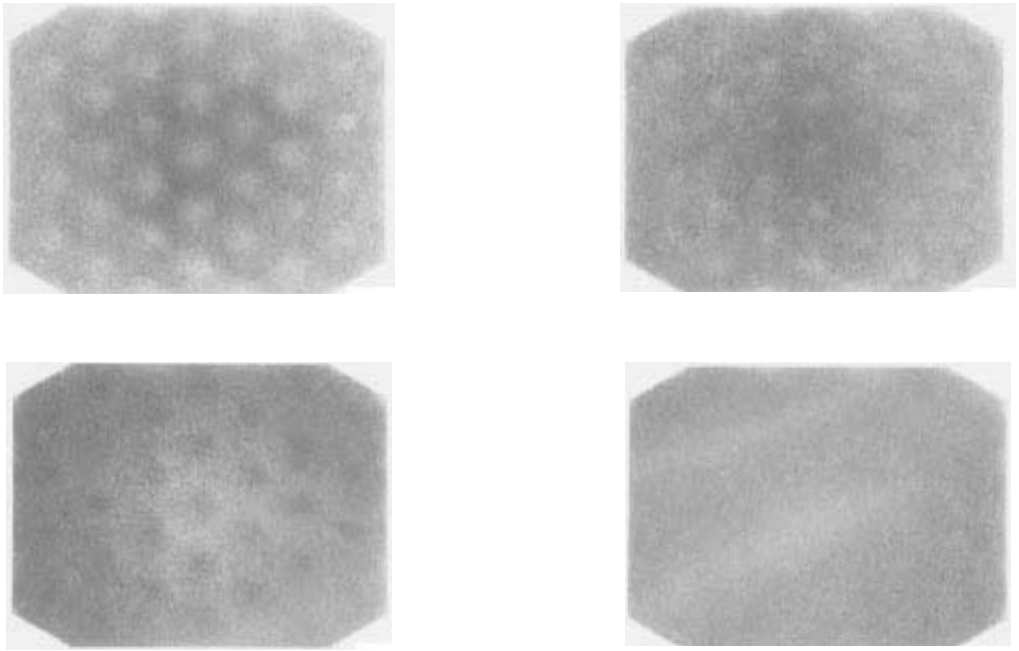

Intrinsic uniformity, ^{67}Ga, 20% energy windows set at 93, 184 and 300 keV, 3 million counts each image.

TL: Uniformity for 300 keV energy window.
TR: Uniformity for 185 keV energy window.
BL: Uniformity for 93 keV energy window.
BR: Uniformity for all three energy windows together.

Results: Each image shows a different non-uniformity. However, the sum image is uniform.

Note: The light diagonal shadows over the BR image are from poor hard copy quality and not from camera non-uniformity.

Comments: This camera is acceptable for imaging ^{67}Ga only if all three energy windows are used. If one of the energy windows is not used, as might be the case in dual radionuclide studies, then the summed image will not be uniform. The uniformity must be checked with the clinically used combination of energy windows.

2.2.3.3B. Example: Uniformity — ^{67}Ga — separate and sum of energy windows (2)

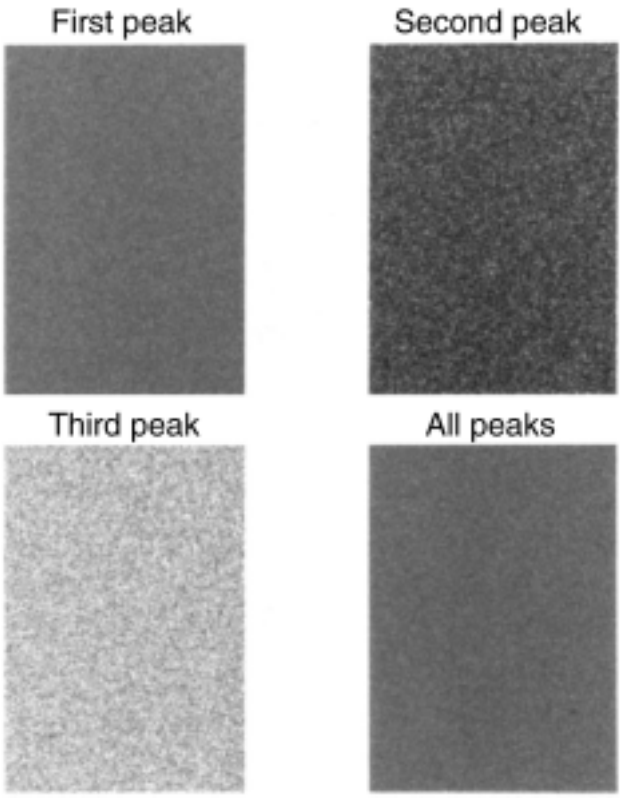

Intrinsic uniformity, ^{67}Ga using three separate energy windows and the sum of these separate energy windows, with the summed image giving 5 million counts, 256 × 256 matrix, pixel size 2.24 mm.

TL: Peak 1 (93 keV), 25% energy window (3.2 million counts).
TR: Peak 2 (184 keV), 20% energy window (1.4 million counts).
BL: Peak 3 (300 keV), 20% energy window (0.4 million counts).
BR: Sum of these three peaks (5 million counts).

Results: Each image from a single energy peak shows the contribution to the total summed image. (Note the difference in total counts for each energy window.) Each image shows a uniform response. Acceptable result.

2.2.3.3C. Example: Uniformity — ^{67}Ga — sum of three energy windows — poor

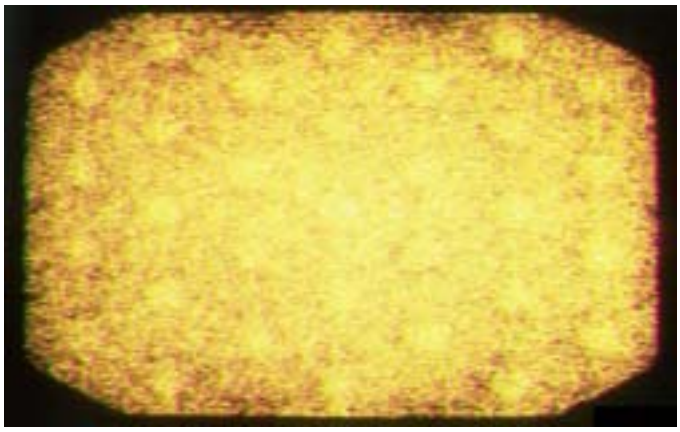

Intrinsic uniformity, ^{67}Ga, 3 million count image obtained from the sum of 20% energy windows set at 93, 184 and 300 keV.

Results: Considerable non-uniformity throughout the image. Each PM tube is visible as a hot spot. Unacceptable. Service is required.

Comments: The summed image of ^{67}Ga is formed by the combined images from three energy windows, which span a wide energy range. The uniformity for ^{67}Ga is therefore influenced by the uniformity of the camera system at each of these energies. This scintillation camera cannot be used for clinical studies of ^{67}Ga until service has solved the non-uniformity problem.

Note: Some scintillation cameras allow a uniformity correction data set for each radionuclide. If this is the case, then the data set should be collected and applied appropriately.

2.2.3.4. Example: Uniformity — ^{18}F

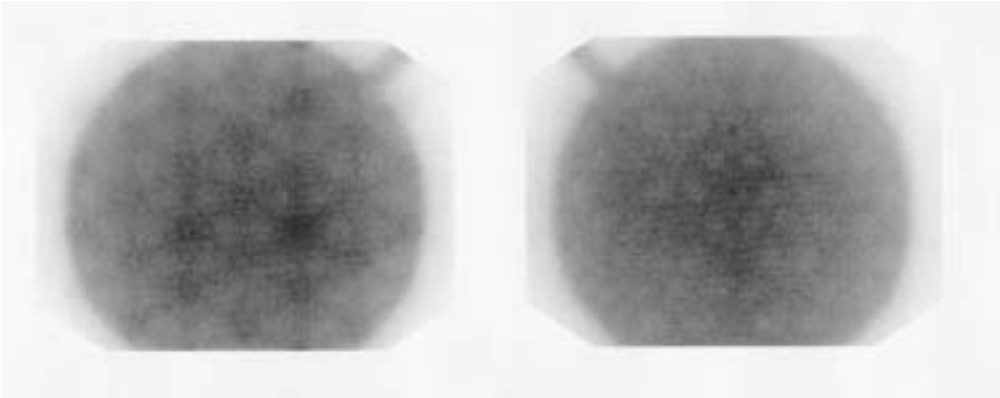

Dual detector coincidence camera, extrinsic uniformity using a round flood source, ultra-high-energy collimator, ^{18}F energy window (511 keV), single photon mode, 4 million counts each image, no specific uniformity correction map applied.

L: Detector 1.
R: Detector 2.

Results: Non-uniformity response is observed for both detectors. Moreover, the response from each detector is different. Both detectors also show a central area of increased counts.

Comments: The non-uniformity observed for ^{18}F is unacceptable in clinical use, unless a ^{18}F specific uniformity correction is applied

2.2.4. Uniformity — quantification

2.2.4.1. Example: Uniformity — ^{99m}Tc at different count densities

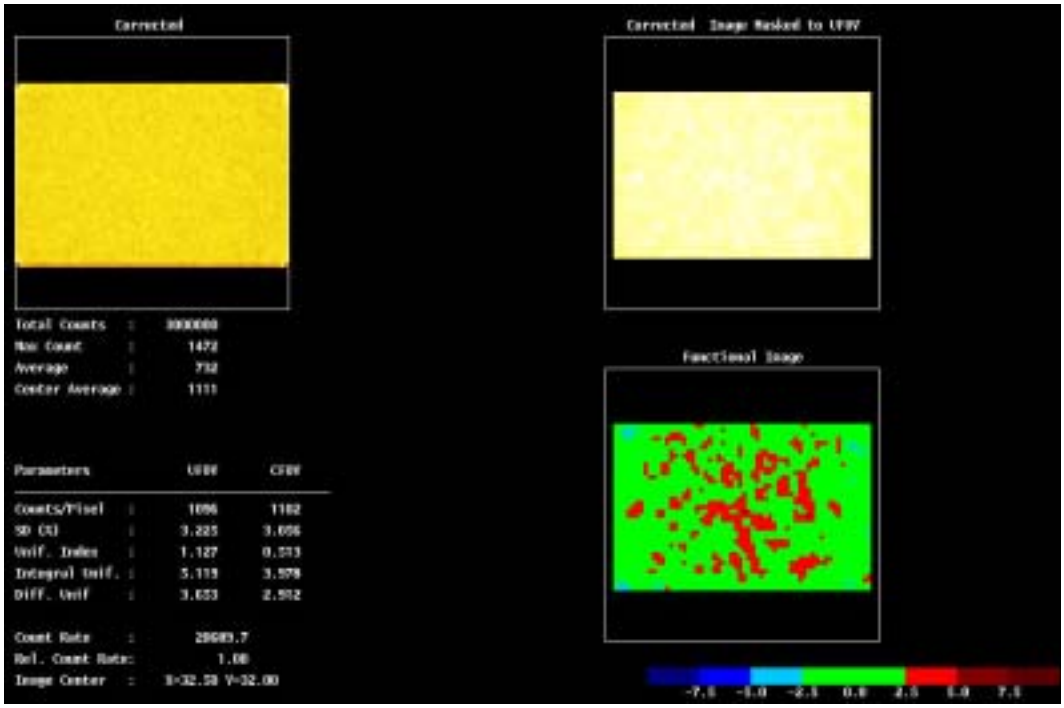

A

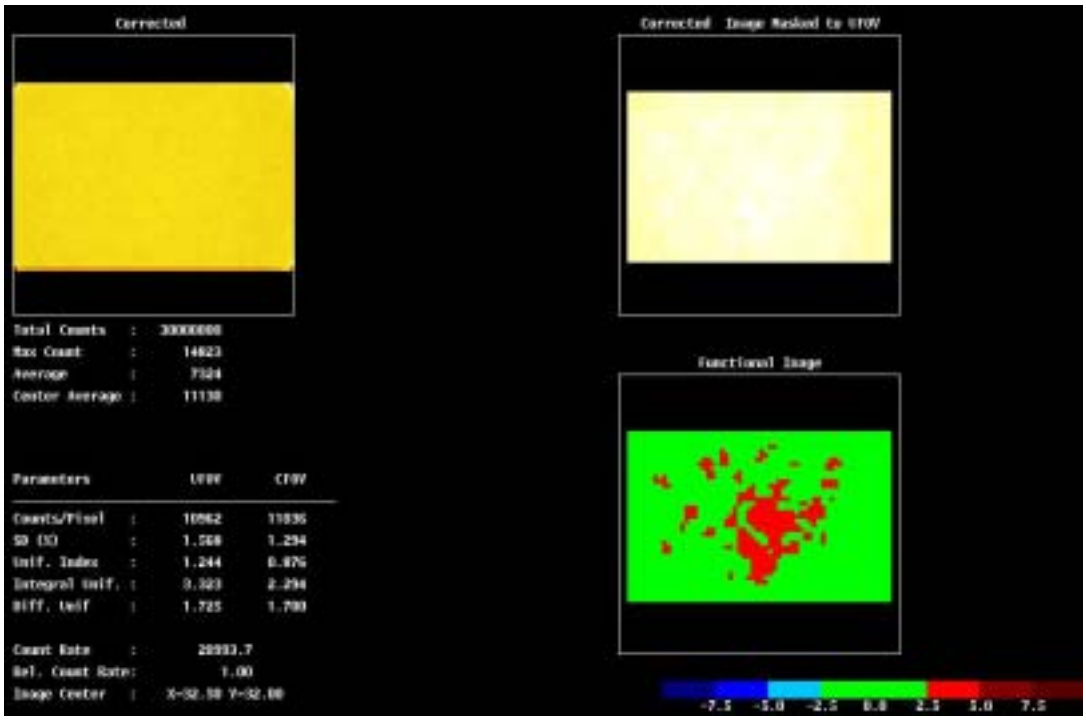

B

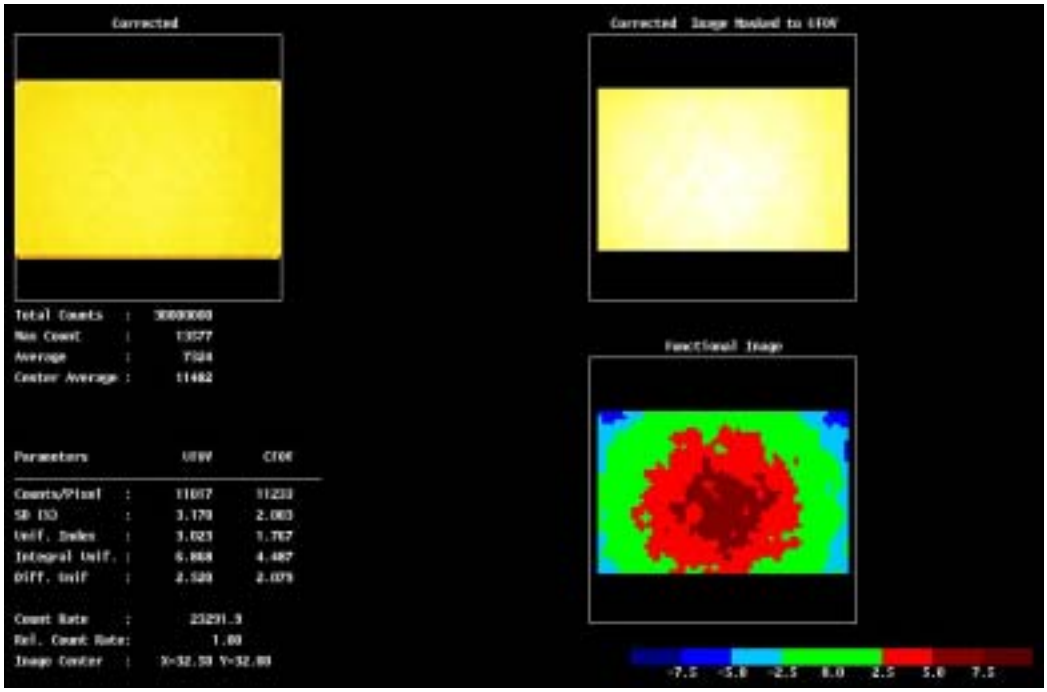

C

^{99m}Tc, 15% energy window, 64 × 64 matrix, intrinsic uniformity using a point source positioned at 5 FOV distance from the crystal (A and B) and also, for demonstration purposes only, at 3 FOV distance from the crystal (C) (FOV = 53 cm). Total counts: A, 3 million; B, 30 million; C, 30 million.

Results: Uniformity quantification documentation showing the following information. For each quantification documentation:

TL: Raw acquired uniformity image.
TR: Nine point smoothed image, masked to the UFOV.
BR: Functional image colour coded to show changes in 2% of average counts.

Numerical data include total acquired counts, average counts, standard deviation of count distribution, uniformity index and NEMA values.

NEMA PARAMETERS

	Integral			Differential		
	A	B	C	A	B	C
Distance (m)	2.5	2.5	1.5	2.5	2.5	1.5
Counts (millions)	3	30	30	3	30	30
Uniformity						
UFOV (%)	5.1	3.3	6.8	3.6	1.7	4.8
Uniformity						
CFOV (%)	3.9	2.2	2.5	2.9	1.7	2.0

Comments: The image of 3 million counts is typical of a daily uniformity check. Owing to the low count statistics (about 1000 counts per pixel), NEMA quantification at this count density is not useful.

The NEMA uniformity parameters are based on a numerical value of only 2 pixels, and the high statistical noise results in a falsely high impression of non-uniformity. For monitoring uniformity and using the NEMA parameters for action levels, the pixel counts must approach 10 000.

For quantification of a low count uniformity image, one could consider the use of other parameters that are less dependent than the NEMA parameters on individual pixel count statistics (e.g. a uniformity index as described in the reference below).

The image set C has been included in this example to demonstrate the effect of source geometry. In C the source to detector distance is about 3 FOV rather than the recommended 5 FOV (i.e. the source is too close to the detector to produce a uniform flux of photons on the detector surface).

Reference: COX, N.J., DIFFEY, B.L., A numerical index of gamma camera uniformity, Br. J. Radiol. **49** (1976) 734–735.

2.2.5. Uniformity — multihead systems

General comments

(1) Each uniformity item presented in Sections 2.2.1–2.2.4 also applies to each head of a multihead system.
(2) The performance of each head should be within specifications.
(3) According to the configuration of the heads, the geometry of the source and the detector may influence the uniformity results.
(4) The manufacturer's specifications and instructions for calibrations and QC procedures should be followed.

2.2.6. Corrections (linearity, energy, uniformity)

2.2.6.1. Example: Illustration of the effect of no linearity or energy corrections being applied

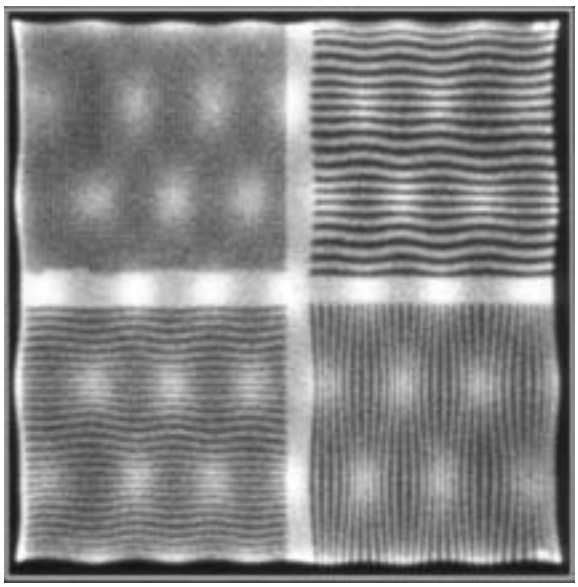

Four quadrant bar pattern, intrinsic uniformity, ^{99m}Tc, 4 million counts.

Results: The bar pattern image shows wavy lines, compressed towards the centre of the PM tubes and expanding between the tubes. This is due to non-linearity. The hot areas corresponding to PM tubes are an effect of no energy correction being applied. The appearance of the image is in part due to engineering designs that are focused on improving intrinsic spatial resolution at the expense of intrinsic uniformity. Energy and linearity corrections are then used to produce satisfactory intrinsic uniformity.

Comments: This example illustrates the typical response when no linearity and energy corrections are applied.

2.2.6.2. Example: Effect of linearity and energy corrections but no uniformity correction

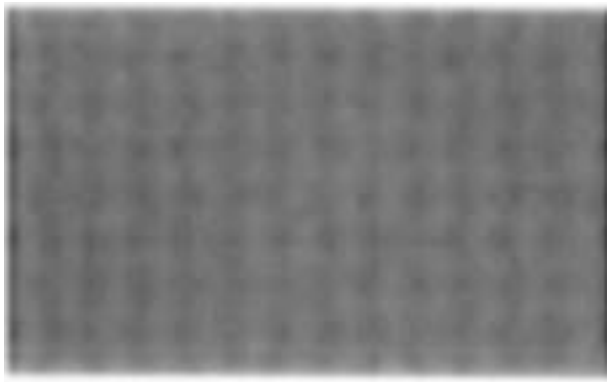

Intrinsic uniformity, ^{99m}Tc, 4 million counts, linearity and energy corrections have been applied, but no high count uniformity map has been applied.

Results: The image shows a distinct pattern of non-uniformity that is characteristic of one particular manufacturer. Other patterns will be seen with cameras produced by other manufacturers.

Comments: A uniformity correction map must be applied for clinical use. In many cameras the correction maps are radionuclide specific.

2.2.6.3A. Example: Comparison of images acquired with and without a uniformity correction map

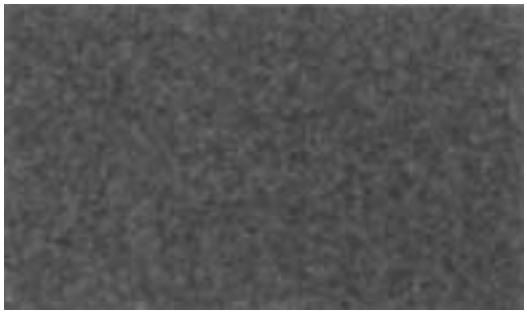

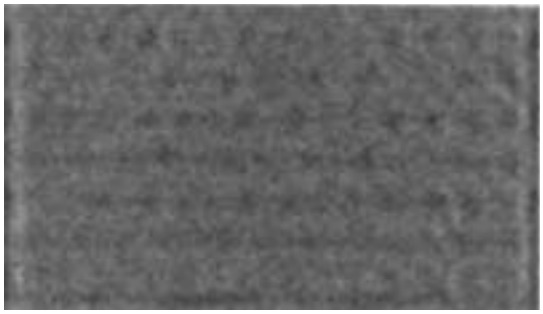

Extrinsic uniformity, LEHR collimator, ^{99m}Tc, 15% energy window, 4 million counts each image; linearity and energy corrections have been applied.

L: Uniformity obtained after application of a uniformity correction map.
R: Uniformity obtained without the uniformity correction map.

Results: The image without uniformity correction (R) shows a pattern of non-uniformity. This has been corrected by application of a uniformity correction map (L).

Comments: Most scintillation camera systems require some further correction in addition to the linearity and energy corrections. This correction uses a high count uniformity correction map, which may or may not need to be energy specific and which may be an intrinsic or an extrinsic correction (dependent on the system). The uniformity of the system must be monitored to ensure the suitability and validity of the correction map.

If possible, the image should be periodically acquired both with and without the uniformity correction map.

2.2.6.3B. Example: Comparison of images acquired without and with a ^{99m}Tc intrinsic uniformity map correction

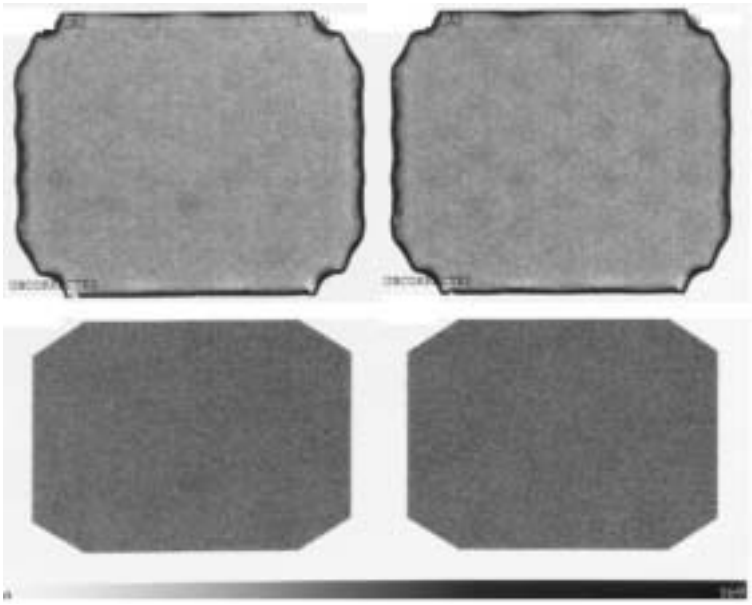

Dual head SPECT system, ^{99m}Tc, 20% energy window, 4 million counts each image, intrinsic uniformity. Images were acquired without and with an intrinsic ^{99m}Tc uniformity correction map applied.

TL and TR: Detectors 1 and 2, no uniformity correction, electronic mask (or iris) turned off.
BL and BR: Detectors 1 and 2, with uniformity correction, electronic mask (or iris) turned on.

Results: Images acquired without application of the intrinsic ^{99m}Tc uniformity correction and with the electronic mask (or iris) turned off revealed edge packing and some non-uniformity. Detector 1 (left side) showed several warm areas throughout the FOV corresponding to PM tubes. Images acquired with the uniformity correction map applied showed satisfactory uniformity by visual inspection, although one of the PM tubes in detector 1 (in the centre in the long dimension and about two thirds down in the short dimension) is still faintly visible.

Comments: These images were acquired with the linearity and energy corrections applied and using a symmetric energy window. The result still gave a non-uniform response that required further correction using a high count uniformity map.

If it is possible to turn off intrinsic radionuclide specific correction maps, uncorrected images should be periodically acquired. Even though the non-uniformity may be subtle in intrinsic images, the presence of scatter in clinical studies may produce non-uniformity. Some vendors use the additional uniformity correction map (in addition to energy and linearity corrections) to correct for residual non-uniformity and collimator imperfections. Other vendors use the renormalization only to correct for detector non-uniformity associated with different radionuclides.

2.2.6.3C. Example: Comparison of images acquired without and with a ^{99m}Tc intrinsic uniformity map correction — defective PM tube

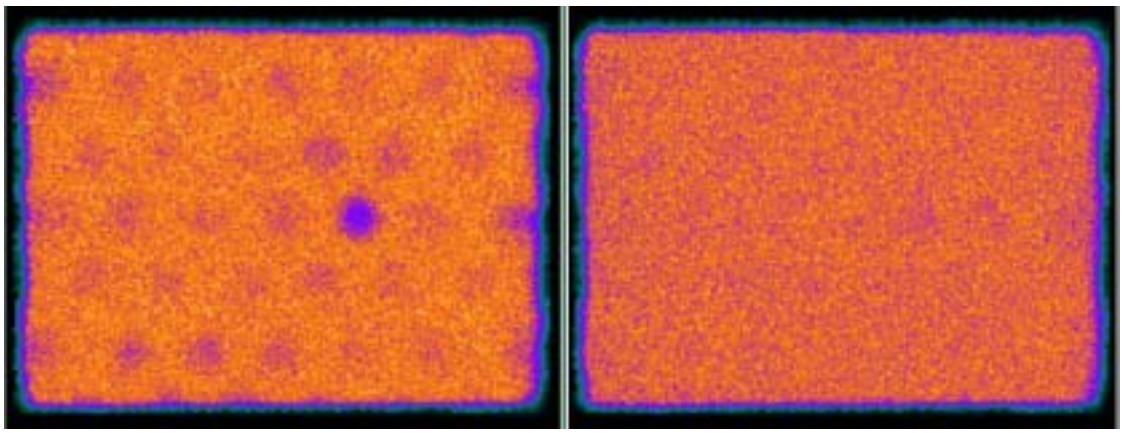

Intrinsic uniformity, ^{99m}Tc, 15% energy window, 4 million counts each image.

L: Image acquired with energy and linearity corrections and no uniformity correction map applied.
R: Image acquired after a uniformity correction map had been acquired with the camera in the condition shown on the left.

Results: The left image shows multiple cold areas corresponding to PM tubes, and a very cold spot due to a defective PM tube. The existence of the defective PM tube was unknown at the time, and a uniformity correction map was obtained and applied. This produced the image on the right, which is reasonably uniform, although some residual cold patches are still seen in the region of the defective PM tube. The PM tube was replaced and all corrections reacquired.

Comments: The energy and uniformity correction maps were acquired by service personnel who had only checked final uniformity (after energy and uniformity correction maps had been applied), so that the defective PM tube was missed. The above images were acquired afterwards by the department as a check of the maps acquired during service.

This example demonstrates the absolute necessity of checking images with and without corrections applied, and of checking all maps directly after they are acquired.

2.2.6.4. Example: Faulty energy correction map — clinical study

Patient study of ^{99m}Tc monoclonal antibody distribution in the lower abdomen immediately after a hardware energy calibration was performed. Anterior view, LEHR collimator, 20% energy window.

Results: The image shows a regular pattern over the whole FOV, an obvious artefact resulting from the energy calibration.

Comments: The energy calibration was faulty, but this was not discovered prior to the patient study, because no check of the validity of the calibration by means of a low count uniformity flood image had been made. The energy calibration was redone, after which a uniformity flood image showed acceptable results.

A check of correct functioning of calibrations is essential before clinical operation is resumed. The additional time required for such a check must be planned for together with the calibration itself.

2.2.6.5. Example: Problems with the energy correction in the same scintillation camera

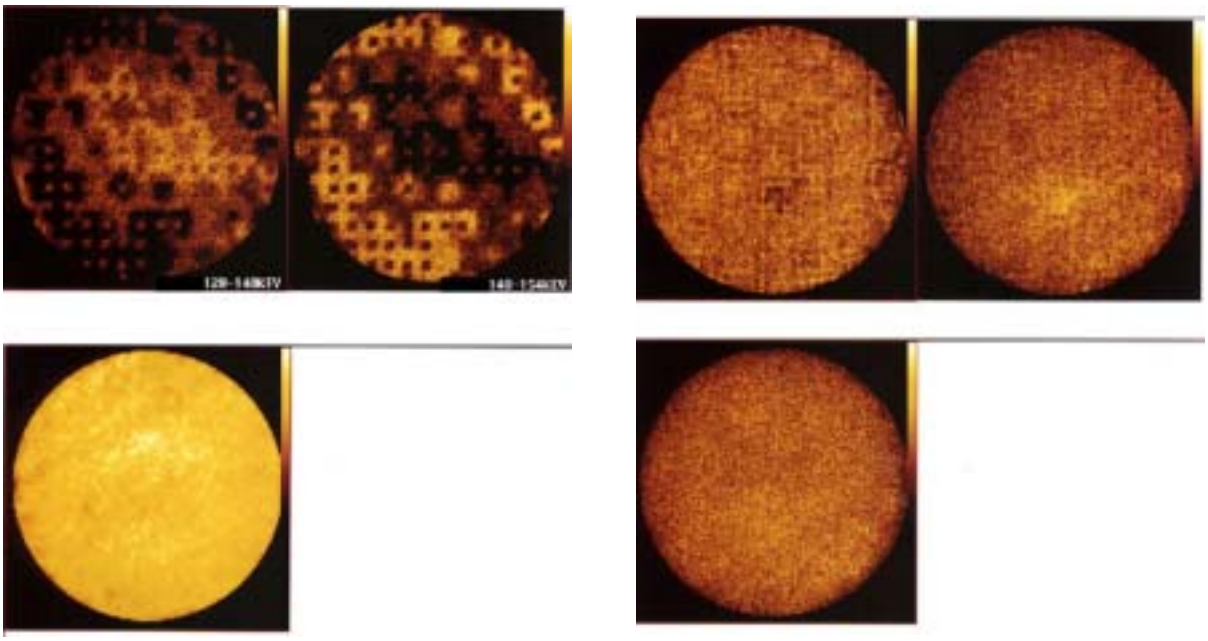

A B

This example is from the same scintillation camera as in example 2.2.6.4. As this camera aged, the energy correction, a hardware operation that was performed monthly by the user, became increasingly unreliable and sometimes had to be repeated with slight adjustments to the energy window setting until it gave results free of artefacts.

A standard set of three images was made each time the calibration was performed. Two image sets are shown here: on the left at calibration A, and on the right at calibration B. For each set of three images:

TL: Asymmetric low energy window (128–140 keV).
TR: Asymmetric high energy window (140–154 keV).
BL: Symmetric energy window at 140 keV.

Results: The set of images on the left shows serious problems due to the energy calibration, as can be seen in the symmetric window image and particularly in both asymmetric window images. These results are unacceptable. The right hand set of images shows less of a problem with the energy calibration (only a faint raster due to the energy correction matrix remains). However, the poor performance of the camera is evident and is seen on all three images.

2.2.6.6. Example: Problems with linearity correction

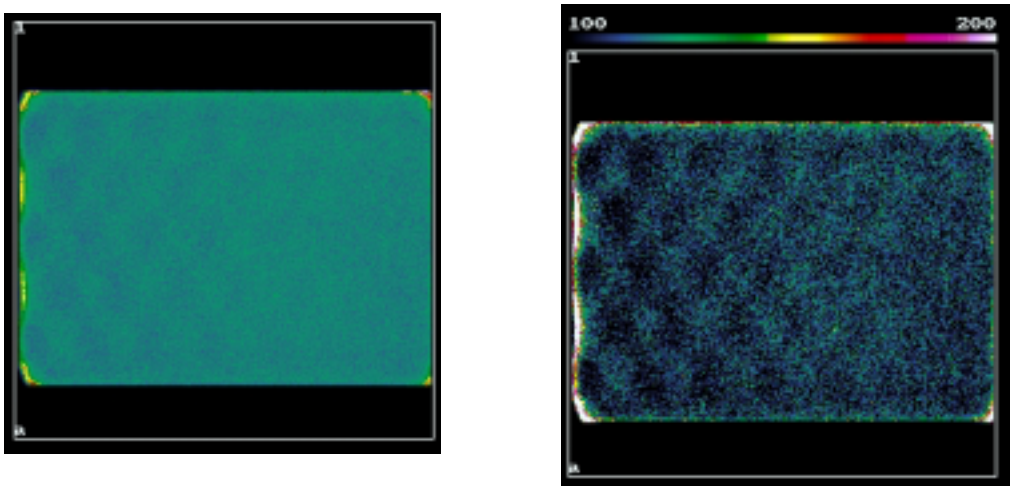

Intrinsic uniformity, ^{99m}Tc, 3 million counts each image.

L: Uniformity with no contrast enhancement.
R: Uniformity with contrast enhancement.

Results: The images show a pattern corresponding to PM tubes that is particularly visible in the left hand portion of each image. This is caused by image co-ordinates that are not aligned with the co-ordinates of the linearity correction, so that the linearity correction is not properly applied.

A new linearity of the correction matrix should be acquired.

2.2.7. Detector crystal

General comments

The detector crystal is extremely fragile and susceptible to thermal changes and mechanical impact. Whenever the collimator is removed and the crystal exposed (e.g. during collimator changes, intrinsic tests and servicing), the utmost care is required to ensure its integrity.

Points to remember:

(1) Thermal changes: Thermal drafts and rapid changes in temperature should be avoided. The general rule regarding allowable changes in temperature is a maximum change of 5ºC per hour, and some manufacturers recommend a maximum change of 3ºC per hour.
(2) Puncture: No object should be placed on the crystal housing. The object could be forgotten and cause puncture and crystal breakage when the collimator is replaced.
(3) Impact: Dropping anything on the crystal should be avoided. Whenever intrinsic tests are being performed where a radioactive source is placed above the detector, a thin Perspex (Lucite) cover should be placed on the detector to protect it from the source accidentally falling onto the crystal surface.
(4) Contamination: Whenever intrinsic tests using liquid point sources are being performed, the detector should always be covered with a plasticized sheet in order to avoid contaminating the surface of the crystal housing.
(5) Hydration: The NaI crystal detector is hygroscopic. If affected by moisture, the crystal discolours and the light transmission characteristics change. This will be seen on images as hot or cold spots or areas, depending on the energy window used and the location and extent of the hydration. Crystal hydration can be monitored by high count uniformity images using symmetric energy windows and asymmetric energy windows. For more details see the general comments in Section 2.2.7.4.

Replacing a defective crystal is very costly and time consuming. It should be avoided if at all possible.

2.2.7.1A. Example: Detector — loss of hermetic seal/optical coupling

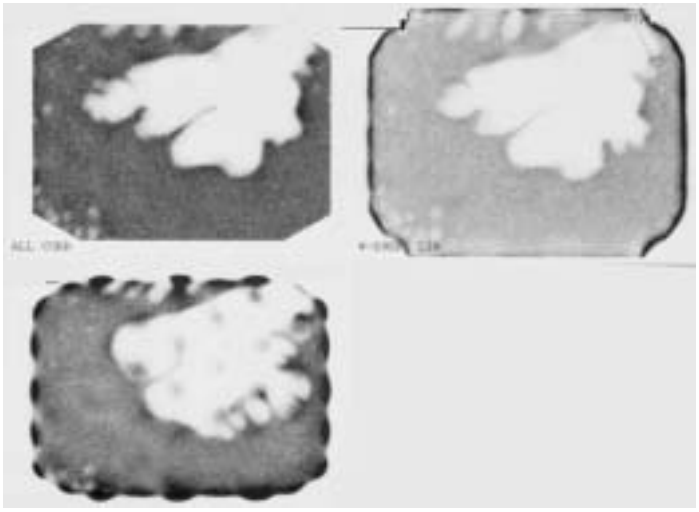

The normal 4 million count daily QC flood from one detector of a dual head system.

TL: Image acquired with the detector facing downward and with the uniformity correction activated.
TR: Image acquired with the uniformity correction map (renormalization) circuit turned off but with the energy and linearity corrections operating.
BL: Image showing the effect of rotating the detector so that it faced upward.

Results: A large irregular region with virtually no counts is seen in all images. The irregular pattern changes its shape when the detector is rotated 180º, from facing downward to facing upward. This cold area was caused by a loss of the hermetic seal of the crystal housing and the introduction of air into the crystal canister housing so that the crystal was decoupled from the glass exit window. This effect dramatically reduced the transmission of light from the crystal to the PM tubes. When the correction circuit was turned off (TR), the pattern was unchanged, indicating that the problem was not due to a change in the intrinsic ^{99m}Tc uniformity correction map. When the detector was turned upside down, the effect of gravity produced a change in the shape of the air bubbles between the crystal and the glass exit window of the crystal canister.

Comments: The QC images and clinical studies that were acquired the previous day were satisfactory. A loss of optical coupling between the crystal and the exit glass window of this magnitude would obviously have a dramatic effect on clinical studies. However, a much less dramatic loss of coupling might affect the interpretation of clinical studies but be understood as a camera problem only if QC images were acquired.

2.2.7.1B. Example: Loss of optical coupling

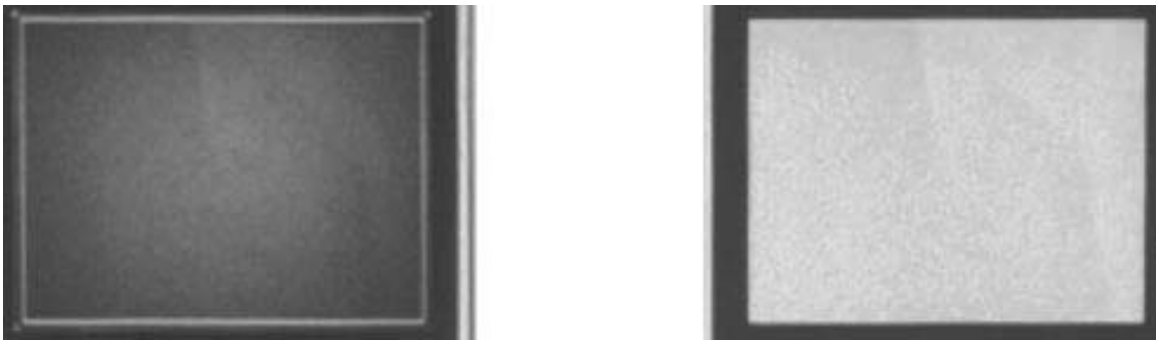

2.5 million count intrinsic flood image acquired with ^{99m}Tc on a triple head SPECT system. The point source was centred between the detector heads, which were retracted maximally. Detector to source distance was only about 1 UFOV.

L: Raw data.
R: Raw data corrected for the curvature produced by the short distance between the source and the detector.

Results: Regions of altered intensity with clearly defined borders are seen in both images. This was caused by a decoupling between the PM tubes and the glass exit window of the crystal housing.

2.2.7.2A. Example: Cracked crystal — puncture/impact (1)

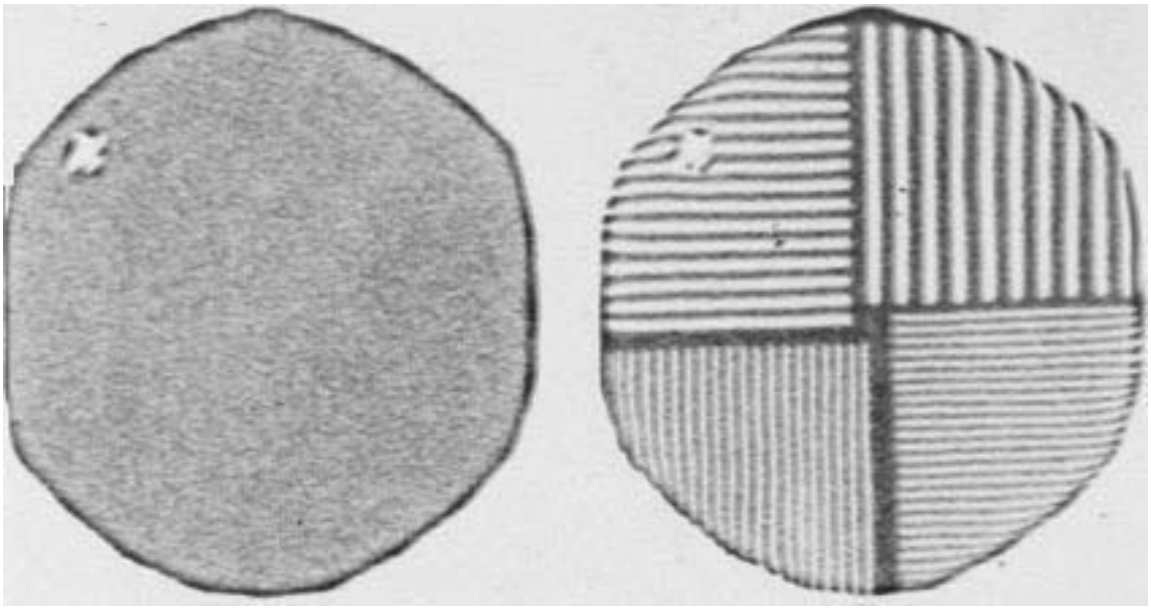

Intrinsic tests, ^{99m}Tc, 20% energy window, 3 million counts each image.

L: Uniformity image.
R: Resolution image obtained with a quadrant bar pattern.

Results: Both images show a small discrete cold area (almost like a small cross) in the top left part of the image. Note that the edge of the cold area is lined by a hot border due to light reflection at the crack in the crystal. This was caused by a puncture of the crystal.

Comments: This camera is still usable for planar imaging in the part of the crystal unaffected by the puncture. The crystal must nevertheless be replaced. It would be unwise to use it for SPECT, unless extreme care is exercised in positioning the organ of interest in the unaffected part of the FOV, well separated from the cracked area.

2.2.7.2B. Example: Cracked crystal — puncture/impact (2)

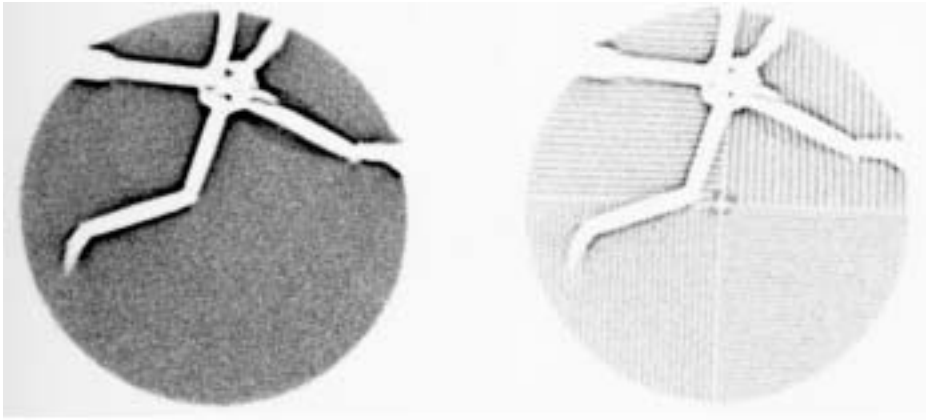

These routine uniformity (L) and spatial resolution (R) images show large, cold zigzag cracks with hot edges. This was caused by impact on the crystal. The camera is unusable until the crystal is replaced.

2.2.7.2C. Example: Cracked crystal — puncture/impact (3)

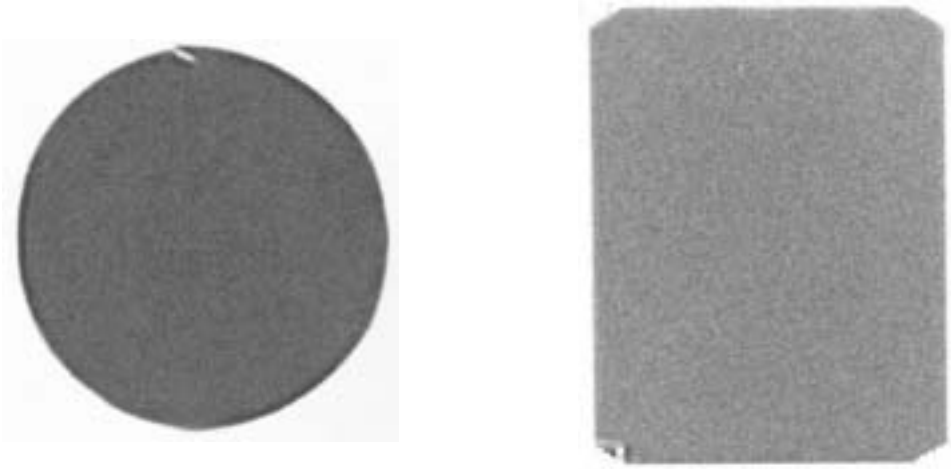

Two different examples of a routine intrinsic flood field uniformity image showing a small crystal crack at the edge of the detector.

Results: On the left image, the crack is seen as a slight cold stripe with a hot edge at the top edge of the FOV. On the right image, the crack is seen as an L shaped focal defect at the lower left corner of the detector.

In both situations, when the collimator was replaced, the crack was covered, so that the detector was still usable. In both cases the detector was not replaced.

2.2.7.2D. Example: Cracked crystal — puncture/impact (4)

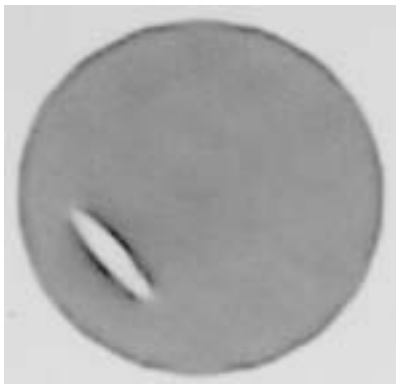

Camera A

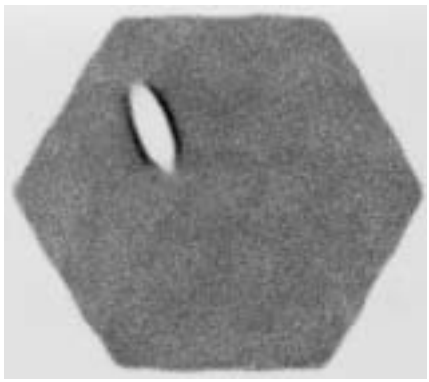

Camera B

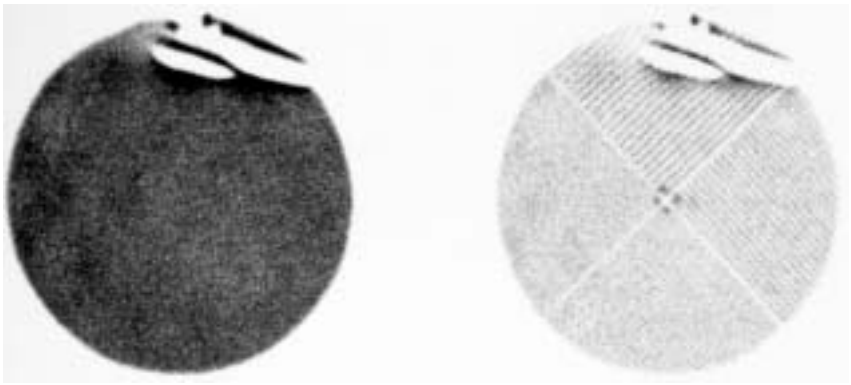

Camera C

Three examples of a crystal crack due to puncture or impact in three different scintillation cameras.

TL: Uniformity image. The crystal housing was undamaged.
TR: Uniformity image. An object had been placed on the detector and so had crushed the detector as the collimator was mounted.
BL: Uniformity image.
BR: Four quadrant bar pattern image.

Results: In all images the crack is visualized as a cold area or areas with hotter edges. Note the deformity in the spatial resolution image (BR) at the edge of the crack.

Comments: The crystal is a delicate part of the scintillation camera. Care must always be taken not to place anything on the detector or collimator. In addition, care is needed not to jar or jolt the detector and thereby cause a break due to impact.

2.2.7.3. Example: Cracked crystal — thermal

A

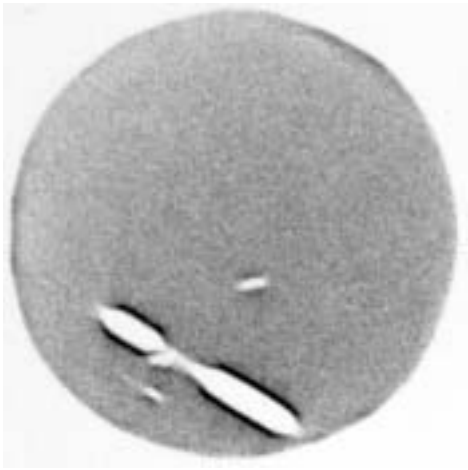

Routine intrinsic uniformity image shows various cold areas with hot edges. These are due to a thermal crack.

B

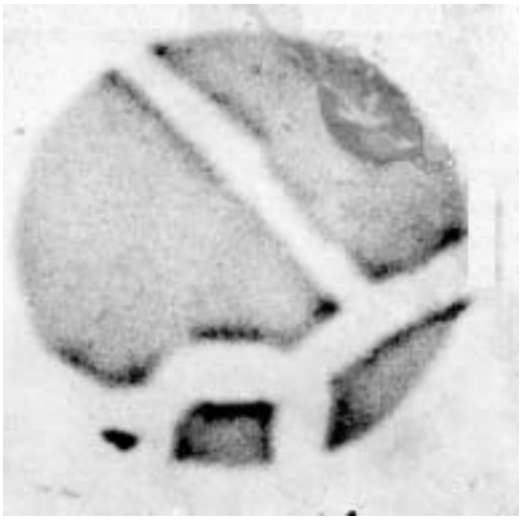

Another example of a thermal crack in the crystal. The smudges in the image (near the upper right hand edge of the FOV) resulted from poor film processing.

2.2.7.4. Crystal hydration

General comments

See also Section 2.2.2 and the general comments of Section 2.2.7.

The NaI(Tl) detector crystal is hygroscopic and is therefore hermetically sealed. This seal is not always perfect, so moisture can enter and cause oxidation of the colourless NaI crystal. The result is yellowing of the crystal, which in turn absorbs light.

Hydration is known to occur at the edge of the crystal and to spread inward, or to occur as discrete points anywhere in the FOV. The hydration process can be monitored by high count uniformity images and asymmetric energy windows. Asymmetric energy windows are particularly sensitive for detecting hydration. Images using an asymmetric low energy window will show the hydration as hot spots (due to the lower light transmission), and images using an asymmetric high energy window will show the reverse — cold spots.

Points to remember:

(1) Crystal hydration is the result of a defect in the cladding surrounding the crystal. Defects may be present from the time of manufacture throughout the life of the crystal.
(2) If crystal hydration starts at the edge of the detector, it is probably caused by an imperfect seal. It will spread inward.
(3) Crystal hydration is more obvious on images obtained with an asymmetric energy window. On asymmetric low images, hot spots are seen; on asymmetric high images, cold spots are seen.
(4) Crystal hydration is often seen as spots at any random place in the image. This phenomenon is often referred to as freckles or measles. It is more evident in images made with an asymmetric energy window (see Section 2.2.2).
(5) If crystal hydration is observed, its progress should be monitored carefully, in order to allow sufficient time for replacement of the detector. It can progress slowly or rapidly. When the hydration is visualized on flood field uniformity images obtained with clinically used energy window settings, then the crystal requires replacement.

2.2.7.4A. Example: Crystal hydration (1)

Intrinsic uniformity, ^{99m}Tc, 15% energy window symmetrically positioned over the 140 keV photopeak.

Results: Various random small hot spots are visible in the uniformity image, indicative of crystal hydration.

Comments: For confirmation of crystal hydration, additional images should be made with an asymmetrically positioned energy window. The hydrated areas will appear more obviously as hot spots on the asymmetric low image and in the corresponding positions as cold spots on the asymmetric high image (see Section 2.2).

2.2.7.4B. Example: Crystal hydration (2)

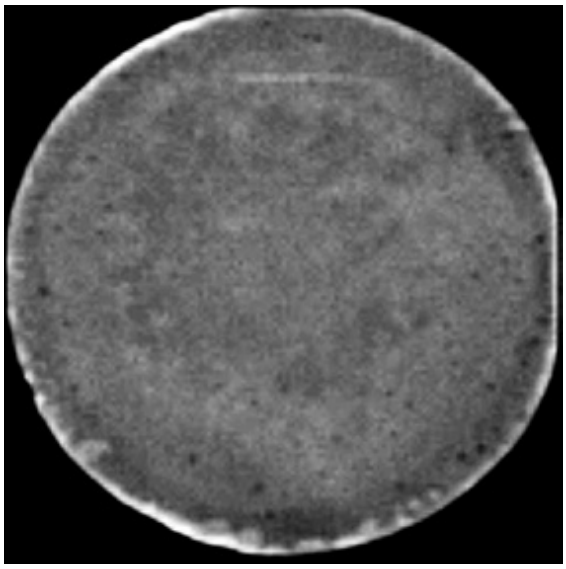

High count intrinsic uniformity, ^{99m}Tc point source, symmetric 20% energy window, 128 × 128 matrix, 120 million counts total.

Results: The flood field image shows multiple cold spots (black spots) throughout the image. These are caused by crystal hydration. The edge and spots at the edge appear hotter (whiter). The central 'cloud' of non-uniformity is due to a change in the optical grease between the crystal and the PM tubes. Some of the PM tubes can be distinguished.

This image gave the following NEMA uniformity parameter values:

Integral uniformity: UFOV = 15.3%, CFOV = 10.7%.
Differential uniformity: UFOV = 11.3%, CFOV = 7.5%.

The white line at the top was an artefact of the camera–computer interface.

This camera is unusable, and the only solution is to replace the detector head.

2.2.7.4C. Example: Crystal hydration (3)

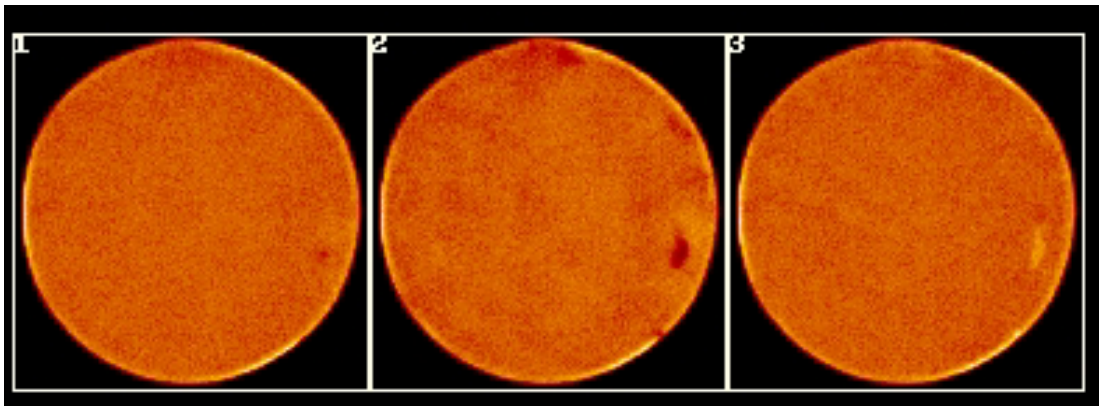

Intrinsic uniformity, ^{99m}Tc, 3 million counts, 256 × 256 matrix.

L: Symmetric energy window.
M: Energy window set asymmetric high by 5%.
R: Energy window set asymmetric low by 5%.

Results: Hydration is observed as cold flecks along the right hand border of the FOV even in the symmetric window image. It is seen particularly well as cold areas on the asymmetric high image and as corresponding hot areas on the asymmetric low image.

Comments: The hydration is sufficient also to affect the on-peak image, but its location at the edge of an uncollimated crystal has as yet no influence on clinical images. This situation requires careful monitoring.

2.2.7.4D. Example: Crystal hydration (4)

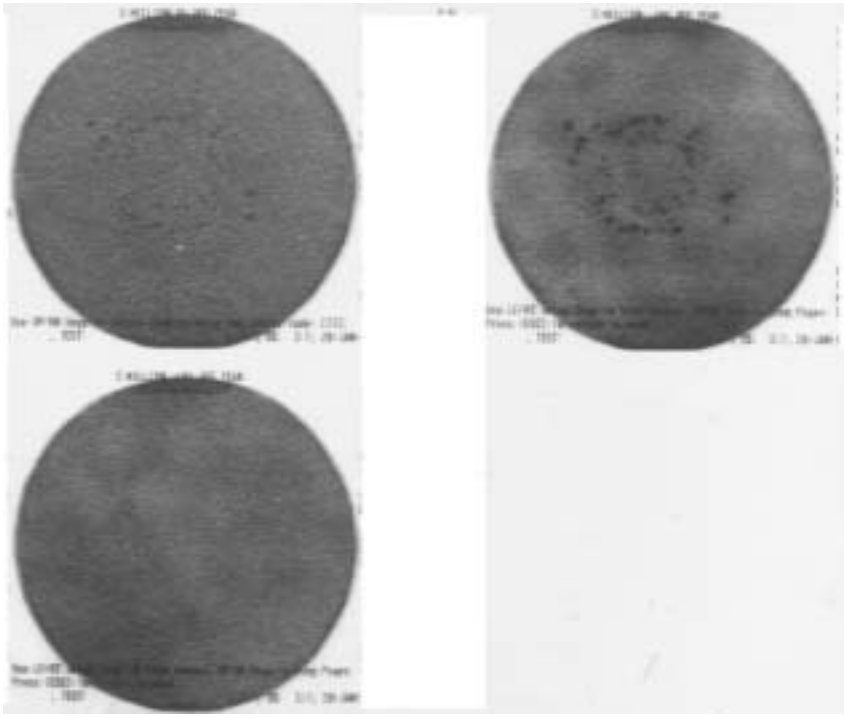

Intrinsic uniformity, ^{99m}Tc, 5 million counts each image, 64 × 64 matrix.

TL: Symmetric energy window.
TR: Energy window set asymmetric low by 10%.
BL: Energy window set asymmetric high by 10%.

Results: The symmetric image shows a series of discrete small hot spots scattered throughout the middle part of the FOV in an otherwise uniform image. These are indicative of crystal hydration (measles). The asymmetric low image shows the same hot spots but significantly more intense; the surrounding non-uniformity shows PM tubes visible as hotter areas. The asymmetric high image shows the PM tubes visible as cold areas, but discrete small spots (in this case expected to be cold), as seen in the other two images, are not discernible. In spite of the fact that the asymmetric high image does not show the characteristic cold discrete spots corresponding to the hot spots seen in other images, this crystal exhibits hydration.

This camera should immediately be put out of operation owing to the high risk of producing artefacts in clinical images. This crystal requires replacement.

2.2.7.4E. Example: Crystal hydration (5)

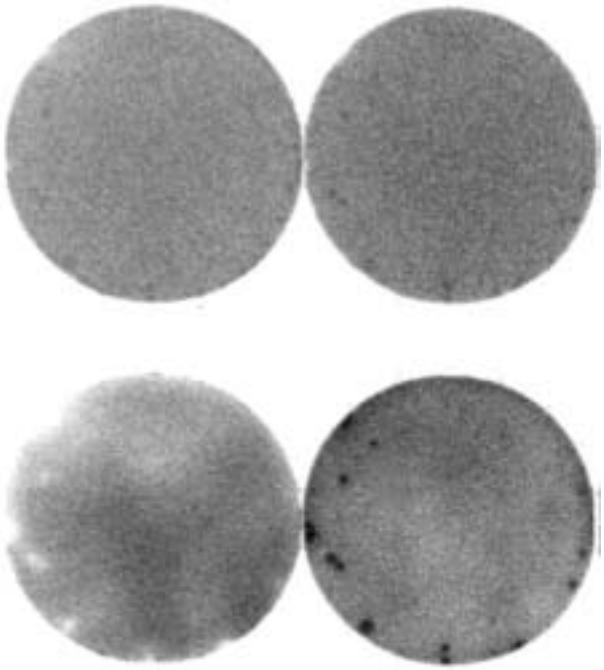

A set of analogue images was acquired as part of a QC programme. A ^{99m}Tc point source was used to acquire 1.25 million counts in each image.

TL: Count rate ~30 000 counts/s, symmetric energy window.
TR: Count rate ~75 000 counts/s, symmetric energy window.
BL: Asymmetric energy window set high.
BR: Asymmetric energy window set low.

Results: The asymmetric energy window images clearly show the hydration as cold spots in the asymmetric high image (BL) and as hot spots in the asymmetric low image (BR). The hydration is quite advanced, as can be seen by the fact that hydration is now visible in the symmetric window images at low (~30 000 counts/s) and high (~75 000 counts/s) count rates. Also, note that in this example the high count rate image shows the hydration more clearly than the low count rate image.

Comments: When hydration can be seen in images obtained with the symmetric energy window, the detector must be replaced. This camera must be used with care until it is replaced.

2.2.7.4F. Example: Crystal hydration (6)

Intrinsic flood images, ^{99m}Tc point source, 20% energy window, 3 million counts each image.

L: Symmetric energy window.
M: Asymmetric energy window set low.
R: Asymmetric energy window set high.

Results: Both asymmetric energy window images show clearly multiple focal spots due to crystal hydration: discrete hot spots in the asymmetric low window image (M) and discrete cold spots in the asymmetric high window image (R). These are as yet not seen on the symmetric window image (L). This detector needs to be monitored regularly and will eventually need to be replaced when the spots become visible in flood images obtained with the clinical energy window setting.

Note also the intense non-uniform patterns in the asymmetric window images due to poor tuning of this camera.

2.2.7.5. Example: Crystal manufacture — irregularities within the crystal

A

Acceptance testing, intrinsic uniformity, 15% symmetric energy window, 30 million counts.

T: Smoothed uniformity image.
B: Photograph of part of the crystal taken after it had been removed for replacement. A strong light was shone into the crystal in order to illuminate its structure.

Results: The uniformity image shows dark (wavy) lines which appear to have a lighter shading. The larger of the crystal defects is seen as the same wavy line in the photograph. This results from a defect within the crystal itself, probably due to the manufacturing procedure. The crystal was replaced.

B

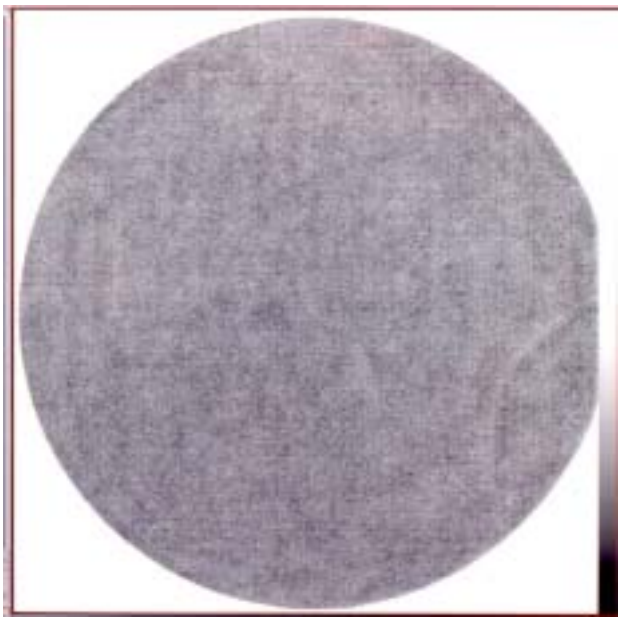

Acceptance testing, intrinsic uniformity, 15% symmetric energy window, 30 million counts, 512 × 512 matrix, some contrast enhancement.

Results: The digital uniformity image shows a crescent shaped line in the lower right part of the FOV, a dark pattern with a lighter shadow. This image manifests the same problems as in the images of A. The crystal was replaced.

Note: The image shows light vertical and horizontal stripes due to ADC non-linearities.

Comments: This example illustrates how important it is to assess the crystal at acceptance testing and to be prepared for surprises.

2.2.8. PM tube and associated electronics

2.2.8.1. Example: Uniformity — defective PM tube (old generation camera)

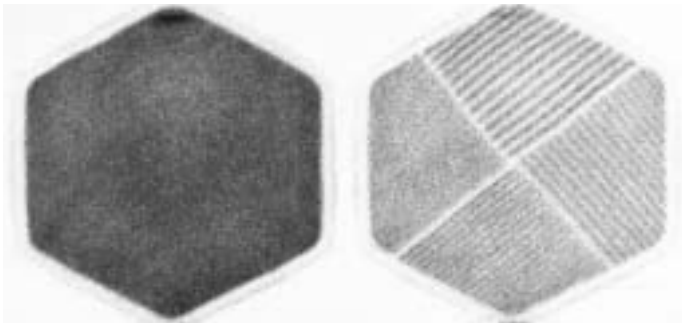

No uniformity correction

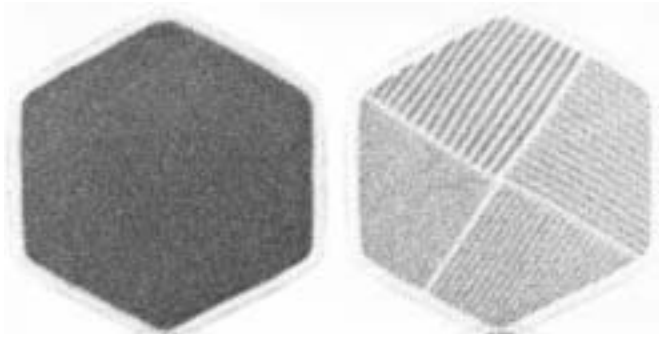

With uniformity correction map

Analogue camera with no linearity or energy corrections, ^{99m}Tc, 20% energy window, 3 million counts each image. Images of flood field uniformity and spatial resolution using a four quadrant bar pattern. The uniformity correction in this camera was obtained by a count skim calibration.

T: No uniformity correction applied.
B: With a uniformity correction applied.

Results: The flood field image obtained without the uniformity correction map shows a diffuse cold area in the upper part of the FOV (T). This was due to a malfunctioning PM tube. The spatial resolution image shows poor linearity (curved images of bars) and overall poor spatial resolution, especially over the area of the defective PM tube. Uniformity correction corrected for the non-uniformity but not for the poor spatial resolution and linearity. Service is required.

Comments: Often a uniformity correction map is applied in order to improve residual non-uniformity. Such a correction map will disguise a problem due to a defective PM tube. Therefore the camera uniformity should be checked both with and without such a correction map applied.

QC of the spatial resolution image is a necessary supplement to the uniformity flood image. Deteriorated spatial resolution will indicate any problem that has not already been detected with the uniformity image.

See also example 2.3.1.9.

2.2.8.2. Example: Uniformity — defective PM tube

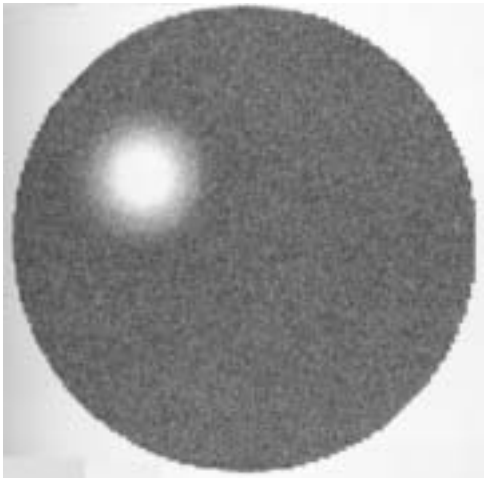

Daily QC image of flood field uniformity, ^{99m}Tc, 15% energy window, 4 million counts.

Results: The image shows a large, circular cold area that was due to a defective PM tube. Note the inner halo of lower counts and the outer halo of higher counts at the edge of the defect. Service is required.

2.2.8.3. Example: Uniformity — defective PM tube (new digital generation camera)

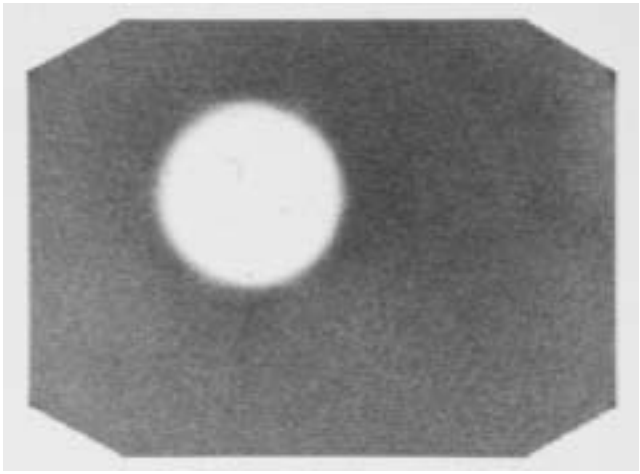

^{99m}Tc, 15% energy window, 10 million counts, modern camera.

Results: Large, circular cold area due to non-functioning PM tube. Service is required.

Comments: The image registration in new generation cameras is such that a non-functioning PM tube will give an unmistakable circumscribed cold spot in the location of the PM tube. Note that the tube itself, the preamplifier or subsequent circuits could be defective. In this example, the fault is in the middle of the FOV and the scintillation camera cannot be used. Service is required before clinical work can resume.

2.2.8.4. Example: Uniformity — defective PM tube at edge of FOV

^{99m}Tc, 15% symmetric energy window, 256 × 256 matrix, 10 million counts.

Results: A discrete, semicircular cold indentation is seen at the top of the FOV. This is due to a defective PM tube. Service personnel replaced the PM tube.

Comments: Although service must take place to repair the defect, this camera could still be used for planar and SPECT imaging, provided that the organ of interest lies well below the defective PM tube, but it could not be used for whole body imaging.

2.2.8.5. Example: Clinical bone scan — defective PM tube

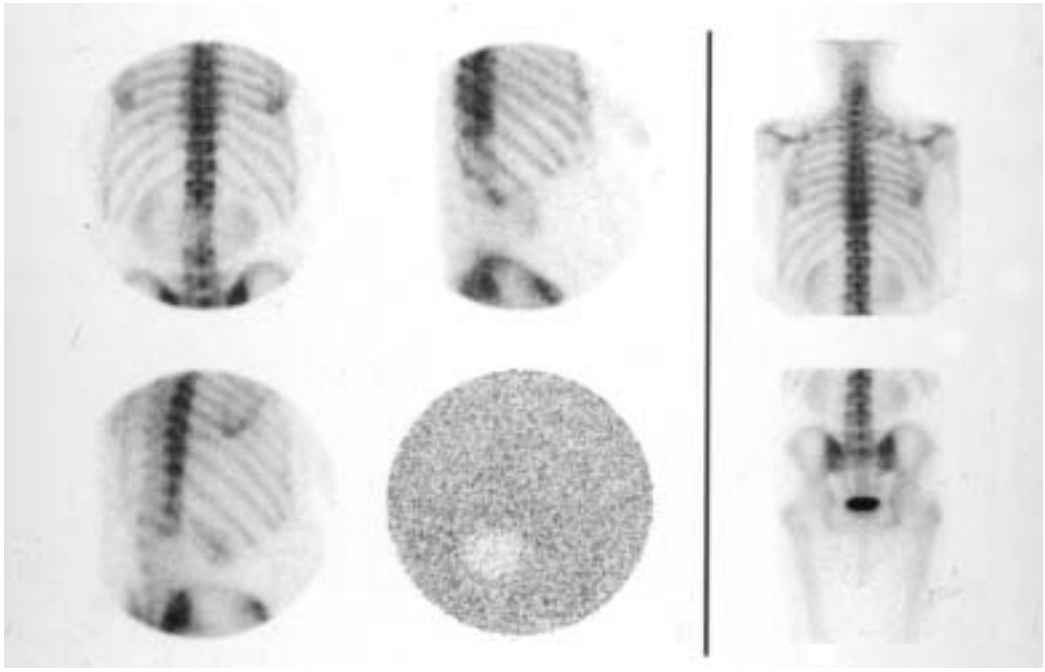

Bone scan of patient using ^{99m}Tc phosphonate, 15% energy window.

TL, TM and BL:	Camera A — different single spot views of the skeleton: posterior, right anterior and right anterior oblique, respectively.
BM:	Camera A — flood field image taken after the spot views.
TR and BR:	Camera B — posterior spot views of the same patient.

Results: The spot views from camera A show an area of apparent decreased activity in the lower skeletal area that is especially evident in the TL and BL images. This was due to a defective PM tube, as demonstrated in the uniformity flood field image (BM).

Images of the same patient made with scintillation camera B show a normal ^{99m}Tc phosphonate distribution in the lower spinal column (TR and BR).

Comments: This patient was imaged on two different scintillation systems because the cold area in the lower spine was not considered to indicate pathology but to be an artefact. The artefact, caused by a defective PM tube, was confirmed by a subsequent uniformity image (BM).

If a second camera had not been available, the patient position could have been shifted so that the lower skeleton could be imaged in another part of the camera FOV.

Unusually, the patient positions in the TL, TM and BL images are such that the defective area is over the same part of the spine. More usually there would be translation between successive views, so that the artefact would be more easily seen. A smaller defect, however, would be more difficult to see.

2.2.8.6. Example: Clinical scan — defective PM tube

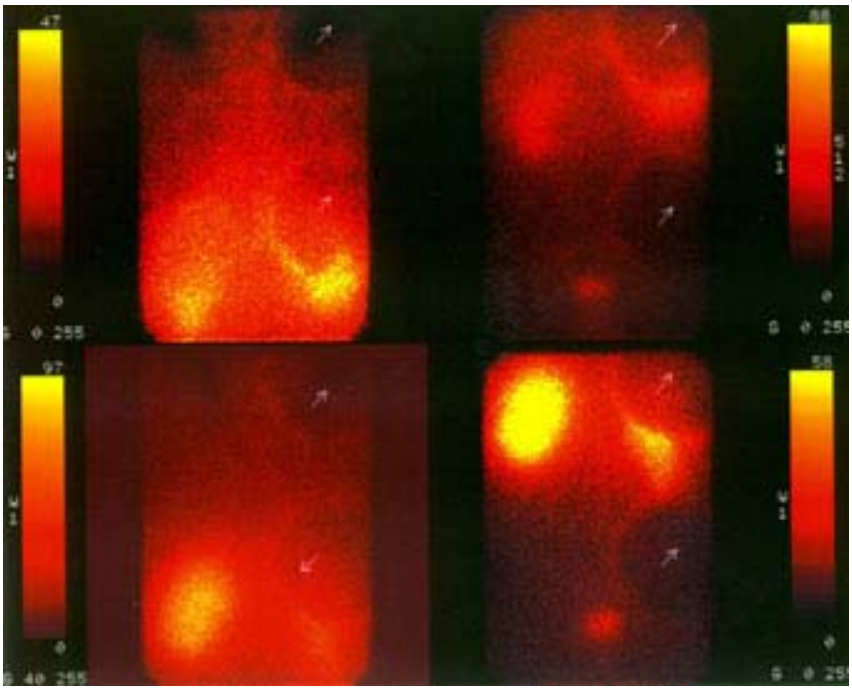

A

B

A: Clinical ^{111}In somatostatin receptor study. Upper and lower abdomen in the anterior view (top two images), and upper and lower abdomen in the posterior view (bottom two images).
B: Uniformity image obtained after the clinical study.

Results: The clinical study showed two large, circular colder areas (indicated by arrows). These were verified by the uniformity image on the right, which shows two large cold areas with a hot border due to defective PM tubes.

Comments: The non-uniformities in this example were large enough to be recognized in the patient's images. Routine uniformity QC images were only taken on a weekly basis on this camera, and the non-uniformity was not detected prior to the patient study.

Later this non-uniformity turned out to recur intermittently, with no obvious reason, and appeared even after tuning. The scintillation camera was replaced.

2.2.8.7. Example: Maladjusted PM tube amplifier

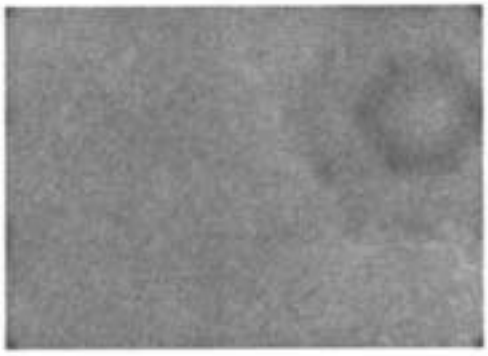

Routine intrinsic uniformity, ^{99m}Tc, 15% energy window, 128 × 128 matrix. The image has been contrast enhanced.

Results: Within the upper right quadrant of the image, there is a distinct non-uniformity: a hexagonal pattern delineated by two borders of increased counts. This was due to a fault in the adjustment of a PM tube amplifier.

2.2.8.8. Example: Loss of coupling between PM tubes and light pipe

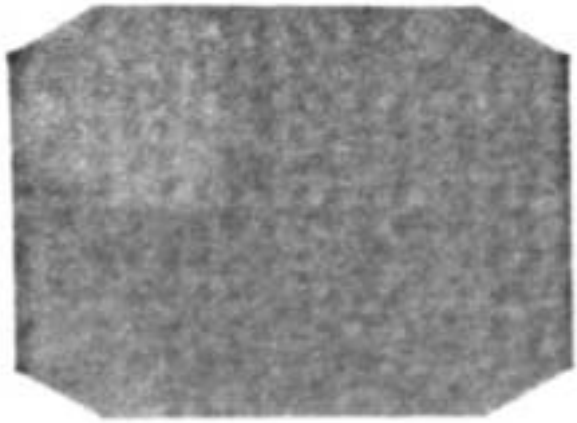

A 4 million count intrinsic ^{99m}Tc image was acquired with a symmetric 20% window at ~75 000 counts/s, with the intrinsic ^{99m}Tc uniformity map correction turned off.

Results: The cold region in the upper left quadrant was considerably larger than a single tube and has a distinct edge. Service personnel opened the detector head and recoupled eight PM tubes to the plastic light pipe.

Comments: This condition had been seen previously using off-peak images, but use of a ^{99m}Tc intrinsic flood correction made the problem less visible.

2.2.8.9. Example: Faulty electronics associated with PM tubes

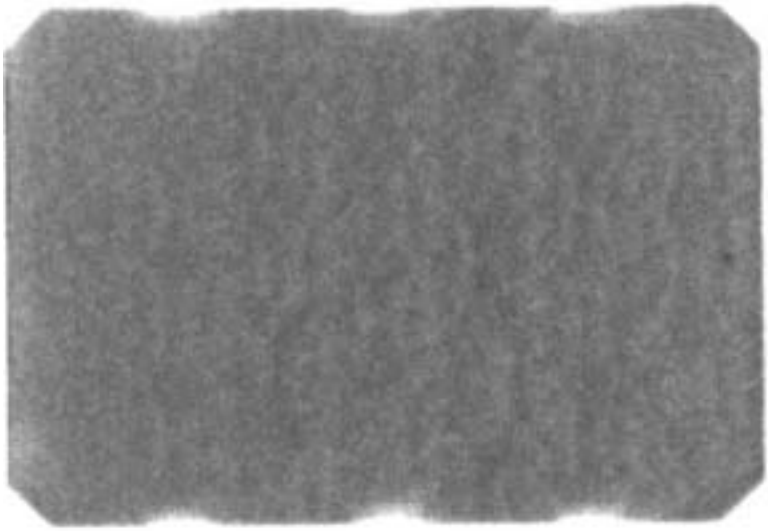

Routine intrinsic uniformity check, ^{99m}Tc, 20% energy window.

Results: Three cold indentations are seen at the upper and lower edges of the image. These were due to faulty electronics associated with the PM tubes.

2.2.8.10. Example: Faulty PM tube preamplifier

Routine intrinsic uniformity check with ^{99m}Tc, 15% symmetric energy window.

L: Uniformity image.
R: Four quadrant bar pattern image.

Results: A diffuse area of reduced counts is seen in the top right corner of the FOV. Note also the deformity in the bar pattern at the same location. This problem was due to a faulty preamplifier.

2.2.8.11. Example: Faulty PM tube circuitry

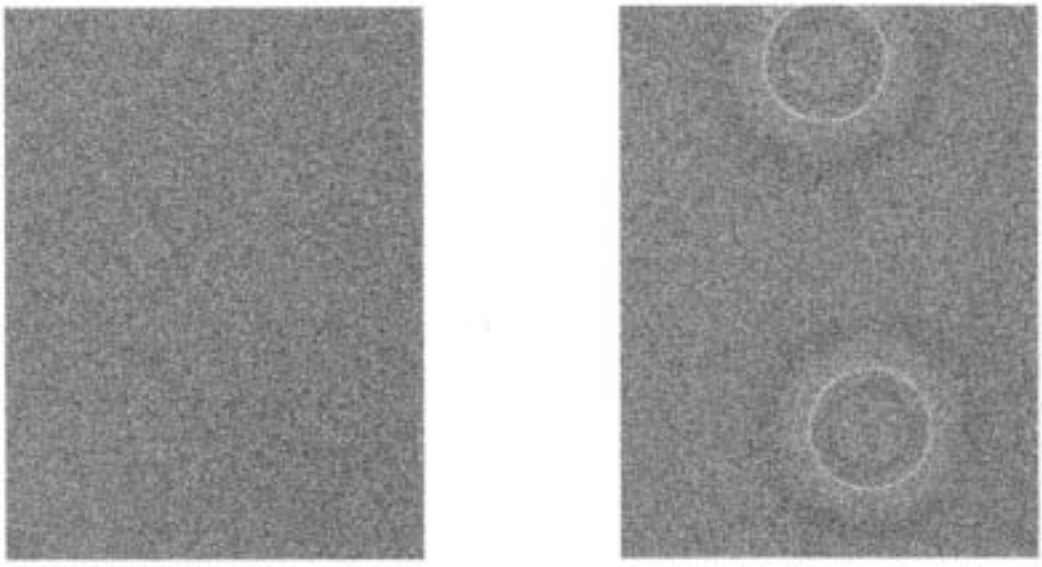

Dual head scintillation camera, intrinsic uniformity, ^{99m}Tc, 15% symmetric energy window, 5 million counts each image.

L: Detector 1.
R: Detector 2.

Results: Detector 1 shows good uniformity, whereas detector 2 shows two large, circular non-uniformities, each consisting of several rings of different intensities. The PM tube circuitry was faulty and required servicing.

2.2.9. Collimator

General comments

The collimator is a potential major source of non-uniformity, and must be carefully checked for uniform response at acceptance testing and periodically thereafter. Image artefacts can arise from defects in septa and hole alignment, septal tears, punctures and scrapes (arising, for example, when collimators are changed or from contact with the pallet of the imaging bed), etc.

The most common test to assess collimator integrity (especially in the case of damage) is that of extrinsic uniformity. However, a point spread function image obtained from a ^{99m}Tc point source placed at several metres from the collimator is also sensitive for detecting defects and discontinuities in the septa and hole alignment (see figure below). Usually the point source has to be moved opposite to different parts of the collimator in order to image each area of the collimator.

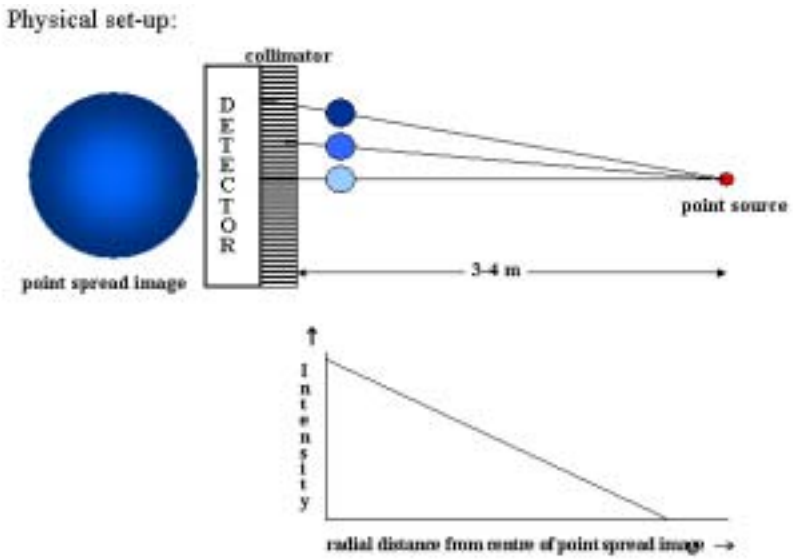

2.2.9.1. Example: Representative extrinsic flood field uniformity images — low, medium and high energy parallel hole collimators

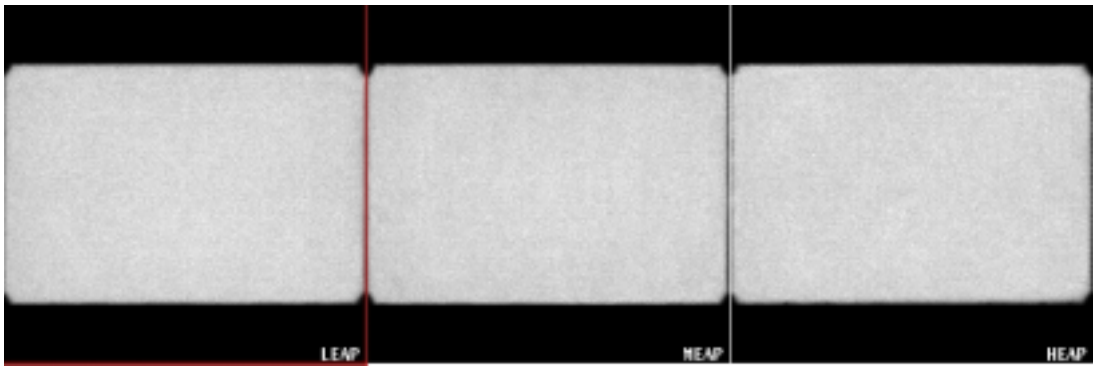

Routine extrinsic uniformity images, ^{99m}Tc fillable flood source, 20% energy window, 30 million counts each image.

L: Low energy collimator.
M: Medium energy collimator.
R: High energy collimator.

Results: All images show a uniform response.

2.2.9.2. Example: Collimator septa and hole alignment assessed by a distant point source — cast and foil collimators

A

Medium energy cast collimator

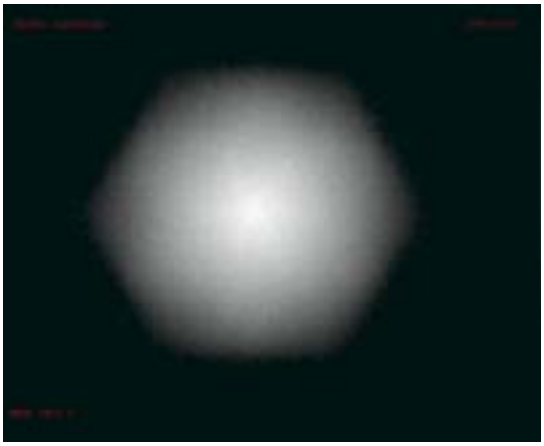

High energy cast collimator

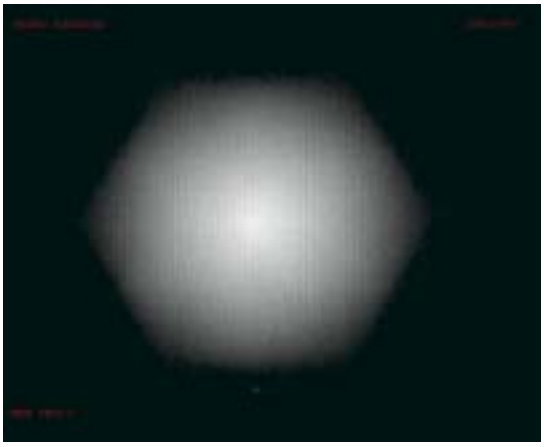

Circular FOV scintillation camera, ^{99m}Tc point source (about 220 MBq) positioned at about 3 m (approximately 6 FOV) distance from the collimator, 3 million counts each image.

L: Medium energy cast collimator.
R: High energy cast collimator.

Results: Images from both collimators show the expected pattern of counts, indicating that the holes are perpendicular and parallel. Acceptable.

B

Medium energy foil collimator

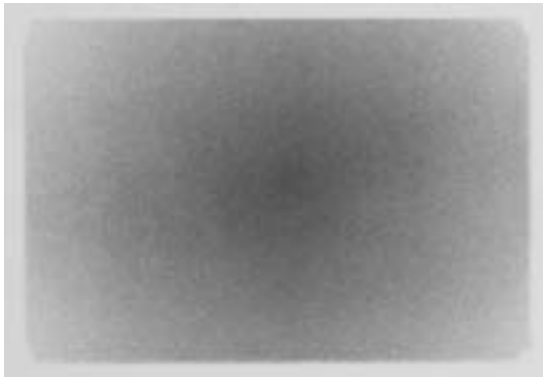

High energy foil collimator — left FOV

High energy foil collimator — right FOV

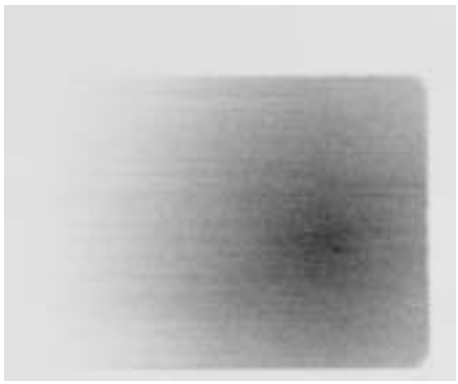

Rectangular FOV scintillation camera, ^{99m}Tc point source (180 MBq) positioned at about 4 m (approximately 7.5 UFOV) distance from the collimator, 3 million counts each image.

T: Medium energy foil collimator.
BL and BR: High energy foil collimator — point source positioned off-centre to image the left and right parts of the collimator.

Results: Although there is some irregularity in the image from the medium energy collimator and a striped effect from the high energy collimator, these images are still acceptable.

2.2.9.3. Examples: Collimator septa and hole alignment assessed by a distant point source — low energy collimator problems

Examples from different scintillation cameras. In each example, a ^{99m}Tc point source (about 220 MBq) was positioned at about 4 m distance from a low energy collimator. 3 million counts each image. All images below were obtained at acceptance testing.

Results:

A

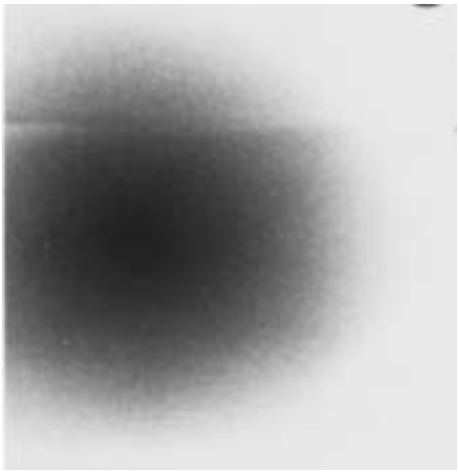

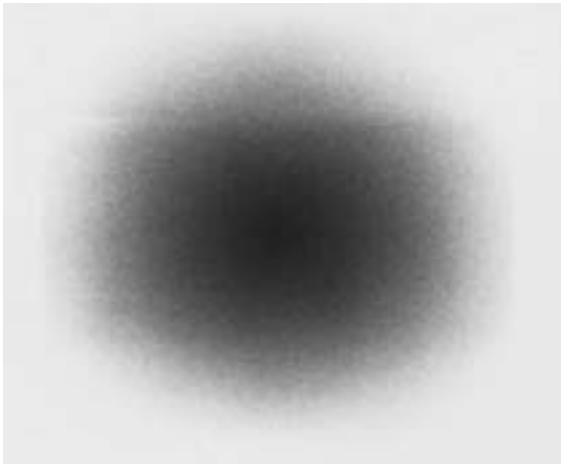

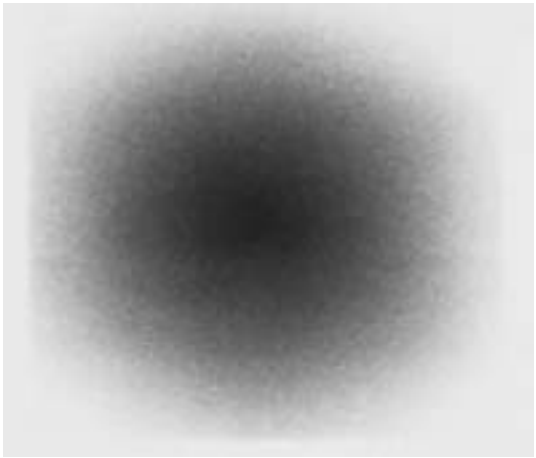

Rectangular FOV scintillation camera. Images were obtained with the point source opposite to different parts of the collimated FOV.

TL and TR: Point source off-centred in order to check the hole alignment in the upper quadrant of the collimator. A line of discontinuity in the point spread function is seen (across the short axis of the collimator) in the upper part of the FOV in both images.

B: Point source moved to image the middle part of the collimator. The response is uniform. Nevertheless, the collimator is unacceptable and requires replacement.

Note: The images have been cropped to show only the point spread response of the images, not the whole FOV.

B

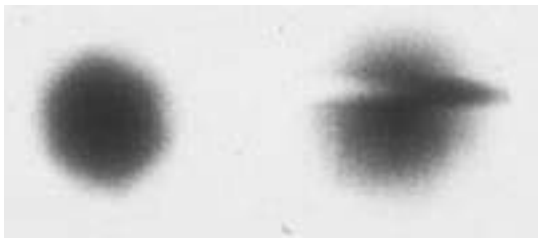

LEAP LEHR

Round FOV camera. The left image from the LEAP collimator shows a satisfactory response. The LEHR collimator (right) shows a distinct streak artefact due to hole misalignment with respect to the crystal face. This collimator requires replacement. These images were acquired at acceptance testing.

C

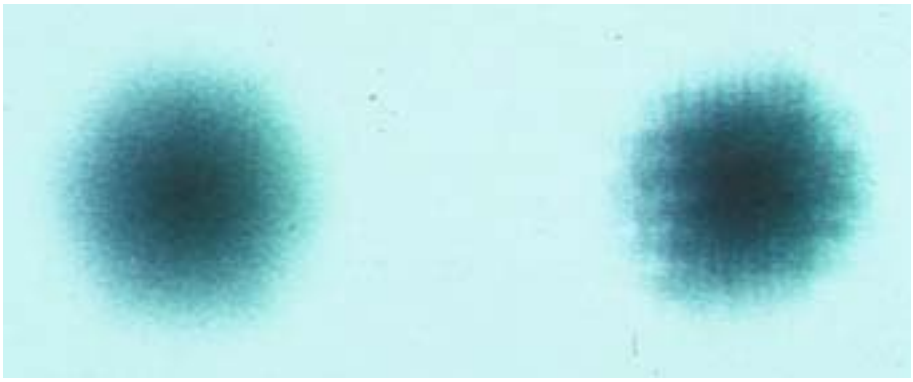

LEAP LEHR

L: The LEAP collimator shows no abnormality in the image of the distant point source.

R: The striped response in both *x* and *y* directions indicates severe collimator hole angulation problems at manufacture, i.e. the axes of the holes are not parallel to one another and perpendicular to the surface of the collimator. This collimator is unacceptable and requires replacement.

D

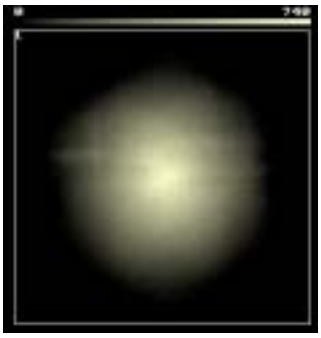

Digital acquisition made in a 256 × 256 matrix. The horizontal stripes show that there is hole misalignment for several rows of holes in this collimator. The collimator requires replacement.

E

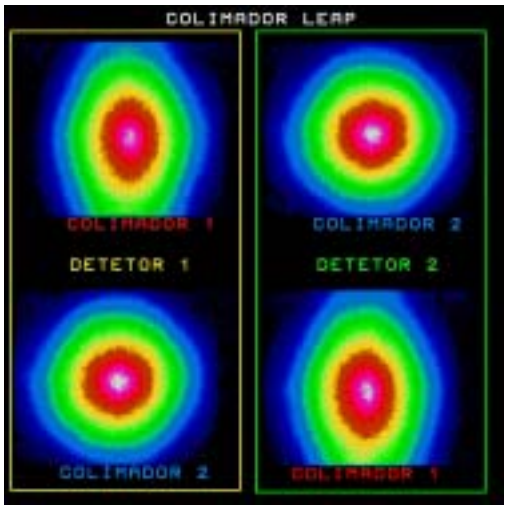

Dual detector scintillation camera. LEAP collimators, digital acquisitions made in a 256 × 256 matrix. Images on the left are from detector 1, those on the right from detector 2.

TL: Collimator 1 on detector 1.
TR: Collimator 2 on detector 2.

In the bottom row the collimators have been exchanged (possible with this system but not with all dual head cameras).

BL: Collimator 2 on detector 1.
BR: Collimator 1 on detector 2.

Results: The oval shaped responses in the TL and BR images were both obtained with collimator 1 and indicate a divergence in the angulation of the septa of the collimator. By exchanging the collimators it was shown that the oval shape was not due to a problem with the *x* or *y* gain of the detector. This collimator requires replacement.

F

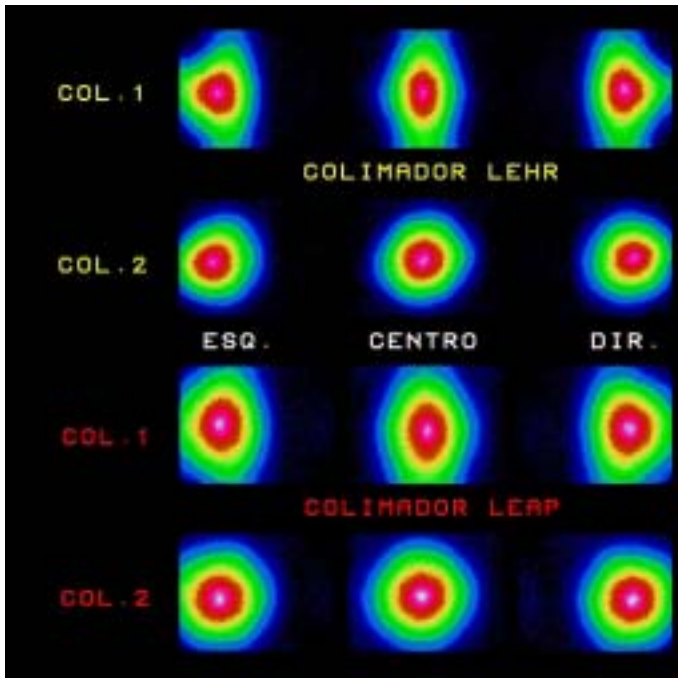

These images were made with the same dual head scintillation camera as in the previous example (E). Digital acquisitions were made in a 256 × 256 matrix.

The left column of images is from the left side of the collimator, the middle column from the central part of the collimator and the right column from the right side of the collimator. The collimators were mounted on their corresponding detectors.

First row: LEHR collimator 1.
Second row: LEHR collimator 2.
Third row: LEAP collimator 1.
Fourth row: LEAP collimator 2.

Results: Both LEHR collimator 1 and LEAP collimator 1 show an oval elongation in the image from a distant point source. Both collimators are unacceptable and require replacement.

LEHR collimator 2 shows a slight irregular shape from the point source, and LEAP collimator 2 shows a very reasonable isotropic response. Both these collimators are acceptable.

Comments: It is unusual to find two collimators (in this case both for detector 1) that have a similar hole angulation problem. The previous example (E), where collimator 1 was imaged on both detectors, demonstrated that there was no problem with the image gain in *y*.

G

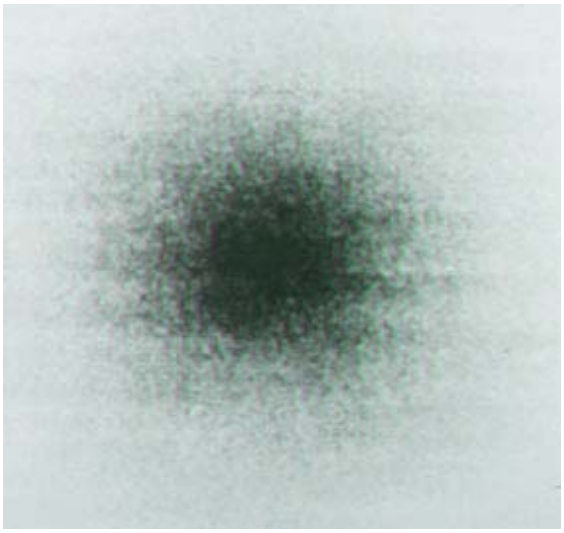

This LEAP collimator shows some subtle hole angulation errors but is still acceptable. This type of pattern is generally associated with foil collimators.

H

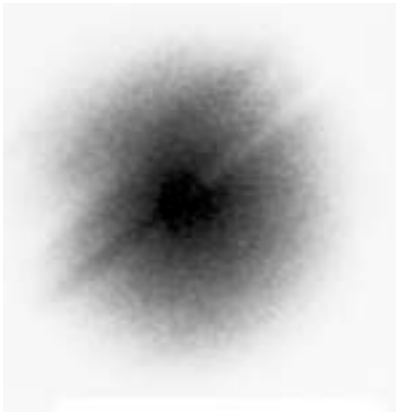

This image was made with a remanufactured scintillation camera supplied with an old collimator. The image shows severe angulation errors, and the collimator requires replacement. Users should be especially careful to check the collimators supplied with refurbished or remanufactured cameras.

I

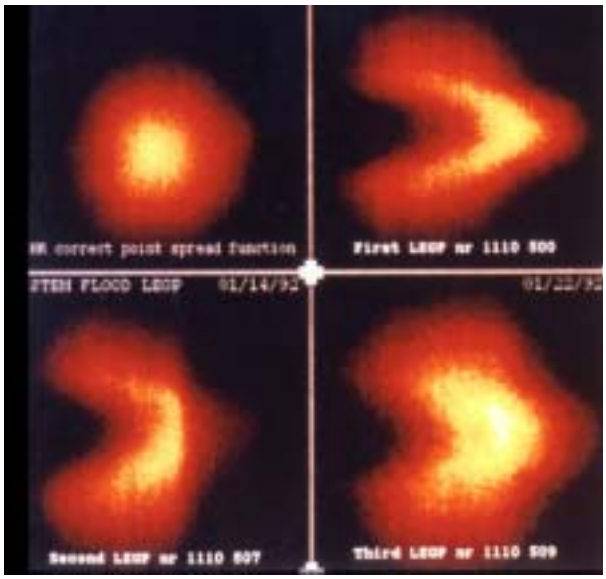

A series of point spread images from four different collimators supplied for the same scintillation camera.

TL: A good response, as would be expected. This is the only acceptable collimator of this series.

TR, BL and BR images all show a crescent shaped image from the distant point source, indicating severe misalignment of the septa and holes to a greater or lesser degree in the *x* direction from a section of the collimator. The lower images were from collimators obtained to replace the first defective collimator (TR). Only after two replacements that had similar defects was an acceptable collimator delivered.

2.2.9.4. Example: System uniformity — collimator septa damage — puncture

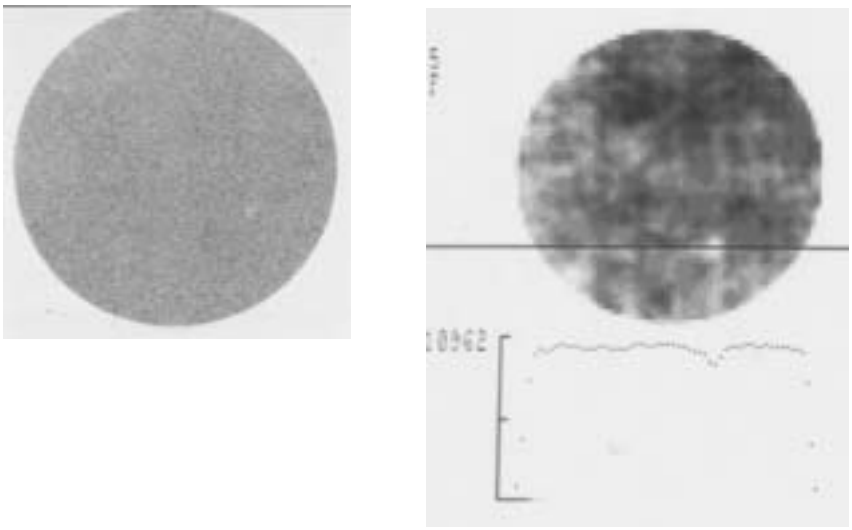

Routine extrinsic uniformity check, LEHR collimator, ^{99m}Tc flood source, 3 million counts.

L: Analogue uniformity image.
R: High contrast digital image with a profile superimposed at the level of the small cold spot in the lower right quadrant. The count profile shows a definite dip in counts corresponding to the cold spot.

Results: The extrinsic analogue uniformity image shows a very small discrete cold area in the lower right quadrant of the FOV (L). This was due to a slight dent in the collimator that caused a few holes to be occluded. This was almost overlooked on visual inspection of the flood field image. The quantitative uniformity parameters signalled the problem by showing an unexpected increase in non-uniformity of 3% in the NEMA integral and differential uniformity parameters (compared with previous values). The digital image with count profile shows clearly the dip in counts due to the occluded septa.

Comments: This camera was being used for SPECT. Such a small discrete area would have produced a distinct ring artefact. Use of the collimator was discontinued until the damage had been repaired, a matter of straightening out the septa. Fortunately the damage could be repaired on-site. The collimator manufacturer was able to straighten the bent septa using the original septal pins used during manufacture.

Such a small local area of septal damage can easily be overlooked. Careful evaluation of the flood field image and its quantitative results, as well as regular physical inspection of collimators, are essential.

2.2.9.5. Examples: System uniformity — collimator septa damage — scraped

A

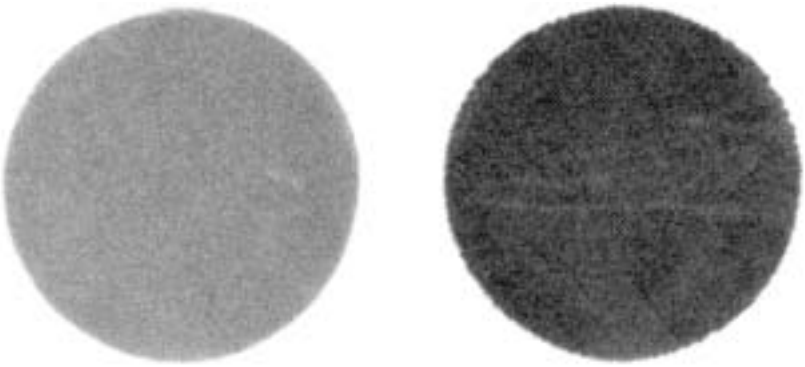

B

Routine system uniformity, ^{99m}Tc flood source, 20% energy window, 3 million counts.

A: LEHR (left) and high energy (right) collimators on the same scintillation camera.
B: LEAP collimator (on another camera).

Results:

A: The flood field image from the LEHR collimator (left) shows a short diagonal line of decreased count density (at about 3 o'clock) due to septa that were damaged when the collimator was removed from the detector head. The results of the damage are occluded septa and diminished sensitivity.

On the flood image from the high energy collimator (right), various irregular lines of reduced intensity are visible in the image. The septa were deformed by the collimator having been dragged across the mounting hardware on the detector.

B: The flood image from the LEAP collimator shows several diffuse areas of slightly decreased counts resulting from dents in the collimator.

Comments: The damage could be easily recognized on visual inspection of the collimators. The collimators required replacement.

Note: Because collimators can be easily damaged, the operator must be trained to be well aware of the fragility of the collimators and their importance for clinical results. If damage does occur or is suspected, it must be reported immediately so that the collimator can be checked and further action taken as soon as possible.

2.2.9.6. Example: System uniformity — collimator septa tear

^{99m}Tc, 15% energy window, 30 million counts, LEHR collimator.

Results: The image shows a discrete line (in the left middle part of the FOV) of higher counts indicating that the collimator septa are separated. The collimator requires replacement.

This type of problem is likely to occur with a foil collimator and can originate during shipment of a new camera.

2.2.9.7. Example: Defective foil collimator

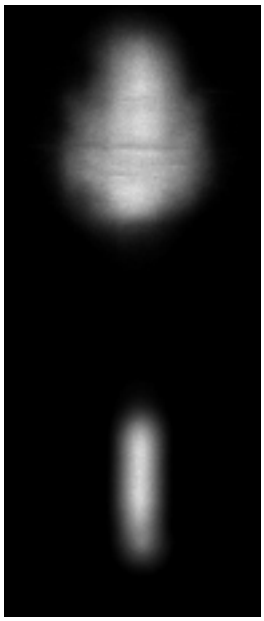

It was noticed that images had increasing sensitivity with distance from the radioactive source when a foil low energy collimator was used. On investigation, the collimator's structure was found to be defective. The septal structure had become detached from the frame of the collimator and had become concave.

In order to investigate the problem, images were obtained of a line source placed at 150 cm below each collimator.

T: Image obtained with the low energy foil collimator.
B: Image obtained with the low energy cast collimator.

Results: The images show the extreme broadening of the line source image from the foil collimator due to the angulation of the septa. The foil collimator required replacement.

2.2.9.8. Example: Clinical study — collimator star pattern

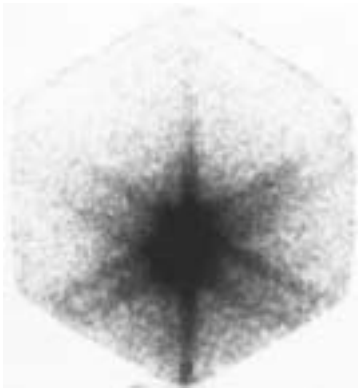

This ^{131}I image of a patient with metastatic thyroid tissue was acquired using a high energy collimator.

Results: An intense star pattern is seen. This is produced by photon penetration of the hexagonal array of collimator holes and septa. Certain directions of travel through the collimator contain a lesser total septal thickness and produce the arms of the star.

Comments: The image shows parallel arms because there are two separate hot regions. The star pattern is an effect usually associated with foil collimators rather than cast collimators, and is inevitable when imaging very hot foci of activity.

2.2.10. Artefacts arising from sources/phantoms

2.2.10.1. Fillable flood sources

General comments

The use of fillable flood sources requires care in order to ensure uniform mixing, to ensure that there are no air bubbles in the area used to assess scintillation camera performance and to ensure that there is no bulging or overfilling with liquid. Bulging can be avoided by using a phantom with thick walls, e.g. 1 cm of Perspex (Lucite). To avoid overfilling, a phantom that is filled horizontally is preferable to one that is filled vertically.

In addition, the seal must be perfect to ensure that there is no leakage of the radioactive contents that would lead to radioactive contamination. Distilled (de-aerated) water should be used if the contents of the phantom are not disposed of after use (after the radioactivity has decayed). The solution should be replenished regularly in order to avoid the growth of algae, which can bind with ^{99m}Tc compounds, causing hot artefacts. The use of ^{99m}Tc pertechnetate is advised. Other ^{99m}Tc radiopharmaceuticals may cause problems.

Careful filling and secure knowledge that a fillable flood phantom is indeed uniformly filled are especially important when the phantom is intended to be used to obtain uniformity (or sensitivity) correction maps and calibration data.

The construction of the flood source can influence the uniformity measured. Phantoms with thick walls and a large volume have shown an increase in counts in the centre of the FOV, which is possibly due to scatter and septum penetration (depending on the collimator and radionuclide used). These effects cause a non-uniform result from a camera which on other tests appears uniform. This is more likely to be a problem when uniformity is very good. The dimension of the flood source should be such that it is several centimetres larger than the collimated FOV. It is often impossible to obtain a good fillable flood source for use with modern scintillation cameras. Larger detector size results in a heavy source, and multiple detectors may prevent sources from being positioned as required. The user is advised to always exercise caution when using fillable flood sources.

2.2.10.1A. Examples: Fillable flood sources — air bubble

Extrinsic routine QC images using a fillable flood source, ^{99m}Tc, 20% energy window.

Results:

A

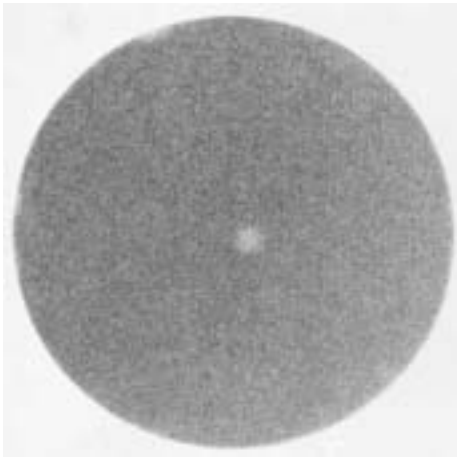

Uniformity image. A discrete circular cold area is seen in the middle of the FOV. Visual inspection of the flood source revealed a large air bubble. The cold indentation at the top left edge of the FOV was also due to an air bubble.

B

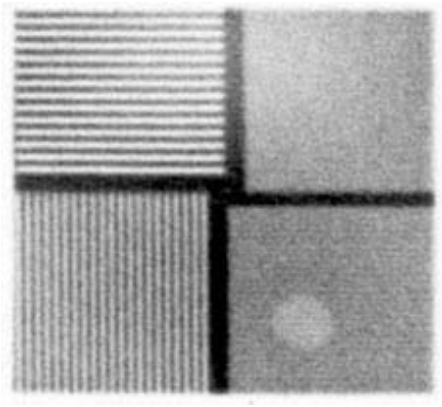

Spatial resolution image using a four quadrant bar pattern. A discrete large circular cold area is seen in the lower right quadrant. By changing the position of the flood source, the position of the cold area was also moved. The cold area was due to an air bubble in the solution that was clearly visible on physical inspection.

C

The image shows an elongated cold area, due to an air bubble, at the left edge of the FOV. This air space was clearly seen and was due to air left in the phantom after filling.

Note: The distinct delineation of the cold area is indicative of an air bubble rather than a defect in the detector.

2.2.10.1B. Example: Fillable flood source — non-uniform mixing

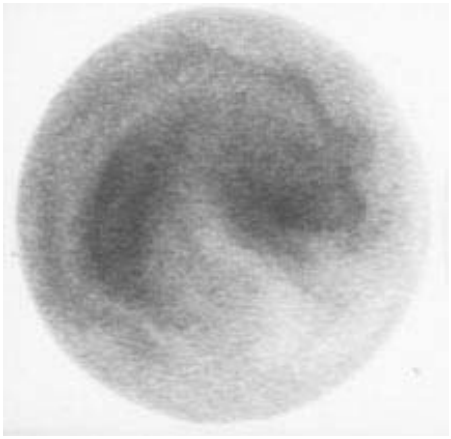

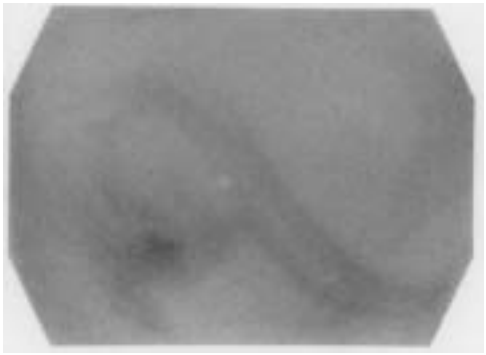

Two different examples of a routine extrinsic uniformity image using ^{99m}Tc in a fillable flood source. In each situation the ^{99m}Tc was injected into the water in the flood source and was left to disperse over a period of about one hour.

Results: The non-uniformity shows that dispersion was insufficient to produce a homogeneous distribution of ^{99m}Tc, and that actual mixing must take place. The right image also shows a small air bubble in the centre of the FOV.

2.2.10.1C. Example: Fillable flood source — bulging sides

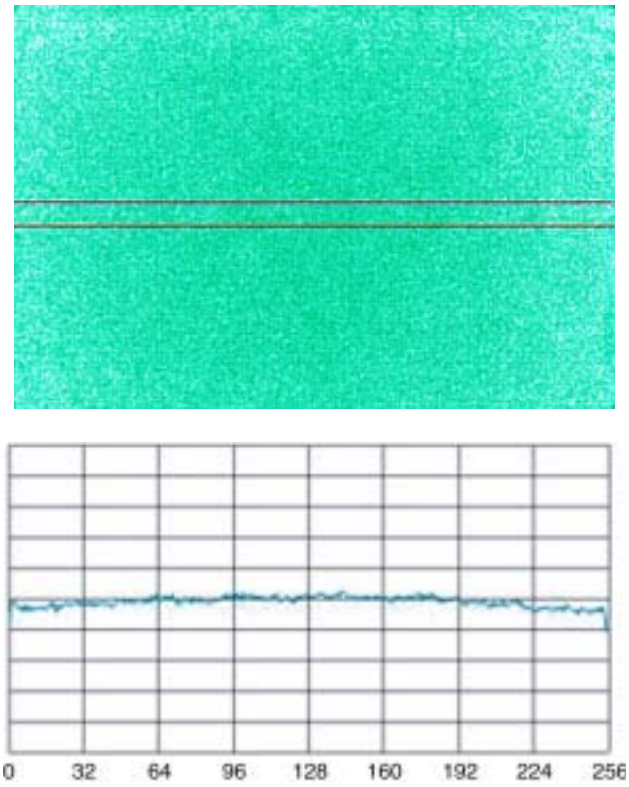

Routine uniformity image obtained with a fillable flood source. The phantom was filled with too much water, which produced bulging of the centre part of the phantom.

Results: The image shows a dome shaped increase in counts at the centre due to the bulging sides of the phantom.

Comments: This phantom had thin walls and, when upended for the purpose of filling, was prone to bulging if overfilled with water. The effect could be avoided by filling the phantom in a horizontal position and with only the correct volume of water.

2.2.10.1D. Example: Fillable flood source — old solution containing algae

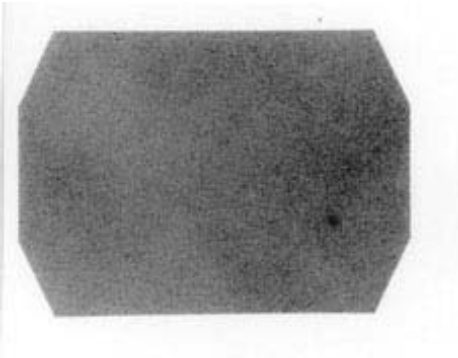

Routine flood image obtained with ^{99m}Tc in a fillable flood source.

Results: The ^{99m}Tc flood image shows an intense small hot spot in the lower right quadrant of the image. This was due to algae.

Comments: Algae may adsorb ^{99m}Tc radiopharmaceuticals. Therefore, when water is allowed to remain in a phantom for a long period of time, algae formation may occur. The use of distilled water is preferable to using tap water. Alternatively, the phantom should be emptied after use (taking the appropriate radiological protection precautions, or after the radioactivity has decayed). It is recommended that ^{99m}Tc pertechnetate be used to minimize problems with algae and adsorption. It is not recommended to use colloids or chelates.

2.2.10.1E. Example: Fillable flood source — adherence of activity to the container at the filling site (algae)

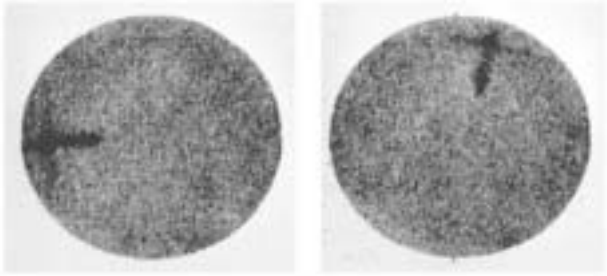

The circular fillable flood phantom was upended to enable radioactivity to be added to the water already within the phantom. The water level was well below the filling hole. Since ^{99m}Tc pertechnetate was not available, ^{99m}Tc MDP was used and was injected with a syringe in a steady stream against the side of the phantom into the water. After removal of air and mixing, flood field uniformity images were obtained (20% energy window, 3 million counts each image). The images show the phantom in two different orientations.

Results: The left image shows an artefact on the left side of a hot line with a less intense line crossing it perpendicularly (forming a cross). When the phantom was rotated by about 90°, this cross also rotated (right).

The artefact was assumed to be due to the MDP pharmaceutical which had adhered to algae on the side of the Perspex (Lucite) material of the phantom as the ^{99m}Tc MDP was injected. When a similar filling process was tried in the same phantom using ^{99m}Tc pertechnetate, no such artefact was observed. Also, when a similar cross was created with ^{99m}Tc MDP on a clean sheet of Perspex (Lucite), which was afterwards immersed in water, there was no remaining image of the cross visible.

It was concluded that ^{99m}Tc in the form of MDP adhered to the algae, and that in the future it would not be used.

Comments: The importance not only of clean phantoms, but also of the radiopharmaceutical used in the solution, is illustrated here as well as in the previous example (D). It is always preferable to use distilled water rather than tap water, and to clean phantoms periodically. The addition of chlorine can prevent the growth of algae. However, cleaning should be done with care, since solvents can cause damage (which is not always seen initially but can result in cracking later).

2.2.10.2. Cobalt sheet sources

General comments

^{57}Co sheet sources form an attractive alternative to fillable flood sources. They are expensive, but for routine QC they are always at hand, and they require less handling (hence produce less radiation burden) than a fillable flood source. However, they must be checked for uniformity before being used for QC.

^{57}Co sheet sources must be used with caution also because of the high energy photons of ^{57}Co itself (692 keV) and those of other cobalt isotopes (^{56}Co, ^{58}Co, ^{60}Co), which may be present as impurities. In particular, the shorter life ^{56}Co and ^{58}Co impurities present in new sources are prone to produce artefacts in flood images, owing to high count rates and pile-up effects from the scatter and septum penetration of the high energy photons. Some scintillation camera systems are more susceptible than others to showing artefacts.

Problems can be avoided by purchasing sources with only 180 MBq (and certainly no higher than 400 MBq), by storing sources for a period of several months after manufacture until the ^{56}Co and ^{58}Co impurities have decayed, and by using a distance of at least 15 cm, and preferably an even larger distance, between the source and the collimator. The specification and certificate of the source should always be checked.

For a more detailed explanation, see BUSEMANN SOKOLE, E., HECKENBERG, A., BERGMANN, H., Influence of high energy photons from cobalt-57 flood sources on scintillation camera uniformity images, Eur. J. Nucl. Med. **23** (1996) 437–442.

2.2.10.2A. Example: New ^{57}Co sheet source

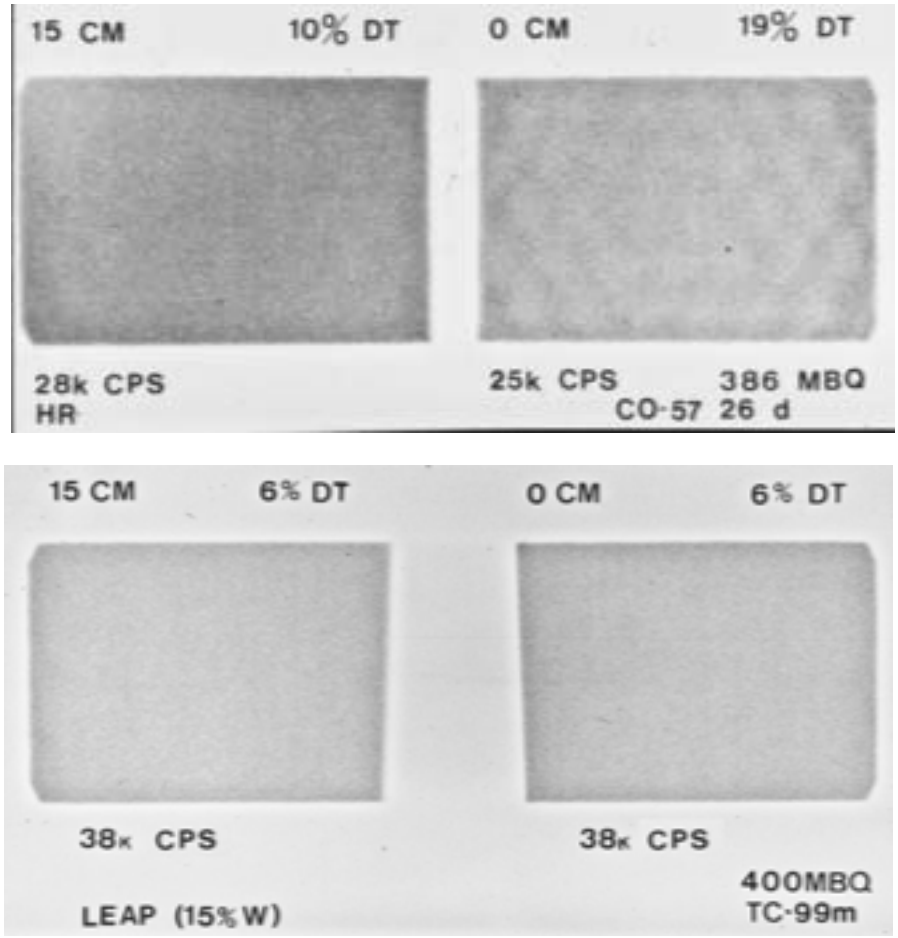

Dual head scintillation camera with the detectors 180° apart, extrinsic uniformity. In this particular camera, a system dead time measurement was supplied.

Top row: LEHR collimator, ^{57}Co, 20% energy window, 3 million counts each image, ^{57}Co sheet source activity 386 MBq, 26 days after calibration date.

TL: ^{57}Co flood image with the source at 15 cm from the collimator of the upper detector, count rate 28 000 counts/s, 10% system dead time.
TR: ^{57}Co flood image with the source placed directly on the collimator of the lower detector, count rate 25 000 counts/s, 19% system dead time.

Bottom row: LEHR collimator, ^{99m}Tc, 15% energy window, 3 million counts each image, ^{99m}Tc fillable flood source activity 400 MBq.

BL: ^{99m}Tc flood image with the fillable flood source placed at 15 cm from the collimator, count rate 38 000 counts/s, 6% system dead time.
BR: ^{99m}Tc flood image with the source placed directly on the collimator, count rate 38 000 counts/s, 6% system dead time.

Results: The ^{57}Co flood image from the lower detector shows distinct artefacts (visible PM tubes) compared with the flood image from the upper detector. The ^{99m}Tc flood images are uniform from both detectors.

Comments: The artefacts are produced by pulse pile-up and misplaced events due to the excessive dead time of the system processing all the detected photons, including a very large number of high energy photons. The number of high energy photons reaching the collimator decreases as the source is moved further away from the collimator, hence the dead time decreases and problems with misplaced events diminish (compare the dead time of the TL and TR images).

Note that in this situation, with this camera and collimator, the source of 386 MBq produced a count rate of 25 000 counts/s in the 20% energy window of ^{57}Co, which is slightly above that recommended (max. 20 000 counts/s) for QC. This count rate reflects only the counts in the 20% energy window set over 122 keV but does not signal the additional high energy photons being processed by the camera.

For comparison, the uniformity images obtained with a flood source filled with 400 MBq of ^{99m}Tc produced only 6% dead time but a count rate of 38 000 counts/s in a 15% energy window set symmetrically over the 140 keV photopeak. The images obtained with this flood source placed at 0 and 15 cm from the collimator were both uniform.

For more details, see BUSEMANN SOKOLE, E., HECKENBERG, A., BERGMANN, H., Influence of high energy photons from cobalt-57 flood sources on scintillation camera uniformity images, Eur. J. Nucl. Med. **23** (1996) 437–442.

2.2.10.2B. Example: New ^{57}Co sheet source

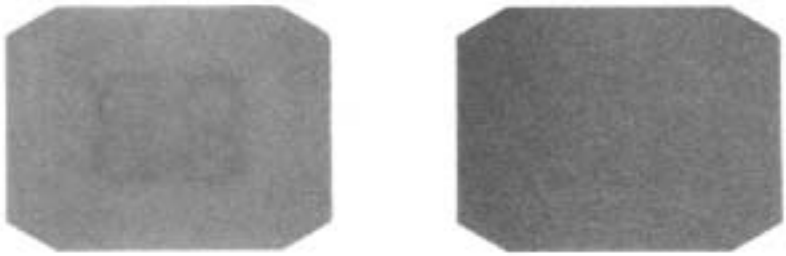

Dual head scintillation camera, low energy collimators, new ^{57}Co sheet source, 20% energy window. Extrinsic uniformity images made with the new ^{57}Co sheet source placed directly on the collimator of detector 1 (L) and at a distance from detector 2 (R).

Results: Detector 1 shows a hotter rectangle within the FOV, which can occur from high energy photons when a ^{57}Co sheet source is placed directly on the collimator.

See example 2.2.10.2A and BUSEMANN SOKOLE, E., HECKENBERG, A., BERGMANN, H., Influence of high energy photons from cobalt-57 flood sources on scintillation camera uniformity images, Eur. J. Nucl. Med. **23** (1996) 437–442.

2.2.10.2C. Example: Cobalt sheet source — non-uniformity in source (1)

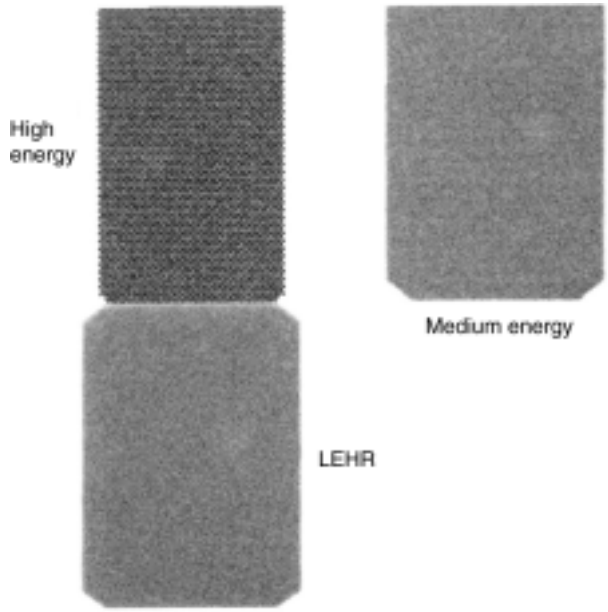

Routine flood field images from different collimators using a ^{57}Co sheet source.

TL: High energy collimator.
TR: Medium energy collimator.
BL: LEHR collimator.

Results: There is a diffuse cold spot in each of the images. For the high energy collimator (TL) the cold spot is in the left half of the image. The ^{57}Co source was rotated 180º, for the images taken with the medium energy and LEHR collimators (TR, BL), so that the diffuse cold spot appeared in the right half of the images.

Note that the diffuse cold spot rotates with the rotation of the sheet source. This cold spot was due to a defect in the sheet source and not to non-uniformity of the camera.

Comments: ^{57}Co sheet sources need to be checked for uniform radioactivity distribution. If in doubt, rotate the phantom through 90º, 180º, 270º, or shift the phantom within the camera FOV. In this example, the phantom exhibited a discrete diffuse circular area of diminished ^{57}Co that was easily recognizable. However, a more subtle non-uniformity could be a slight change in activity over a large area of the phantom, and this requires careful evaluation.

2.2.10.2D. Example: Cobalt sheet source — non-uniformity in source (2)

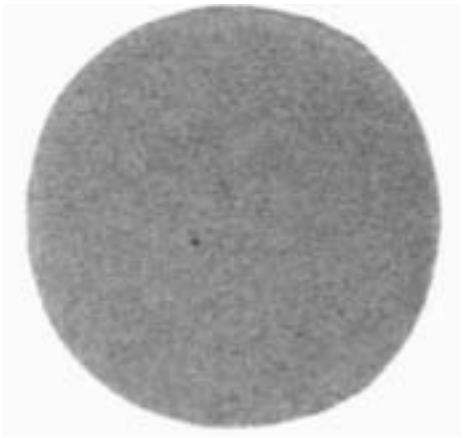

^{57}Co flood image, 20% energy window, low energy collimator, 10 million counts.

Results: A tiny hot spot to the left of centre in the image was produced by non-uniformity in the ^{57}Co flood image.

Comments: Several other problems can produce a similar image. A bad pixel in the uniformity correction can produce a small hot spot. Also, a very similar image can be produced by a minor defect in the collimator.

2.2.10.2E. Example: Cracked cobalt sheet source

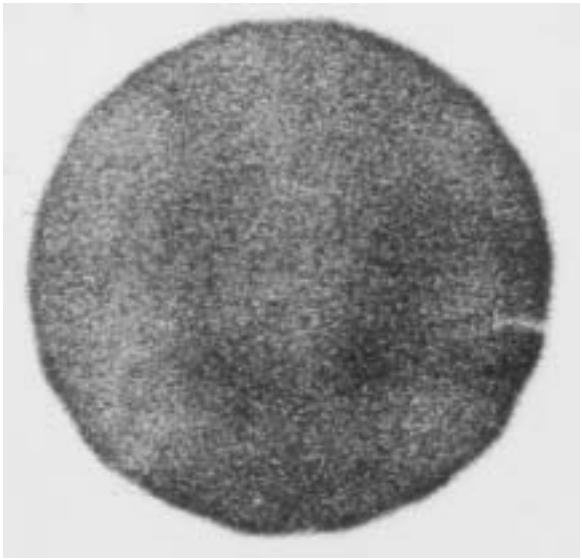

Extrinsic uniformity, ^{57}Co sheet source, 20% energy window, 3 million counts.

Results: Detector uniformity is poor. In addition, a noticeable thin line of absent counts is seen on the right hand edge of the circular FOV (at about 3 o'clock). This was caused by a crack at the edge of the cobalt sheet source.

2.2.10.3. Point sources

General comments

A point source of radioactivity used for intrinsic tests must fulfil criteria for size and shape:

(a) For distances of >5 FOV, the source must be in as small a volume as possible.
(b) If a syringe is used, the volume should be <0.05 mL in a 1 mL syringe and the syringe needle must not be radioactive (remove the original needle used for preparing the source, and preferably use a small cap to seal the syringe, or replace with a non-radioactive needle).
(c) For distances of <1 FOV (e.g. in the case of multihead systems), the source must be a small round point, i.e. a drop of radioactivity.
(d) The syringe or capsule that contains the radioactivity must be suspended or fixed in such a way as to produce an energy spectrum with minimum scatter. If placed on a surface, it should be put in a lead container in order to provide backscatter absorption and to limit the exposure to personnel.

Note: The shape and size of the point source affect the uniformity image obtained. Care must also be exercised to produce a consistent point source and detector geometry in order to compare images. An alternative to a ^{99m}Tc point source could be a ^{57}Co point marker, or a ^{57}Co spot marker, of the appropriate amount of radioactivity. Used consistently, these can easily be employed to routinely monitor detector sensitivity and therefore to monitor changes in energy window setting or window width.

The dome of the measured count distribution is dependent on the source to detector distance. This effect is minimal if a distance of 5 FOV is used between source and detector. When a shorter distance is used, and software corrects for the observed count distribution, then the same distance should be used each time.

2.2.10.3A. Example: Intrinsic uniformity — off-centred point source

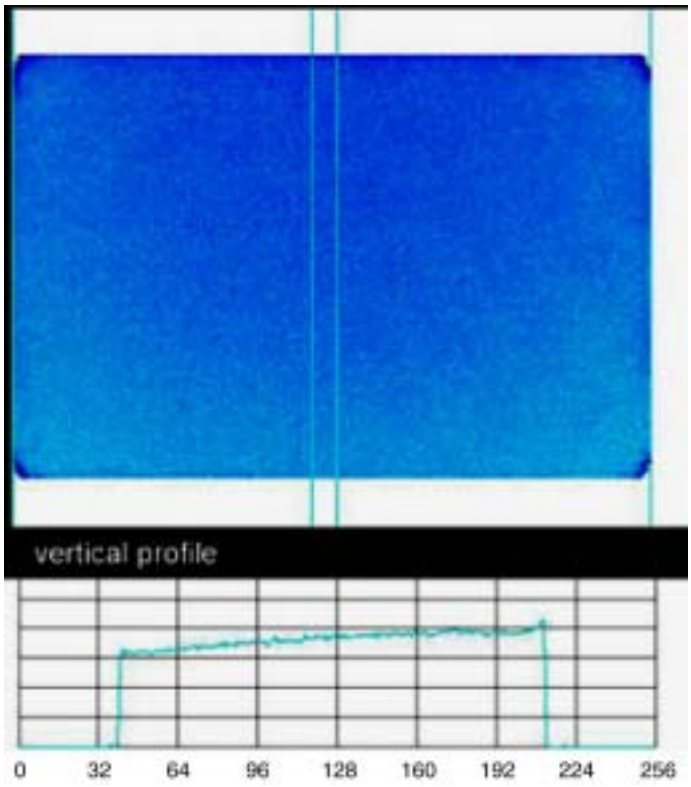

Intrinsic uniformity, ^{99m}Tc point source, 15% energy window, 3 million counts.

Results: The image shows a gradual increase in count density from bottom to top (in the *y* direction). The source was not positioned centrally beneath the detector but was off-centred too far towards the top of the image.

Comments: Even when a point source is at a distance of 5 FOV away from the detector, it must be positioned on a perpendicular line through the centre of the detector in order to irradiate the detector uniformly. This is even more critical when the source is placed at a closer distance.

Note: The same applies if the surface of the crystal does not form a 90º angle with the source–detector axis.

2.2.10.3B. Example: Intrinsic uniformity — geometry of point source and detector — source too close to detector

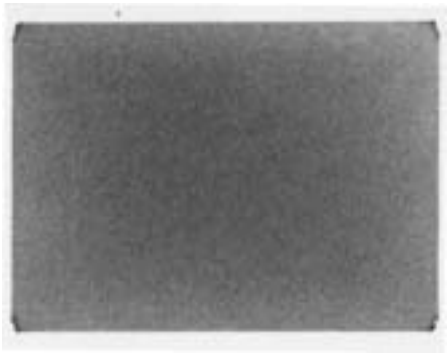

Intrinsic uniformity, ^{99m}Tc point source placed at a distance of about 3 times the maximum FOV from the detector, 15% energy window, 3 million counts.

Results: The count distribution shows an increase in intensity towards the centre of the FOV because the source was too close to the detector and not at a distance of 5 FOV.

Comments: With large FOV detectors it becomes difficult to find an appropriate solution to positioning a point source at a sufficiently large distance from the detector for intrinsic uniformity QC.

For routine QC, when monitoring changes in uniformity is the essence of the test, a point source placed slightly too close, as shown here, is acceptable, provided that the user is aware of the influence of the point source proximity in evaluating the result both visually and quantitatively.

Note: There is a slight, cold, crescent shaped artefact along the right hand part of the upper border of the image. This was due to a PM tube that had been replaced. This artefact was obscured with the collimator in place.

2.2.10.3C. Example: Multihead systems — geometry of point source and detector

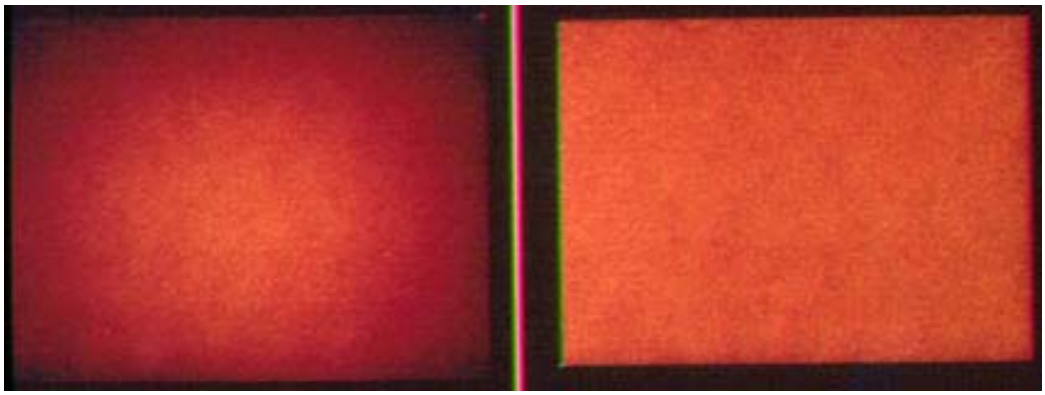

Multihead SPECT system. Intrinsic uniformity using a ^{99m}Tc point source positioned at about 30 cm centrally between the detectors in order to obtain simultaneous flood field images from each detector, 15% energy window, 30 million counts (each detector). The images are from one detector of the system.

L: Raw flood image.
R: Raw image corrected for the curvature in count response (dome effect).

Results:

L: The image shows the pronounced curvature or dome of increased counts towards the centre of the FOV.
R: The vendor provided a program to correct for the curvature, in order to produce a flat field response for further evaluation, quantification and, if a sufficiently high number of counts have been collected, use as an intrinsic part of a uniformity correction map. The image has been corrected using this software.

Comments: With multihead systems it is convenient (and may also be necessary according to the manufacturer's instructions, as in the situation shown here) to place a point source symmetrically between the detector heads in order to acquire data simultaneously with all detectors. In this geometry, the point source is not at the required 5 FOV distance from the detectors but is much closer, thereby forming a dome-like image. Correction for the dome effect by suitable software is required in order to properly assess and monitor the non-uniformity.

The convenience of obtaining a simultaneous intrinsic uniformity by multiple detectors may depend on such a geometry and subsequent correction. The results are highly dependent on the point source being indeed a tiny point of radioactivity and not a slightly elongated source, which will distort the image and give false quantitative values and, if applied, an incorrect uniformity (or sensitivity) map.

Always adhere to the manufacturer's instructions and recommendations.

2.2.10.3D. Example: Intrinsic uniformity — elongated point source/attenuation in source holder

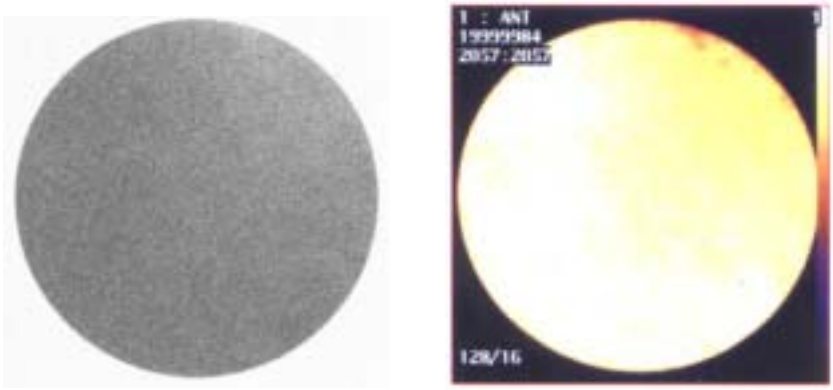

Intrinsic uniformity, ^{99m}Tc radioactivity in a syringe placed in a lead holder suspended from the ceiling above the detector, 20% energy window, 3 million counts. A lead mask was in position on the detector in order to define the collimated UFOV, and a thin sheet of Perspex (Lucite) (supported by the collimator housing) was placed over the detector to protect the crystal from accidental breakage due to impact by an object falling on the crystal.

L: Analogue flood field image.
R: Digital flood field image (128 × 128 matrix, no contrast enhancement).

Results: The flood images show a diffuse area of diminished counts over the upper right quadrant of the image. This was absent in the previous uniformity QC check, suggesting a user error. Investigation showed that the point source had not been properly prepared. The point source was a full 3 mL of ^{99m}Tc solution in a 3 mL syringe, producing an elongated volume of radioactivity that was partially obscured by the lead syringe holder. When this source was replaced by a proper point source, the large area of decreased activity disappeared and a uniform image was produced throughout the FOV, as was expected.

Comments: It is always advisable to check the set-up, as well as to compare new QC results with previous results.

Reference: NATIONAL ELECTRICAL MANUFACTURERS ASSOCIATION, Performance Measurements of Scintillation Cameras, NEMA Standards Publication No. NU1, Washington, DC (1994).

2.3. SPATIAL RESOLUTION AND LINEARITY

2.3.1. Intrinsic spatial resolution and linearity

2.3.1.1. Example: Common types of spatial resolution and linearity test pattern

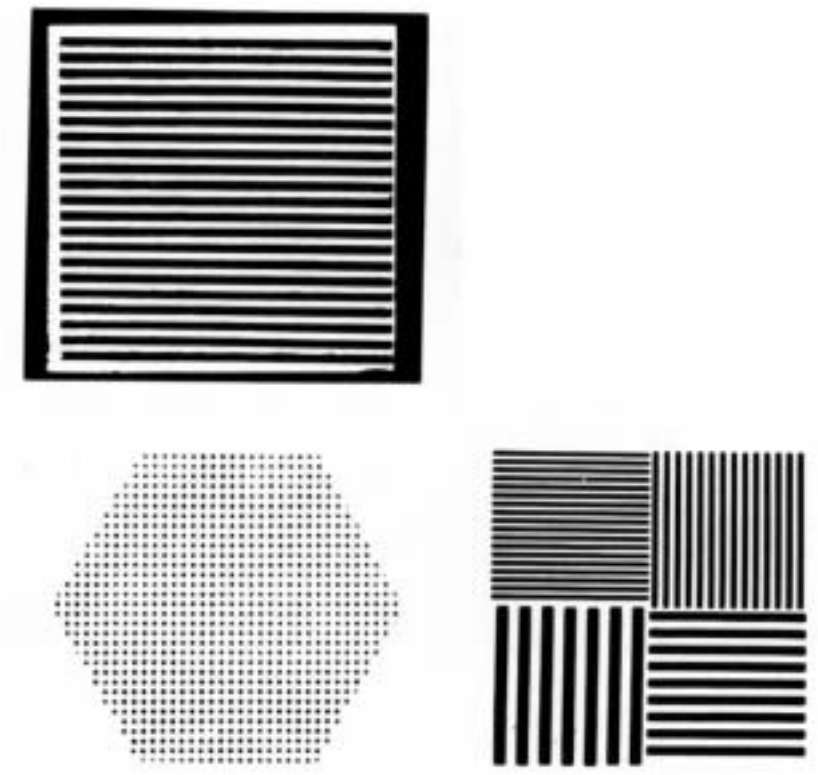

Diagrams of PLES phantom (TL), OHP (BL) and four quadrant bar pattern (BR).

Comments:

Four quadrant bar pattern: The four quadrant bar pattern (or phantom) is the most commonly used phantom for routine assessment of spatial resolution and linearity. For assessing spatial resolution qualitatively, one set of bars should be barely resolvable. Because it has different bar pattern sizes and spacings, this pattern can be used with different scintillation cameras and different spatial resolutions and still meet the criterion of having one set of bars barely resolvable. However, eight images are required to evaluate the spatial resolution over the entire FOV in both *x* and *y* directions (first a set of four images, obtained after rotating the pattern through 90° between images, and then a further set of four images, obtained after flipping the pattern). Sometimes the bar pattern is constructed so that the lead strips are closer to the surface on one side of the phantom than on the other. This will produce slightly different spatial resolution images depending on which side faces the collimator.

PLES phantom: The PLES phantom requires only two images to evaluate the spatial resolution and linearity. However, PLES phantoms with bars of different sizes and spacing are needed for cameras with different spatial resolution. The example below is an image of the PLES phantom for assessing the spatial resolution and spatial linearity in one direction. This image was made after reacquiring a linearity correction map.

OHP: The OHP does not need to be rotated to evaluate the spatial resolution over the entire field, but, as with the PLES phantom, patterns with different size holes may be needed in a department with more than one camera.

The two intrinsic images on the next page were obtained at acceptance testing of a new 16 mm thick crystal detector. The top image was obtained with an OHP with 24 mm hole spacing, the bottom image with 32 mm hole spacing. Note that the 24 mm hole spacing is useful for assessing spatial resolution and the 32 mm hole spacing for linearity. The reason for the PM tube pattern is that the spatial resolution under a PM tube is worse than between PM tubes. This is particularly evident in thick crystal detectors.

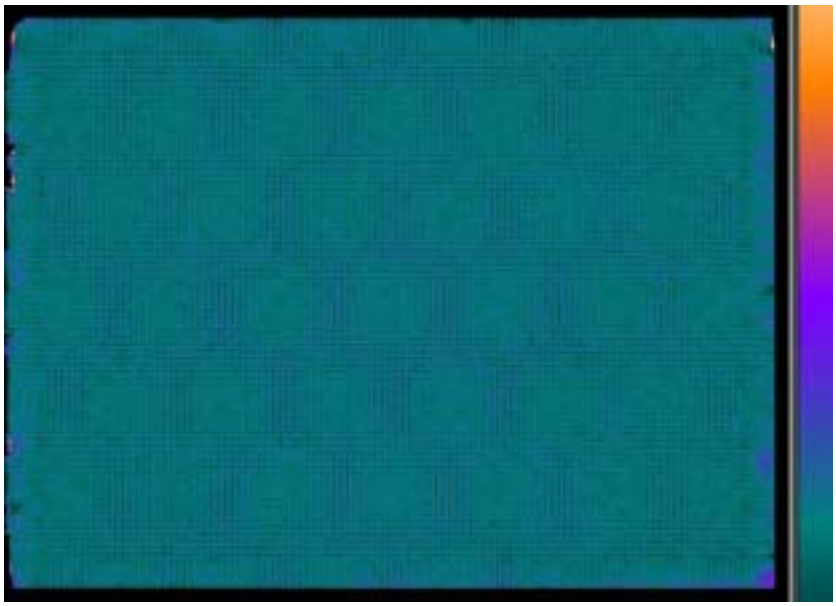

OHP — 24 mm hole spacing

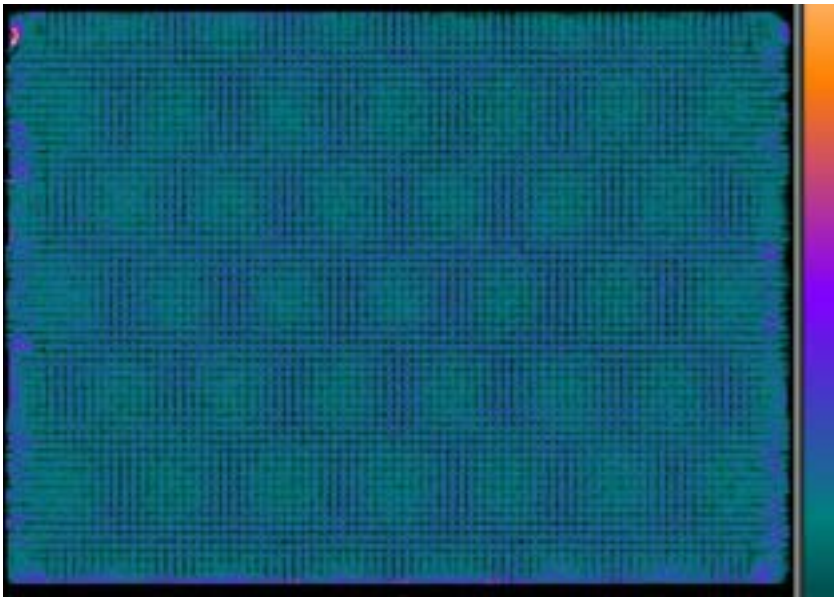

OHP — 32 mm hole spacing

2.3.1.2. Example: NEMA slit pattern — non-linearity

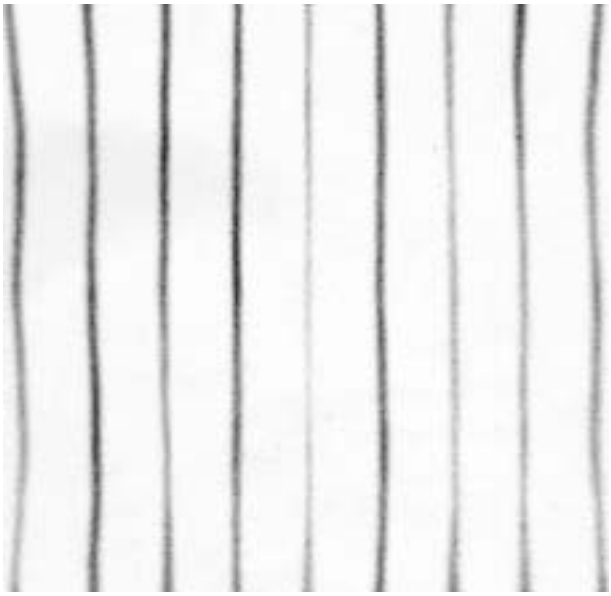

Intrinsic image of the NEMA slit phantom pattern (1 mm wide slits in a sheet of lead with separations of 30 mm) using a distance point source of ^{99m}Tc.

Results: Image shows distinct non-linearity of the lines. Also, the lines have different intensities.

Comments: The slits in the NEMA slit phantom must have uniform width in order to assess the uniformity of the lines imaged. The largest available matrix size must be used in order to ensure that one has several pixels over each line for purposes of quantification of the spatial resolution.

2.3.1.3. Example: NEMA slit pattern showing difference between *x* and *y* spatial resolution

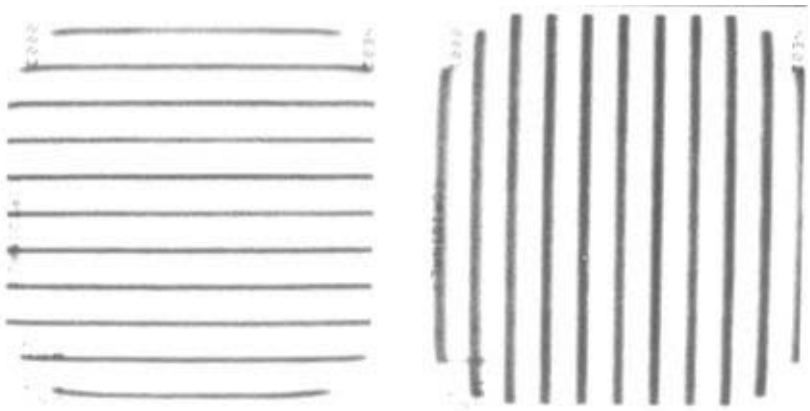

↑ Spatial resolution in *y* direction

→ Spatial resolution in *x* direction

Intrinsic resolution images were acquired with ^{99m}Tc and a NEMA slit pattern (1 mm wide slits in a sheet of lead with separations of 30 mm) during acceptance testing. ^{99m}Tc point source at 5 UFOV distance, 15% window, 3 million counts each image.

L: Slit pattern positioned for assessment of spatial resolution in the *y* direction.
R: Slit pattern rotated by 90° for assessment in the *x* direction.

Results: The image acquired with the slits oriented horizontally (*y* spatial resolution, left image) demonstrated satisfactory spatial resolution and generally satisfactory linearity during acceptance tests. However, when the slits were oriented vertically, the image showed a significant loss of spatial resolution. This problem was caused by a noisy ADC.

Comments: Scintillation cameras may differ slightly in spatial resolution in *x* and *y* directions, but this should not be visually obvious. A difference of >10% should be considered significant. Quantitative measurements must be within specifications.

See also Section 5.

2.3.1.4. Example: NEMA slit pattern — variations in intrinsic spatial resolution

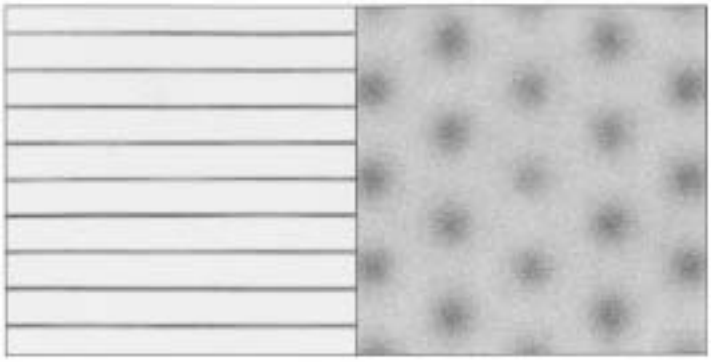

L: Magnified (zoomed) intrinsic 2 million count image of a NEMA slit phantom acquired using ^{99m}Tc with a 20% window and with linearity and energy corrections turned on.
R: Intrinsic uniformity image acquired with the same parameters except that the energy correction was turned off.

Results: Comparison of the two images shows that intrinsic resolution is poorer in the region where the PM tubes are located and is better between the tubes.

Comments: This is a common finding with new digital cameras that do not use a light pipe. Events that occur in the crystal but between two PM tubes are positioned more accurately because the positioning circuitry is more sensitive to small changes in the relative signals of the nearest tubes. Events that occur in the crystal under a tube are not positioned as accurately.

2.3.1.5. Example: Qualitative spatial resolution/linearity — four quadrant bar pattern

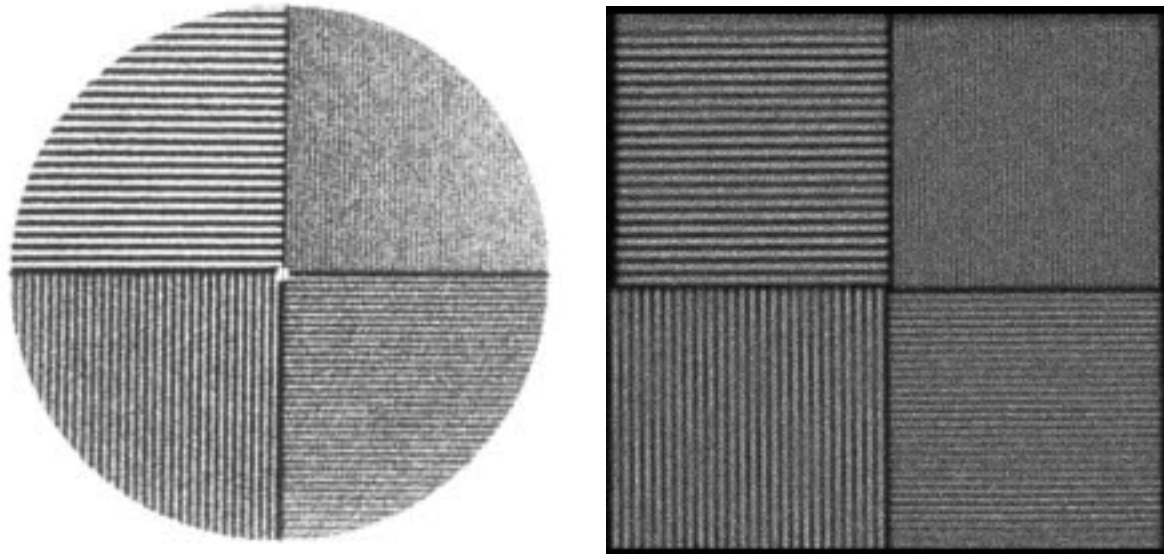

Two intrinsic resolution/linearity images obtained with a four quadrant bar pattern on two different scintillation cameras. ^{99m}Tc point source at 5 FOV distance, 15% energy window, 3 million counts each image.

L: Older camera, 9.5 mm (3/8 inch) thick crystal.
R: New camera, 15.8 mm (5/8 inch) thick crystal.

Results: The four quadrant bar pattern is suitable for checking both linearity and spatial resolution, since one quadrant is barely resolvable (upper right quadrant in these images). The linearity is satisfactory. The spatial resolution does not show any specific problems, although in the upper right quadrant of the left image it appears to decrease slightly towards the edge of the FOV. Note that in the thicker crystal the changes in spatial resolution are quite obvious compared with the thinner crystal.

Comments: In order to check all quadrants of the FOV in both *x* and *y* directions with the smallest recognizable bar spacing, one needs to image the phantom in eight positions: four positions are imaged with the phantom rotated through 90°, and then the phantom is turned over and the procedure is repeated.

The bar spacing should be matched to the scintillation camera spatial resolution such that the bar spacing of one quadrant is just barely resolvable. Note any loss of spatial resolution related to the PM tube position.

2.3.1.6. Example: Intrinsic spatial resolution — influence of digital matrix size

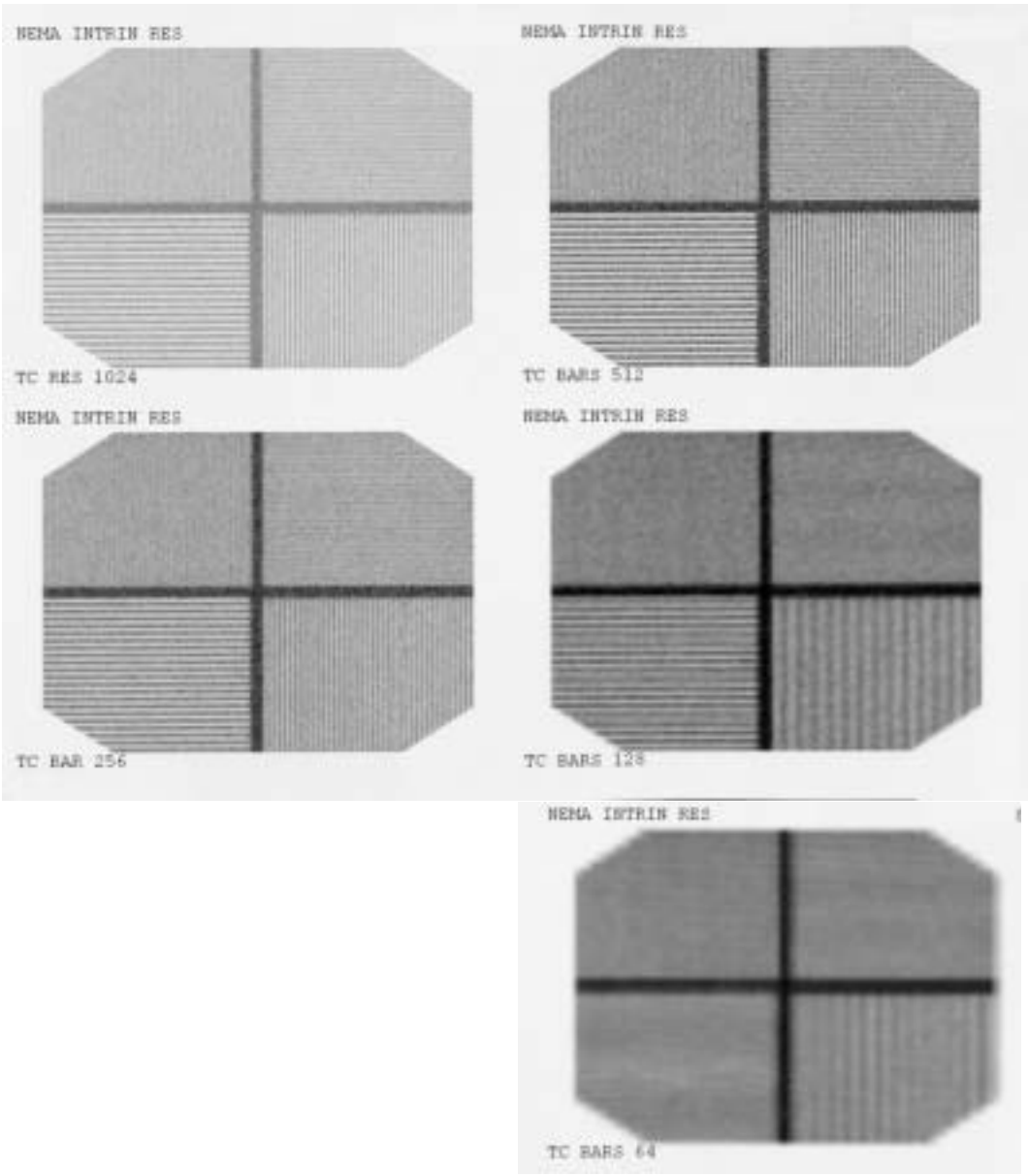

Intrinsic spatial resolution images with a four quadrant bar pattern using a ^{99m}Tc point source at 5 UFOV distance from the detector, 20% energy window, 4 million counts each image. The bar pattern had line spacings of 2.1, 2.5, 3.2 and 4.2 mm. The pixel size was about 0.58 mm for the 1024×1024 matrix. Five different digital matrices were used for the data acquisition without moving or rotating the bar pattern.

TL: 1024×1024.
TR: 512×512.
ML: 256×256.
MR: 128×128.
BR: 64×64.

Results: The images show the effect of different matrix sizes. There is a loss of digital resolution with decreasing matrix size (i.e. increasing pixel size). Note also the artefacts due to aliasing, particularly in the 128 × 128 and 64 × 64 matrices. In these images the bar spacing appears to be doubled, or it disappears at certain spacings.

Comments: The influence of matrix size produces effects similar to the moiré interference patterns seen when using bar patterns with medium and high energy collimators.

For QC purposes, the largest matrix size available (512 × 512 or 1024 × 1024) should be used to acquire bar pattern images in order to minimize the aliasing artefacts demonstrated in this example.

In general, a specific matrix size and zoom factor have little meaning without reference to the pixel size (mm/pixel), because the FOV of scintillation cameras differs between manufacturers and camera types. A rule of thumb is that the minimum pixel size selected for a specific imaging purpose should be about 1/3 the spatial resolution expressed as FWHM, and always less than 1/2 FWHM (Nyquist theorem).

2.3.1.7. Example: Bar pattern — off-centred point source

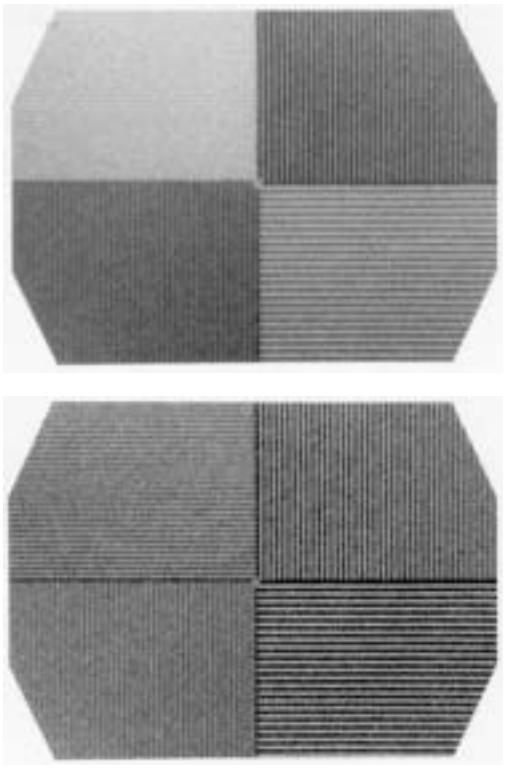

$\rightarrow x$ $\uparrow y$

Intrinsic resolution/linearity images using a four quadrant bar pattern with a distant point source of ^{99m}Tc, 15% energy window, 5 million counts each image.

T: Image obtained with the point source off-centred in the *y* direction.
B: Image obtained with the point source centred in the FOV.

Results:

T: The point source was centred in the *x* direction but off-centred almost to the lower edge of the FOV of the camera in the *y* direction. The photon flux was therefore decreased for the two quadrants with horizontal bars where the crystal was shielded by the bars. The impression is then created of two hot quadrants and two cold quadrants.

B: After the point source was repositioned opposite to the centre of the FOV, each quadrant of the bar pattern showed equal overall intensity.

Comments: Centring of the point source is crucial for intrinsic measurements.

2.3.1.8. Example: Radial loss of spatial resolution

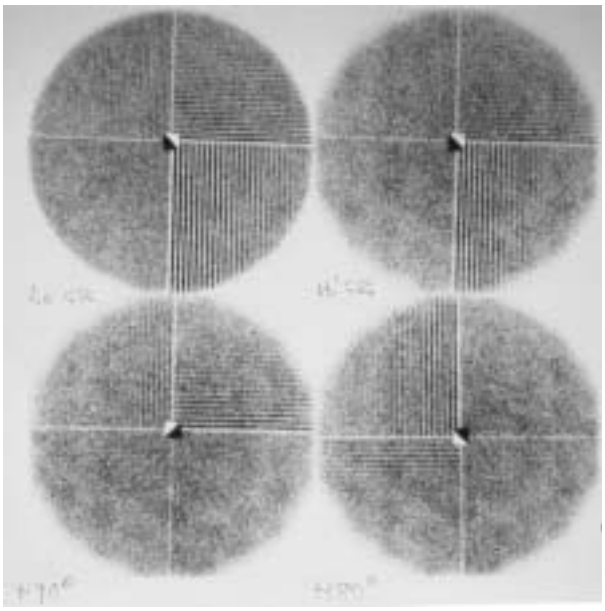

Intrinsic spatial resolution images obtained at acceptance testing. Four quadrant bar pattern, ^{99m}Tc point source, 20% energy window, 2.5 million counts each image.

TL: Low count rate (<20 000 counts/s).
TR: High count rate (~75 000 counts/s).
BL: Bar pattern rotated 90°.
BR: Bar pattern rotated 180°.

Results: All images revealed a marked loss of spatial resolution from the centre to the edge. These images were obtained during acceptance testing and were unsatisfactory.

Comments: Service personnel were not able to correct this problem and the detector was replaced.

2.3.1.9. Example: Defective PM tube — old generation camera

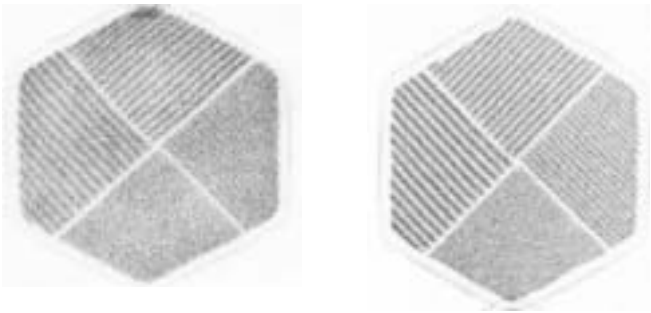

Camera A Camera B

$\rightarrow x \uparrow y$

Spatial resolution images using a four quadrant bar pattern from two analogue scintillation cameras of the same type from the same manufacturer. The cameras had no energy or linearity correction maps, which is typical of old generation cameras. ^{99m}Tc, 20% energy window, 3 million counts each image.

Camera A: Image obtained with no uniformity correction map. There is a defective PM tube in the upper part of the FOV.
Camera B: Image obtained with a uniformity correction map (a count skim uniformity calibration).

Results: The left image from camera A shows poor overall spatial resolution and linearity, in particular in the area of the malfunctioning PM tube. Camera B shows satisfactory spatial resolution and linearity, which is typical for this type of camera.

Note: The gain of the image of camera B is slightly larger in the *y* direction than in the *x* direction. Camera A needs service for the defective PM tube. Camera B needs adjustment of gains.

See also example 2.2.8.1.

2.3.1.10. Example: Regional loss of intrinsic spatial resolution — noisy PM tube

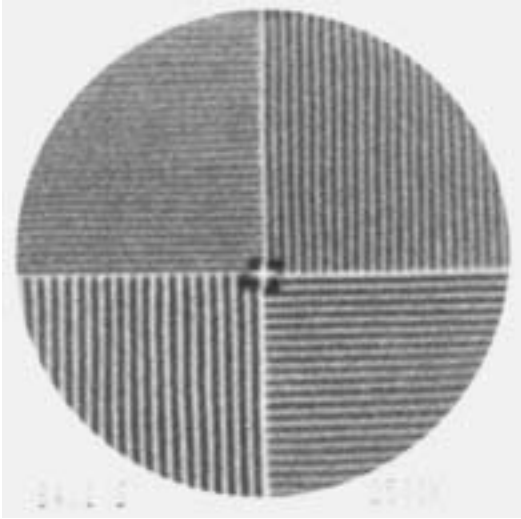

Intrinsic transmission image of a four quadrant bar pattern, ^{99m}Tc, 2.5 million counts.

Results: Image revealed a loss of spatial resolution, shown by blurring and slight distortion of the line pattern, associated with one PM tube in the upper left quadrant. This was due to electronic noise generated within the tube.

2.3.1.11. Example: Intrinsic spatial resolution — faulty linearity correction

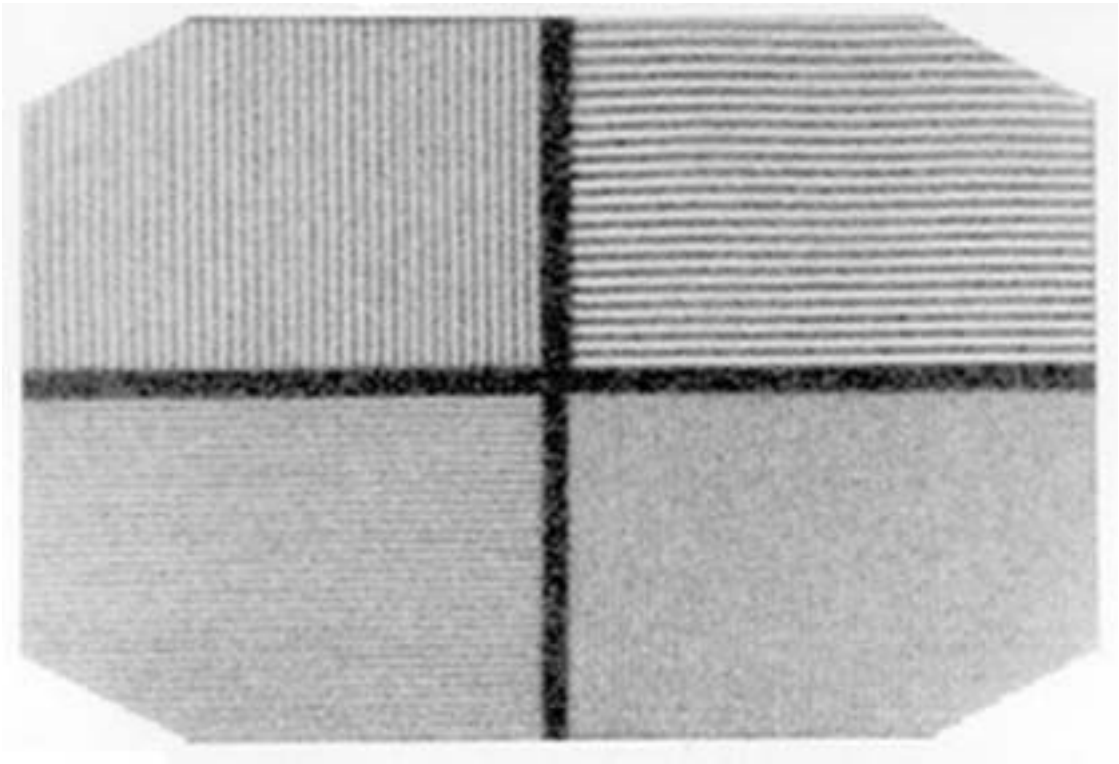

Intrinsic spatial resolution and linearity check, low energy collimator, four quadrant bar pattern, ^{99m}Tc point source, 3 million counts.

Results: The four quadrant bar pattern image shows wavy lines, which are obvious in this image in the upper right quadrant, indicating a problem in the linearity correction of the camera. This was an almost new camera. Service was required.

Comments: This non-linearity problem will cause a loss of spatial resolution in SPECT reconstructed images.

2.3.1.12. Example: Poor spatial linearity and spatial resolution — ^{99m}Tc and ^{67}Ga

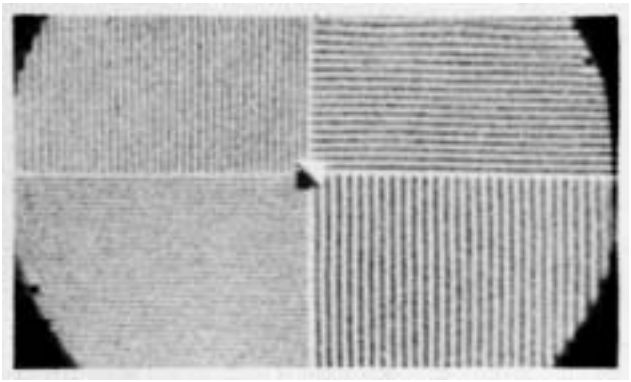

^{99m}Tc

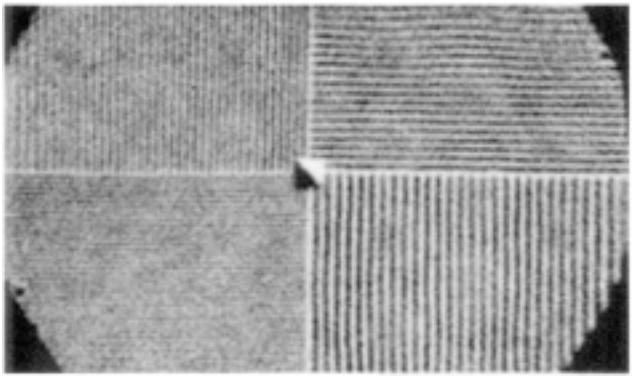

^{67}Ga

Intrinsic spatial resolution images obtained using a four quadrant bar pattern.

T: ^{99m}Tc (20% energy window).
B: ^{67}Ga (sum of three photopeaks — 20% over 93, 184 and 300 keV).

This was a new, modern camera system.

Results: The wavy lines show very poor spatial linearity for ^{99m}Tc, and even worse for ^{67}Ga. There is also a loss of spatial resolution in the vicinity of PM tubes.

Comments: This example demonstrates the usefulness of obtaining intrinsic spatial resolution/ linearity images for radionuclides other than ^{99m}Tc, although the poor performance with ^{99m}Tc is indication enough that there is a problem. This test with ^{67}Ga is also very sensitive to multiple window spatial registration errors (see also Section 2.4). If the images for the three energy windows are not registered accurately, then misalignment will result in blurring of the line pattern.

2.3.1.13. Example: Intrinsic spatial resolution — defect in the bar pattern

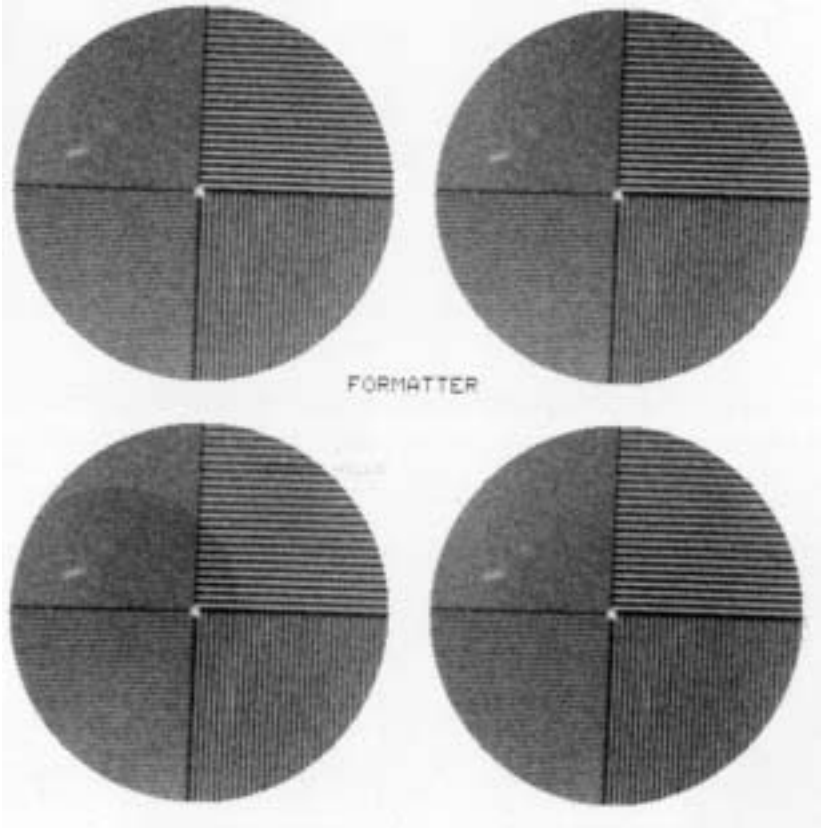

Four sequential intrinsic analogue spatial resolution images of a four quadrant bar pattern, obtained to test an image formatter.

Results: All four images show two cold spots in the upper left quadrant of the bar pattern. These were faults in the bar pattern. (An error in the formatter is unlikely because the images are identical in all quadrants of the formatter's view.)

Note: There is a problem in the formatter, seen as a circular shadow of increased density in the lower left image.

Comments: A method of testing the origin of the cold spot in the bar pattern image could be to rotate the bar pattern through 90° or 180° and determine whether the cold spot always remains in the same position in the bar pattern quadrant. This example emphasizes the need for careful inspection of phantoms and other test equipment before use. If a fault in phantom production is ascertained at acceptance testing of the phantom, then the phantom should be replaced.

2.3.2. System spatial resolution and linearity

General comments

The collimator is a vulnerable component of the scintillation camera. It can be easily damaged, both during transport and during use. QC of the collimator at acceptance and routinely thereafter is essential.

A qualitative or quantitative measurement of system spatial resolution using a phantom or line sources will be influenced by interference of the collimator septa with the pattern of the phantom or the source, which may yield moiré patterns. This is usually not evident when using LEHR or LEUHR collimators but becomes obvious with medium and high energy collimators, so that it becomes difficult to obtain an accurate measure of spatial resolution. Assessment of linearity is also affected.

For quantitative evaluation of system spatial resolution, line sources are recommended. These must be exactly aligned with the axes of the septa and holes of the collimator.

The spatial resolution is a function of the distance from the collimator. Care must be taken to place the phantom or line sources consistently and at a constant distance from the collimator over the whole FOV. Placing a phantom on the collimator directly or in a jig that holds the phantom in place is simple and reproducible. When placing a phantom on an imaging pallet, one must be certain that the pallet is level.

2.3.2.1. Example: Low energy collimator — defective — distortion absent at 0 cm, present at 25 cm

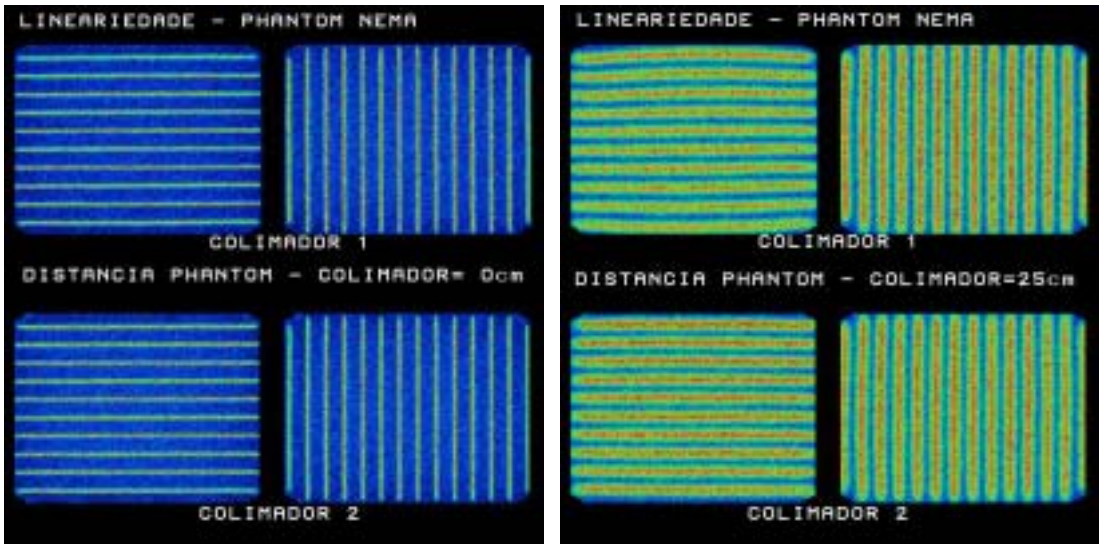

$\rightarrow x$ $\uparrow y$

Dual head camera, LEHR collimators, NEMA slit pattern imaged with slits parallel with x and y directions, 1 million counts each image, 256×256 matrix.

L: Four images obtained with the phantom on the collimator (at 0 cm).
Top row: LEHR collimator 1.
Bottom row: LEHR collimator 2.

R: Four images obtained with a distance of 25 cm between phantom and collimator.
Top row: LEHR collimator 1.
Bottom row: LEHR collimator 2.

Results: The images obtained at 0 cm show good linearity for both collimators. However, at 25 cm the linearity for head 1 of collimator 1 shows distinct curved lines and a convex shape, indicating hole angulation.

Comments: Most tests for linearity are made intrinsically, in order to test the performance of the detector itself. However, introduction of non-linearity due to hole angulation of the collimator leads to loss of resolution and contrast, especially in SPECT. Preservation of linearity at depth is essential, especially for SPECT acquisition. This test is therefore recommended.

See also example 3.4.2.

2.3.2.2. Example: Medium energy collimator (bar pattern: moiré pattern)

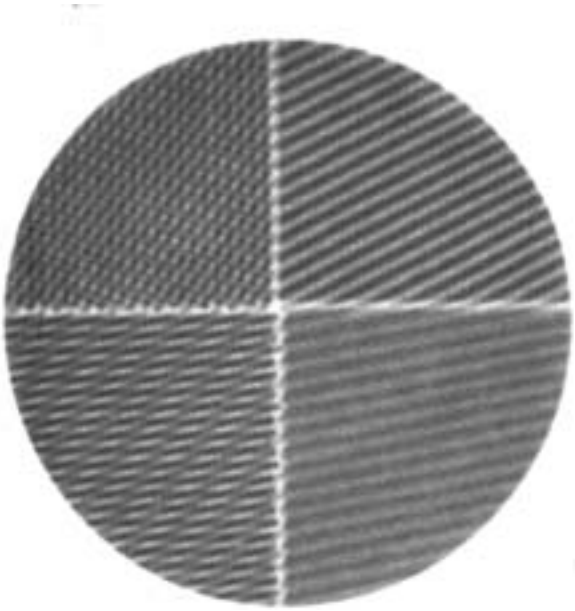

Extrinsic spatial resolution using a four quadrant bar pattern, medium energy collimator, ^{99m}Tc flood source, 15% energy window, 3 million counts. The pattern was at 7.5 cm distance from the collimator.

Results: The image results show moiré patterns from interference between the lead bars of the bar pattern and the lead collimator septa. No assessment of the spatial resolution or linearity can be made from this image.

Comments: Any medium or high energy collimator will produce interference patterns for a bar pattern or other type of spatial resolution phantom. The image depends on the orientation and spacing of the holes and bars.

2.3.2.3. Example: High energy collimator and line source

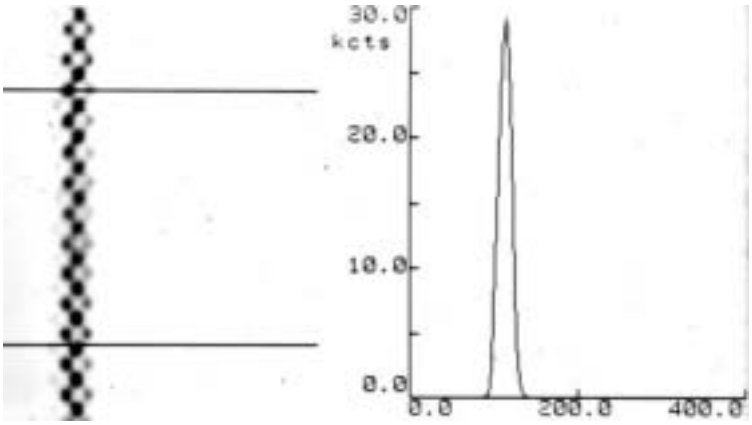

Extrinsic spatial resolution measurement, high energy collimator, ^{99m}Tc line source, 20% energy window, 3 million counts.

L: Image of the line source with wide profile.
R: Line spread function from the profile.

Results: Individual holes of the collimator appear in the image of the line source. Nevertheless, by using a wide profile the effect of the individual holes is smoothed and a continuous line spread function is obtained. This allows a quantitative assessment of the spatial resolution still to be made for the high energy collimator.

2.3.2.4. Example: ^{201}Tl — poor resolution in the *y* direction

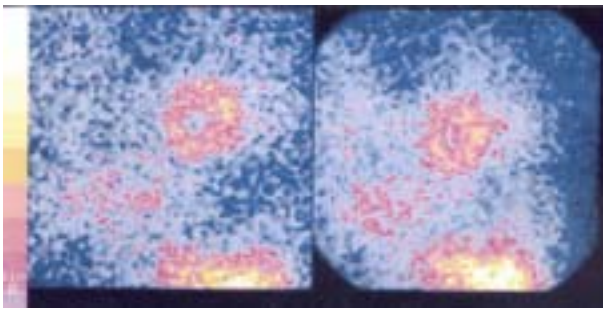

^{210}Tl myocardial perfusion projection image:
SPECT system A SPECT system B

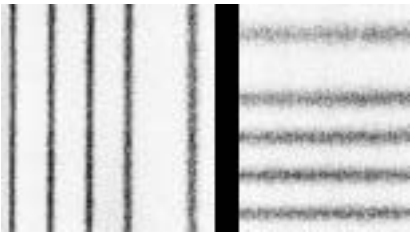

^{99m}Tc spatial resolution: SPECT system B
→ *x* ↑ *y*

^{201}Tl myocardial perfusion SPECT study of a patient. The quality of the study was found to be poor on SPECT system B, so the study was repeated on SPECT system A in the same department. In both systems: low energy collimator, 20% energy window over 60–80 keV photons.

Top row:

L: Projection image from SPECT system A.
R: Projection image from SPECT system B.

Spatial resolution test: In order to investigate the problem, intrinsic spatial resolution images were obtained in both *x* and *y* directions using line sources of ^{99m}Tc and a 15% energy window over 140 keV photons.

Bottom row from SPECT system B: spatial resolution images obtained with a 512 × 512 matrix, zoom ×2.

L: Vertical line sources (spatial resolution in *x*).
R: Horizontal line sources (spatial resolution in *y*).

Results: The spatial resolution images from SPECT system B show different spatial resolution in *x* and *y,* with much poorer spatial resolution in *y* than in *x*. This was caused by an internal ADC problem and explains the poor myocardial images from system B compared with system A. Service was required.

2.4. MULTIPLE WINDOW SPATIAL REGISTRATION

General comments

When an image is made using two or three energy windows (e.g. ^{111}In, ^{67}Ga), then the image produced by each window must superimpose.

Multiple window spatial registration (MWSR) is the term given to the camera's ability to accurately position photons of different energies when imaged through different energy windows. Errors are due to the fact that the images for each of the photon energies are of different size and offset relative to one another. Service can correct the circuitry that performs the corrections.

Assessment of MWSR can be made visually using a spatial resolution pattern, such as a four quadrant bar pattern. For a quantitative measurement of MWSR that can be compared with the camera specification, an intrinsic measurement using a collimated point source of ^{67}Ga is required.

Reference: NATIONAL ELECTRICAL MANUFACTURERS ASSOCIATION, Performance Measurements of Scintillation Cameras, NEMA Standards Publication No. NU1, Washington, DC (1994).

2.4.1. Example: ^{67}Ga MWSR — visual method — acceptable

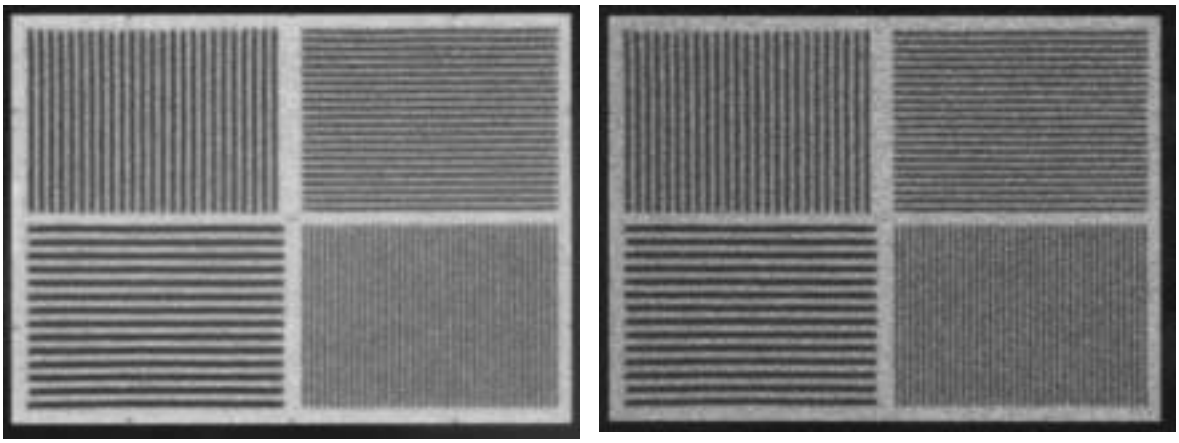

93 keV 183 keV

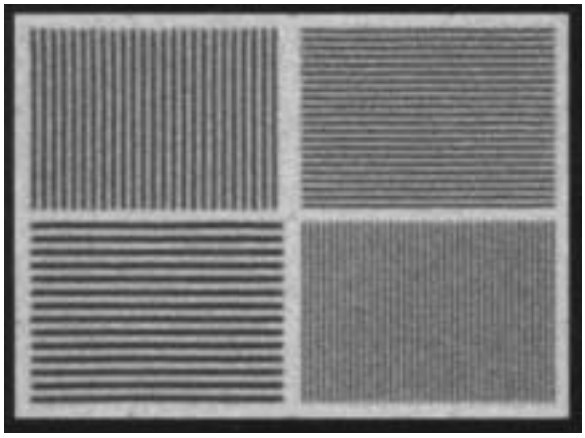

93 + 183 + 296 keV

Intrinsic quadrant bar pattern images obtained with a ^{67}Ga point source, 20% energy window over each photopeak, 512 × 512 matrix, bar widths 3, 4, 5 and 6 mm, acceptance testing.

TL: 93 keV.
TR: 183 keV.
B: Sum of three energy windows: 93 + 183 + 296 keV.

Results: All three images are similar, and there is no loss of image quality from superimposing images from the three energy windows. The MWSR is acceptable.

2.4.2. Example: ^{67}Ga MWSR — visual method — error (1)

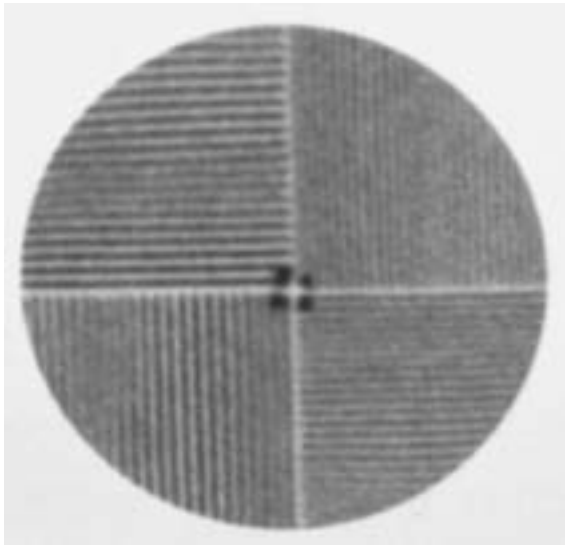

Camera 1

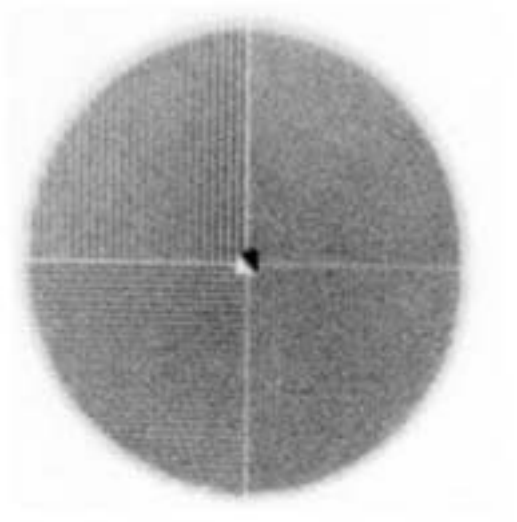

Camera 2

Two examples, from different scintillation cameras, that show similar effects. Intrinsic spatial resolution with ^{67}Ga point source (count rate < 20 000 counts/s), four quadrant bar pattern, 3 million counts each image, preset energy window widths, summed image from 20% energy windows over each of the 93, 183 and 296 keV photopeaks.

Results: Because the three different energies produce images of three different sizes, the superimposition of images from each energy causes bars to disappear at certain spatial positions, similar to an aliasing effect. This results in artefactual variations in apparent spatial resolution.

Note also the double edge in the right image, indicating that the gain in both *x* and *y* directions requires adjustment in one or more windows.

Service is required to correct the errors in the MWSR for both cameras.

2.4.3. Example: ^{67}Ga MWSR — visual method — error (2)

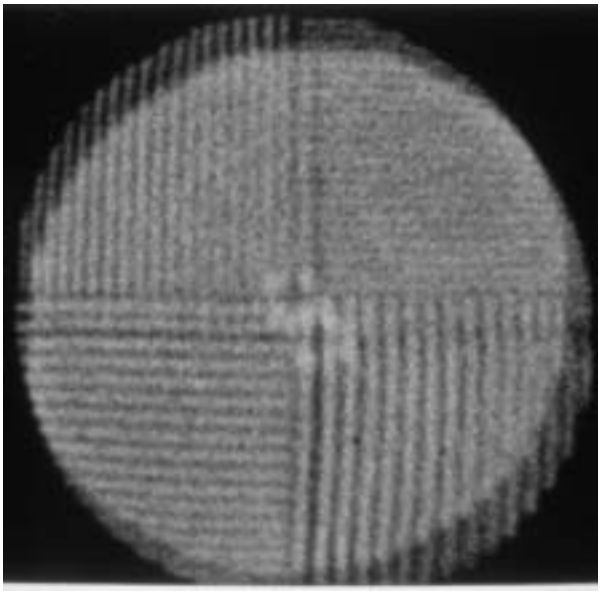

Intrinsic spatial resolution with ^{67}Ga point source (count rate < 20 000 counts/s), four quadrant bar pattern, 3 million counts each image, preset energy window widths, summed image from energy windows set over the 93, 183 and 296 keV photopeaks.

Results: The image, obtained from three energy windows, shows large offsets in both *x* and *y* directions. This MWSR problem requires service.

2.4.4. Example: MWSR — visual method — error; comparison of ^{99m}Tc and ^{67}Ga (1)

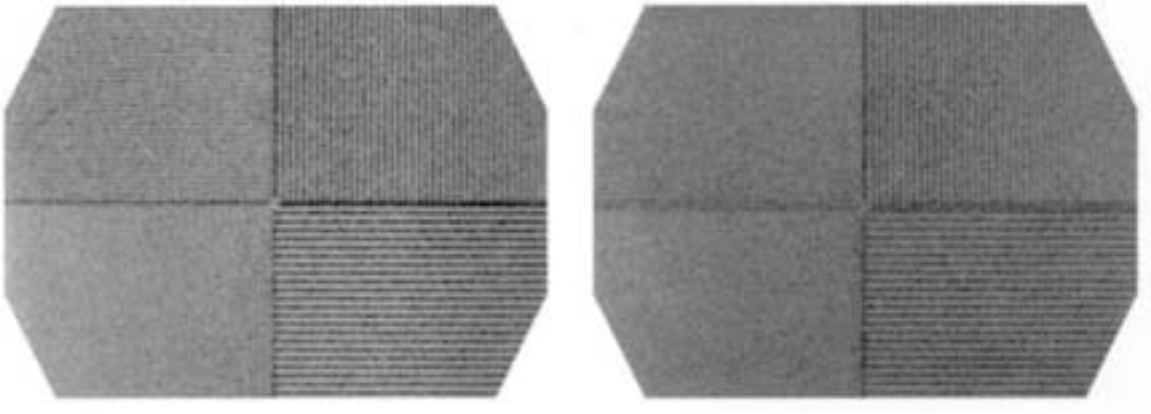

Intrinsic spatial resolution images acquired using a four quadrant bar pattern, 4 million counts each image.

L: ^{99m}Tc.
R: ^{67}Ga (summed image of 93, 183 and 296 keV photopeaks).

Results: The ^{67}Ga image (R) shows a double horizontal line separating the upper and lower halves of the image. Note that this is not seen on the ^{99m}Tc image (L). This is caused by an offset error in the MWSR in the vertical direction, so that there is a difference in the position of the three superimposed images from the 93, 183 and 296 keV peaks of ^{67}Ga.

Comments: This MWSR offset problem can be easily corrected by service personnel by adjusting the ratio circuits.

2.4.5. Example: MWSR — visual method — error; comparison of ^{99m}Tc and ^{67}Ga (2)

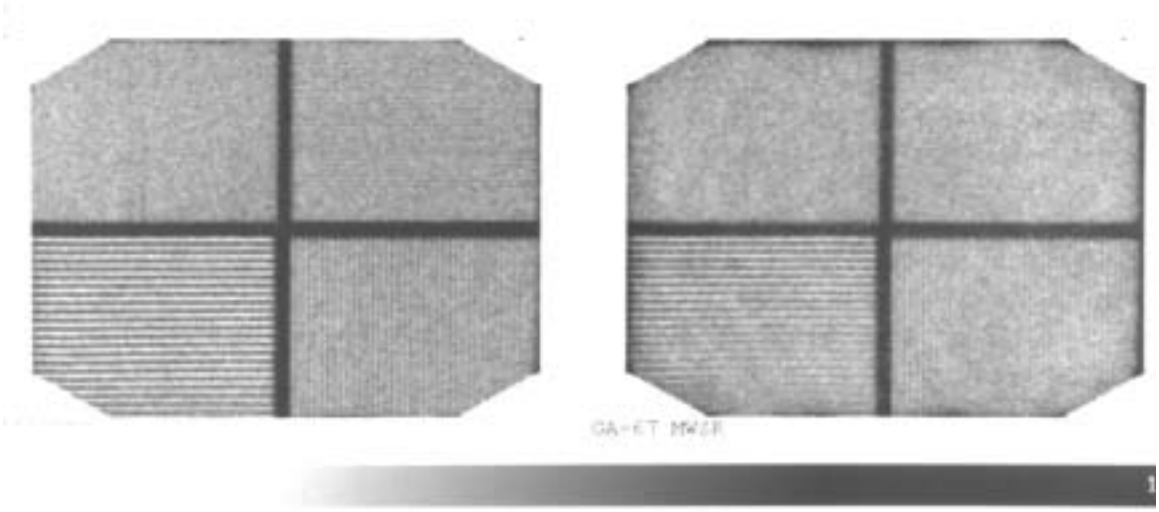

Intrinsic resolution images of a four quadrant bar pattern acquired using ^{99m}Tc and ^{67}Ga (summed images of 93, 183 and 296 keV photopeaks).

L: ^{99m}Tc.
R: ^{67}Ga.

Results: The ^{67}Ga image (R) shows areas with considerable loss of spatial resolution. This is particularly obvious because such areas are not seen on the ^{99m}Tc image (L). This means that there is a difference in the position of the three superimposed images from ^{67}Ga (93, 183 and 296 keV photon peaks).

Comments: This MWSR problem can be easily corrected by service personnel by adjusting the ratio circuits.

2.4.6. Example: ^{67}Ga MWSR error — clinical

^{67}Ga citrate image of the head, medium energy collimator, summed image of three images obtained with the preset energy windows of 93, 183 and 296 keV.

Results: Image shows poor spatial resolution due to poor MWSR. The scintillation camera requires service.

2.5. HIGH COUNT RATE

2.5.1. Example: Changes in uniformity at high count rates

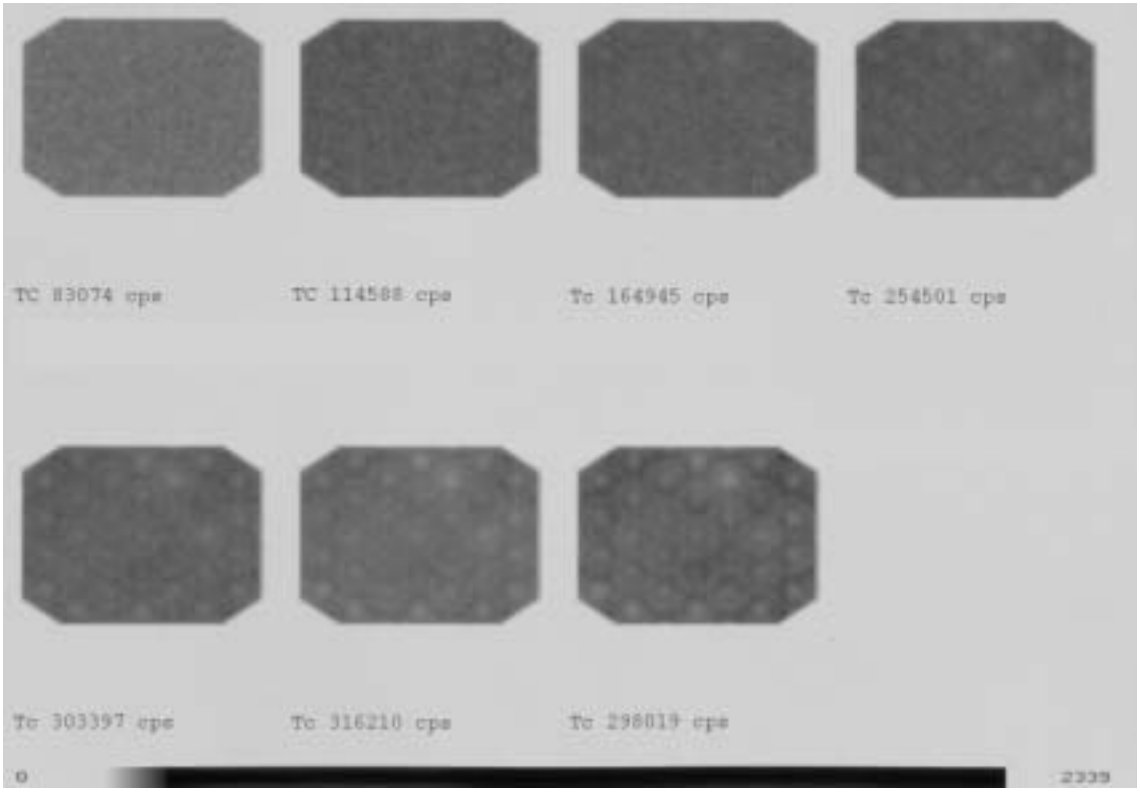

Intrinsic ^{99m}Tc images of 4 million counts were acquired with a 20% energy window for different source activities, producing different count rates.

Top row from left to right: 83 000, 115 000, 165 000 and 255 000 counts/s.
Bottom row from left to right: 303 000, 316 000 and 298 000 counts/s.

Results: With increasing count rate the uniformity deteriorates. Above 115 000 counts/s the PM tubes were visualized as cold areas.

Note that in the bottom row the maximum count rate of the scintillation camera has been reached. In the last image, the maximum count rate has been exceeded, resulting in a reduced count rate in response to increased source activity.

In practice, clinical work is unlikely to produce count rates higher than the lowest value shown here.

2.5.2. Example: Spatial resolution — poor image at high count rate due to misplaced events

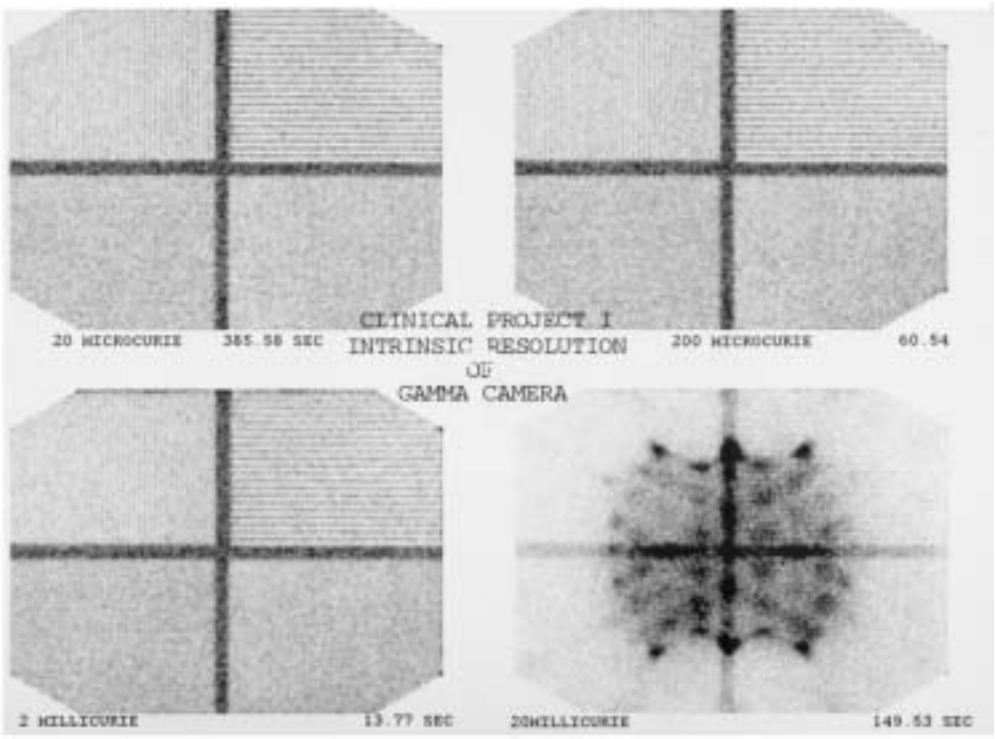

Series of intrinsic resolution images obtained at increasing count rates. The point source activity used has been increased by a factor of 10 between successive images. Each image consists of 1 million counts.

TL: 0.74 MBq (20 μCi), 365 s.
TR: 7.4 MBq (200 μCi), 60 s.
BL: 74 MBq (2 mCi), 13 s.
BR: 740 MBq (20 mCi), 149 s.

Results: The image obtained with 0.74 MBq represents a count rate value with negligible dead time. Only two bars of the four quadrant pattern are resolved. As the activity is increased by factors of 10, the dead time increases. At the highest count rate shown here the image (BR) has completely collapsed and shows an extreme pattern of misplaced events, because the circuitry cannot deal with the very high count rate.

Comments: In order to observe subtle effects of increasing the count rate, a bar pattern which shows bars in each quadrant (of at least three quadrants) would be more effective. In order to determine at what count rate the camera images start to deteriorate, a further set of images is needed for activities between 74 and 740 MBq. However, the intention here is just to show the effects of increasing activity on dead time and spatial resolution.

2.5.3. Example: High count rate — asymmetric energy window

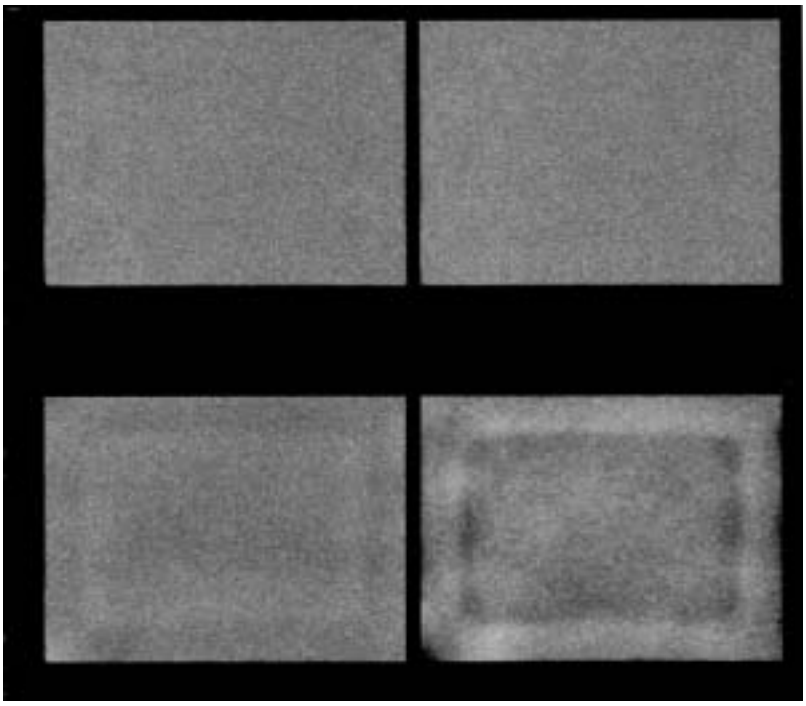

Intrinsic uniformity images, ^{99m}Tc, 4 million counts each image. The top left image was obtained at a count rate of 31 000 counts/s in a 20% symmetric energy window. The other three images were all made with the count rate in the symmetric window of 71 000 counts/s.

TL: 20% symmetric energy window, on-peak, 31 000 counts/s.
TR: 20% symmetric energy window, on-peak, 71 000 counts/s.
BL: 20% energy window shifted to asymmetric high, 56 000 counts/s in this window.
BR: 20% energy window shifted to asymmetric low, 24 000 counts/s in this window.

Results: The symmetric window images acquired with ^{99m}Tc at lower (31 000 counts/s) and at higher (71 000 counts/s) count rates show satisfactory uniformity. The asymmetric window images show some non-uniformity. A faint rectangle of diminished counts is seen in the off-peak high image (BL), and a rectangle of increased counts is seen in the off-peak low image (BR). There is also a very large difference in count rate for the asymmetric windows that could not be explained by window positioning.

The problem should be corrected by service personnel. If local service personnel cannot solve the problem, then it should be passed on to expert engineers in the main office.

Comments: The intrinsic symmetric energy window image shows no visually observable loss of uniformity at the higher count rate. However, in clinical imaging with a higher count rate, the presence of scatter may produce some non-uniformity, as indicated in the non-uniformity in the asymmetric low energy window image (BR).

2.5.4. Example: Uniformity — poor image — misplaced events

Intrinsic uniformity at high count rate, ^{99m}Tc, 20% energy window, 10 million counts in 97 s (103 000 counts/s), 128 × 128 matrix.

Results: There is an accumulation of counts towards the centre of the FOV, indicating misplaced events.

Comments: This type of image can also be observed in high activity, new ^{57}Co sheet sources placed directly on the collimator. The effect of the high energy components from the decay of ^{57}Co, ^{56}Co and ^{58}Co can lead to a high flux of photons onto the detector and a high dead time, even though the counts in the 122 keV energy window of ^{57}Co will not indicate this.

See also Section 2.2.10.2.

2.5.5. Example: High count rate — auto-high operating mode

Analogue scintillation camera, intrinsic uniformity at low (<20 000 counts/s) and high (~75 000 counts/s) count rates, ^{99m}Tc, 20% energy window.

L: Low count rate, camera operated in normal mode.
M: High count rate, camera operated in normal mode (as normally used at low count rates).
R: High count rate, camera operated in auto-high mode (designed for high count rate imaging, whereby the event integration and unblank time are shortened).

Results: A loss of uniformity is seen in the auto-high mode. This can be corrected by adjustment of the electronics by service personnel.

Note: If such an auto-high mode is used clinically, the uniformity must be checked. Some cameras switch automatically to the high count rate mode. With such a system, the uniformity must be checked with a count rate higher than that which causes it to enter the high count rate mode.

2.5.6. Example: Effect of high count rate in normal and fast mode

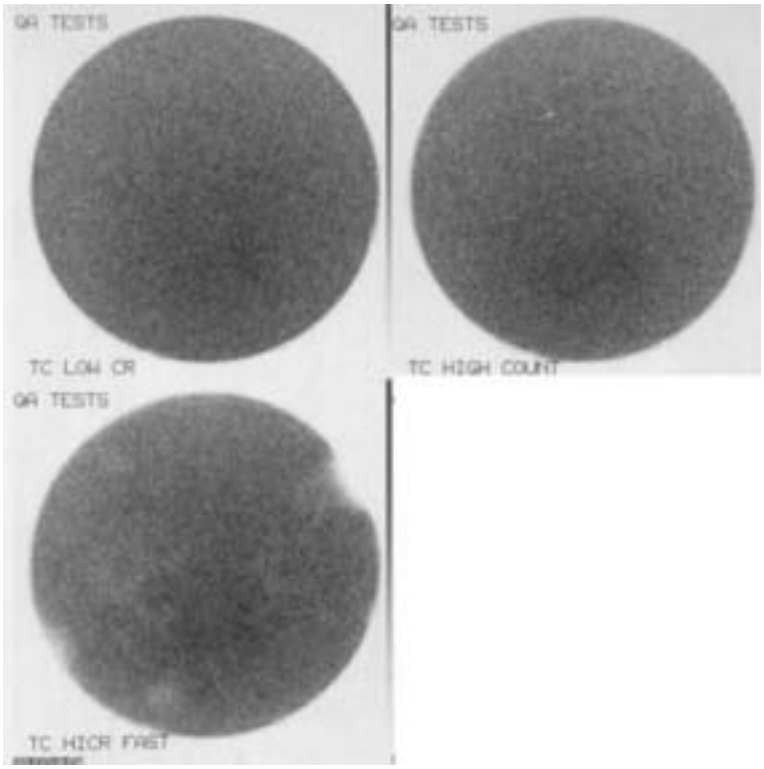

Series of ^{99m}Tc uniformity images (20% energy window) obtained with the following settings:

TL: Low count rate (<20 000 counts/s), symmetric window position, normal mode (as used clinically).
TR: High count rate (~75 000 counts/s), symmetric window position, normal mode.
BL: High count rate (~75 000 counts/s), symmetric window position but switched to fast mode.

Results: The images in normal mode are very similar. However, when the camera is switched to fast mode, severe non-uniformities appear, including at least three cold PM tubes. This requires service.

Comments: If a high count rate mode is used clinically, it should be periodically checked.

2.5.7. Example: High count rate in fast mode

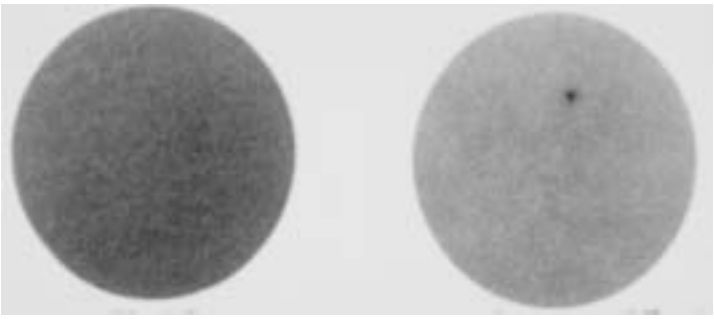

High count rate uniformity images.

L: Normal mode.
R: Fast mode.

Results: The high count rate image obtained with the camera operating in normal mode shows reasonable uniformity. However, when operation is switched to fast mode (intended to give a higher count rate), there is a concentration of counts at one focal spot. This requires service.

3. SPECT

3.1. SPECT UNIFORMITY

3.1.1A. Example: SPECT uniformity simulation — no noise (perfect uniformity)

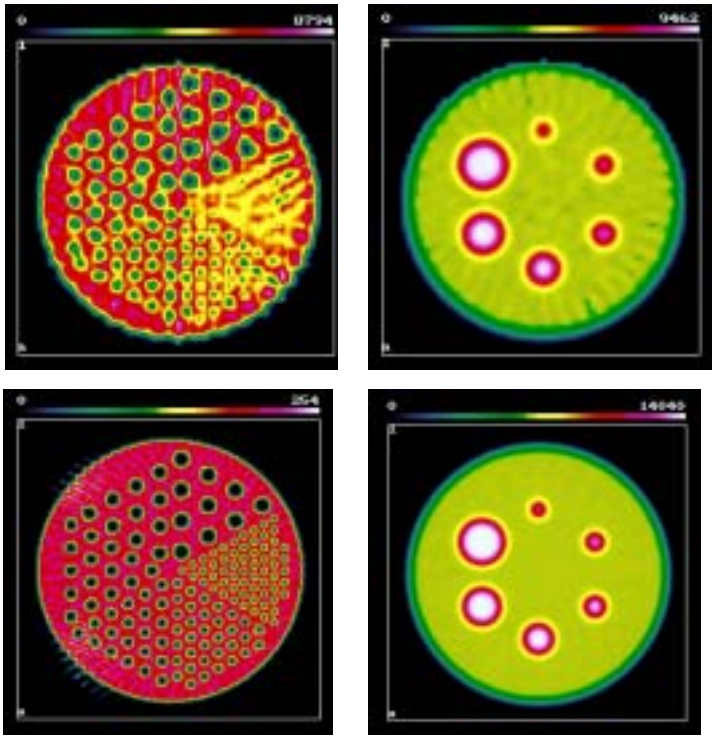

Simulation of a Data Spectrum Deluxe ECT phantom (Jaszczak phantom) with no statistical noise, 37 cm FOV with 1.5 zoom, 360° total angle of rotation, circular orbit, reconstruction with a ramp filter and FBP, no attenuation correction. Perfect uniformity.

Top row: 64×64 matrix, 64 projections. L: rods; R: spheres (pixel size 3.85 mm).
Bottom row: 128×128 matrix, 128 projections. L: rods; R: spheres (pixel size 1.92 mm).

Results: This example represents perfect data (no statistical noise and perfect uniformity). Note the differences in appearance of the phantom due to the change in sampling for tomographic reconstruction, which is inadequate for the noise free data of the upper row. In real clinical SPECT, statistical noise and low pixel counts play an important role, so that larger pixel sizes give adequate results.

Note: In the Deluxe ECT phantom:
Cold rods have diameters of 4.8, 6.4, 7.9, 9.5, 11.1 and 12.7 mm.
Cold spheres have diameters of 9.5, 12.7, 15.9, 19.1, 25.4 and 31.8 mm.

3.1.1B. Example: SPECT uniformity simulation — non-uniformity at the centre of the axis of rotation

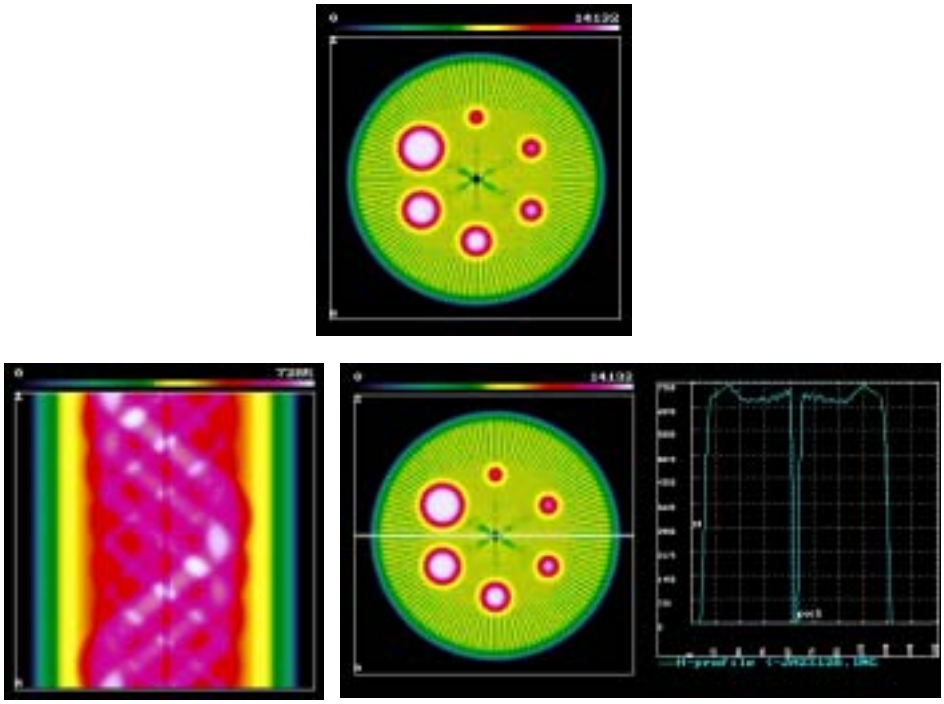

Simulation of a Data Spectrum Deluxe ECT phantom (Jaszczak phantom) with no statistical noise, 37 cm FOV with 1.5 zoom, 360° total angle of rotation, circular orbit, 128 × 128 matrix, reconstruction with a ramp filter and FBP, no attenuation correction. A simulated –5% defect was introduced between pixels 63 and 65 (centre of the FOV).

T: Reconstruction into a transverse slice with a ramp filter.
BL: Sinogram showing the simulated defect as a narrow vertical line of reduced intensity.
BR: Same image of the transverse slice but with a profile through the defect.

Results: The size and depth of the non-uniformity in the reconstructed slice, seen at the centre of rotation and the centre of the phantom, are much greater than the original non-uniformity in the planar images.

Comments: It is important to note that in the simulations shown here (3.1.1A–D), the axis of rotation, the centre of the FOV and the centre of the phantom all coincide. This may not be the case when imaging a real phantom. The centre of the FOV and the axis of rotation will coincide when the centre of rotation corrections are current and are properly applied. However, the centre of the phantom and the axis of rotation will only coincide if great care is taken when setting up the phantom in order to align the centre of the phantom with the axis of rotation.

The effect of a defect on the reconstructed uniformity is always greatest at the axis of rotation, and a ring will be produced whose radius is dependent on the location of the non-uniformity with respect to the axis of rotation. Also, the depth of the reconstructed non-uniformity decreases with increasing distance from the axis of rotation. A hot or cold spot at the axis of rotation is the worst case and is potentially a common artefact.

3.1.1C. Example: SPECT uniformity simulation — 3 pixel wide non-uniformity offset from the axis of rotation

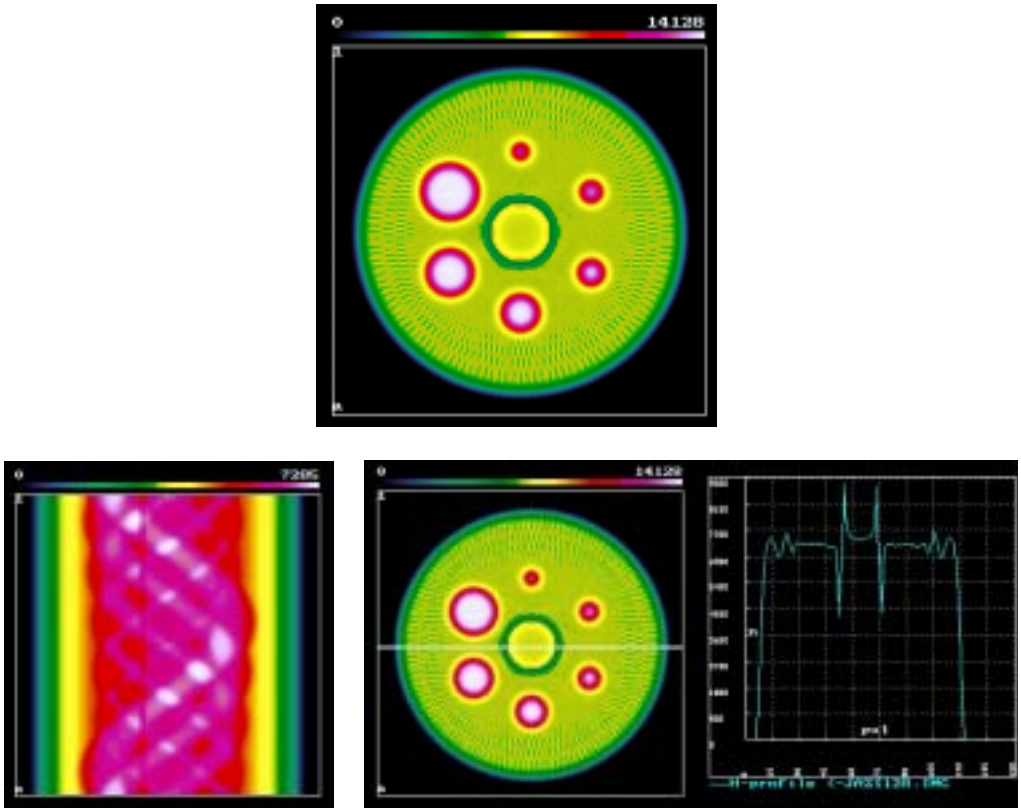

Simulation of a Data Spectrum Deluxe ECT phantom (Jaszczak phantom) with no statistical noise, 37 cm FOV with 1.5 zoom, 360° total angle of rotation, circular orbit, 128 × 128 matrix, reconstruction with a ramp filter and FBP, no attenuation correction. A simulated –5% defect was introduced between pixels 52 and 54 (i.e. offset from the centre of the FOV).

T: Reconstruction into a transverse slice with a ramp filter.
BL: Sinogram showing the simulated defect as a narrow vertical line of reduced intensity.
BR: Same image of the transverse slice but with a profile through the centre of the FOV.

Results: The non-uniformity due to the –5% defect shows as a ring of decreased intensity. The 'ringing', sharp spikes on the profile (BR), is an artefact due to the sharp discontinuities in the uniformity and to the FBP reconstruction method.

Comments: See comments on example 3.1.1B.

The effect of a defect on the reconstructed uniformity is always greatest at the axis of rotation, and a ring will be produced whose radius is dependent on the location of the non-uniformity with respect to the axis of rotation. Also, the depth of the reconstructed non-uniformity decreases with increasing distance from the axis of rotation.

3.1.1D. Example: SPECT uniformity simulation — 16 pixel wide non-uniformity offset from the axis of rotation

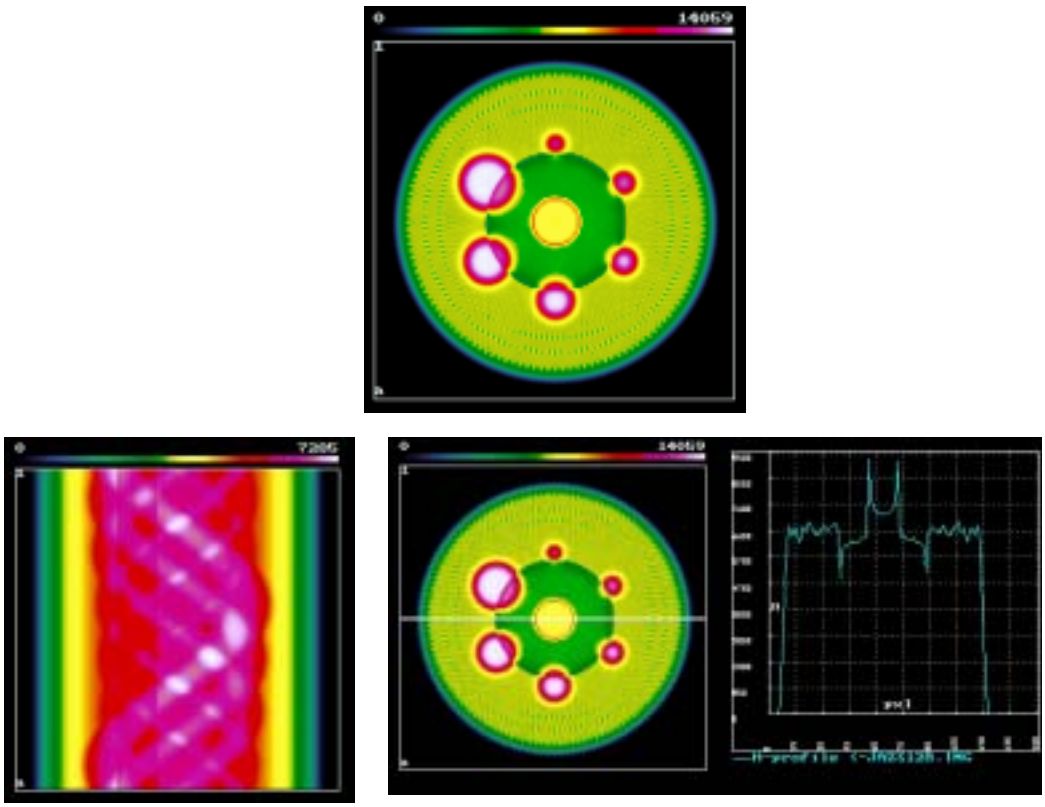

Simulation of a Data Spectrum Deluxe ECT phantom (Jaszczak phantom) with no statistical noise, 37 cm FOV with 1.5 zoom, 360° total angle of rotation, circular orbit, 128 × 128 matrix, reconstruction with a ramp filter and FBP, no attenuation correction. A simulated –5% defect was introduced between pixels 40 and 55 (offset from the centre of the FOV).

T: Reconstruction into a transverse slice with a ramp filter.
BL: Sinogram showing the simulated defect as a broad vertical line of reduced intensity.
BR: Same image of the transverse slice but with a profile through the centre of the FOV.

Results: The non-uniformity due to the –5% defect shows as a wide ring of decreased intensity that partially passes through the spheres of the simulated phantom. The ringing and increased central activity (see profile) are artefacts due to the sharp discontinuities in the uniformity and to the FBP reconstruction method.

Comments: See comments on example 3.1.1B.

The effect of a defect on the reconstructed uniformity is always greatest at the axis of rotation, and a ring will be produced whose radius is dependent on the location of the non-uniformity with respect to the axis of rotation. Also, the depth of the reconstructed non-uniformity decreases with increasing distance from the axis of rotation.

3.1.2. Example: SPECT uniformity — single head SPECT — ring artefacts — real data

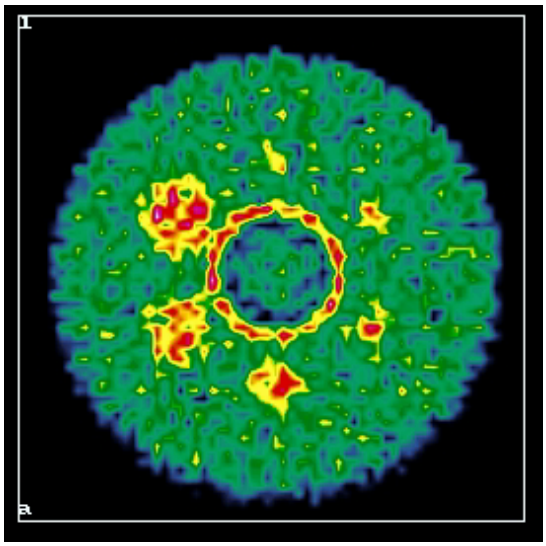

Single head SPECT, Data Spectrum ECT phantom (Jaszczak phantom), 360° total angle of rotation, reconstruction using ramp filter and FBP, with attenuation correction. Note that no smoothing filter has been applied. Transverse slice through the spheres of the phantom.

Results: The transverse slice shows a hot ring. The ring is due to non-uniformity in the detector. A uniformity correction map is required to correct for this non-uniformity.

3.1.3. Example: SPECT uniformity — high and low (clinical) count density

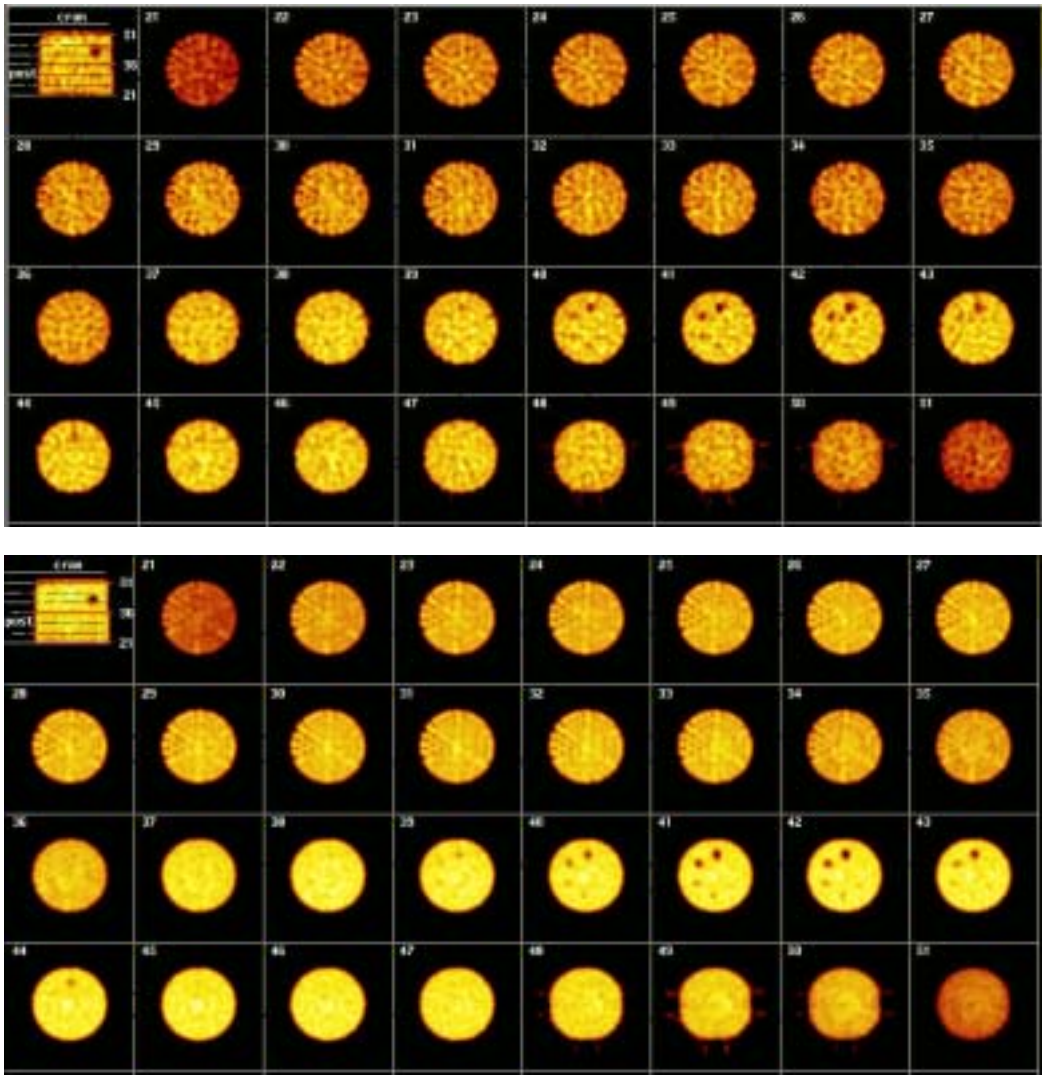

Two examples of reconstructed transverse slices from the Data Spectrum ECT phantom (Jaszczak phantom) with cold inserts to illustrate effects of count statistics. The phantom was filled with 500 MBq ^{99m}Tc pertechnetate.

Acquisition: 15% energy window, high resolution collimator, 360° total angle of rotation, 60 projections, 64 × 64 matrix, 50 000 and 500 000 counts per projection.

Reconstruction: Butterworth filter and FBP, with attenuation correction.

Top images: Transverse slices from 50 000 counts per projection (3 million counts total).
Bottom images: Transverse slices from 500 000 counts per projection (30 million counts total).

Results: These images illustrate the apparent loss of spatial resolution when low count images are obtained. Typically, clinical studies contain a total number of counts within the range between these two count levels.

3.1.4. Example: SPECT uniformity — single head SPECT — three different cameras (same manufacturer) — ECT phantom

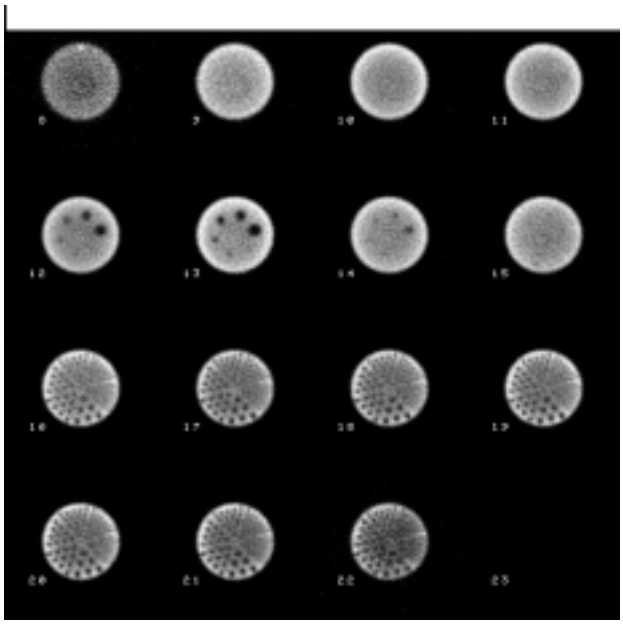

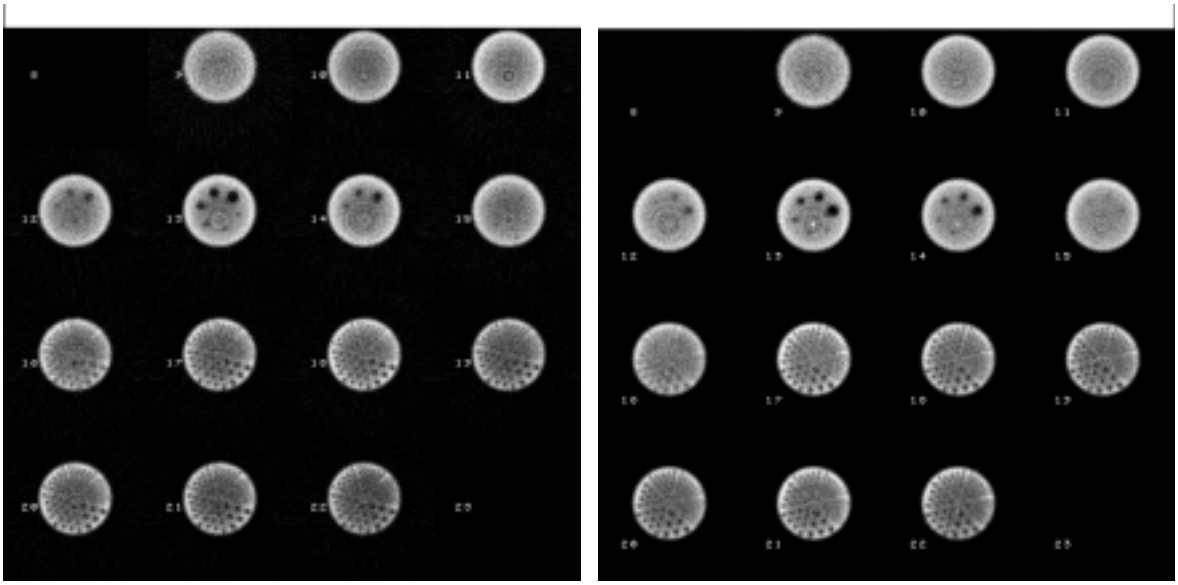

Data Spectrum ECT phantom (Jaszczak phantom) filled with ^{99m}Tc pertechnetate and imaged on three different single head SPECT systems from the same manufacturer, each with a different collimator. The SPECT acquisition and reconstruction techniques were the same for each camera.

Acquisition: ^{99m}Tc, 15% energy window, 360º total angle of rotation, radius of rotation 15 cm, circular orbit, 800 000 counts per projection, 128 × 128 matrix, 120 projections.

Reconstruction: FBP reconstruction into transverse slices with Butterworth prefilter (order 5, cut-off 0.5 Nyquist frequency), slice thickness 1.2 cm, no attenuation correction.

T: Camera A with LEUHR collimator.
BL: Camera B with LEHR collimator.
BR: Camera C with LEHR collimator.

Results: All three SPECT systems show equivalent performance for this phantom and this technique. Full ring artefacts are present in various slices in each series of images. They result from non-uniformity in the collimated detector and the 360º rotation. The rings are centred around the axis of rotation and not the centre of the phantom. Note the difference in appearance of the rings in different slices and between the three different cameras. Note also that the rings are more difficult to identify in the rods section of the phantom. The increase in intensity towards the outer edge of each transverse slice is the result of there being no attenuation correction. A very large number of counts (about 100 million) were acquired to enable artefacts to be seen clearly. With clinical numbers of counts, artefacts would be less obvious.

Comments: Non-uniformity rings can be caused by: (a) poor detector uniformity, (b) collimator defects, (c) poor count statistics in the uniformity correction data, (d) scatter correction, (e) ADC non-linearity (see example 3.1.5).

Ring artefacts are always centred around the axis of rotation, or the centre of the FOV if they coincide, and not the centre of the phantom.

See also comments on example 3.1.1B.

3.1.5. Example: SPECT uniformity — ring artefacts typical of ADC non-linearity

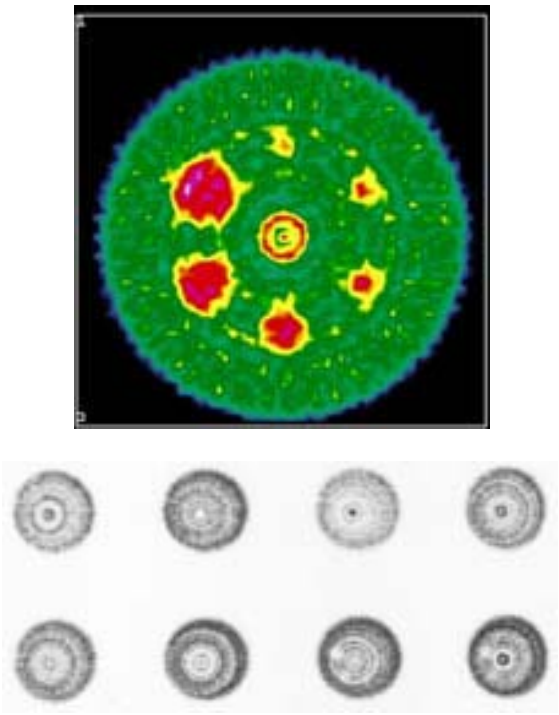

Top: Simulation, single head SPECT system, Data Spectrum ECT phantom (Jaszczak phantom) with hot inserts, 128 × 128 matrix, 360° total angle of rotation, circular orbit, reconstruction into transverse slice with a ramp filter and FBP, attenuation correction applied.

Bottom: Real data acquisition, single head SPECT system, Data Spectrum ECT phantom (Jaszczak phantom) with cold inserts, 64 × 64 matrix, 360° total angle of rotation, circular orbit, reconstruction into transverse slices with a ramp filter and FBP, no attenuation correction. Eight consecutive images from the data set are shown here. The phantom was positioned slightly off-centre with respect to the axis of rotation.

Results:

Top: The single transverse simulated slice shows multiple ring artefacts. These are very obvious at the centre of rotation, where a hot centre and hot ring are clearly seen. At increasing radial distance the rings have decreased count density and become more diffuse.

Bottom: Each image shows discrete hot and cold sharp rings centred around the axis of rotation. The appearance of the rings and central spot is different in each image. This pattern is typical for both detector and ADC non-uniformity.

The cold spheres of the phantom are visible in the lower right two images. The intense border and less intense centre are typical of reconstructions without attenuation correction.

3.1.6. Example: SPECT uniformity — dual head SPECT — partial ring artefacts

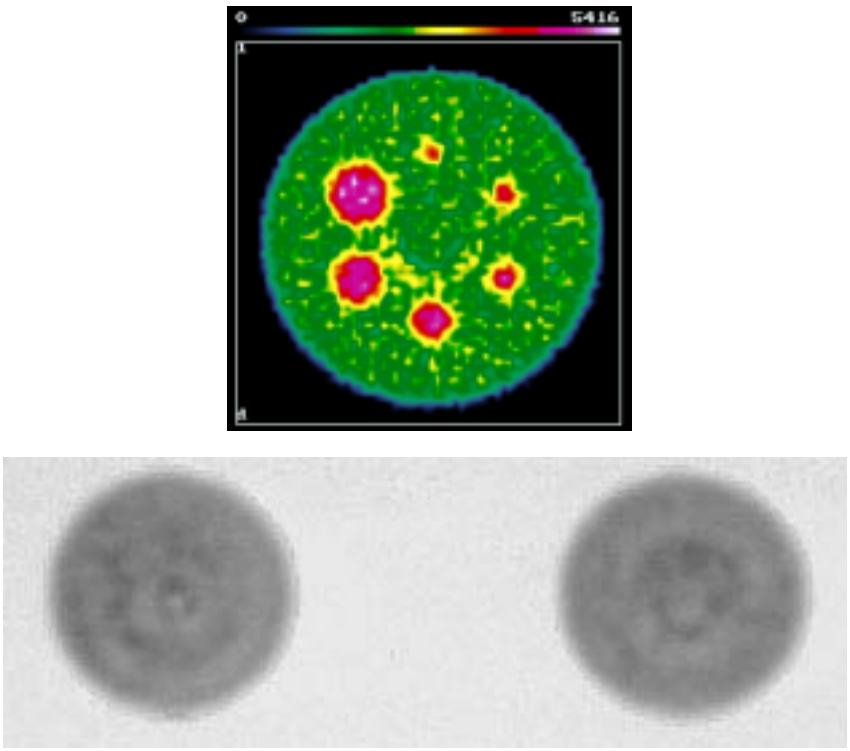

Simulated (top) and real (bottom) images, dual head SPECT system with heads at 180° from each other, 360° total angle of rotation (each detector rotates through 180°), circular orbit.

Top: Simulated data of a Data Spectrum ECT phantom (Jaszczak phantom) with hot inserts, 128 × 128 matrix, reconstruction into a transverse slice with a ramp filter and FBP, attenuation correction applied. One of the detectors has a non-uniformity.

Bottom: SPECT acquisition of a uniform cylinder, no attenuation correction and no uniformity correction applied. Two images from the set of transverse slices are shown.

Results:

Top: The transverse slice shows a semicircular ring of increased counts with respect to the surrounding background in the lower half of the image (yellow).

Bottom: Different non-uniform artefacts are seen in the transverse slices. In the left image, the centre of the innermost ring corresponds to the centre of rotation. Note that the phantom was positioned off-centre so that this ring artefact does not correspond exactly to the centre of the phantom. Other artefacts are semicircles centred around the axis of rotation, and not full rings as would be expected from a 360° rotation of a single head SPECT system.

Comments: In multihead SPECT systems, each head will contribute to the non-uniformity of the resultant SPECT uniformity. Since the non-uniformity in each head will be different, the resultant pattern observed in the reconstructed images will not be rings but partial rings.

3.1.7. Example: SPECT uniformity — dual head SPECT — partial ring artefacts — clinical study

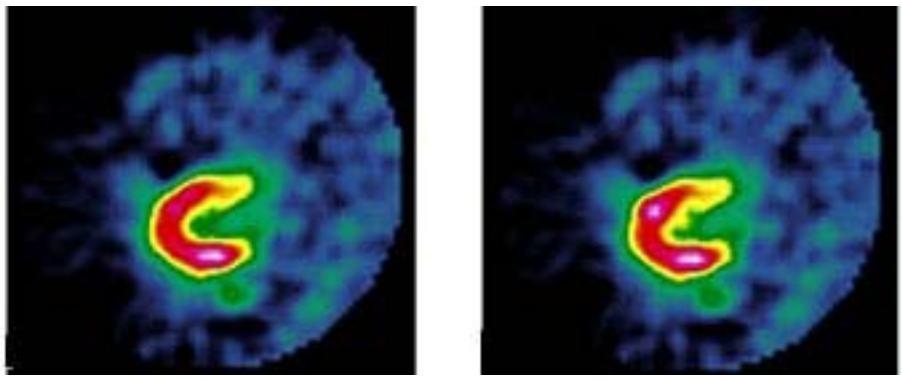

This example demonstrates the subtleties of the effect of planar non-uniformity in clinical SPECT results. Transaxial slices from a clinical ^{99m}Tc myocardial perfusion study. Dual head SPECT system.

Acquisition: 180º total angle of rotation, each head rotated through 90º, 64 × 64 matrix size.

Reconstruction: FBP with a Parzen window cut-off at 1 Nyquist.

L: Transaxial slice with no simulated non-uniformity.
R: Transaxial slice with a simulated non-uniformity in one detector, consisting of a 5 pixel wide, +10% planar non-uniformity introduced at 10 pixels from the centre of the FOV.

Results: The left image shows a relatively uniform distribution within the myocardium, although the inferior wall shows a slight increase in counts. The right image, with simulated non-uniformity, shows a less uniform distribution of counts within the myocardial walls and some distortion and thickening of the myocardium. Although artefacts alter the image, a clinical user would not be aware that he or she is viewing a distorted image. This emphasizes the value of proper QC procedures.

3.1.8. Example: Non-uniformity in SPECT image caused by a high ambient temperature

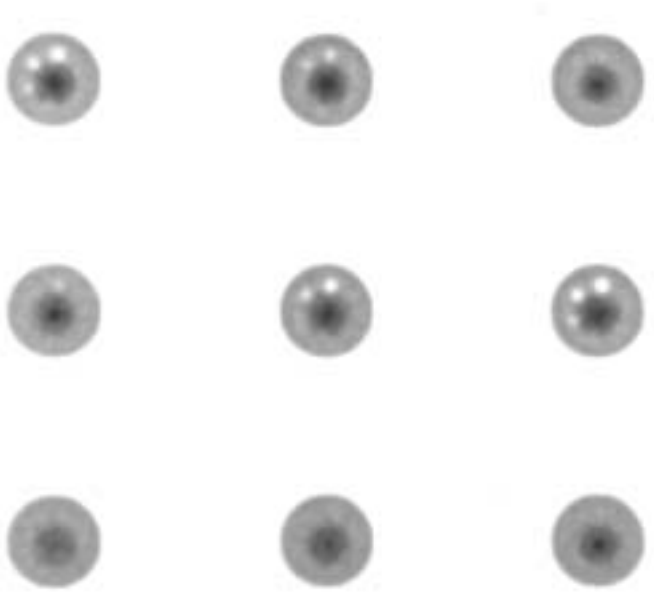

Data Spectrum ECT phantom (Jaszczak phantom) images were acquired using ^{99m}Tc, 500 000 counts in the first view, a 64 × 64 matrix and 64 views on a triple head SPECT system. Data were reconstructed into transverse slices with a Hann filter, 1 Nyquist cut-off, FBP and attenuation correction (Chang method). The images shown here were from one detector head.

Results: Because the room was too warm, the images from one of the detectors had large hot spots in the centre of the images. The temperature of the room was lowered and repeat tests were satisfactory for all three detectors.

Comments: The cameras from some vendors are more sensitive to high ambient temperature than others.

See also Section 6.

3.1.9A. Example: SPECT non-uniformity due to phantom (1)

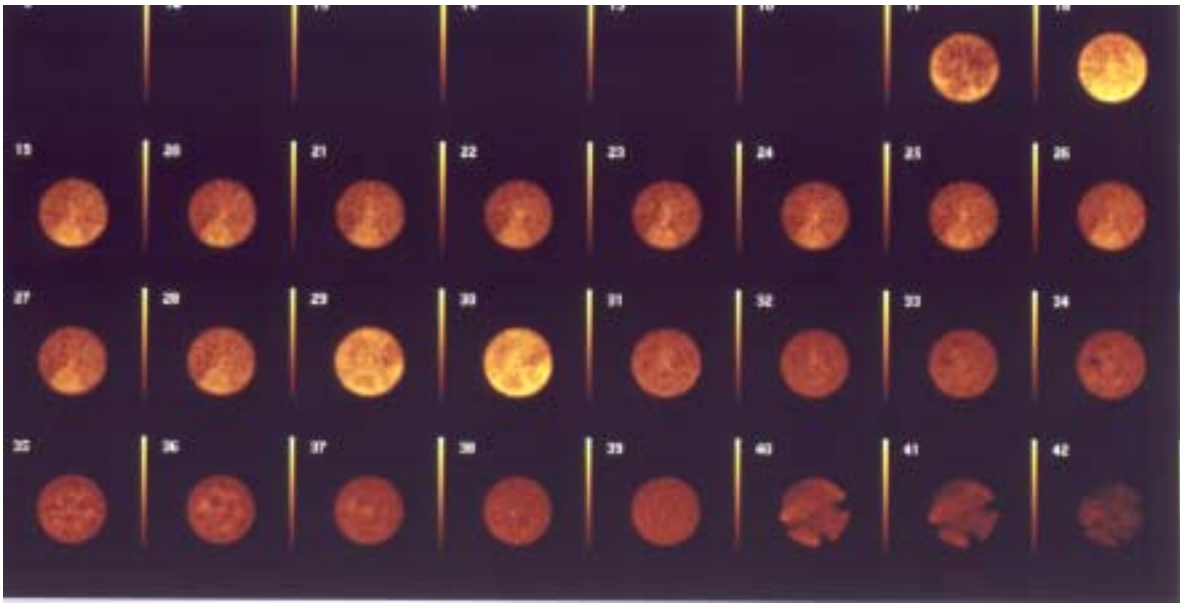

Transverse slices from a Data Spectrum ECT phantom (Jaszczak phantom) filled with ^{99m}Tc DTPA. The ^{99m}Tc DTPA was injected into the water filled phantom. The phantom contents were mixed, but the phantom was then left for a period of time standing upright with the rods at the bottom.

Results: The images show non-uniform distribution of radioactivity. The hotter transverse slices are those at the bottom of the phantom and those above the division between the rods and spheres sections. This is probably due to the specific density of the DTPA, which is relatively dense compared with water, and which therefore in this situation sank to the bottom of the phantom and was also trapped by the Perspex supports of the rods section. It also appears to have adhered to the Perspex rods.

Note: The cold indentations in the last three images (40–42) are due to the jig holding the phantom in place.

Comments: It is always preferable to use ^{99m}Tc pertechnetate rather than another ^{99m}Tc radiopharmaceutical.

See also Section 2.2.10.1.

3.1.9B. Example: SPECT non-uniformity due to phantom (2)

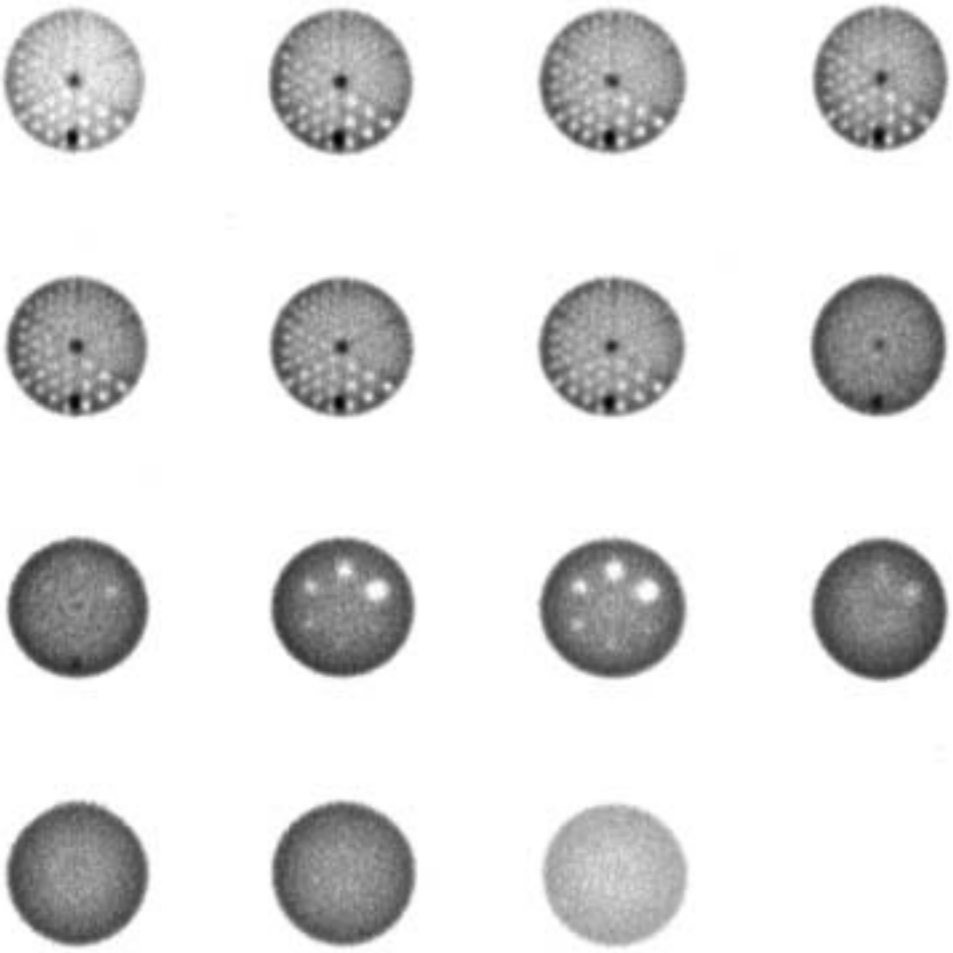

Transverse slices (no attenuation correction) from a Data Spectrum ECT phantom (Jaszczak phantom) filled with ^{99m}Tc pertechnetate. A large amount of activity of ^{99m}Tc was injected into the water filled phantom, which was then left overnight so that the radioactivity could disperse naturally before imaging took place the next day. A series of the SPECT transaxial slice images are shown.

Results: The images show two unusual hot spots in the ECT phantom, in the rods section at the centre and at the periphery (at 6 o'clock). This was caused by adherence of the radioactivity to the central and peripheral rods that support the phantom, and probably occurred because the radioactive solution had been left in the phantom for such a long time. Otherwise, the phantom results are acceptable.

3.2. UNIFORMITY CALIBRATION CORRECTION

3.2.1. Example: SPECT uniformity — with and without uniformity correction — single head

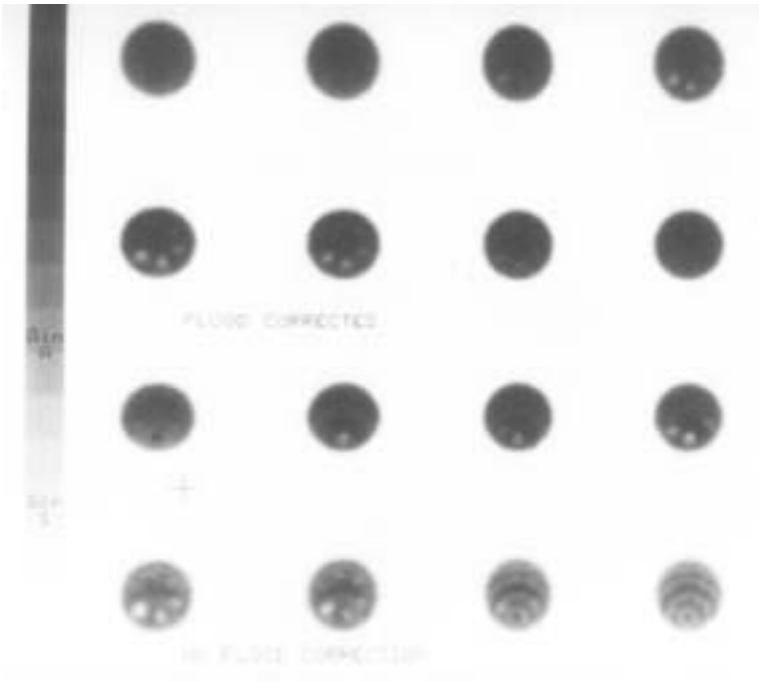

Single head SPECT system, high resolution collimator, check of SPECT uniformity correction using a Data Spectrum ECT phantom (Jaszczak phantom) filled with a homogeneous solution of ^{99m}Tc, SPECT acquisition using 360° total angle of rotation, FBP reconstruction of transverse slices with attenuation correction.

Top two rows: Data reconstructed with uniformity correction applied.
Bottom two rows: Data reconstructed with no uniformity correction applied.

Results: Hot and cold ring artefacts in the transverse slices of images without uniformity correction are especially visible in the bottom row. These ring artefacts were no longer seen after the uniformity correction was applied.

3.2.2. Example: SPECT uniformity — phantom study with and without outdated uniformity correction

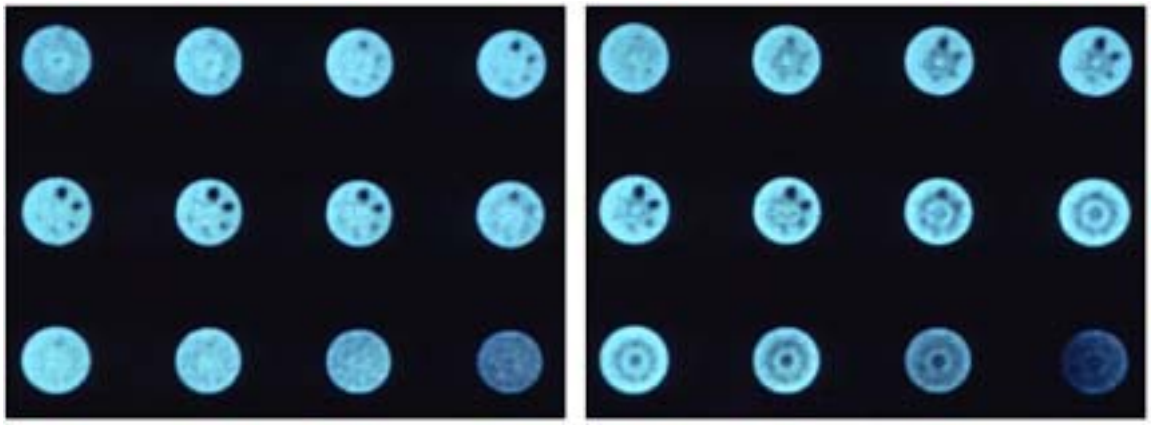

A B

Single head SPECT system, LEHR collimator, periodic check of SPECT uniformity using a Data Spectrum ECT phantom (Jaszczak phantom), ^{99m}Tc, SPECT acquisition using a 360° total angle of rotation, 64 × 64 matrix, 60 projections, reconstruction of transverse slices using a Hann smoothing filter with 1 Nyquist cut-off, FBP and Chang attenuation correction.

A: Data reconstructed with no uniformity correction.
B: Data reconstructed with a high count uniformity correction map that was about two weeks old.

Results: Transverse slices of A, without uniformity correction, show diffuse rings in various transverse slices. Transverse slices of B, with uniformity correction, show distinct rings, and hot and cold spots at the centre of rotation. The uniformity correction map was not current and was no longer valid. New uniformity correction maps were subsequently obtained.

Comments: These data show the importance of regular QC of the uniformity correction applied to SPECT data.

Firstly, a check is needed directly after collecting the uniformity correction map, in order to determine whether the uniformity correction has been properly acquired, with the correct image orientation, and whether the correction can be used with confidence to correct subsequent SPECT data.

Secondly, a check is required thereafter in order to determine whether changes have occurred and whether the correction is still applicable. The frequency of such a check depends on the frequency of acquiring uniformity correction maps and on the stability of the SPECT system. Strict planar QC checks can give a good indication of uniformity changes, but a SPECT acquisition and reconstruction of a uniformly filled cylinder is a check of the whole system.

This camera should not be used for clinical studies using the outdated uniformity correction map.

3.2.3. Example: Myocardial perfusion SPECT — with and without uniformity correction

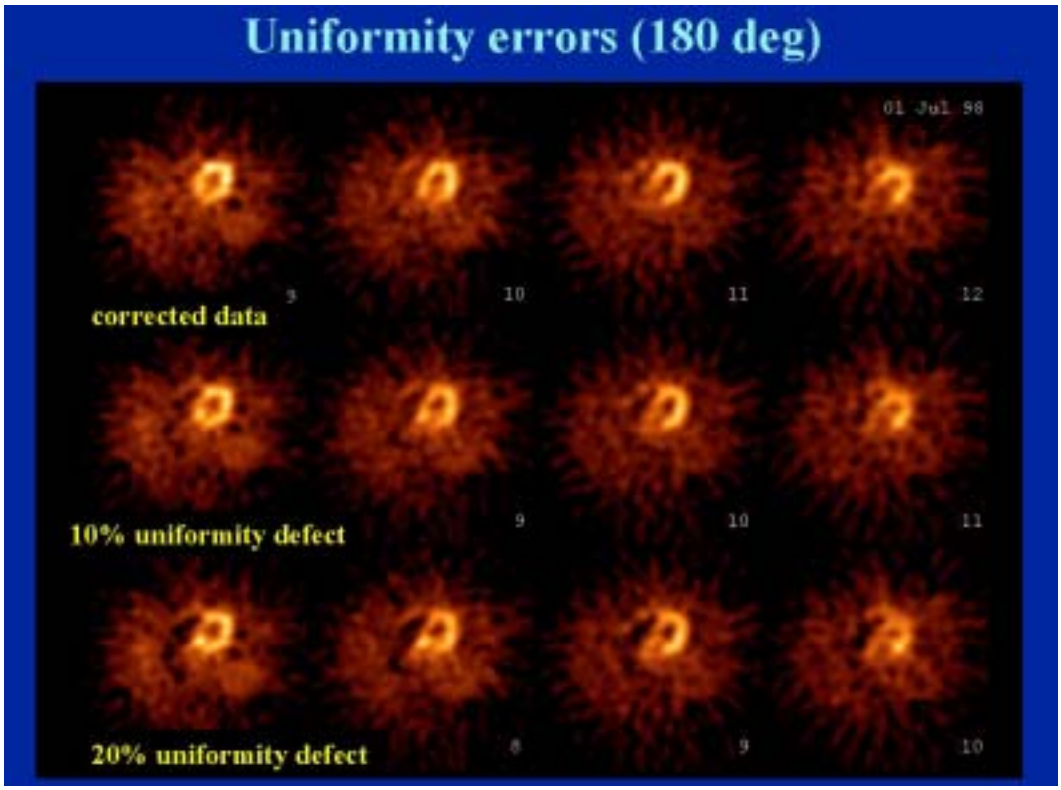

Myocardial perfusion SPECT study, 180º data acquisition. Reconstruction into transaxial slices with FBP.

Top row: After a high count uniformity correction.
Middle row: With a 10% uniformity defect (throughout the 180º data acquisition), no uniformity correction.
Bottom row: With a 20% uniformity defect (throughout the 180º data acquisition), no uniformity correction.

Results: The effect of the defect is seen as a semicircular low count area that corresponds mainly with the right ventricular cavity. The counts are also reduced in the septal wall.

Comments: The location of a uniformity defect in a SPECT myocardial perfusion image can introduce an apparent perfusion abnormality, even if the ring artefact is not clearly identified.

Reference: DE PUEY, E.G., How to detect and avoid myocardial perfusion SPECT artefacts, J. Nucl. Med. **35** (1994) 699–702.

3.2.4. Example: Refurbished SPECT system — phantom study using ^{201}Tl

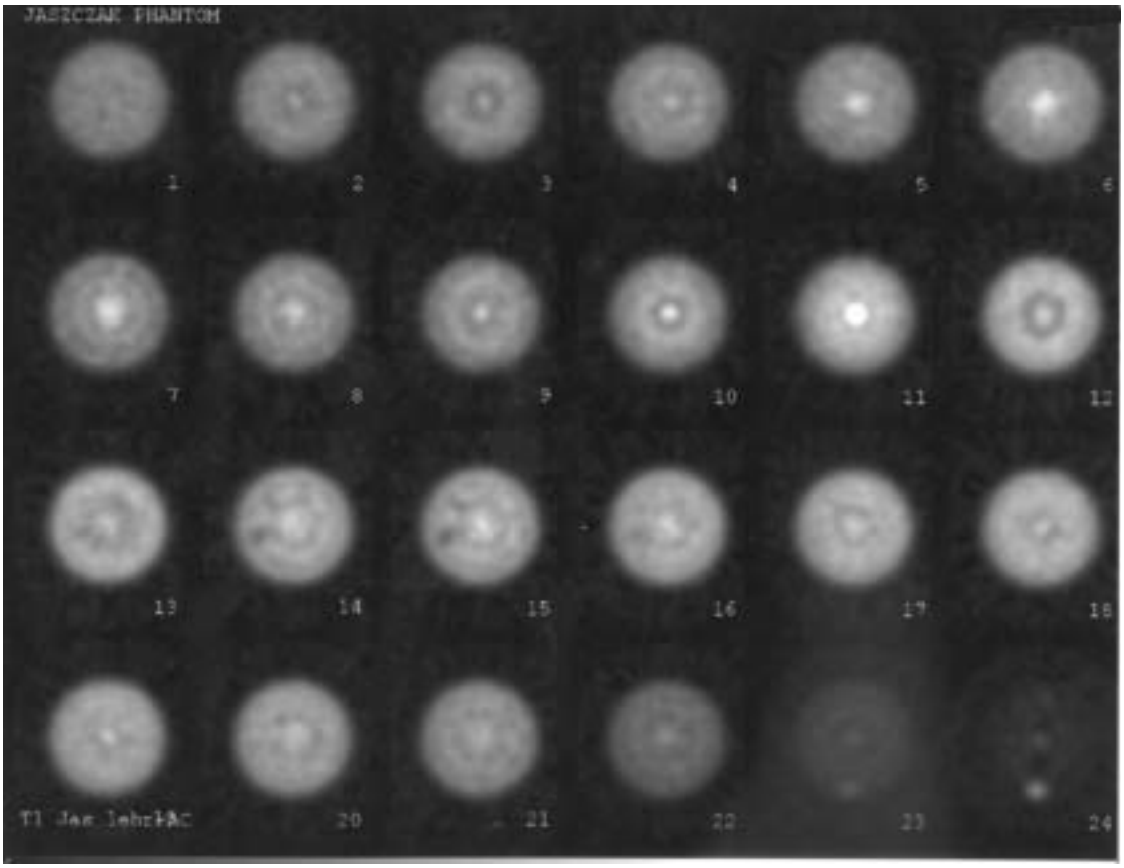

Single head refurbished SPECT system, Data Spectrum ECT phantom (Jaszczak phantom) containing ^{201}Tl.

Acquisition: 64 projections over 360º total angle of rotation, 200 000 counts in the first view, 64 × 64 matrix.

Reconstruction: FBP using a Hann filter and 1 Nyquist cut-off, with attenuation correction.

Images were obtained at acceptance testing.

Results: All but one of the transverse images had serious ring artefacts. Some images had an intense hot spot in the centre corresponding to the centre of rotation. The contrast was very poor. Several electronic circuit boards were replaced and a new ^{201}Tl uniformity correction map was acquired. A repeat study gave satisfactory images.

3.2.5. Example: Clinical study with ^{111}In, using a ^{99m}Tc uniformity correction map

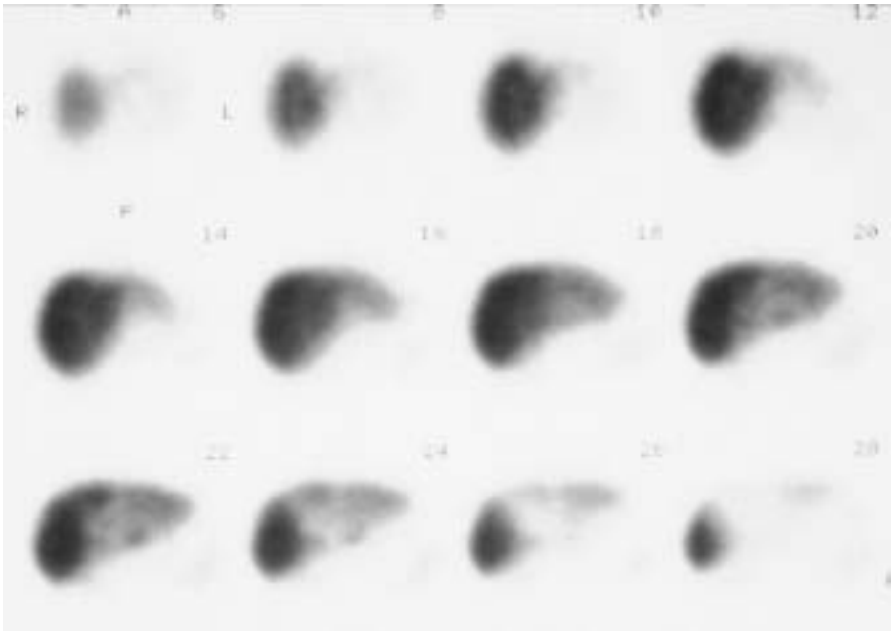

Single head SPECT system, monoclonal antibody liver SPECT study using an ^{111}In labelled radiopharmaceutical. Data acquisition took place using both photopeaks of ^{111}In (171 and 245 keV) but acquired data were corrected for non-uniformity using a high count ^{99m}Tc uniformity correction. Data were reconstructed by FBP into transverse slices.

Results: In the transverse slices (incomplete), ring artefacts are seen towards the right side, between the liver and spleen activity (lower two rows). These are due to non-uniformity remaining after the uniformity correction.

Comments: For most SPECT systems, a ^{99m}Tc uniformity correction cannot be used for ^{111}In. A uniformity correction map collected with ^{111}In must be used.

3.3. CENTRE OF ROTATION (COR) OFFSET (*x*)

3.3.1. Example: Simulations of a point source reconstructed with different COR offset errors

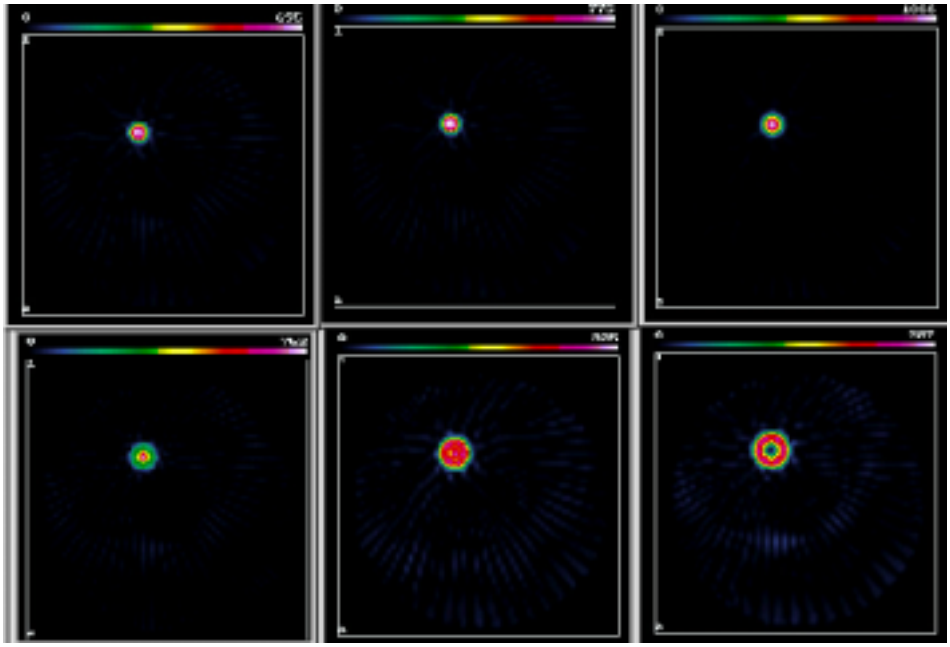

Simulated reconstruction of a point source with different COR errors. Acquisition: 37 cm FOV with 1.5 zoom, 64 × 64 matrix, 360° total angle of rotation, 64 projection angles, circular orbit. Reconstruction into transverse slices using a ramp filter and FBP. No correction was made for the COR offset error. Pixel size 3.85 mm.

TL: 0 pixel offset (perfect data).
TM: 0.25 pixel offset error.
TR: 0.5 pixel offset error.
BL: 1 pixel offset error.
BM: 1.5 pixel offset error.
BR: 2 pixel offset error.

Results: The image with no COR offset error (TL) shows the best possible image resolution for the point source. As the COR offset error is increased, the reconstructed spatial resolution increases (i.e. deteriorates) until finally the point source appears as a small ring.

Comments: The effect of a COR offset is a loss of reconstructed spatial resolution and contrast. A correction for an offset error must be made.

Note that in modern SPECT systems the acceptable limit for COR offset is ±1 mm, which here corresponds to about a 0.25 pixel offset.

3.3.2. Example: Simulations of a phantom reconstructed with different COR offset errors — no statistical noise

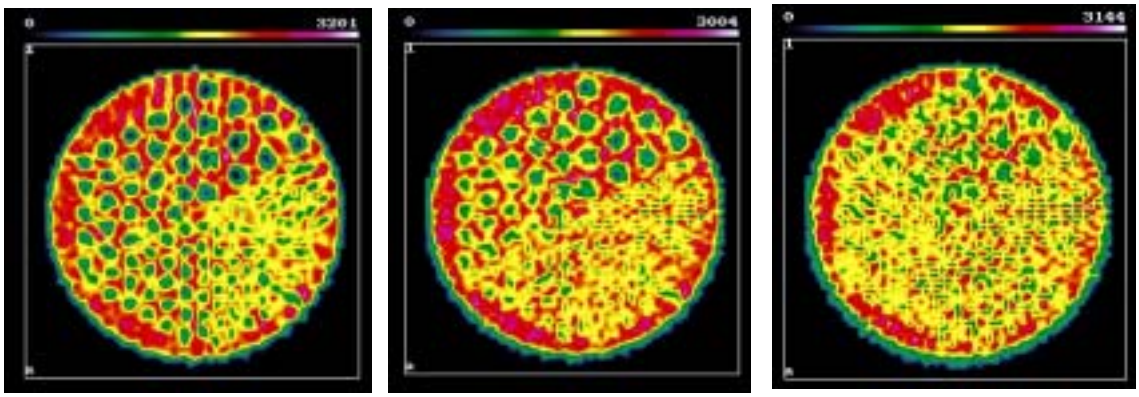

Simulations with different COR offsets of a reconstructed transverse slice through the rods of a Data Spectrum ECT phantom (Jaszczak phantom). Acquisition: No statistical noise, 37 cm FOV with 1.5 zoom, 64 × 64 matrix, 360º total angle of rotation, 64 projection angles. Reconstruction into transverse slices using a ramp filter and FBP, no attenuation correction. No correction was made for the COR offset error. Pixel size 3.85 mm.

L: 0 pixel offset (perfect data).
M: 0.25 pixel offset error.
R: 0.5 pixel offset error.

Results: The simulated transverse slice with 0 pixel offset error is the reference image. The image obtained with a 0.25 pixel offset error shows slight degradation. However, at 0.5 pixel offset error, considerable degradation is seen.

Comments: A COR offset error of 0.5 pixel already has an impact on the quality of the image. The offset error needs to be well below this value, or a COR offset correction must be made. Note that in modern SPECT systems the acceptable limit for COR offset is ±1 mm, which here corresponds to about 0.25 pixel offset.

3.3.3. Example: Point source — reconstruction with different COR offset errors (real data)

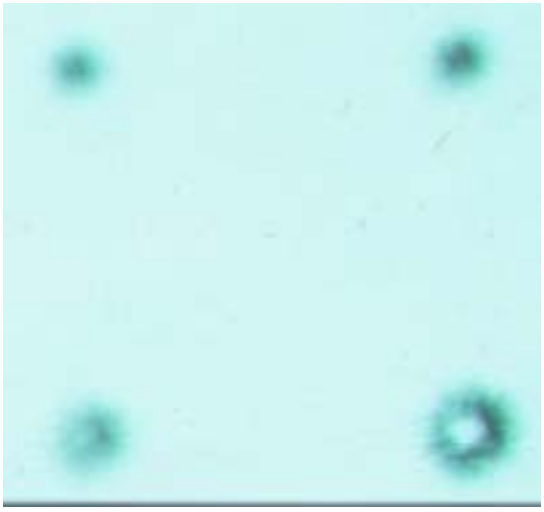

Single head SPECT system, point source of ^{99m}Tc acquired with 360° total angle of rotation. Reconstruction with different COR offsets. One transverse slice through the middle of the point source is shown for each COR offset.

TL: 0 pixel offset.
TR: 0.4 pixel offset.
BL: 1.4 pixel offset.
BR: 2.4 pixel offset.

Results: As the COR offset increases, the reconstructed point source image broadens to eventually become a ring. This means there is a loss of resolution and contrast. Any COR offset must be corrected.

Compare with the simulated data of example 3.3.1.

3.3.4. Example: Phantom reconstructed with and without COR offset error (real data)

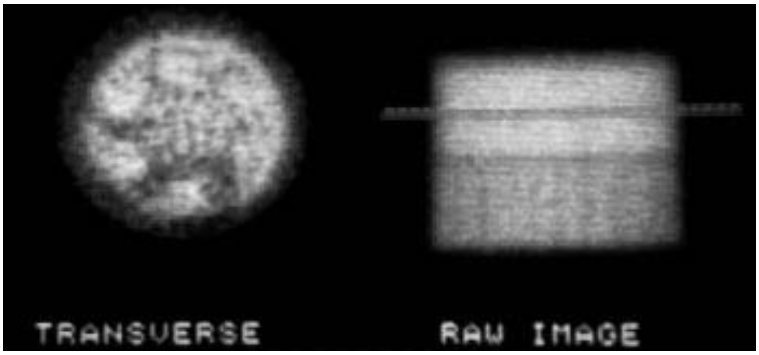

A

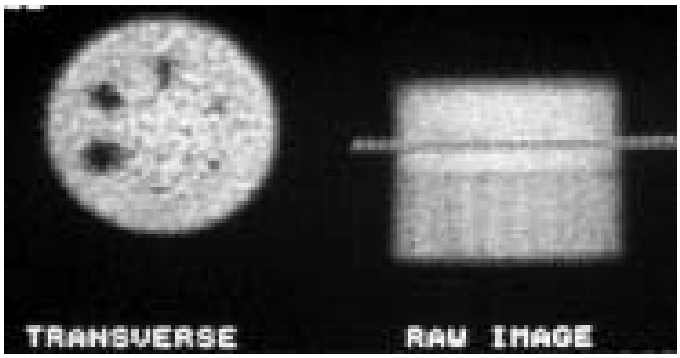

B

Single head SPECT system, Data Spectrum ECT phantom (Jaszczak phantom) imaged with and without COR offset correction where the offset was 3 pixels, 360° total angle of rotation. Reconstruction with FBP and a Hann filter. The left image in both A and B shows the transverse image (6 mm thick slice) at the level shown as a horizontal line on the raw image data (right images).

A: Uncorrected for a COR offset of 3 pixels.
B: Corrected for COR offset.

Results: The transverse slice in B shows acceptable resolution and contrast, whereas the transverse slice in A shows considerable loss of resolution and contrast due to the large COR offset.

Comments: It is easy to ascertain poor quality SPECT images of a known phantom, since the structure is known. In clinical images this becomes much more difficult, and degradation of images due to a COR offset can be overlooked. A regular QC check of the integrity of the COR offset calibration and correction is essential.

3.3.5. Example: Simulations of a point source acquired over 180º and reconstructed with different COR offset errors

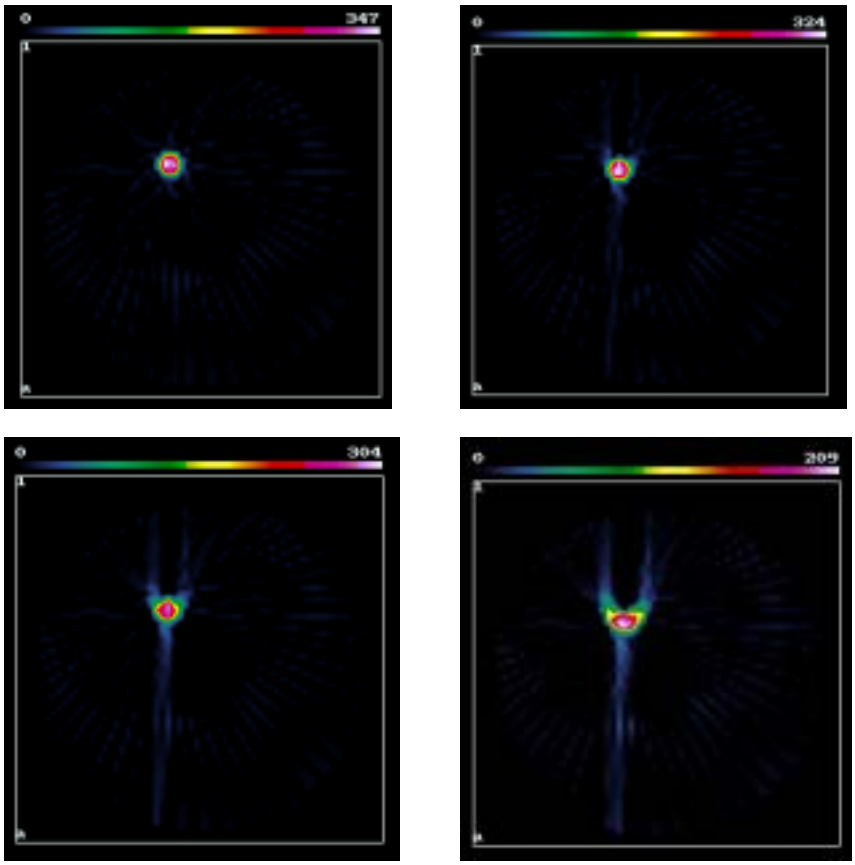

Simulations of a reconstructed image of a point source acquired with a 37 cm FOV with 1.5 zoom, 64 × 64 matrix, 180º angle of rotation, 32 projection angles. Reconstruction using a ramp filter and FBP. No correction for COR offset errors. Pixel size 3.85 mm.

TL: 0 pixel offset (perfect data).
TR: 0.5 pixel offset error.
BL: 1 pixel offset error.
BR: 2 pixel offset error.

Results: The image with no pixel offset error (TL) shows the best possible resolution for the point source when acquired with a 180° total angle of rotation. As the COR offset error is increased, the reconstructed spatial resolution increases (i.e. deteriorates). For a 0.5 pixel COR offset error, some preferential lines are seen from the FPB reconstruction. At 1 and 2 pixels COR offset error, the point source no longer looks like a point but rather like a tuning fork.

3.3.6. Example: Reconstruction of a line source acquired over 180º and reconstructed with different COR offset errors (real data)

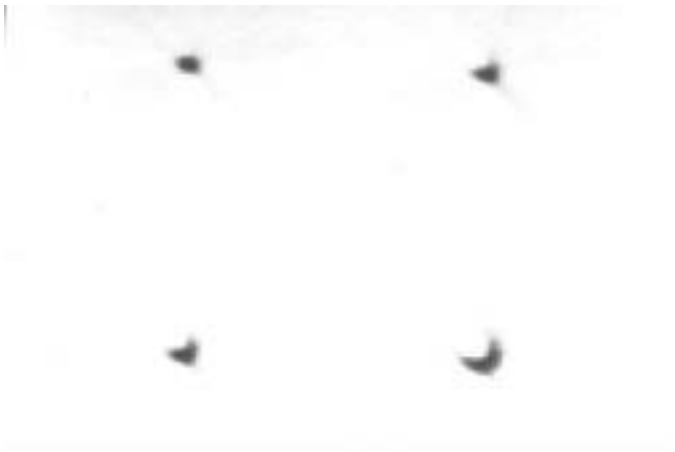

Magnified line source images (128 × 128 matrix, 120 projections over 180° rotation) were reconstructed with different COR offset errors using a ramp filter and FBP. A single transverse slice through the line source is shown with:

TL: 0 pixel offset.
TR: 0.5 pixel offset.
BL: 1 pixel offset.
BR: 2.5 pixel offset.

Results: A reconstructed line source image without a COR calibration error is symmetric and generally has a Gaussian profile (TL). Some distortion was visible when a 0.5 pixel error was present (TR), and 1.0 pixel errors produced more distortion (BL). A 2.5 pixel error produced a tuning fork artefact (BR).

Comments: COR errors greater than 0.5 pixel produce a significant loss of spatial resolution. Very large errors dramatically distort clinical images.

3.3.7. Example: COR calibration analysis

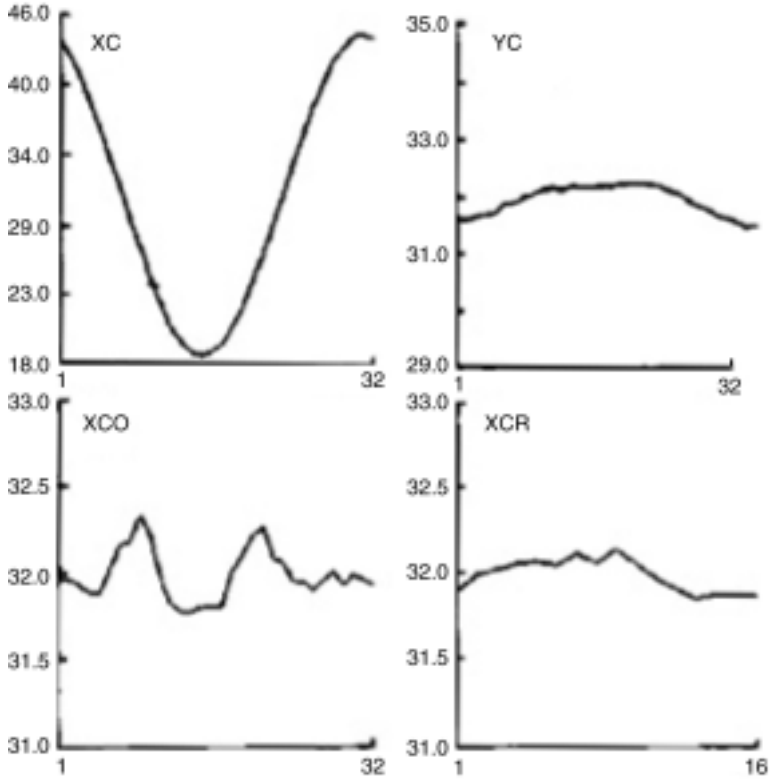

A point source of ^{99m}Tc was used to acquire data for the COR calibration. 64 × 64 matrix, 32 projections, 360º total angle of rotation. The manufacturer's software produced four graphs with measurement results and calibration data.

TL: Angular *x* position sinogram of the calibration point source.
BL: Angular position difference between the sinogram and a fitted sine wave.
TR: Angular *y* position of the point.
BR: Angular variation of the COR value.

Results: In the ideal situation, the calibration point source should follow a perfect sine wave in *x* and a straight line in *y* during rotation of the detector.

In this example, the upper left graph gives the measured sinogram, or angular position of the point source in *x* during rotation. The lower left graph gives the difference between the measured and the perfect sinogram. The lower right graph shows the COR variation with angle. The upper right graph shows that the detector is tilted relative to the axis of rotation. These data indicate that the detector is not properly aligned with the axis of rotation at some angular positions.

Comments: Each manufacturer has its own method of acquiring and analysing the COR offset. The method prescribed should be followed. Users should carefully review the data analysis associated with COR calibrations, and should be especially aware of the values of the axes and of the fact that the parameters on the axes may not be clearly defined or labelled.

3.3.8. Example: Clinical study with large COR offset error

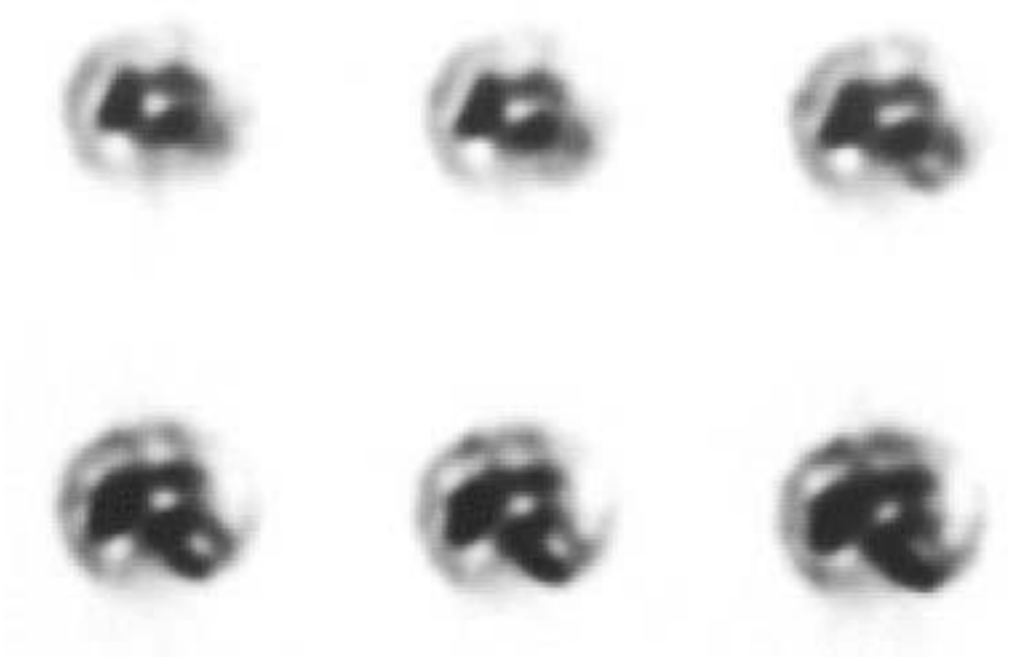

Clinical SPECT transaxial images of the liver using ^{99m}Tc sulphur colloid. The camera had just been installed and the COR calibration had not been done correctly.

Results: Because the COR calibration was done incorrectly, there was a very large COR error. The images were so distorted that the organ could not be recognized.

Comments: When acceptance tests are performed on a new system, tomography should be performed with a line or point source and the images reconstructed with a ramp filter. The spatial resolution (FWHM) in the tomographic images should be compared with a planar image at the same distance as the average radius of rotation. The loss of resolution in tomographic studies should not exceed 10%.

3.3.9. Example: Clinical brain blood flow SPECT –effect of different COR offsets

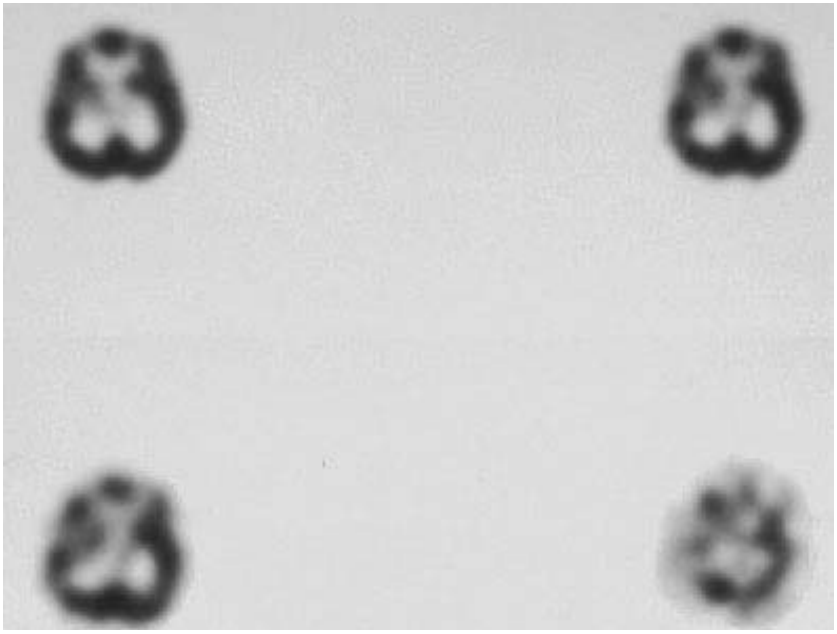

Single head SPECT system, normal ^{123}I IMP brain perfusion SPECT study, 360° total angle of rotation, 64 × 64 matrix. Data were collected and reconstructed by FBP into a single reconstructed transverse slice with four different COR offsets.

TL: 0 pixel offset.
TR: 0.5 pixel offset.
BL: 1.0 pixel offset.
BR: 2.5 pixel offset.

Results: As the COR offset increases, the images become more blurred and distorted. One can easily recognize poor quality in the fourth image (BR), but in routine practice the second and third images made with COR offsets of 0.5 and 1.0 pixel could mistakenly be passed as acceptable (since no comparable data are available).

Comments: Determining the optimum image quality possible in clinical SPECT images is difficult. Degradation of images due to a COR offset can be overlooked. A regular QC check of the integrity of the COR offset calibration and correction is essential.

3.3.10. Example: Dual head system — line source — incorrect COR in one head

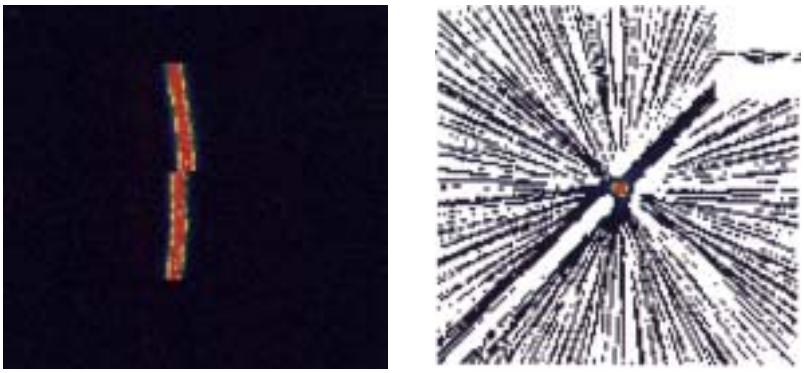

A

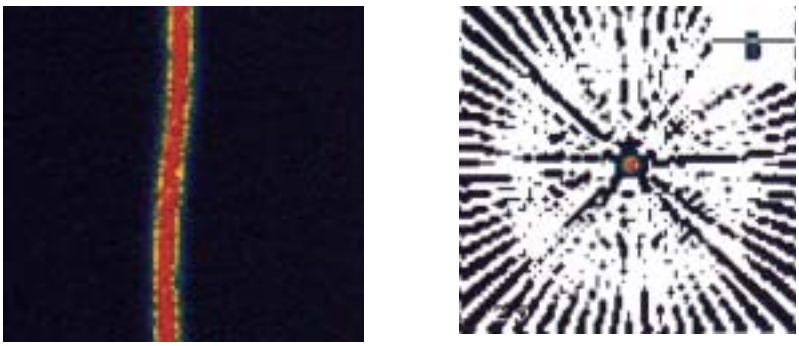

B

In both A and B, a line source was approximately centred between the two heads of a dual head SPECT system with the heads in a configuration of 180º. Data acquisition was made with each head rotated 180º for 360º total rotation, 128 × 128 matrix. Filtered back-projection reconstruction using a ramp filter.

For A, the data were acquired with a COR offset correction that was invalid for one detector, but this was unknown at the time of the study.

TL: Sinogram for one row of pixels through the raw data of the line source.
TR: One reconstructed transverse slice through the line source.

For B, a new COR calibration was performed and the test repeated.

BL: Sinogram for one row of pixels of the raw data.
BR: One reconstructed transverse slice through the line source.

Results: In both sinograms (TL and BL), the lower half of the sinogram is from one detector head and the upper half from the other. In A, the sinogram shows a distinct discontinuity between the two halves of the study, indicating that the COR correction is not valid. The reconstructed transverse slice (TR) shows some distortion and the classic tuning fork artefact. The rays projected by the FBP reconstruction technique are not uniform and show preferential distortion.

After recalibration of the COR, the reconstructed transverse slice (BR) shows a point source without distortion, and the rays projected by the FBP reconstruction are uniform and evenly spaced.

Comments: Data that have been corrected for COR offset should show no discontinuity in the sinogram obtained from multiple heads. Also, the reconstructed line source should show regular rays at regular angular intervals. In order to see the rays, it may be necessary to lower the upper threshold of the display. The lower threshold must be set at zero.

This test of a line source (or point source) is sensitive for checking the COR offset calibration of the system.

3.3.11. Example: COR offset — dual head SPECT — myocardial perfusion study

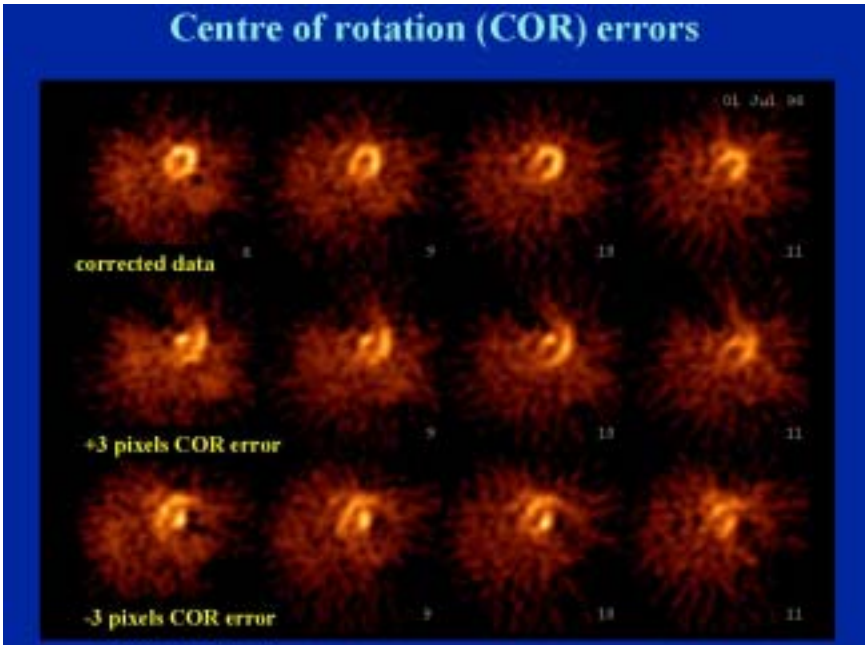

Myocardial perfusion patient study. Dual head SPECT system, detectors in 90° configuration, total angle of rotation 180°. Reconstructed transverse slices of the myocardium. COR offsets were simulated by shifting the images by ±3 pixels.

Top row: COR offset has been corrected.
Middle row: +3 pixel COR offset of both detector heads.
Bottom row: –3 pixel COR offset of both detector heads.

Results: The transverse slices with no COR offset (i.e. with a COR correction applied) show a uniform horseshoe shaped myocardium. The middle row with the +3 pixel offset shows a pair of opposite perfusion defects, an apparent hot spot in the septal region and flaring from the anterior wall. When the pixel offset is –3 pixels, the effect appears to reverse, with the hot spot located in the lateral wall. These effects occur because of local smoothing of every point in a circular direction, as illustrated below.

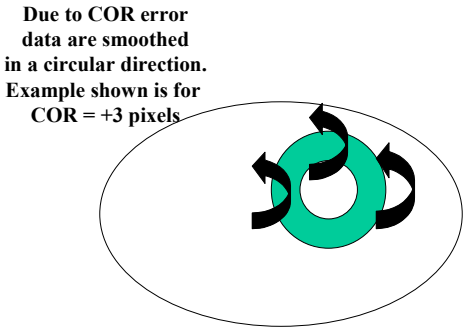

3.4. IMAGE ALIGNMENT IN *y* FOR MULTIHEAD SPECT SYSTEMS

General comments

Data acquisition with a dual head SPECT system is most often performed such that one detector collects data from one half of the angle of rotation and the other detector collects data from the other half, and the full data set is a concatenation of these two halves. Similarly, for a triple head SPECT system, each detector collects a third of the data, and these data are concatenated to form the full acquisition data set.

Using more than one detector head means that, in addition to the COR, there are stringent requirements for the image alignment and image size in the *y* direction (parallel with the axis of rotation) between the detectors.

The manufacturer's COR and multiple head image registration calibration methods should always be carefully followed. In addition, simple tests using point sources can be carried out to test the image alignment and image size.

3.4.1. Example: Dual head SPECT system — misalignment in *y*

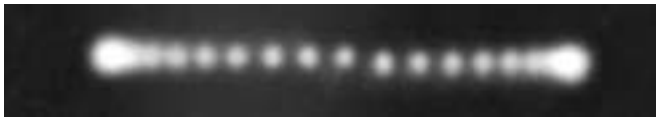

Dual head SPECT system, detectors in 90º configuration, LEHR collimators, 128 × 128 matrix, total angle of rotation 180º, each detector rotating 90º, 16 images total. A point source of ^{99m}Tc was placed off-axis, and a SPECT acquisition was made with a total of 16 images (8 images per head). The raw data were summed to form one image.

Results: The summed image shows discontinuity of the point source data between detector 1 (left half of the series of point sources) and detector 2 (right half of the series of point sources).

Comments: A SPECT acquisition of a point source placed considerably off-axis, with subsequent summation of the raw data, is a sensitive test to check both head registration and detector head tilt. The summed point source images should all lie along a horizontal line with no jump in data either above or below this line between one detector and the other(s).

3.4.2. Example: Dual head SPECT — image misalignment in *y* — point source sinograms

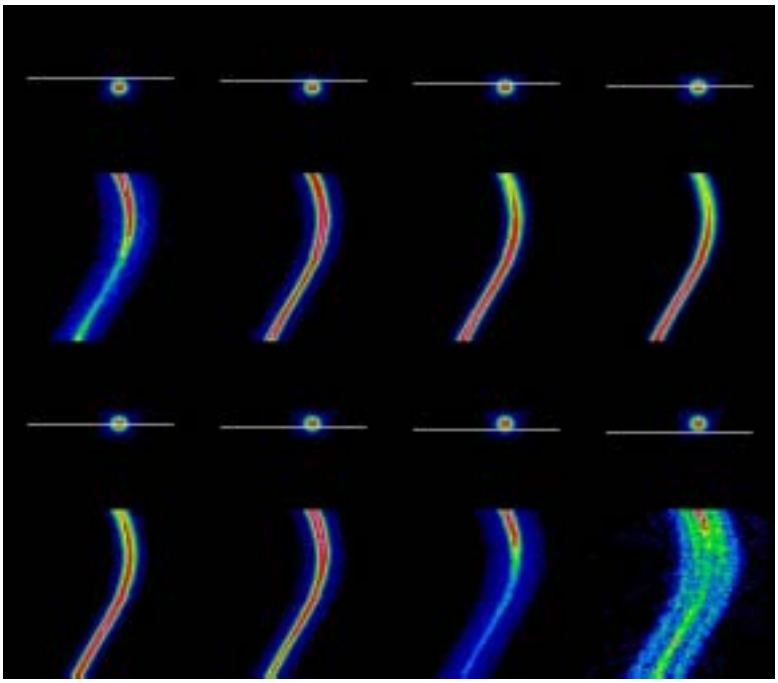

Dual head SPECT system, detectors in a 90° configuration, LEHR collimators, ^{99m}Tc, 15% energy window, 128 × 128 matrix, total angle of rotation 180°, each detector rotating 90°, with a radius of rotation of 25 cm. A point source of ^{99m}Tc was suspended in air at 10 cm off-axis. Eight sinograms of the raw data are shown for eight values of *y* passing through the point source. The level of the sinogram is shown by the profile through the point source above each sinogram.

Results: The lower half of the sinogram is from detector 1, the upper half from detector 2. In this example, the activity in the lower half appears later and disappears earlier, indicating a misalignment of the concatenated data from the two detectors. Thus detector 1 appears to have a slightly smaller FOV than detector 2.

The expected sinograms should show lines of continuous uniform activity along their total length, indicating proper alignment (registration) and FOV in *y* for both detectors.

Comments: Inspection of all the data through a point source by means of sinograms at *y* levels passing through the point source is a sensitive method of assessing head registration. These data were obtained using the collimators of example 2.3.2.1. In this example, the differences in the collimator hole angulation produced the discrepancy in FOV between data from head 1 and from head 2, and not the image gain of the detectors.

3.4.3. Example: Triple head SPECT — image misalignment in *y* — sinogram

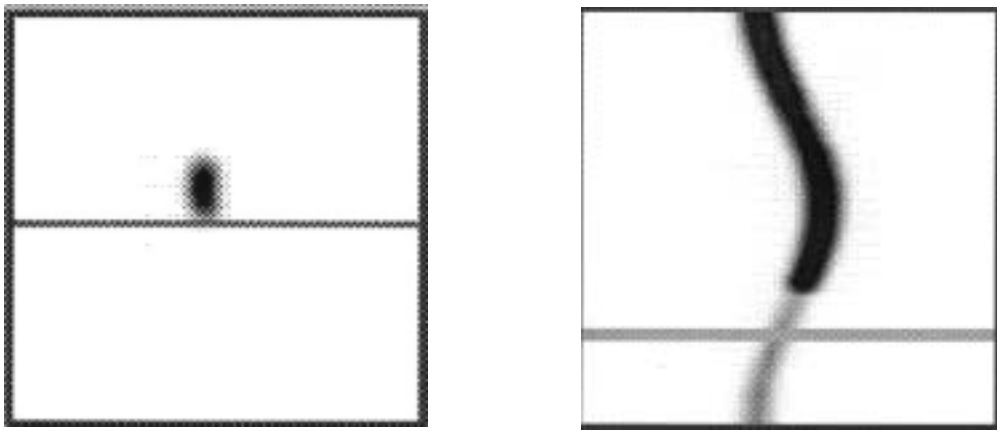

Triple head SPECT system, detector heads in a triangular configuration, ^{123}I, 15% energy window, medium energy collimators, 64 × 64 matrix, total angle of rotation 360°, 60 projections in total, each detector head acquiring 20 projections (each detector rotating through 120° total angle of rotation). A 20 mL plastic bottle containing ^{123}I solution was placed on the headrest attachment of the patient pallet.

L: One image from the raw data set. The profile marks the *y* position of the sinogram shown on the right.
R: Sinogram from 360º angle of rotation. The lower third of the sinogram is from detector 1, the middle third from detector 2 and the upper third from detector 3. The profile marks the position of the raw projection image shown on the left.

Results: The review of the raw acquisition data by means of a cine showed a downward jump in the images when the data changed between detector 1 and detectors 2 and 3. The sinogram of the study shown on the right confirms this effect. It was obtained at a *y* value at the lower edge of the bottle as viewed by detector 1 (as indicated in the left projection image). The sinogram is built up with the first-third projection data from detector 1, second-third projection data from detector 2 and last-third projection data from detector 3. The discontinuity in activity in the sinogram indicated that detector 1 images the bottle at a different *y* level from the other two detectors; hence there is a misalignment in *y* between detector 1 and the other detectors. This was caused by an error at calibration of the COR and head registration. After recalibration the problem disappeared.

Comments: A QC check after collection of calibration data is an essential task to determine that the calibration, which will be applied to subsequent clinical data, is correct. In this example, the problem of misalignment was first discovered in a clinical study. The reason for the misalignment was never clarified, and the problem occurred only once.

3.4.4. Example: Triple head SPECT — image offset and misalignment in *x* and *y* — point source

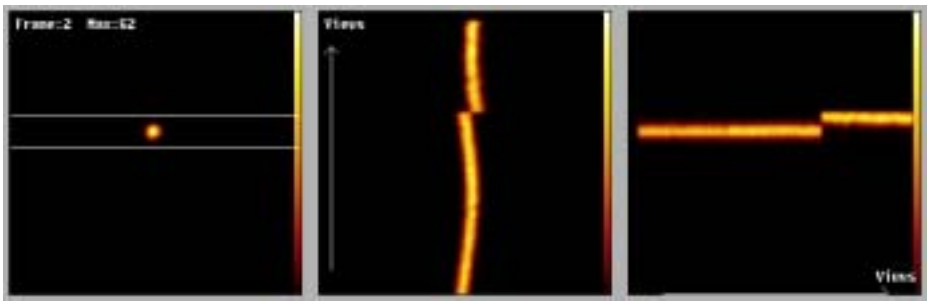

A raw image sinogram — *x* compressed image — *y*

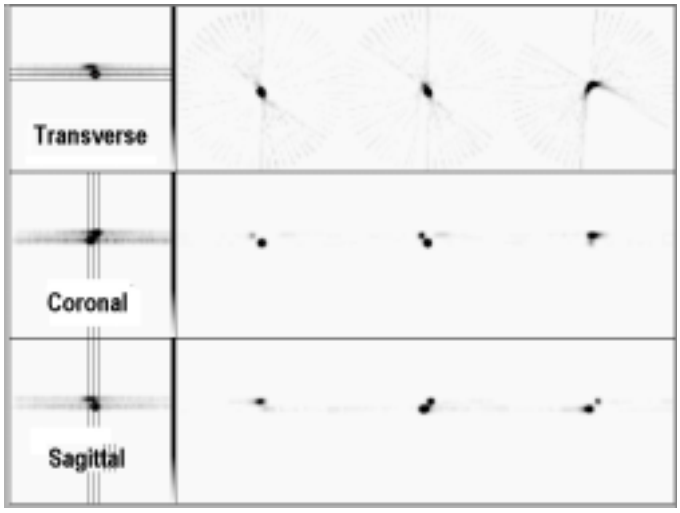

B reconstructed images

Triple head SPECT system, detector heads in a triangular configuration, LEHR collimators, point source of ^{99m}Tc suspended in air between the detectors, 64 × 64 matrix, 360º total angle of rotation, each detector rotating through 120º, 60 projections, 20 from each detector.

A: Top set of images

L: One image from the raw data with a wide profile encompassing the point source.
M: Sinogram from the profile (data in *x*). The bottom two thirds of the sinogram is from detector heads 1 and 2, the top third from detector head 3.
R: Compressed image (data in *y*, comparable to the sinogram). The first two thirds of the line is from detector heads 1 and 2, the last third from detector head 3.

B: Bottom set of images

Three images of the reconstructed point source in transverse, coronal and sagittal views. The levels of the images are shown in the image overviews on the left side.

Results: Both the sinogram and the compressed images (A) show a discontinuity between detector head 2 and detector head 3 indicating a serious misalignment between the heads and a severe offset in both *x* and *y* of detector head 3. The reconstructed images show the creation of a double source and deformation of the point source in the transverse images. Recalibration of the COR and head alignment solved the problem.

Recalibration:

Persistence mode

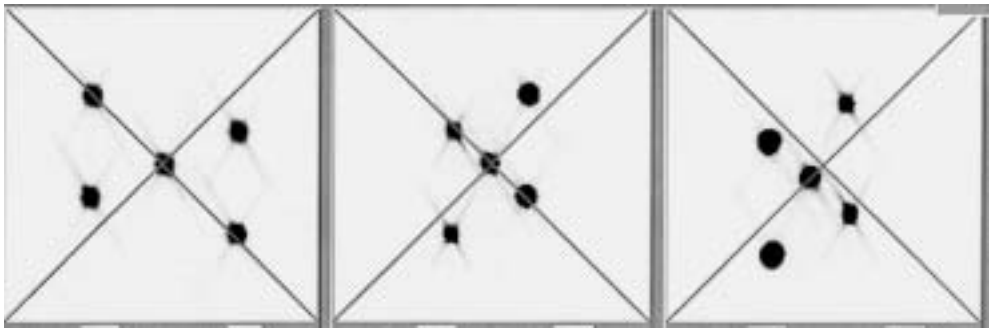

Detector 1 at 0º Detector 2 at 120º Detector 3 at 240º

A recalibration of COR and head alignment was performed using five point sources placed in a special jig supplied by the manufacturer. The persistence mode images taken during set-up, i.e. before the recalibration started, are shown.

L: Head 1 at 0º, detector parallel with the plane of the point sources.
M: Head 2 at 120º.
R: Head 3 at 240º.

A diagonal cross was drawn on the images in order to simplify the positioning of the sources prior to starting the calibration data acquisition.

Results: Detectors 1 and 2 show the middle point source at the interception of the diagonal lines, and three point sources intercepting the diagonal line going from top left to bottom right. Detector 3 should also show this image. However, detector 3 clearly shows the offset of the point sources in both *x* and *y* before recalibration.

3.4.5. Example: Reconstructed phantom images from a dual head SPECT system

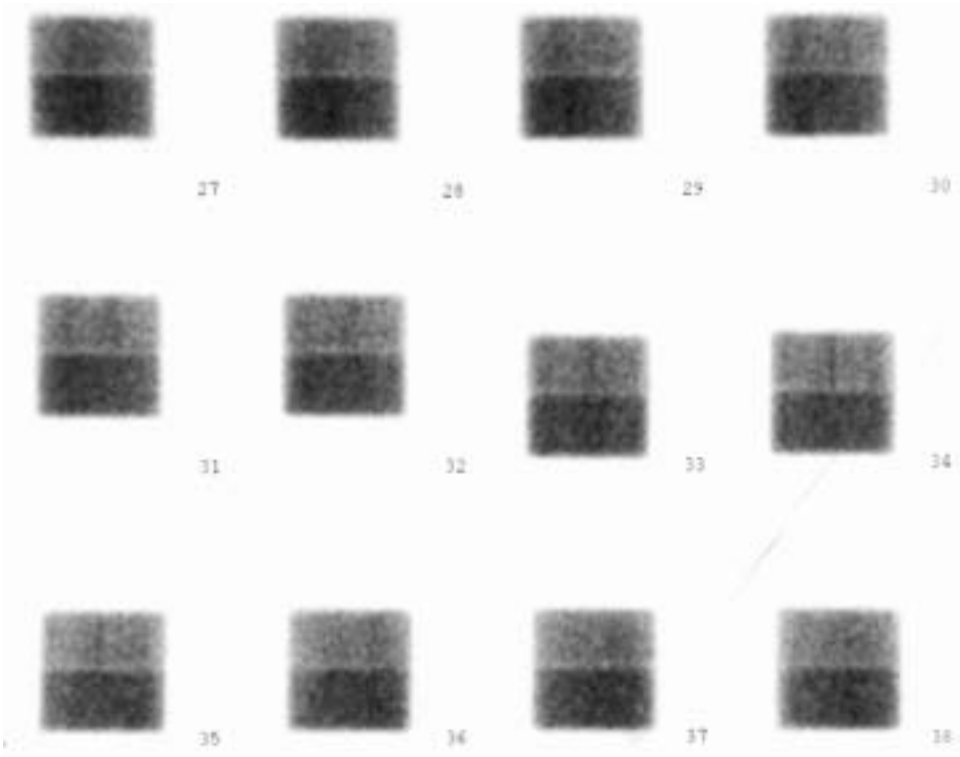

A: projection images

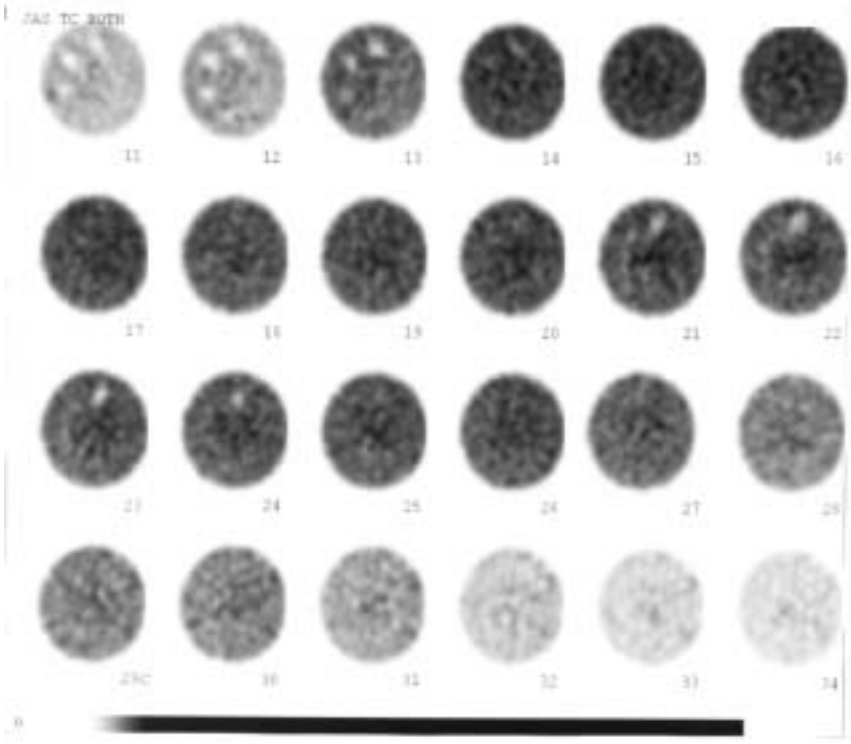

B: reconstructed transverse slices

Data were acquired using 500 000 counts (first view) on a dual head SPECT system using a 64×64 matrix with a total of 64 projections. Data from the first 32 projections were from head 1 and data from the second 32 projections were from head 2. Images were magnified using a zoom of 1.46. Reconstruction was performed with a Hann filter using a 1.0 Nyquist cut-off and attenuation correction (Chang method). Data Spectrum ECT phantom (Jaszczak phantom).

A: 12 projection images (images 27 to 38). Images up to 32 were from head 1 and images from 33 to 38 were from head 2.
B: Reconstructed transverse images.

Results: The raw data showed a dramatic vertical downward shift of the phantom image between frames 32 and 33 (image 32 is from detector 1, image 33 from detector 2). The reconstructed transverse images show some of the cold spheres in the phantom in two different groups of reconstructed images: transverse slices 11–14 (top row) and 21–24 (second and third rows).

Comments: The acquisition was repeated after reinstallation of the software. The projection data and reconstructed images were then satisfactory.

3.5. DETECTOR HEAD TILT

General comments

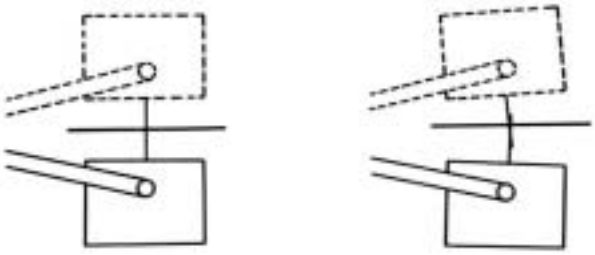

Head tilt can be caused by the detector head(s) not being parallel with the axis of rotation but can also be a problem of misalignment of the parallel holes of a collimator. The schematic diagram on the left shows 180° opposing projections with no head tilt; the image on the right shows the same projections with tilt.

Simple QC test of head tilt

A simple test to check detector head tilt is to place a radioactive point source off-axis, acquire a SPECT study and then add all the projection images. In the summed image, all point images should lie along one *y* value and form a horizontal line. If there is head tilt or collimator hole angulation, an ellipse will be formed. This test is also sensitive to mechanical movement problems as the detector heads rotate.

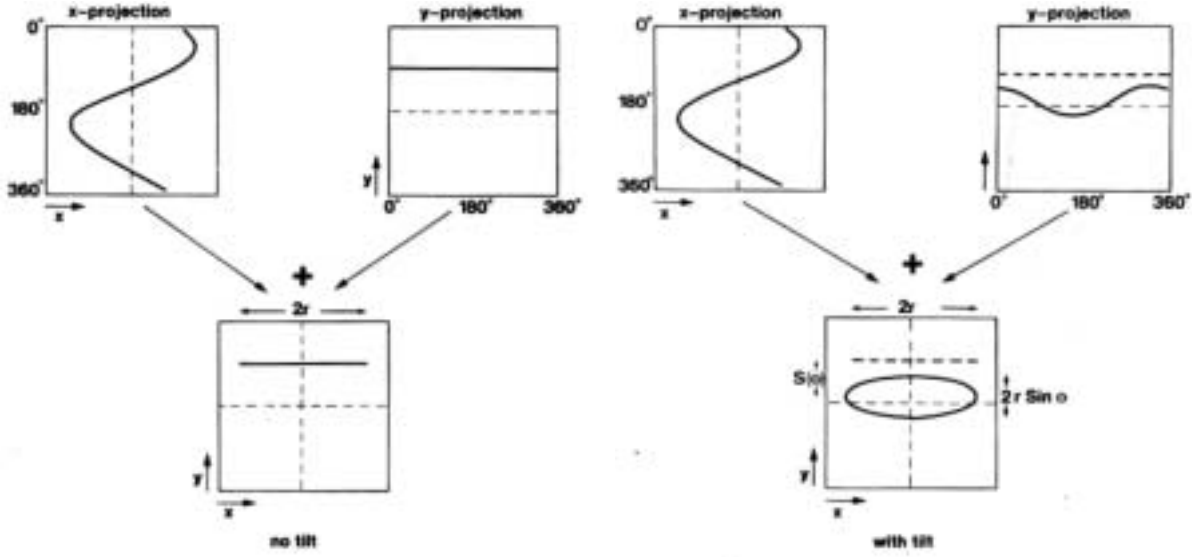

Reference: BUSEMANN SOKOLE, E., Measurement of collimator hole angulation and camera head tilt for slant and parallel hole collimators used in SPECT, J. Nucl. Med. **28 (**1987) 1592–1598.

3.5.1. Example: Head tilt — offset point source — good result

One projection image | Sinogram | Summed projection images

Triple head SPECT system, LEHR collimators, detector heads in a triangular configuration, ^{99m}Tc, 15% energy window, 64 × 64 matrix, total angle of rotation 360°, each detector rotating through 120°, point source placed at about 13 cm off-centre from the axis of rotation.

L: One projection image of the point source.
M: Sinogram of the point source at the *y* level shown by the profile through the middle of the point source image shown on the left.
R: Sum of all projection images, with a line profile drawn through the resulting image.

Results: The left and middle images show that the point source is positioned at the edge of the FOV. The change in count density within the sinogram is a result of the varying distance of the off-axis point source from the collimator during rotation. The image of the summed projection data (right) shows that all data lie along the same *y* value and that there is no head tilt or misalignment between detector heads.

3.5.2. Example: Head tilt — offset point source — comparison of increasing head tilt

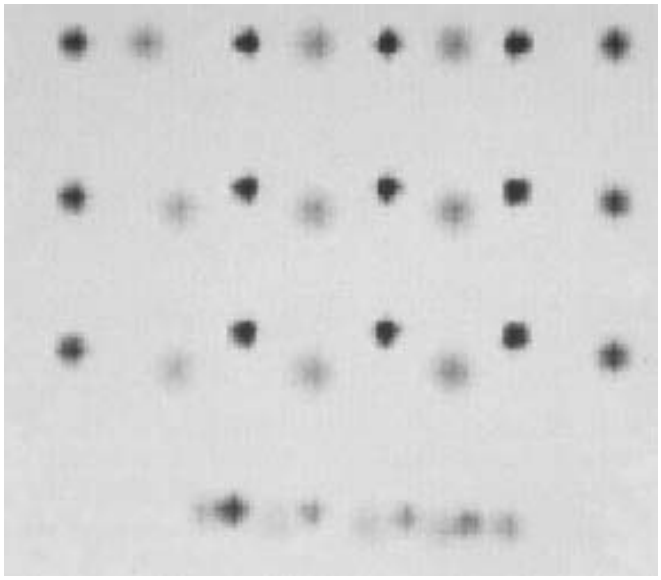

Single head SPECT system, LEHR collimator, ^{99m}Tc, 15% energy window, 64 × 64 matrix, 360° total angle of rotation, point source placed off-axis. Data were acquired with:

Top row: No head tilt.
Second row: 2° head tilt.
Third row: 4° head tilt.
Fourth row: About 2º tilt with gantry flexing.

Instead of summing all images of the projection data, only eight projections were summed for each data set for 45º incremental angles.

Results: The point source images with no head tilt (top row) lie in a straight line along one *y* value. With increasing head tilt, the point sources describe an ellipse with increasing minor axis value. The point source image intensity depends on the distance of the source from the collimator.

The bottom row shows the point sources sloping downwards, i.e. not along the same *y* value, indicating that the whole gantry mechanism was changing position (flexing) during rotation.

For more information on assessment of detector head tilt, see BUSEMANN SOKOLE, E., Measurement of collimator hole and angulation and camera head tilt for slant and parallel hole collimators used in SPECT, J. Nucl. Med. **28** (1987) 1592–1598.

3.5.3. Example: Myocardial perfusion study obtained with no head tilt and with 2.5º head tilt

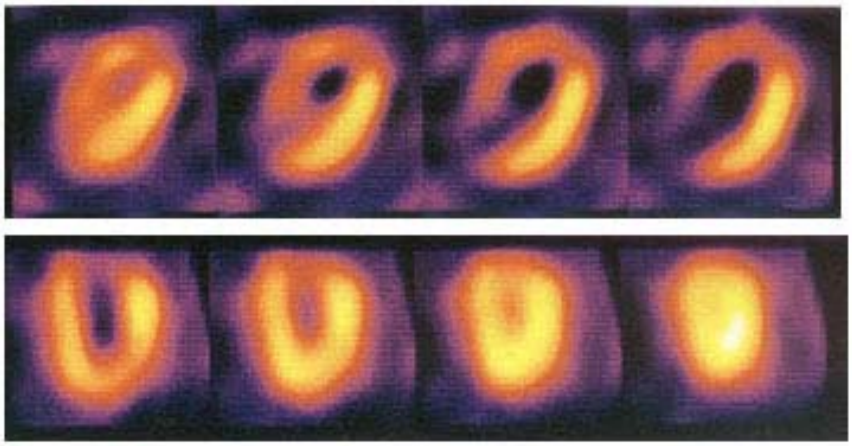

No head tilt (upper: transverse; lower: oblique sagittal)

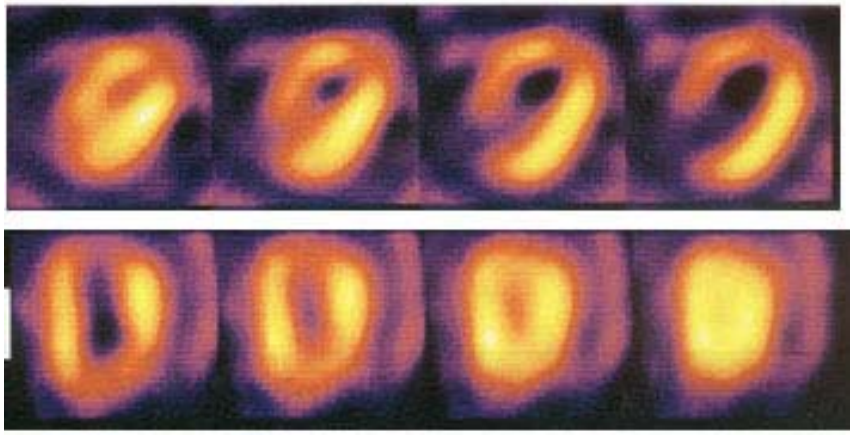

With 2.5° head tilt (upper: transverse; lower: oblique sagittal)

Clinical ^{99m}Tc myocardial perfusion SPECT study obtained with a single head SPECT system, high resolution collimator, 180º total angle of rotation. The patient had one-vessel coronary artery disease with 85% narrowing of the left anterior descending (LAD) coronary artery.

Top two rows: No head tilt
Bottom two rows: With 2.5º head tilt.

For each set of images:

Upper row: Transverse slices.
Lower row: Oblique sagittal slices.

Results: The images obtained with 2.5º head tilt, when compared with the images obtained without any head tilt, show a larger area of decreased activity, particularly in the apical region.

3.5.4. Example: Clinical SPECT study — collimator hole angulation

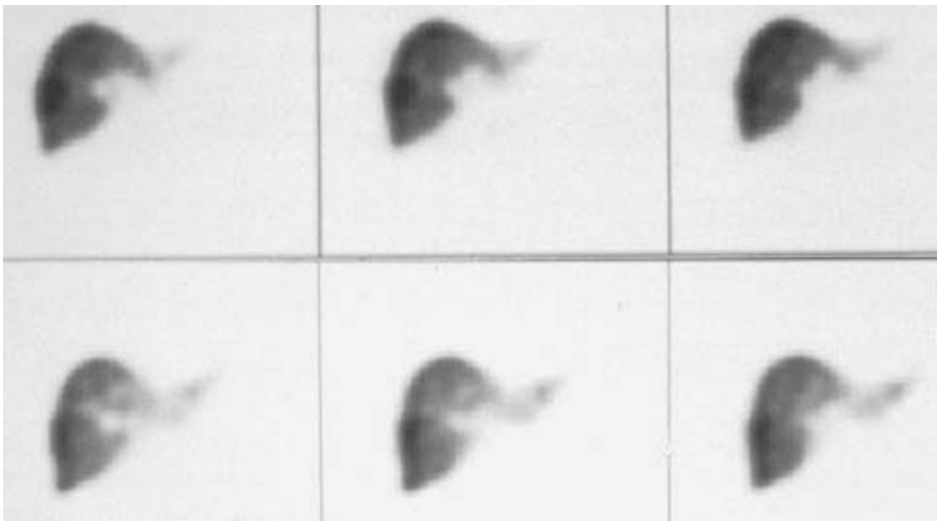

Transaxial slices from a clinical SPECT study of the liver.

Top row: Images obtained with a low energy, high resolution collimator that has significant hole angulation.
Bottom row: Images from the same patient obtained with a new, replacement collimator that has acceptable hole angulation.

Results: The images obtained with the satisfactory collimator (bottom row), as compared with those obtained with the collimator with significant hole angulation errors (top row), show considerably improved spatial resolution in the transverse slices. This is demonstrated by the central defects due to the biliary structure, and arterial and venous vessels.

Comments: Because the images show different structures, different diagnoses could be possible. Therefore a check of the collimator hole angulation is essential.

3.6. MULTIHEAD SYSTEMS — OTHER PROBLEMS

3.6.1. Example: Triple head SPECT — electronic fault of image data in one head

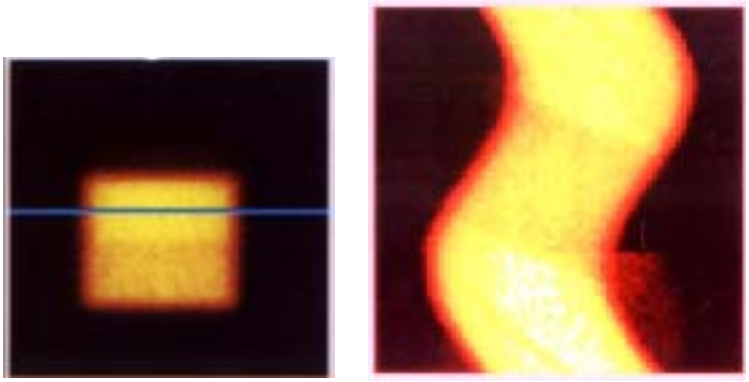

A: phantom one projection image sinogram

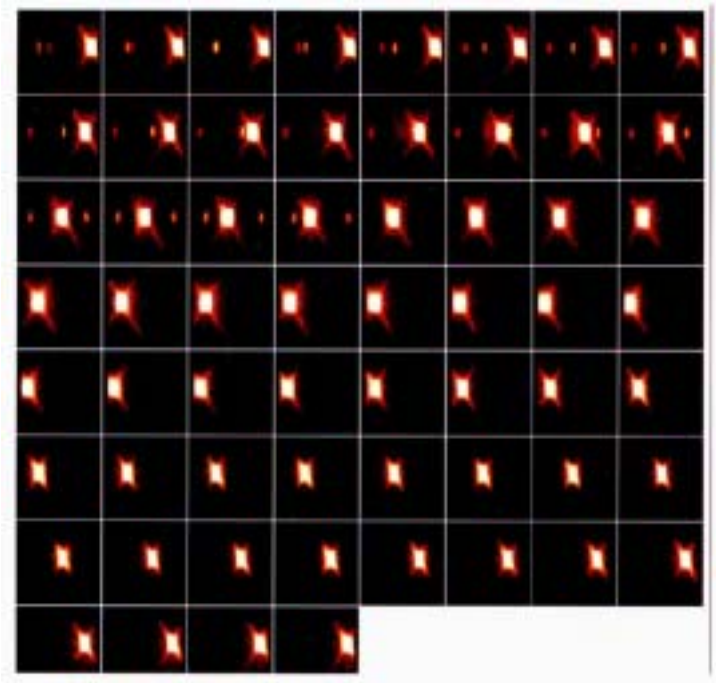

B: small bottle 60 projection images

detector 1 at 0º detector 2 at 120º detector 3 at 240º

C: small bottle persistence mode

Triple head SPECT system, LEHR collimators, detector heads in a triangular configuration, ^{99m}Tc, 15% energy window, 64 × 64 matrix, total angle of rotation 360°, each detector rotating through 120°.

A: These images are from a cylindrical phantom placed on the patient pallet. The right image is a sinogram of the projection data at the level shown in the projection image (left). The sinogram is built up of the bottom third projection data from detector 1, the middle third projection data from detector 2 and the top third projection data from detector 3. Notice the 'shadow' of counts to the right of the actual phantom in the bottom third of the sinogram.

B: SPECT projection images (total of 60) from the small bottle shown in persistence mode in C. Reading from left to right starting at the top row: images 1–20 are from head 1, images 21–40 from head 2 and images 41–60 from head 3.

C: In order to investigate this further, a small bottle filled with ^{99m}Tc was placed off-axis and a SPECT data acquisition was made. Persistence mode images from each detector head prior to data acquisition:

L: Image from detector 1.
M: Image from detector 2.
R: Image from detector 3.

Results: In the sinogram of the cylindrical phantom (A), low intensity (ghost) counts are seen outside and to the right of the actual phantom data, but only in the bottom third of the sinogram corresponding to acquisition data from detector 1. (The lower count intensity in the middle of the sinogram is due to absorption from the patient pallet.)

The test to investigate this problem used a small bottle placed off-axis. The persistence mode image made to check the set-up prior to data acquisition shows the intense image in the off-centred bottle, and on each side faint ghost images from the bottle in the same locations as the images of detectors 2 and 3.

In the projection data of the off-axis bottle (C), all of the first 20 images from detector 1 show these additional ghost images of the bottle from the other detectors.

The reason for these artefacts in the images from detector 1 was interference of counts from the images of the other two heads, each acquiring data at an angle of 120º to detector 1. The actual intensity of the interfering counts was very low, and for this reason the ghost images were only discovered when imaging a hot source positioned considerably off-axis and by increasing the image contrast.

Comments: It took a long time to discover the cause of the ghost counts in the sinogram of the cylindrical phantom. Clinically it was impossible to identify these effects, as was also the case in routine QC tests. It was only when a much higher amount of activity was accidentally used (MBq being supplied instead of the requested μCi!) and the test measurement was made with the source placed considerably off-axis that the problem became clear. It was caused by a problem in the multiplexer, an electronic component that handles the signals from single heads, and that in this case was malfunctioning. Once identified, the problem was soon rectified.

Detector head 1 of this SPECT system had also exhibited a puzzling higher count rate when high count rate tests were performed during acceptance testing, when all heads were activated. This was not initially linked with the problem described above. However, the two situations were caused by the same problem: a small fraction of the image counts of heads 2 and 3 were being superimposed on the image of head 1.

This example emphasizes the need to follow up all strange patterns and test results seen, and to occasionally use off-centred sources in performing SPECT QC.

3.7. DATA ACQUISITION AND RECONSTRUCTION

3.7.1. Example: Simulation of an ECT phantom reconstructed with an incomplete number of projections

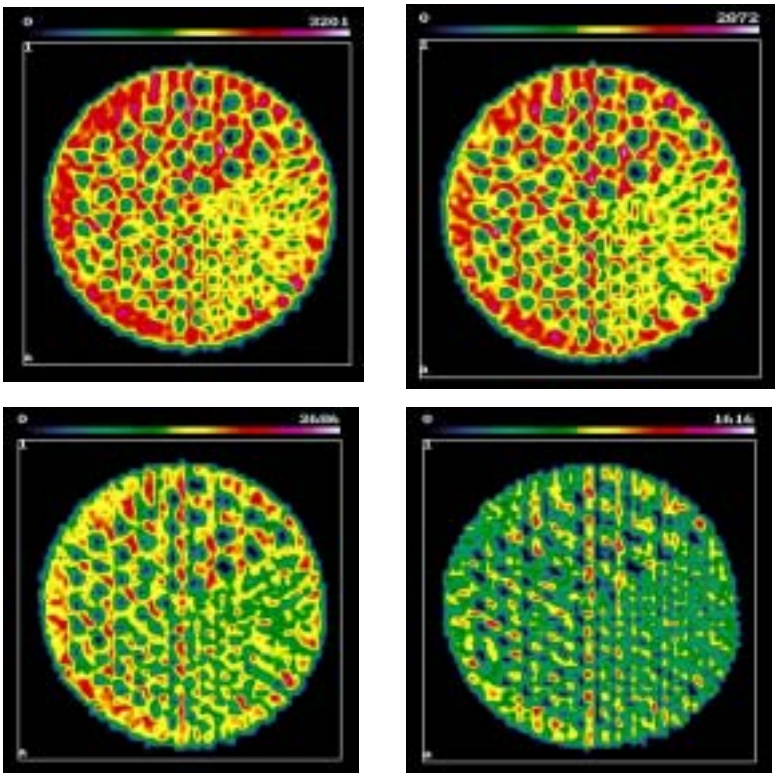

Simulation of a transverse slice through the cold rods of a Data Spectrum ECT phantom (Jaszczak phantom). Data acquisition: 64 projection angles, 360º total angle of rotation, 64 × 64 matrix. Reconstruction using a ramp filter and FBP, no statistical noise.

TL: Reconstruction with the full 64 projections (360º rotation).
TR: Reconstruction using only 54 projections (304º rotation).
BL: Reconstruction using only 44 projections (247º rotation).
BR: Reconstruction using only 21 projections (118º rotation).

Results: As the number of projection angles used for the reconstruction is decreased, the images show more degradation.

3.7.2. Example: Clinical study — reconstruction with half the acquired projection angles

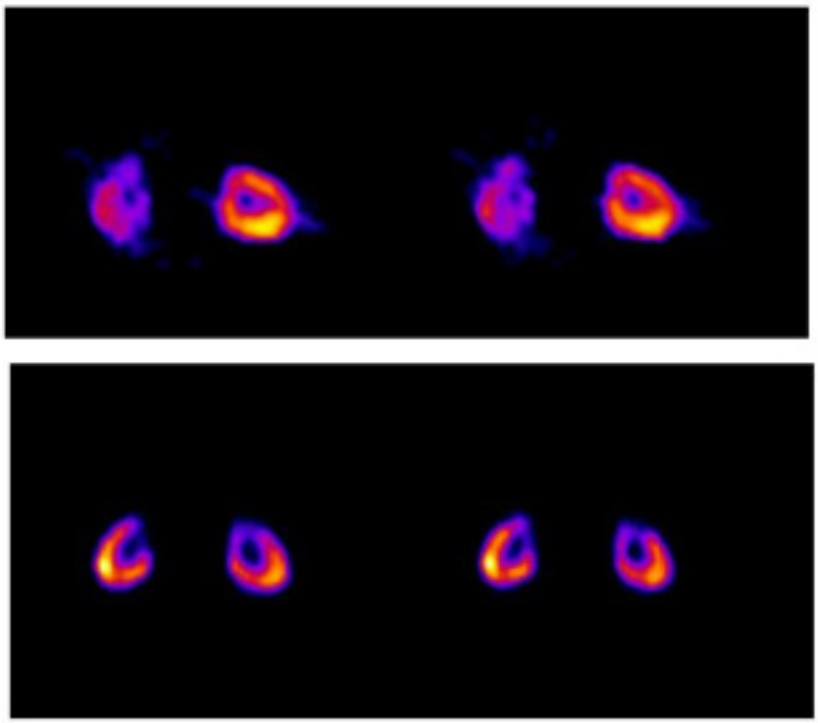

Patient SPECT study of the kidneys performed using ^{99m}Tc-succimer (DMSA). Dual head SPECT system with the detectors in a 180° configuration, 64 × 64 matrix, 360° total angle of rotation, with each detector acquiring 30 projections over 180°, 60 projections total. Reconstruction into transverse slices using FBP.

Top: Reconstruction using only 30 projections (180°).
Bottom: Reconstruction using all 60 projections (360°).

Results: The transverse slices obtained using only half the acquired data set showed a distinct difference between the two kidneys, which was not seen on the raw projection images. It turned out that the reconstruction had been made with only half of the projection views. The bottom row shows the same study after reconstruction using all the projections.

Just before this procedure, a clinical myocardial SPECT study had been reconstructed using data over only 180°.

Comments: It is essential to be sure of all reconstruction parameters prior to starting a procedure.

3.7.3. Example: Phantom data — comparison of acquisition and reconstruction over 180º and 360º projection angles

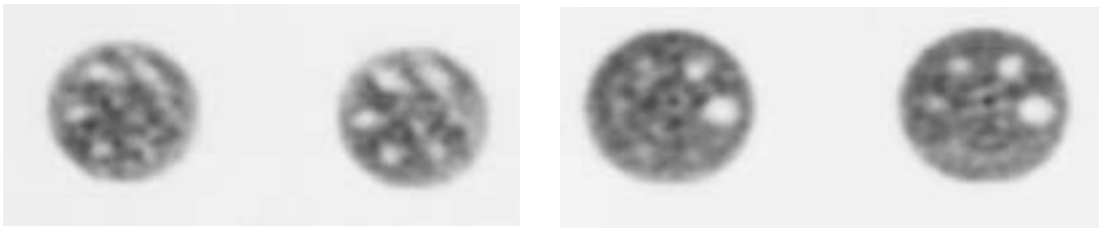

A: 180º rotation B: 360º rotation

SPECT study of a Data Spectrum ECT phantom (Jaszczak phantom). Data were acquired over 180º and 360º using a 64 × 64 matrix and 32 views (500 000 counts in the first view). The images were FBP reconstructed with a Hann filter using a 1 Nyquist cut-off.

A: Two transverse slices from 180º acquisition.
B: Two transverse slices from 360º acquisition.

Results: Note that most of the cold spheres in the ECT phantom were visualized in the 180º acquisition but most of them are elongated because the data set was not complete (did not cover 360º). The reconstructed images acquired over 360º accurately reflect the shape of the cold spheres.

Comments: When data are acquired over 180º, the contrast will strongly depend on the locations of the spheres relative to the 180º sweep of the detector(s).

3.7.4A. Example: Effect of truncation on a myocardial perfusion study

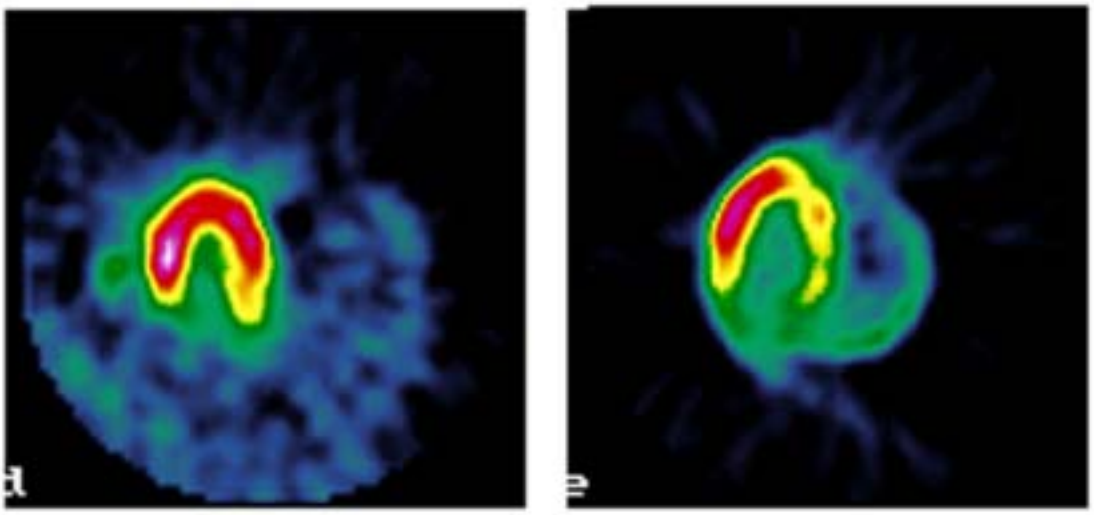

Patient myocardial perfusion study. Data acquisition: 64 × 64 matrix, 180º total angle of rotation, 32 projection angles. Reconstruction using FBP with a Parzen window and a cut-off at 1 Nyquist.

L: Transaxial image with no truncation. All 64 rows of the matrix were used for the data.
R: Transaxial slice from severe truncation, which has been simulated by using a row of only the 20 centremost pixels of the matrix (i.e. ±10 pixels from the axis of rotation).

Results: With truncation, the myocardium is still defined but is severely distorted.

3.7.4B. Example: Effect of truncation using a fan beam collimator

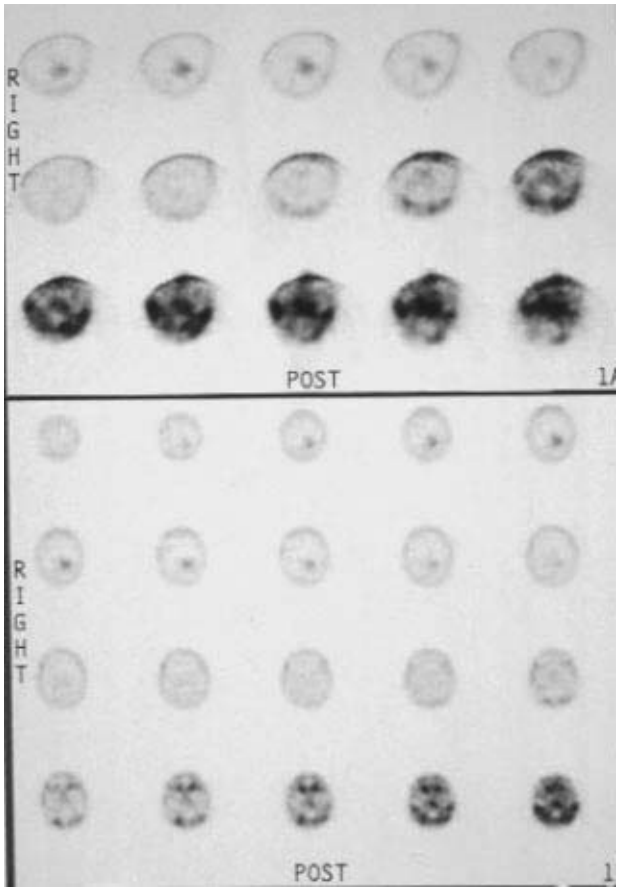

^{201}Tl SPECT study of the brain. The intense spot in the upper row(s) of each set of images is a brain tumour.

Top set: Transverse slices of a study performed using a fan beam collimator and a radius of rotation that was too large, so that truncation occurred.

Bottom set: Transverse slices of a study of the same patient performed using a parallel hole collimator.

Results: The images obtained with the fan beam collimator are totally distorted owing to the truncation. The expected reconstructed images are shown using the parallel hole collimator, for which the full brain was imaged in all acquired projection images.

Comments: Fan beam and other convergent collimators have to be used with extreme care so that the organ of interest is fully encompassed by the limits of the FOV at each projection throughout the rotation. In the case of the fan beam collimator, the limits of the FOV have a triangular shape in the *x* direction. The head must then be positioned as close to the collimator as possible, and within a certain specified radius of rotation, in order to ensure that the head falls within this triangle at all projection angles, thus avoiding truncation of data.

3.8. DATA RECONSTRUCTION — ATTENUATION CORRECTION

3.8.1. Example: Comparison of a phantom without and with attenuation correction

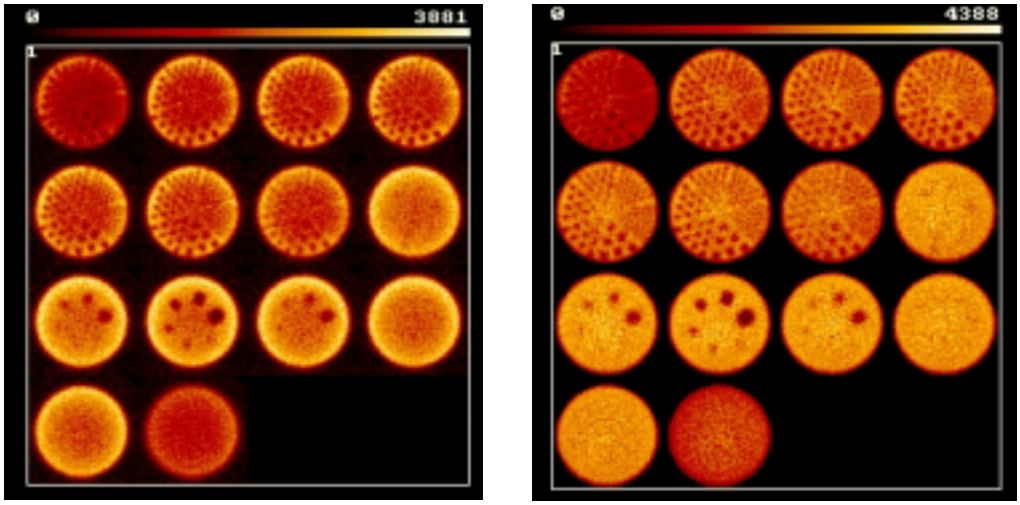

A: no attenuation correction B: with attenuation correction

Data Spectrum ECT phantom (Jaszczak phantom) filled with ^{99m}Tc, dual head SPECT, LEHR, 15% energy window.

Acquisition: 128 × 128 matrix, 360º total angle of rotation, 128 projections, 800 000 counts in the first projection, radius of rotation 19 cm, circular orbit, pixel size 3.2 mm.

Reconstruction: FBP with a Butterworth filter, transverse slices. For display purposes, the slice width is 3 pixels.

A: Transverse slices without attenuation correction.
B: Transverse slices corrected with first order Chang attenuation correction, with attenuation coefficient $\mu = 0.12$ cm^{-1}.

Results: The images from the phantom are as expected without and with applying the attenuation correction.

3.8.2. Example: Effect of uniform attenuation correction with different attenuation coefficients — phantom

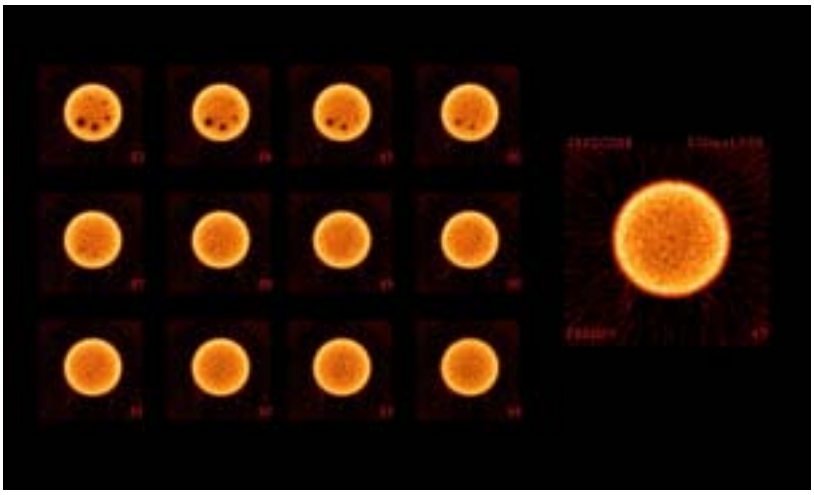

A: uncorrected for attenuation

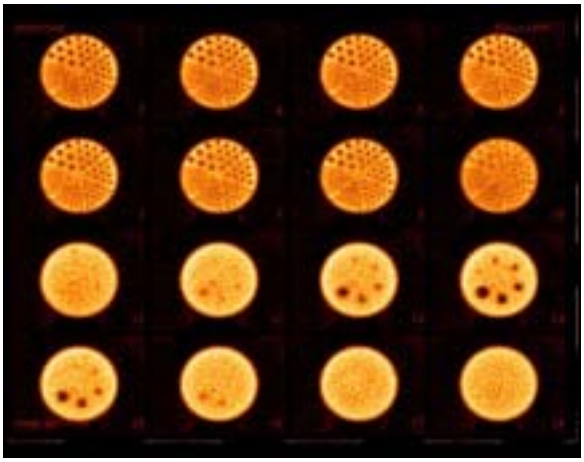

B: attenuation correction, $\mu = 0.08\ cm^{-1}$

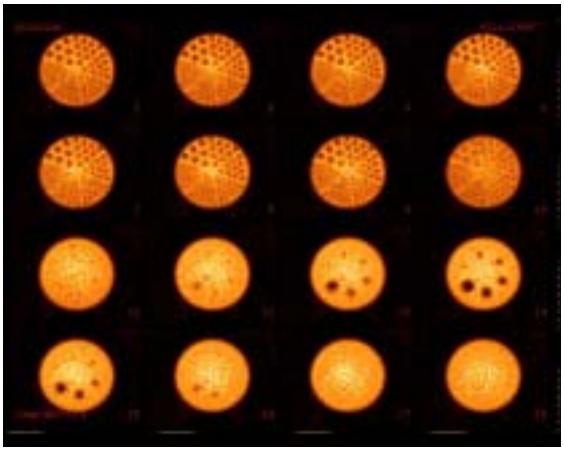

C: attenuation correction, $\mu = 0.14\ cm^{-1}$

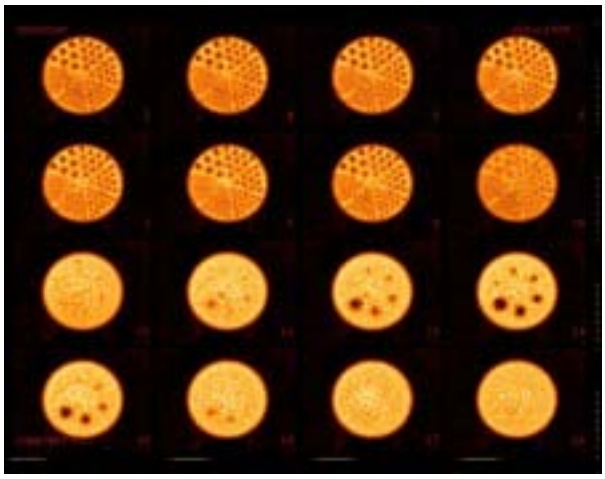

D: attenuation correction, $\mu = 0.11\ cm^{-1}$

Data Spectrum ECT phantom (Jaszczak phantom) filled with ^{99m}Tc, dual head SPECT, LEHR, 15% energy window.

Acquisition: 128 × 128 matrix, 360º total angle of rotation, 128 projections, 800 000 counts in the first projection, radius of rotation 19 cm, circular orbit, pixel size 3.2 mm.

Reconstruction: FBP with a Butterworth filter, transverse slices, attenuation correction using the Chang method and different linear attenuation coefficients.

A: 16 images with no attenuation correction. A symmetrically placed boundary to be used for correction is shown on the right image (in red).
B: Undercorrection ($\mu = 0.08$ cm^{-1}).
C: Overcorrection ($\mu = 0.14$ cm^{-1}).
D: Adequate correction ($\mu = 0.11$ cm^{-1}).

Results: The top transverse image set (A) shows an intense border with decreasing counts towards the centre of the phantom, which is typical when no attenuation correction is applied.

The middle left series of images (B) shows a slightly hotter border, indicative of undercorrection for attenuation.

The middle right series (C) shows an increase of counts towards the centre of each phantom image. This is due to overcorrection for attenuation.

The bottom series of images (D) shows similar count densities from the border towards the central area, indicative of adequate attenuation correction.

Comments: Care must always be taken when creating the boundary, especially for a symmetric organ (e.g. the brain). The attenuation correction is also dependent on a correct pixel size and attenuation factor.

Note: The attenuation correction determined using a fairly homogeneous water filled phantom is not always correct when applied to a non-homogeneous patient. Attenuation correction in clinical imaging must be used with care.

3.8.3. Example: Profiles to check the accuracy of attenuation correction

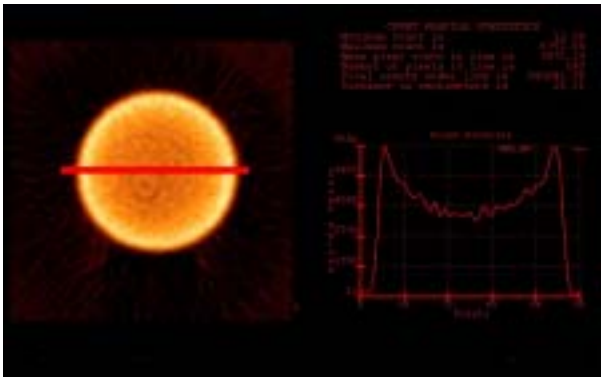

A: no attenuation correction

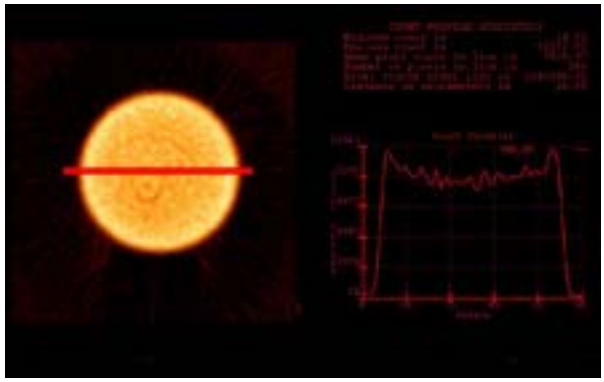

B: attenuation correction with $\mu = 0.08$ cm^{-1}

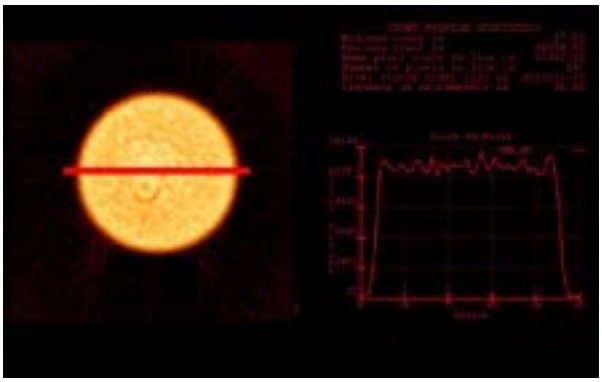

C: attenuation correction with $\mu = 0.11$ cm^{-1}

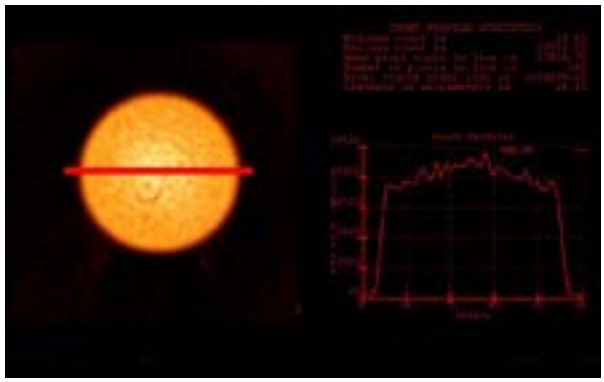

D: attenuation correction with $\mu = 0.14$ cm^{-1}

A cylindrical phantom, 20 cm in diameter, containing a homogeneous solution of ^{99m}Tc was used to acquire a high count data set. Dual head SPECT, LEHR, 15% energy window.

Acquisition: 128 × 128 matrix, 360º total angle of rotation, 128 projections, 800 000 counts in the first projection, radius of rotation 19 cm, circular orbit, pixel size 3.2 mm.

Reconstruction: FBP with a Butterworth filter, transverse slices. Attenuation correction was applied using different linear attenuation coefficients (Chang method). A profile was drawn across one of the transverse slices.

A: No attenuation correction.
B: Attenuation correction with $\mu = 0.08$ cm^{-1}.
C: Attenuation correction with $\mu = 0.11$ cm^{-1}.
D: Attenuation correction with $\mu = 0.14$ cm^{-1}.

Results: Only for the attenuation correction using $\mu = 0.11$ cm^{-1} is the profile through the slice essentially flat, apart from statistical fluctuations in the profile, indicating that the attenuation correction software is correct. For the image with a profile that is lower in the centre (B), the attenuation coefficient was too small. For the image with a profile that is higher in the centre (D), the attenuation coefficient was too large.

3.8.4. Example: Attenuation correction — incorrect boundary — cylindrical phantom

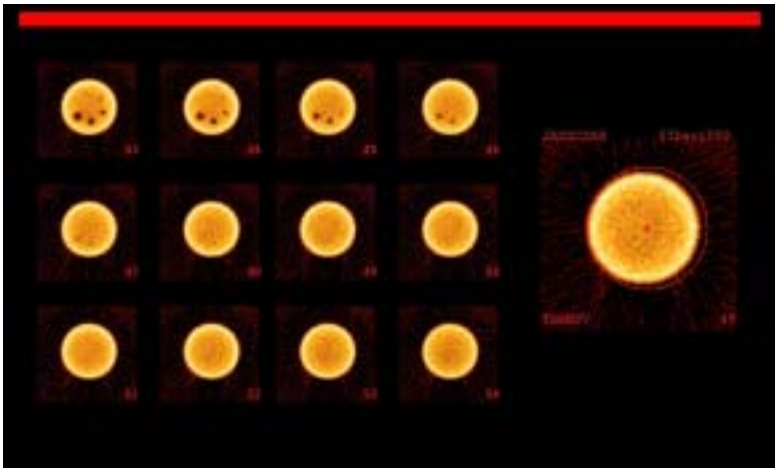

A

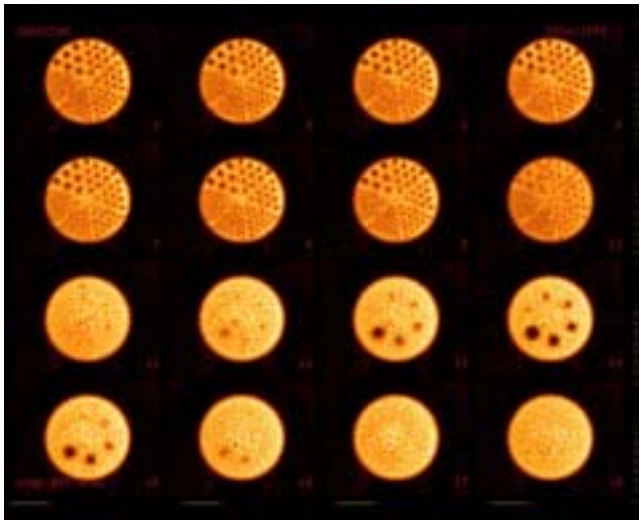

B

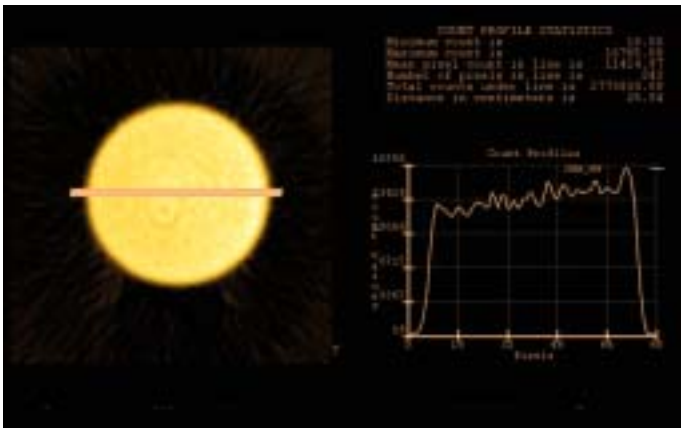

C

Data Spectrum ECT phantom (Jaszczak phantom) filled with ^{99m}Tc, dual head SPECT, LEHR, 15% energy window.

Acquisition: 128 × 128 matrix, 360º total angle of rotation, 128 projections, 800 000 counts in the first projection; radius of rotation 19 cm, circular orbit, pixel size 3.2 mm.

Reconstruction: FBP with a Butterworth filter, transverse slices, attenuation correction used Chang method.

The application of the attenuation correction requires the delineation of a circular boundary around the image of this phantom.

A: Series of transverse slices through the phantom, uncorrected for attenuation. The larger image on the right shows the boundary (in red) to be used for attenuation correction. This boundary is asymmetric to the right of the circular image.
B: Series of transverse images corrected with an attenuation coefficient of 0.11 cm^{-1} using the asymmetric boundary of A.
C: One attenuation corrected transverse slice through the uniform section of the phantom with a count profile through the centre of the phantom.

Results: The series of images in B and the image with profile in C show that there is overcorrection for attenuation correction on the right side of the image due to the asymmetric profile.

3.8.5. Example: QC procedure for non-uniform attenuation correction — scanning ^{153}Gd line source

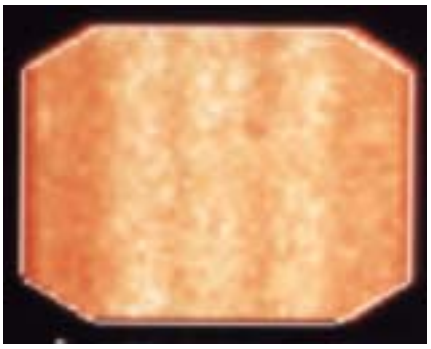

The 'reference scan' is a QC image for non-uniform attenuation correction of a SPECT study. Some vendors require that it be performed before clinical emission/transmission studies are carried out. The image indicates the 'apparent' variation in intensity of the collimated ^{153}Gd line source beam as it scans across the detector.

Results: The transmission image shown here has a variation in intensity that is most likely due to fluctuations in speed as the line source scans across the field. The calculated integral uniformity was well within acceptance limits specified by the vendor.

3.9. Clinical SPECT — other examples

3.9.1. Example: Unstable PM tube — myocardial perfusion SPECT study

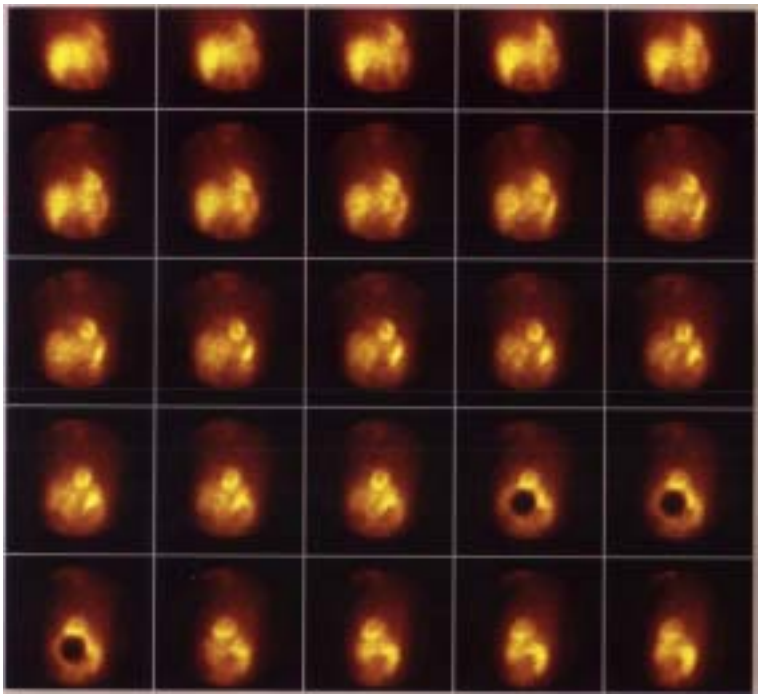

Single head SPECT, ^{99m}Tc, 15% energy window, myocardial perfusion study, 360º total angle of rotation. Twenty-five projection images are shown.

Results: Three images show a large, circular cold area corresponding to a PM tube that intermittently failed.

Comments: In order to ascertain the integrity of the projection data of the SPECT study, it is essential that the raw data be reviewed before the patient leaves the department and before reconstruction.

3.9.2. Example: Unstable energy window — triple head SPECT — myocardial perfusion study

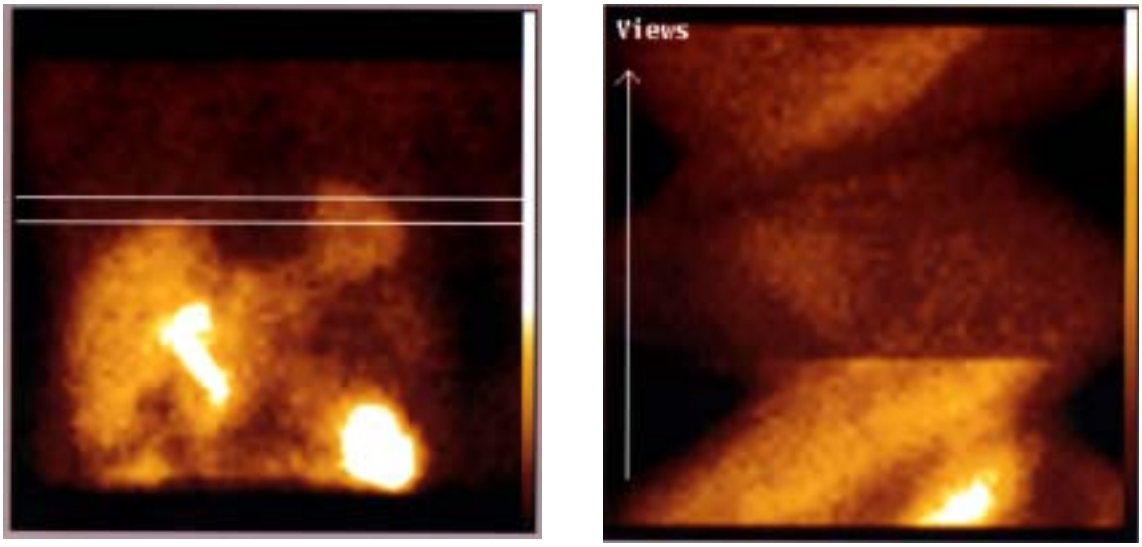

Myocardial perfusion SPECT study. Triple head SPECT system, LEHR collimators, detector heads in a triangular (120º) configuration, ^{99m}Tc, 15% energy window, 64 × 64 matrix, total angle of rotation 360°, each detector rotating through 120°.

L: One projection image.
R: Sinogram made from the profile over the myocardium as indicated on the projection image. The lower third part of the sinogram is from head 1, the middle third from head 2 and the upper third from head 3.

Results: The sinogram (right) should show a smoothly changing image, and not the sharp discontinuity shown here. The lower third part of the sinogram, from head 1, shows data with the energy window set correctly. The upper two thirds of the sinogram, from heads 2 and 3, shows a decrease in counts due to a shift in energy window for both these heads. Service was required to solve the problem.

Comments: It is essential that the raw data and the sinogram be reviewed before the patient leaves the department, in order to ascertain the integrity of the projection data of the SPECT study.

3.9.3. Example: Patient lateral movement — single head SPECT — cerebral perfusion study

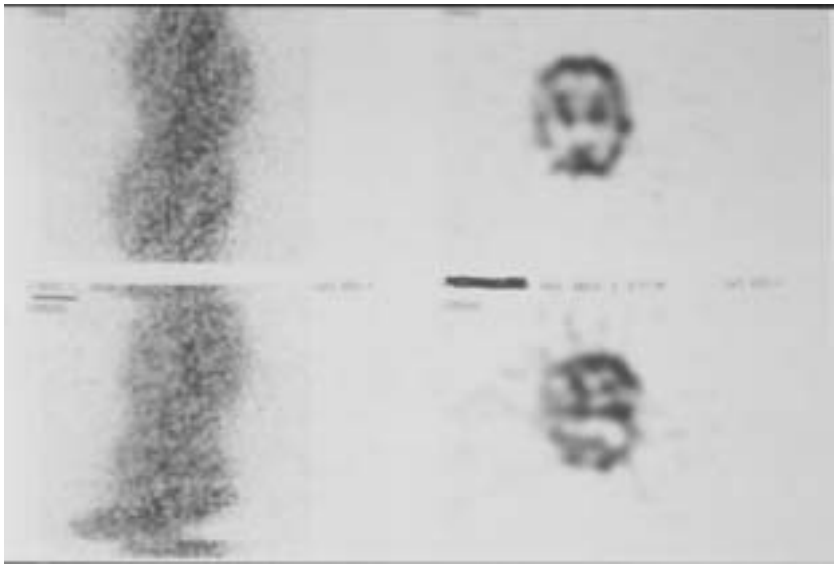

Single head SPECT, 360º total angle of rotation. Cerebral perfusion study obtained without patient movement and with patient movement.

Top row: Sinogram (L) and reconstructed transverse slice (R) from a study with no head movement.
Bottom row: Sinogram (L) and reconstructed transverse slice (R) from a study with lateral head movement.

Results: The lower sinogram shows considerable head movement during acquisition, especially at the beginning of acquisition (bottom part of the sinogram). This is recognized from the laterally displaced projections and disjointed appearance of the sinogram. The reconstructed transverse slices showed considerable distortion, so that the study could not be interpreted. The study had to be repeated with head restraint and with care to ensure no head movement (upper study).

Comments: Patient movement can render a SPECT study useless. Utmost care is required to ensure that the patient remains still.

In the case of cerebral SPECT, the condition of the patient may be suboptimal for movement free data acquisition. Head restraints are always necessary, as well as vigilance on the part of the technologist to ensure that the study progresses as required. Also, the extra time required in order to reassure the patient before starting data acquisition is well worth spending, if it can lead to an optimally acquired study and avoid reacquiring a suboptimally acquired study.

3.9.4. Example: Simulation of movement in *x* or in *y*

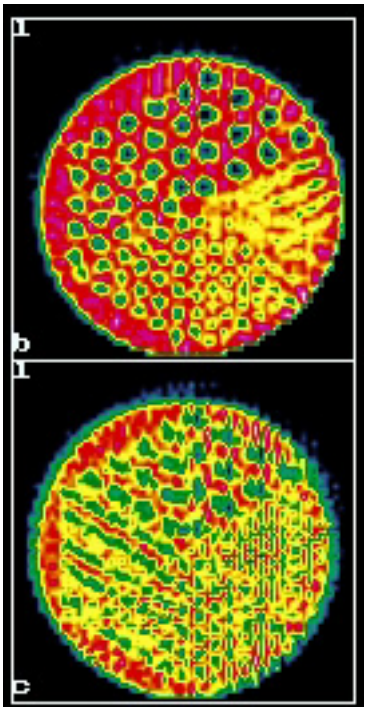

Shift in *x*

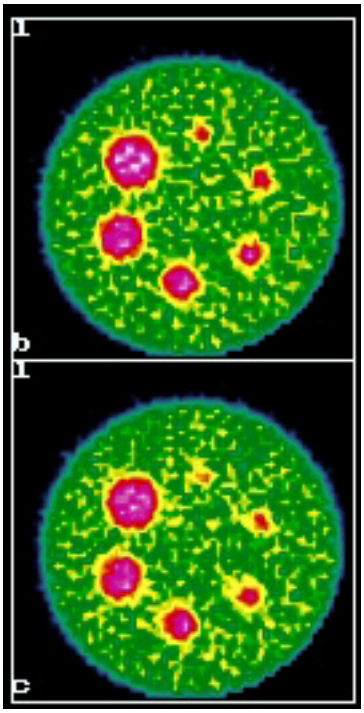

Shift in *y*

Simulated transverse slices of a Data Spectrum ECT phantom (Jaszczak phantom). In each set of images, the top image is without movement, and the bottom image includes a shift in 20 of the 64 projection images, in order to simulate lateral movement (shift in *x*) or vertical movement (shift in *y*).

Left: Transverse slice through the rods of the phantom, top image without a shift, bottom image with a 3 pixel shift in *x* (to simulate lateral movement).

Right: Transverse slice through the hot spheres of the phantom, top image without movement, bottom image with a 2 pixel shift in *y* (to simulate vertical movement).

Results: For the lateral *x* shift of 3 pixels (L), there is considerable loss of SPECT resolution in the reconstructed transverse slice (bottom) compared with the image without movement (top). For the vertical *y* shift of 2 pixels (R), there is some loss of contrast of the smallest sphere.

Comments: Some software corrects for patient motion, usually in the *y* direction only and rarely in both *x* and *y* directions. It must always be used with care, and each projection of the corrected raw images must be reviewed along with the sinogram.

3.9.5. Example: Movement in *y* — multihead SPECT — myocardial perfusion phantom study

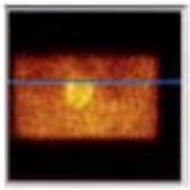

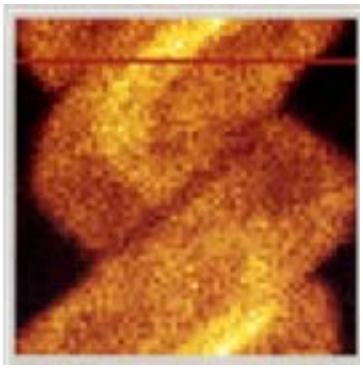

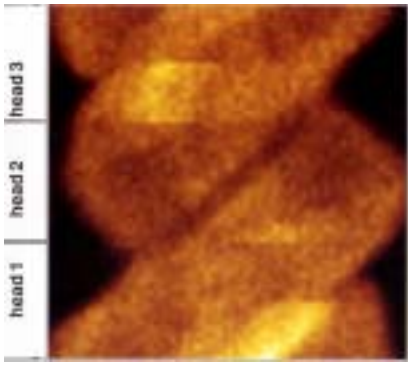

A: no movement B: 3 cm movement

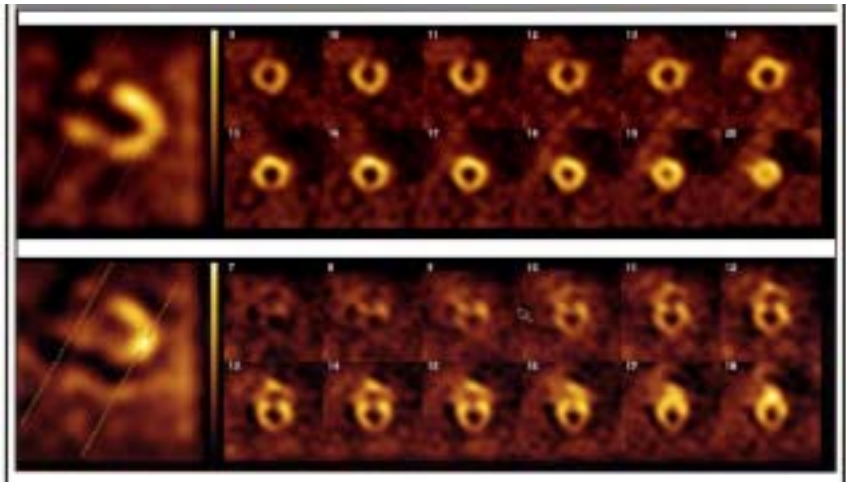

C: reconstructed short axis slices

Data Spectrum torso phantom with the myocardial insert containing a cold defect. Triple head SPECT system, LEHR collimators, detector heads in a triangular (120º) configuration, ^{99m}Tc, 15% energy window.

Acquisition: 64 × 64 matrix, total angle of rotation 360°, each detector rotating through 120°.

Two SPECT studies were made: with the phantom stationary on the patient pallet throughout data acquisition, and with the patient pallet moved axially by 3 cm about halfway through data acquisition.

A: No movement, phantom stationary. The left image is one projection image and the right is the sinogram at the *y* level at the top of the 'myocardium'. The sinogram is built up from concatenated projection data from the three heads as follows: the lower third projection data are from head 1, the middle third from head 2 and the upper third from head 3.

B: With movement. Equivalent images as in A, but the phantom was moved axially 'down' by 3 cm about halfway through data acquisition. The *y* level of the sinogram was positioned at the top edge of the cardiac insert, so that the myocardium moved out of its view when the phantom was axially moved.

C: Series of reconstructed short axis slices through the phantom.

Top row: Phantom stationary.
Bottom row: Phantom moved by 3 cm.

Results: When using a multihead SPECT system, any movement (or change in activity distribution) is detected by each head.

In this example, using a cardiac phantom and careful selection of the *y* level at the edge of the myocardium, the sinogram of B shows discontinuous data in all three heads. Only the first half of the acquisition from each head shows the myocardium (before it is moved down by 3 cm).

The sinogram without movement shows a smooth transition from each projection as expected.

The reconstructed slices with movement (bottom row of C) show a disjointed myocardial image, looking almost like a figure of eight. This would be a clinically useless study. The top row of C shows the expected short axis slices with the defect in the inferior wall.

Comments: Motion during the SPECT data acquisition can invalidate a study. In order to detect motion, the sinogram should be defined at the edge of the organ. This is usually achieved by the user defining a profile at the desired *y* level. A cine, or movie, of the raw data will also show movement.

It is recommended that SPECT projection data be reviewed as a cine as well as a sinogram prior to the patient leaving the department and prior to reconstruction. Any abnormality observed should be questioned and assessed, and any necessary action taken. For example, it should be determined whether an abnormality can be corrected by software, if the SPECT study must be repeated immediately (without further reinjection) or if there is a fundamental fault in the SPECT system so that no further studies can be acquired until the fault is rectified.

3.9.6. Example: Clinical myocardial perfusion study — effect of 'cardiac creep'

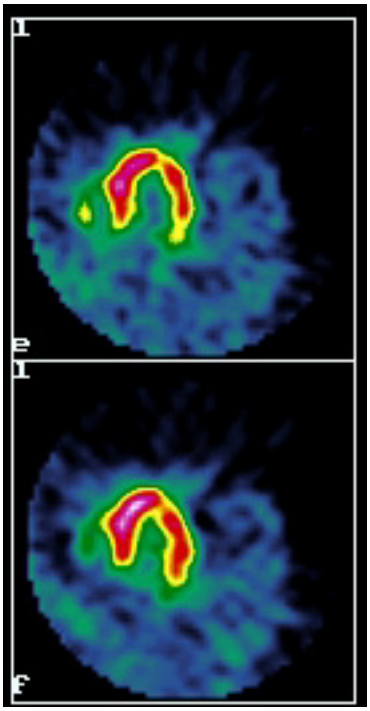

Horizontal long axis slice from a patient myocardial perfusion study. Using the same data, a progressive 'cardiac creep' (i.e. a vertical shift of the heart) has been simulated by introducing a progressive 0 to 2 pixel vertical shift, increasing with time.

Acquisition: 64 × 64 matrix, 180° acquisition, 32 projection angles.

Reconstruction: FBP with a Parzen window cut-off at 1 Nyquist.

Top image: No simulated creep.
Bottom image: With simulated creep.

Results: Compared with the top image, the bottom image with creep shows some disjointing at the apex, thickening of the left myocardial wall and some loss of contrast (as seen by the loss of the hot point of activity outside the left myocardium).

3.9.7. Example: Effect of poor labelling and hot liver on myocardial perfusion images

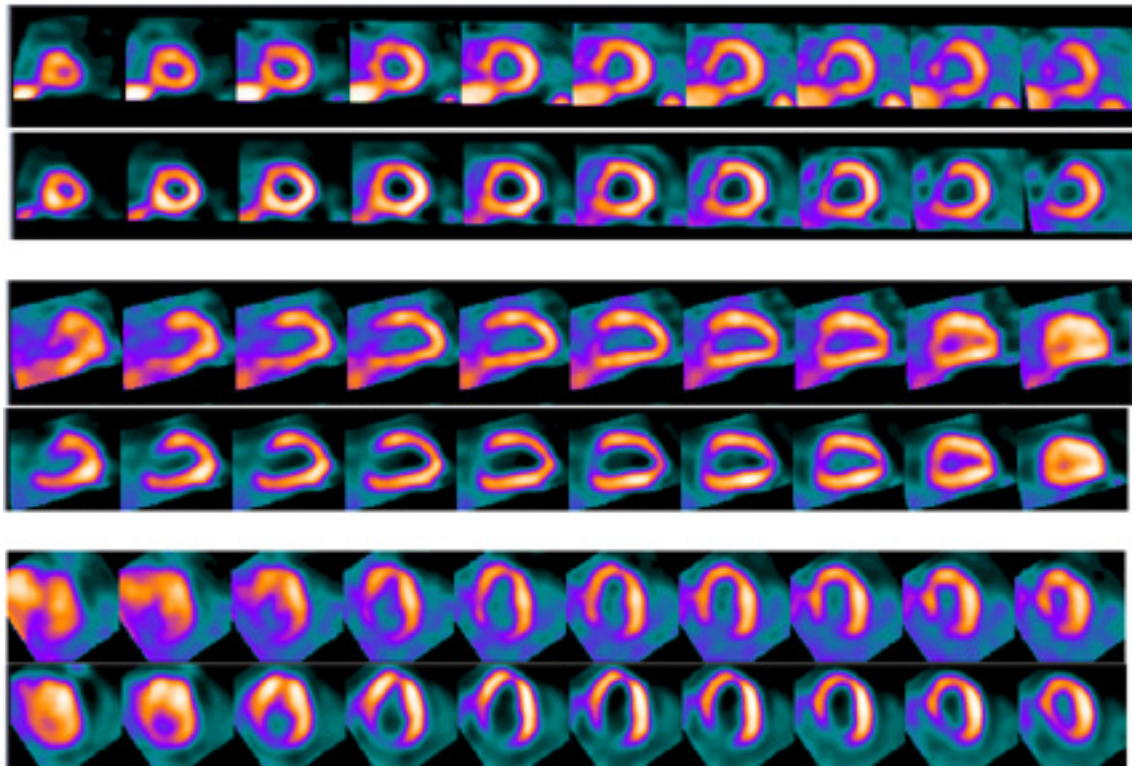

Patient myocardial perfusion SPECT study using ^{99m}Tc-sestamibi. Reconstruction using FBP.

The top row of each group of images is the result of poor radiopharmaceutical labelling, causing reduced myocardial uptake and an increase in background and liver activity. The bottom row of each group is from the same patient, but this time after good radiopharmaceutical labelling that resulted in a decrease in background and liver activity.

T: Short axis slices.
M: Horizontal long axis slices.
B: Vertical long axis slices.

Results: Comparison of the two groups of images shows that the images obtained with the poor labelling have less contrast, show less uniform perfusion and have a defect introduced in the septum (as a consequence of the FBP method and the high liver uptake), as seen in the short axis slices.

Comments: It is important to ensure that pharmaceutical labelling is within the limits specified by the supplier. Poor labelling may alter uptake and distribution, and consequently may affect the diagnosis.

3.9.8A. Example: FBP streak artefacts — hot organ activity outside of organ of interest — liver study

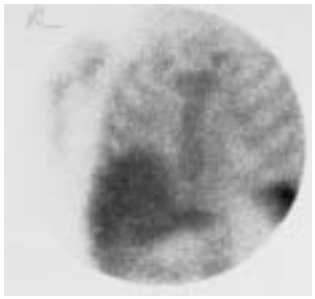

Anterior

Posterior

A: planar images

Zoomed

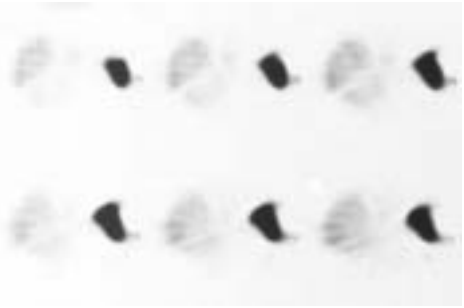

Unzoomed

B: SPECT transaxial slices

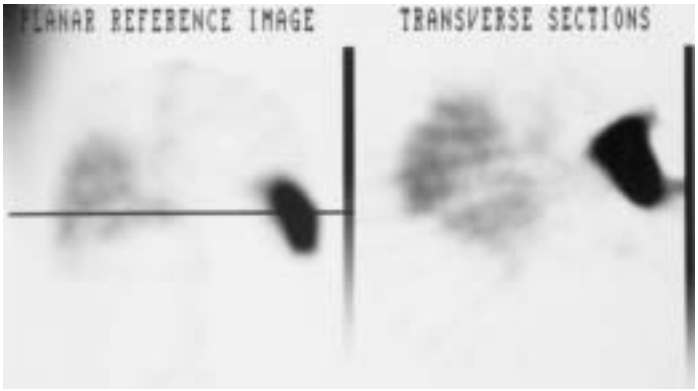

C: SPECT review

Single head SPECT, total angle of rotation 360°, 64 × 64 matrix. Clinical study using ^{99m}Tc labelled leucocytes. Planar study was obtained first and was followed by a SPECT study with particular interest in the liver. SPECT reconstruction used FBP reconstruction and a software zoom over the liver area.

A: Anterior (L) and posterior (R) planar images prior to the SPECT study.
B: Six transverse slices through the liver using the software zoom (L) and without the software zoom (R).
C: L: One projection image. R: Reconstructed transverse slice at the *y* level indicated by the profile on the left. No zoom used.

Results: The planar images did not reveal the extreme difference in ^{99m}Tc uptake by the liver and spleen. The zoomed liver transverse slices show distinct streaks. These were due to the extremely hot spleen and the filtered back-projection reconstruction method. Only after reviewing the raw data and an unzoomed reconstruction was the origin of the streaks clarified.

Comments: This example dates back to an early period of SPECT. However, this example of intense accumulation of radioactivity in an organ outside of the area of interest remains relevant today (e.g. hot gall bladder activity in a myocardial study, hot bladder). Only the zoomed reconstructed liver images were presented to the nuclear medicine physician, who attempted to report on these data without referral to the raw projection images. Only through a review of the study as a whole did it become clear why the transverse images of the liver were of such poor quality and why there were streaks. The raw SPECT data must always be reviewed prior to reconstruction.

3.9.8B. Example: FBP streak artefacts — hot organ activity outside of organ of interest — myocardial perfusion study

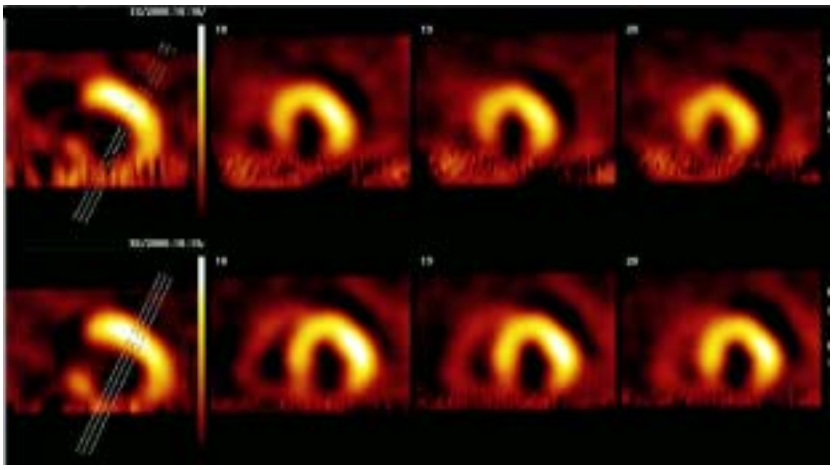

A: short axis slices: exercise (top) and rest (bottom)

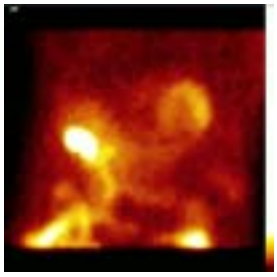

B: projection image

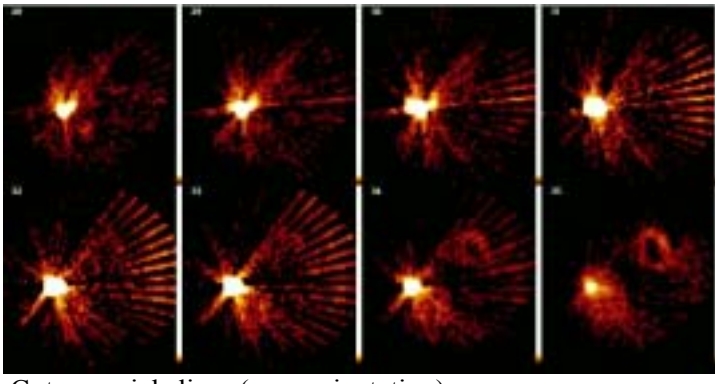

C: transaxial slices (no reorientation), no zoom

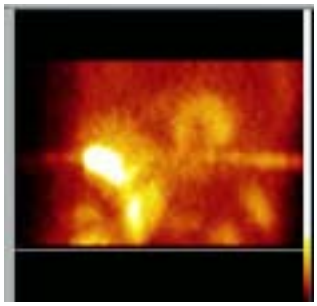

D: coronal reference image

Myocardial perfusion SPECT study using ^{99m}Tc tetrafosmin (two day protocol). Data acquisition used 64×64 matrix and 60 projection angles.

A: Three short axis slices from the stress study (top series) and the rest study (bottom series), reconstructed with a software zoom of 2, FBP and a Wiener prefilter, with no attenuation correction.

B: One projection image.

C: Series of FBP transverse slices (no reorientation), using only a ramp filter. The lower threshold was set to 0% and the upper threshold was set to 5% in order to show the myocardial activity.

D: Reference image in coronal view, showing artefacts due to the very hot gall bladder and the FBP reconstruction.

Results: The short axis slices (A) were obtained using a zoom factor of 2, thus eliminating the gall bladder from the image. These images revealed streaks that interfered with the inferior wall of the myocardial image. These were the rays produced by FBP reconstruction software. From the projection data it was found that the gall bladder had about 2–3 times more counts per pixel than the myocardium (B). Reconstruction of the exercise study (C) into straight transverse slices with no smoothing filter but only a ramp filter, and no zoom, emphasized the effects of the rays emanating from the gall bladder activity, and the superimposition of these rays on the inferior part of the myocardial activity.

The reference coronal image (a sum of several coronal slices) also shows artefacts from the FBP reconstruction from the very hot bladder.

Comments: The user should be aware of possible artefacts due to hot activity outside, but in the vicinity of, the organ of interest. In such situations, the use of iterative reconstruction will reduce the artefacts.

Reference: NUYTS, J., et al., A study of liver–heart artifact in emission tomography, J. Nucl. Med. **36** (1995) 133–139.

3.9.9. Example: Effect of smoothing filter and count statistics — clinical study

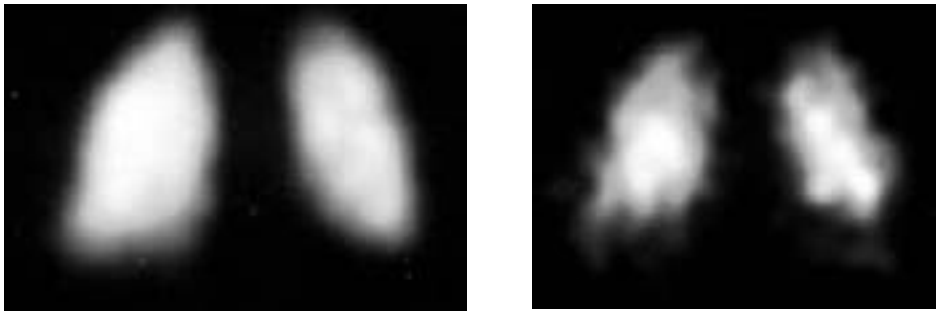

Triple head SPECT in triangular (120º) configuration, total angle of rotation 360°, each head rotating through 120º, 64 × 64 matrix. Simultaneous ventilation and perfusion SPECT studies of the lungs, using ^{99m}Tc macroaggregates for the perfusion study and continuous inhalation of ^{81m}Kr gas for the ventilation study.

Dual isotope data acquisition resulted in about six times more activity being collected for the perfusion study than for the ventilation study. Reconstruction for both perfusion and ventilation data used the same technique and the same smoothing filter and filter parameters (Butterworth filter). One coronal slice is shown from each data set.

L: Perfusion SPECT image.
R: Ventilation SPECT image.

Results: The perfusion image (L) shows a homogeneous image of activity in the lungs, whereas the ventilation image (R) shows a patchy image. The raw projection data (not shown here), viewed as a cine, showed both perfusion and ventilation distributions to be homogeneous. The patchiness of the ventilation image was due to the poor count statistics available. Another filter or other filter parameters may have improved the ventilation image.

Comments: The smoothing filter applied during reconstruction is crucial to the appearance of the final SPECT images. Oversmoothing and undersmoothing can both lead to misinterpretation of the images. Unfortunately, there are no absolute rules that can be applied, and different users have different preferences regarding the amount of smoothing present. Moreover, the implementation of filters by different manufacturers of nuclear medicine software differs, so that one must exercise caution when applying the ‘same’ filter in two different SPECT systems.

Updates of software might include changes to smoothing filters, and the user must be aware of such changes and verify the results of old and new filters, using an existing set of patient data, before switching to the new software.

3.9.10. Example: Effects of colour table — myocardial perfusion study

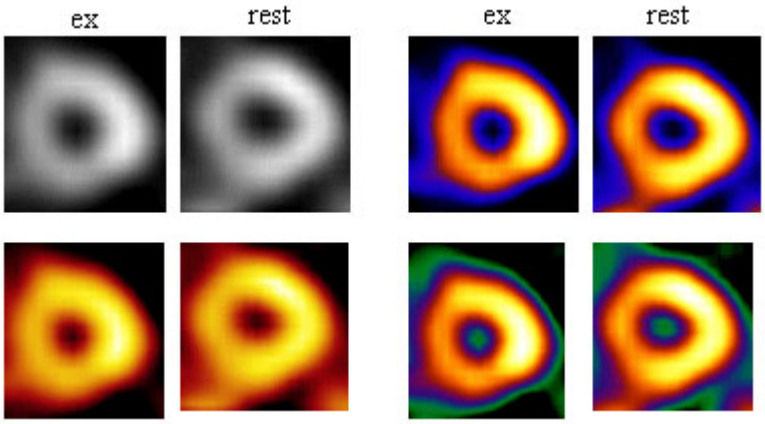

Triple head SPECT, high resolution collimator, ^{99m}Tc, 15% energy window, total angle of rotation 360°, 64 × 64 matrix, no correction for non-uniform attenuation correction. Myocardial perfusion study, reconstructed into short axis slices. Two short axis slices are displayed with four different colour tables.

Results: The images appear slightly different in each colour table.

Comments: This example is included only as a demonstration of the effects of colour table on a particular type of study. Criteria for the selection of a particular colour table depend on the study type and changes in counts that need to be observed. This applies both for clinical studies and for QC studies.

One problem with myocardial perfusion imaging without correction for non-uniform attenuation correction is the decrease in apparent activity in the apical and inferior myocardial wall. In this example, this is less obvious in the monotone colour table and grey scale (L row) than in the multiple colour tables (R row).

The colour table selected is an essential part of reviewing images. The user is required to choose it carefully, to use it consistently and to be aware of possible consequences like those in this example.

Note: A person who has ‘defective’ colour vision will perceive the images differently.

4. WHOLE BODY

4.1. SCAN SPEED

4.1.1. Example: Uniformity of scan speed — uniform response

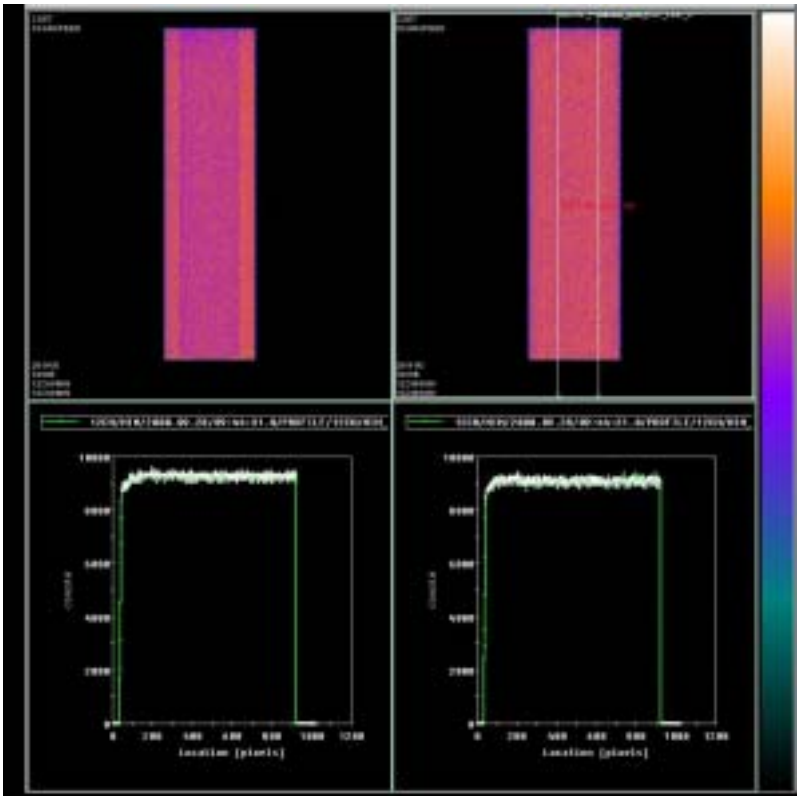

Whole body images from a dual detector scintillation camera. A ^{57}Co flood source was placed on the lower detector (detector 2) throughout the scan, and whole body images were obtained for both detector heads simultaneously.

T: Whole body scans. L: detector 1; R: detector 2.
B: Graphs of counts versus pixels along the length of the scan, from a broad profile, as shown in the top right scan image.

Results: Both the images and the count profiles show uniform response, indicating that the scan speed is uniform. The stripe of decreased counts in the top left image from detector 1 is from the imaging bed. The profile shows a slow increase in counts at the start of the scan, while the electronic shutter is opening, indicating a slightly too fast opening of the electronic shutter. This is not seen at the end of the scan.

4.1.2A. Example: Uniformity of scan speed — non-uniform response

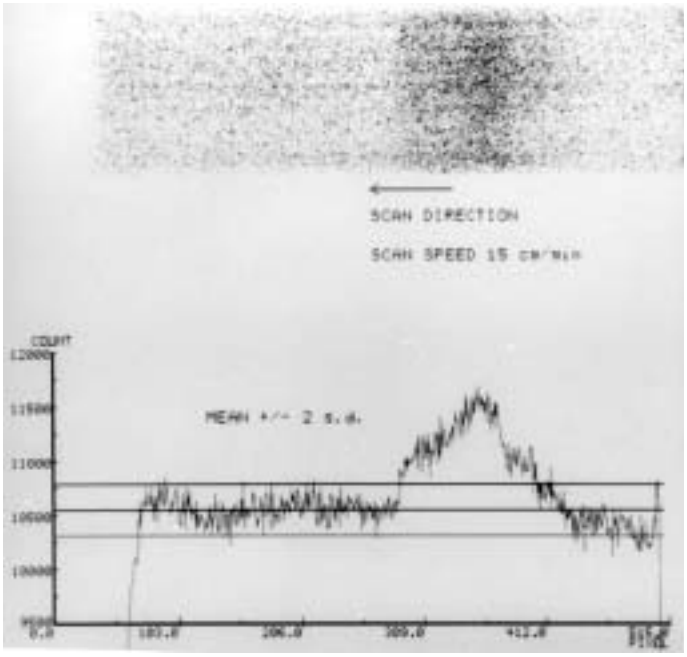

200 cm long whole body image from a single head scintillation camera. A ^{57}Co flood source was placed on the detector throughout the scan, and a whole body image was made with a speed of 15 cm/min.

T: Whole body image of the flood source. The motion was from right to left.
B: Counts versus distance from a wide profile set along the length of the whole body image.

Results: The image and the count profile show an area of increased counts indicating a problem with the scan speed. The decrease in counts on the left of the image, and the corresponding steep decrease of the profile, are due to the acquisition being stopped during the mechanical shutter closing. The non-uniformity during the whole body scan is unsatisfactory, and service is required.

4.1.2B. Example: Uniformity of scan speed — non-uniform response

→ scan direction

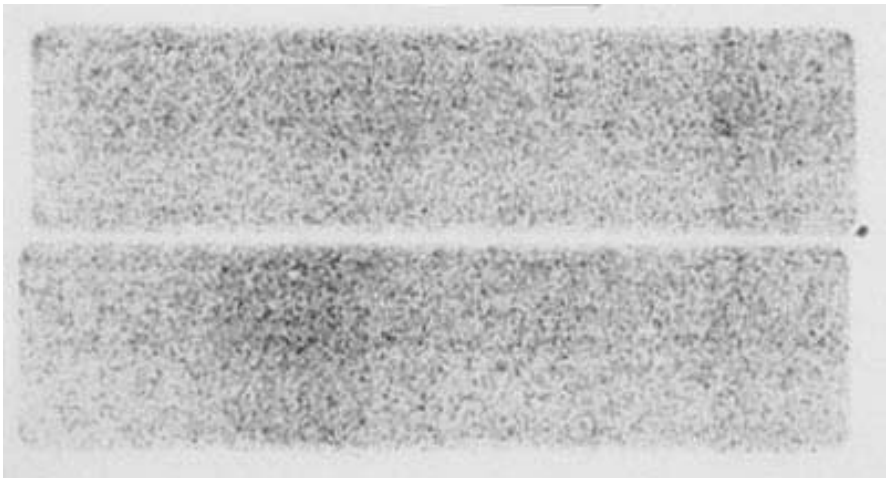

← scan direction

200 cm long whole body images from a single head scintillation camera. A ^{57}Co flood source was placed on the detector while the whole body scans were made.

T: Scanning motion in one direction (left to right).
B: Scanning motion in the opposite direction (right to left).

Results: Both whole body scans show a non-uniform response, indicating scan speed variations during the scans. The speed variations are not identical in both scan directions. The increased count density at the right of both images indicates a problem with the electronic shutter speed. It should also be noted that the top image is slightly smaller than the bottom image owing to the malfunction of a position encoder, but only in one direction. This is an unsatisfactory result, and the camera requires service.

4.1.3. Example: Clinical whole body bone scan — change of scan speed during scan

Routine whole body bone scan. Motion of the scan was from head to feet. The whole body scan started correctly as the electronic shutter opened, but during the subsequent motion the scan speed changed.

Results: When the scan speed changed, the position encoder did not recognize this. The mismatch between the scan speed and the position encoder resulted in the blurred image. This was a single occurrence and the cause was unknown.

4.1.4. Example: Clinical whole body bone scan — motion stopped midway

Routine whole body bone scan. Motion of the scan was from head to feet. The scintillation camera was stationary, the bed was moving. During motion the bed stopped, but data acquisition continued.

Results: The image shows a large change in image intensity, and therefore in count density, between the moving and the stationary parts of the scan. The image size, however, remains the same. This was an intermittent problem that required service.

4.2. IMAGE SIZE

4.2.1. Example: Whole body scan — misregistration of position signals

→ scan direction

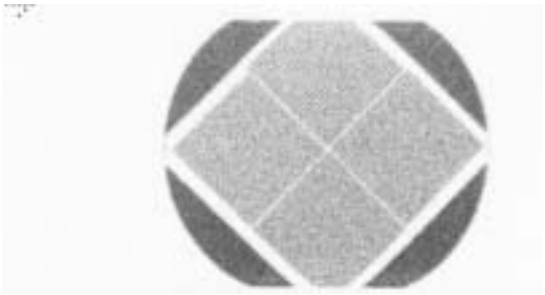

Scintillation camera with whole body scanning option, LEHR collimator, ^{57}Co, 20% energy window. Whole body scans were obtained at acceptance testing in order to assess the spatial resolution during whole body acquisition. A circular ^{57}Co sheet source was placed on the scanning bed, a four quadrant bar pattern was placed on top and the collimated detector was brought as close as possible to the bar pattern.

T: Whole body scan, scanning from left to right, scan speed 10 cm/min.
B: After service, repeat of the whole body scan with the same bar pattern and flood source.

Results: The first whole body scan (T) shows a diamond shaped bar pattern instead of the expected square pattern, owing to a misregistration of the position signals during scanning. This problem was solved after service. The repeat scan was acceptable.

4.3. MULTIPLE SCAN PATHS

4.3.1. Example: Whole body spatial resolution — multiple scan paths

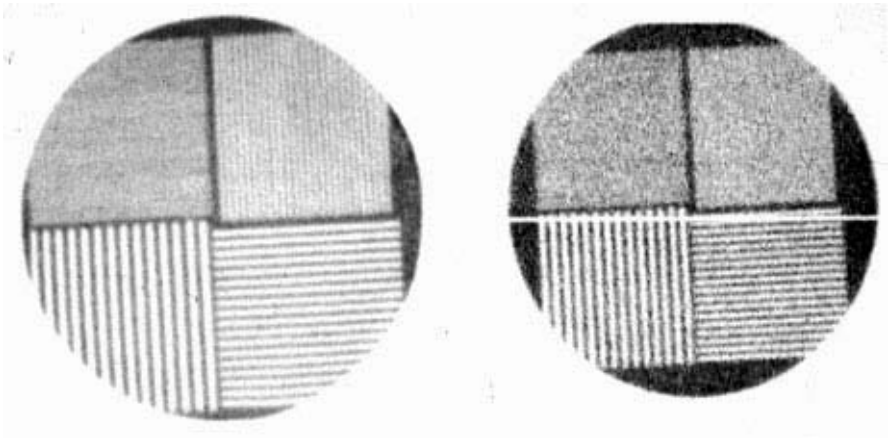

The spatial resolution in whole body mode imaging was checked using a four quadrant bar pattern and ^{99m}Tc filled circular flood source, 20% energy window. The scintillation camera made two scan paths.

L: Static image of the four quadrant bar pattern.
R: Whole body image of the same bar pattern in the same set-up, using two scan paths. The count statistics of these two images were similar.

Results: There is a loss of spatial resolution between the static image and the whole body image, especially evident in the top right hand quadrant. The horizontal white line in the whole body image indicates that the two scan paths (upper and lower) are not properly aligned. Both aspects require service.

4.3.2A. Example: Multiple scan paths — misalignment of paths — clinical

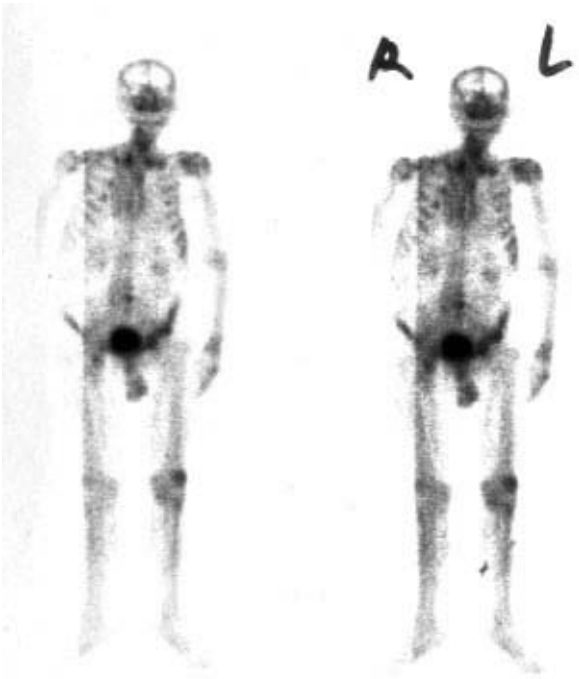

Whole body image of the skeleton, in the anterior view, was made using three scan paths. Two images were documented on film with a multiformatter, using two different spot intensities.

Results: Both images show that the scan path on the right side of the body has a lower intensity than the scan paths from the middle and left sides of the body. Also, the right side scan path is not properly aligned with the other two paths, which are reasonably matched. This requires service.

Note: Since both images show the same effect, a problem with the multiformatter can be ruled out.

4.3.2B. Example: Multiple scan paths — skeleton

Whole body image of the skeleton using ^{99m}Tc MDP, 20% energy window. Three scan paths were used.

Results: The whole body image shows missing data in the scan paths on the right and left sides of the body. All three paths are poorly aligned. The problem lay in the lateral bed movement, which was resolved by service.

Comments: A simple QC check of the alignment of the multiple paths will reveal this problem. For example, a scan using three paths of a flood source or a spatial resolution pattern, placed at an angle to the scanning path, will reveal misalignment and overlap of the scans. If such problems are observed, then making individual static images that cover the skeleton (using the same total time per image) will be better than attempting a whole body scan.

Note: The poor quality of this image was also due to low count statistics and poorly focused spots of the electronic formatter.

4.4. DETECTOR UNIFORMITY

4.4.1A. Example: Whole body scan — faulty PM tube

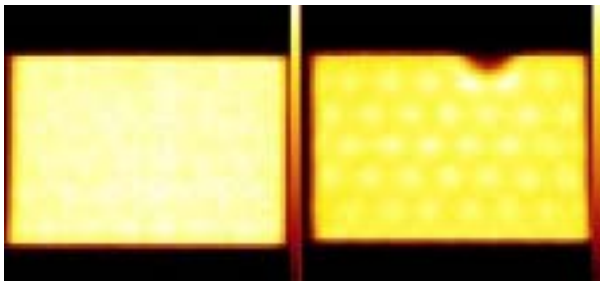

Static: head 1 head 2

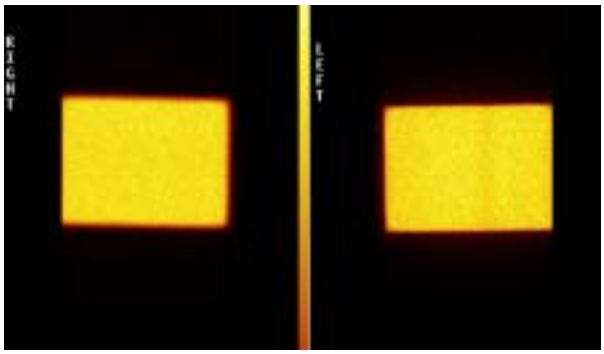

Scan: head 1 head 2

Dual head whole body system, detectors in a 180° configuration, ^{57}Co, 20% energy window, LEHR collimators. Static images and whole body scans were made (both heads simultaneously) with a ^{57}Co flood source positioned symmetrically between the detectors and in the middle of the scan length. Left row: head 1; right row: head 2.

T: Static images.
B: Whole body images. The whole scan path is not shown, only the scan of the flood source during scan motion.

Results: The static images show that head 2 (right) has a PM tube malfunction at the top edge of the FOV. The other PM tubes appear as hotter areas. This required new linearity and energy maps to be acquired. Head 1 (left static image) shows better uniformity than head 2.

The whole body scans show a uniform response for head 1 (left) and a reasonably uniform response for head 2 (right), except for a faint vertical stripe of lower count density due to the faulty PM tube.

Both problems were corrected by service.

Note: These images only show the effect of the PM tube during scan motion. See example 4.4.1B for the effect of a faulty PM tube and of poor linearity and energy corrections for the whole scan length.

4.4.1B. Example: Whole body scan — faulty PM tube — old linearity and energy corrections

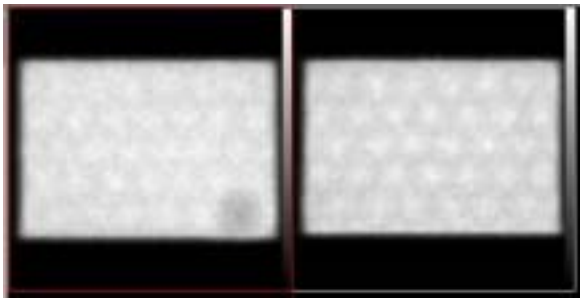

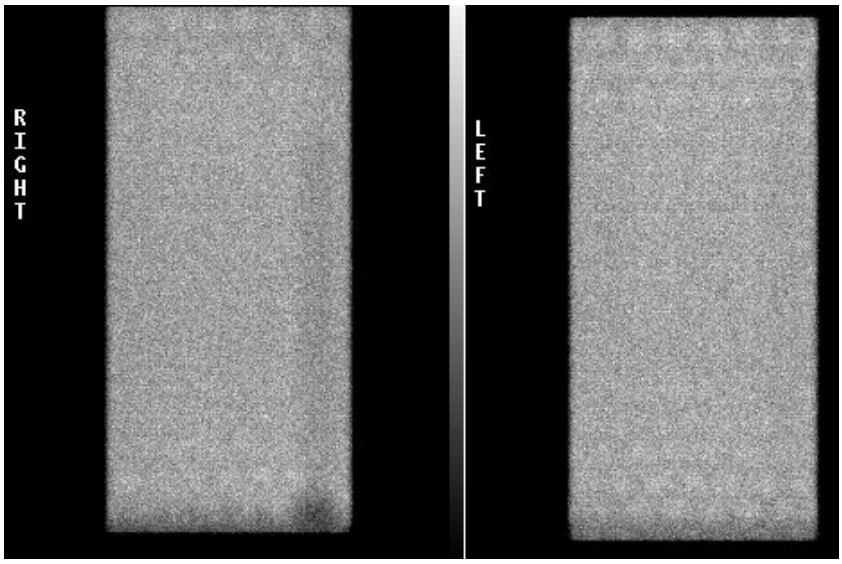

Head 1 Head 2

The same dual head whole body system as in example 4.4.1A. Heads in a 180° configuration, ^{57}Co, 20% energy window, LEHR collimators. Images were obtained with both heads simultaneously. L: head 1; R: head 2.

T: Static images of a ^{57}Co flood source placed symmetrically between the heads.
B: Whole body scans made with the flood source placed on the lower detector throughout the scan. There was no imaging table between the camera heads.

Results: Both static images show a distinct pattern of PM tubes due to outdated linearity and energy correction maps. In addition, head 1 shows a PM tube malfunction in the lower right quadrant of the static image. The whole body images also show non-linearity in the top and bottom of the scan, where the detector is stationary and only the electronic shutter opens (at the beginning) and closes (at the end). At the end of the scan, when the detector is stationary, the malfunctioning PM tube also shows as the circular defect. During the section of the scan where the camera is in motion, the non-linearity is blurred out. Only a faint vertical line of diminished counts is seen from the faulty PM tube.

Comments: New linearity correction maps are urgently required for this camera. Use of this camera for clinical whole body scans should be undertaken with caution, and only with the patient positioned outside the path of the malfunctioning PM tube.

4.5. ENERGY WINDOW

4.5.1A. Example: Whole body bone scan — ^{57}Co versus ^{99m}Tc energy window

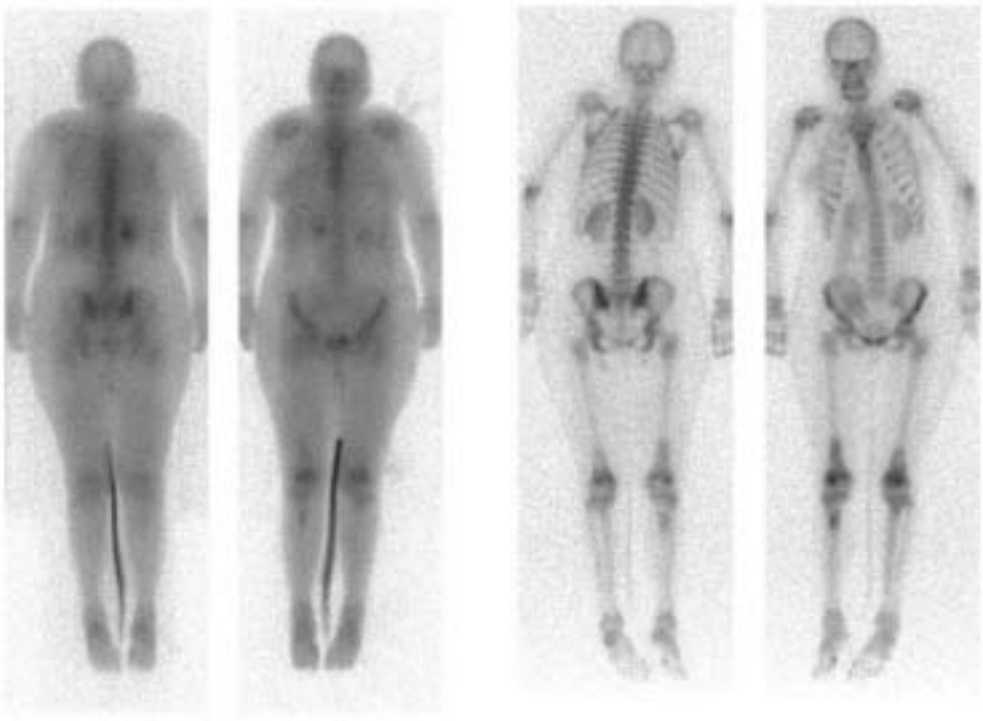

^{99m}Tc in ^{57}Co window ^{99m}Tc in ^{99m}Tc window

Whole body scans of the skeleton, 740 MBq ^{99m}Tc phosphate radiopharmaceutical, LEHR collimator.

L: Anterior and posterior scans were inadvertently obtained with a 20% ^{57}Co energy window at 3 h post-injection. The physician suspected that the images had been obtained with a ^{57}Co energy window, but the patient had already left the department. The patient was therefore rescanned the next day.

R: Anterior and posterior scans obtained with the correct ^{99m}Tc energy window at 24 h post-injection.

Results: The left images of ^{99m}Tc obtained with the ^{57}Co energy window show complete loss of contrast and an unrecognizable skeleton. The right images of ^{99m}Tc obtained with the correct ^{99m}Tc energy window show normal contrast and spatial resolution. Although the counts were much lower at 24 h, an excellent image of the skeleton was still obtained owing to use of the correct energy window.

Comments: The images in the ^{57}Co energy window were obtained after daily QC using a ^{57}Co source. No check of the ^{99m}Tc window setting had been made before starting clinical imaging. It is imperative that images be reviewed and any poor quality images evaluated and reacquired before the patient leaves the department.

4.5.1B. Example: Whole body skeleton imaged in wrong energy window

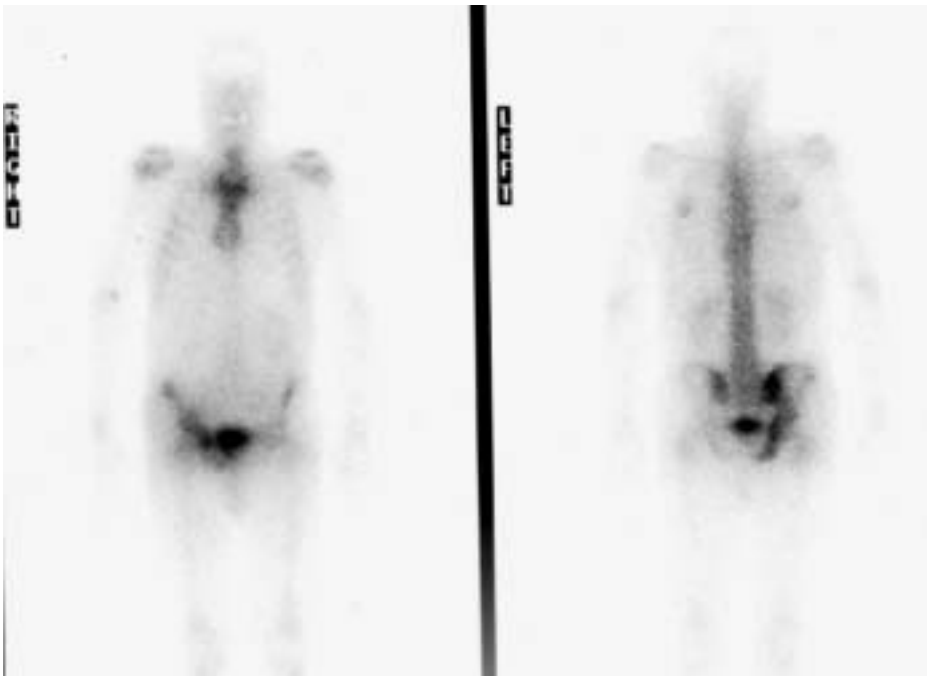

Whole body scans in anterior and posterior views of the skeleton, ^{99m}Tc phosphate radiopharmaceutical, LEHR collimator, 15% energy window. The images were inadvertently made with the ^{57}Co energy window.

Results: The images show poor contrast and spatial resolution, because the images were obtained with the ^{57}Co energy window instead of the ^{99m}Tc energy window. The images were not repeated with the correct energy window.

Compared with the images of example 4.5.1A, there is still some structure visible. However, these images should have been repeated with the correct ^{99m}Tc energy window.

Comments: Alertness to poor image quality is essential. Action should be undertaken before the patient leaves the department, and images should be checked by an experienced member of staff.

4.6. RADIOACTIVE CONTAMINATION

4.6.1A. Example: Whole body scan — radioactive contamination on a handkerchief

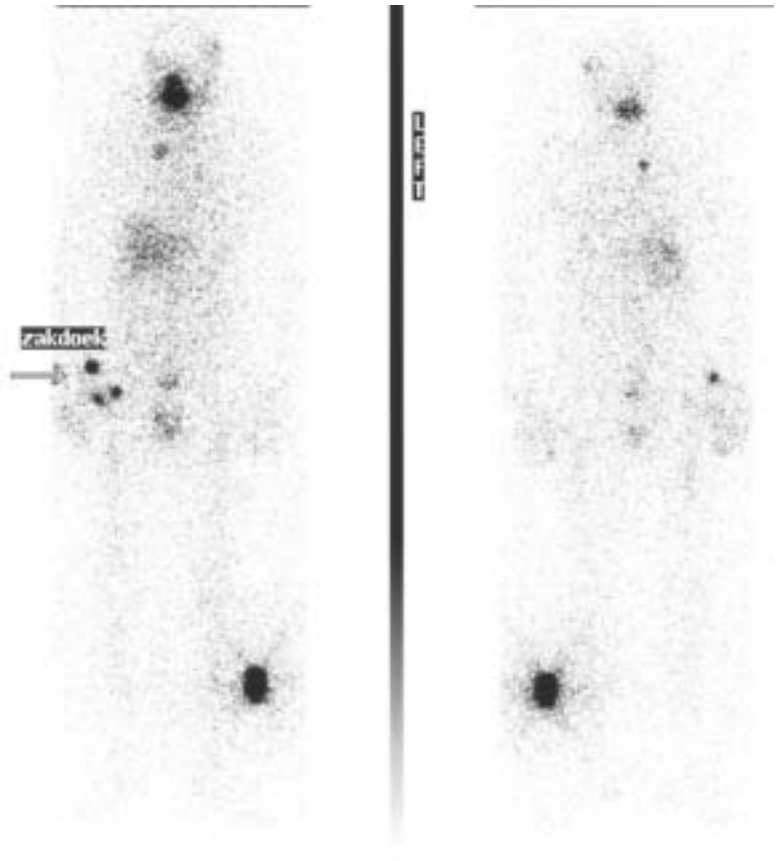

Whole body scan three days after administration of a therapeutic amount of ^{131}I iodide.

L: Anterior view.
R: Posterior view.

Results: The three hot spots on the right hand side of the body (indicated by the arrow) were due to ^{131}I contamination on a handkerchief in the patient's pocket.

Note: The large hot spot with a star effect on the lower left side of the patient is a known amount of activity from a 'radioactive standard' imaged together with the patient in order to estimate iodide uptake in thyroid tissue. Less activity should have been used for this purpose.

4.6.1B. Example: Whole body bone scan — radioactive contamination on clothing

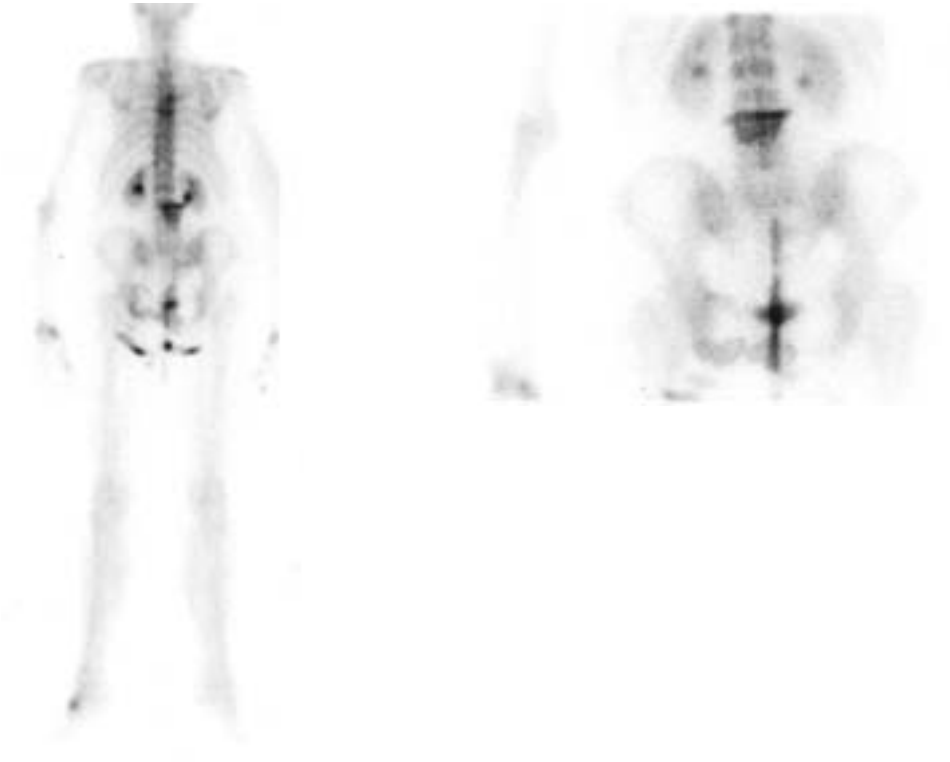

Whole body scan Static image

Whole body scan and static images of the skeleton in posterior view. The vertical and horizontal hot areas in the static scan do not correspond with skeletal features. They were due to radioactive urine contamination on the patient's clothing.

5. SCINTILLATION CAMERA–COMPUTER INTERFACE

5.1. ADC NON-LINEARITY

5.1.1A. Example: Non-linearity in ADC

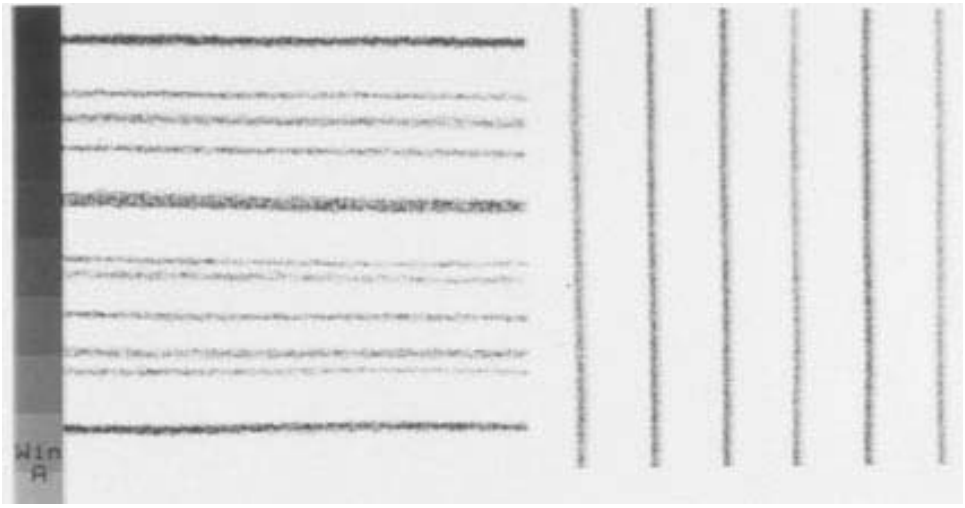

$\rightarrow x$ $\uparrow y$

Intrinsic linearity images were acquired with ^{99m}Tc and a NEMA slit pattern (1 mm slits in a sheet of lead with separations of 30 mm) during acceptance testing.

Results: The image acquired with the slits oriented vertically (*x* spatial resolution) demonstrated generally satisfactory linearity of the ADC, and the lines are equally spaced (R). When the slits were oriented horizontally, the spacing varied owing to a malfunctioning ADC (L). The lines in the *x* direction also are not straight.

5.1.1B. Example: Non-linearity due to noise in ADC

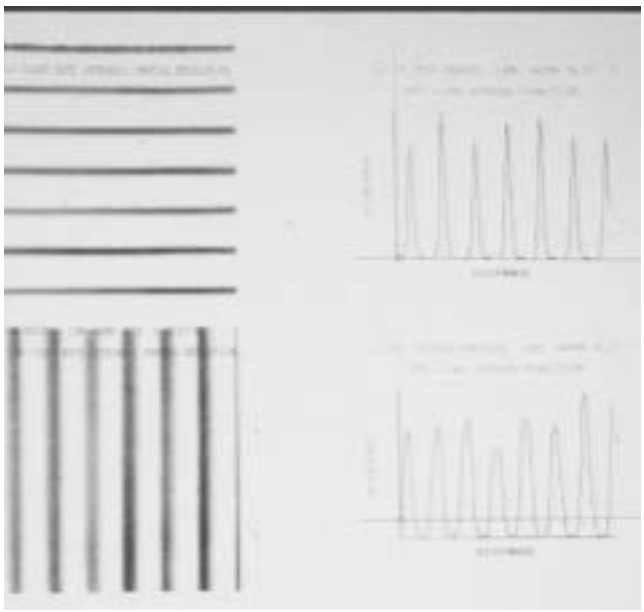

$\rightarrow x$ $\uparrow y$

NEMA slit pattern showing difference between *x* and *y* spatial resolution. Images were acquired with a ^{99m}Tc point source at about 5 FOV distance from the detector and a NEMA slit pattern (1 mm slits in a sheet of lead with separations of 30 mm) during acceptance testing.

Top row: Image obtained with slits positioned parallel with *x* (horizontal) to test *y* direction spatial resolution. The count profile on the right is from a vertical profile.

Bottom row: Image obtained with slits positioned parallel with *y* (vertical) to test *x* direction spatial resolution. The count profile on the right is from a horizontal profile.

Results: The image acquired with the slits oriented horizontally (*y* spatial resolution, top left image) demonstrated satisfactory spatial resolution and generally satisfactory linearity during acceptance tests. However, when the slits were oriented vertically, the image showed a significant loss of spatial resolution. This is seen clearly in the count profiles, where the bottom profile shows wider line spread curves than in the top profile. The problem was caused by a noisy ADC.

5.1.2. Example: Simulation of differential non-linearity in ADC

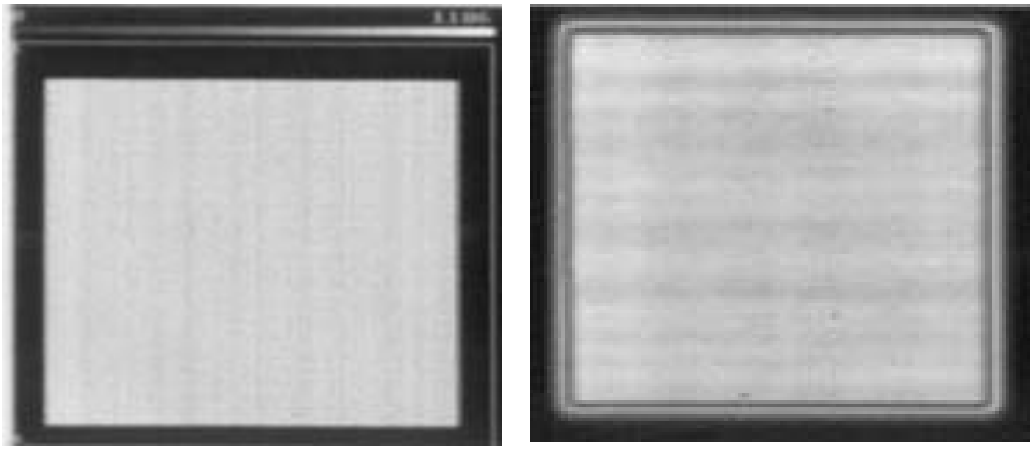

$\rightarrow x$ $\uparrow y$

Simulations made to show the effect of differential non-linearity on a flood field image.

L: Simulation of differential non-linearity in the *x* ADC.
R: Simulation of differential non-linearity in both *x* and *y* ADCs.

Results: The left image shows stripes only in the vertical direction (parallel with *y*). The right image shows both horizontal and vertical stripes.

The example here shows simulations. In the real situation, the ADC circuit boards would need to be replaced.

5.1.3. Example: Differential non-linearity in ADC — stripes in uniformity image in *x* and *y* directions

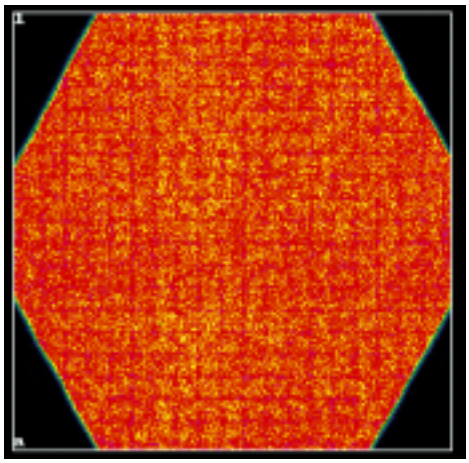

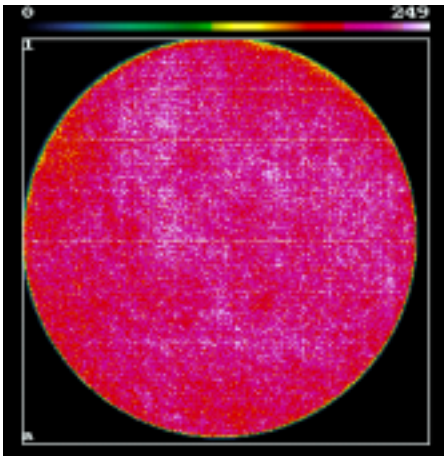

$\rightarrow x$ $\uparrow y$

Two examples of non-linearity in ADC in different scintillation camera/computer systems. Real flood field images, ^{99m}Tc, 15% energy window, 5 million counts each image.

Results:

L: Digital flood field image from a camera that has a hexagonal FOV. The classic stripes seen in both vertical and horizontal directions are due to the ADC interface.

Note: The gain of the image in both *x* and *y* directions is too large (i.e. the full FOV of the image falls outside of the matrix).

R: The digital image from a circular FOV. The more diffuse stripes seen are indicative of differential non-linearity. There is a slight offset in both the *x* direction (towards the left) and the *y* direction (upwards).

Comments: There may be a specific reason to adjust the gain so that the square matrix cuts off the outer part of the FOV, for example in order to obtain a small magnification for planar cardiac studies. However, such an adjustment must ensure that the pixel size in both *x* and *y* directions is the same, and must be carefully checked.

5.1.4. Example: Differential non-linearity in ADC — effect of matrix size

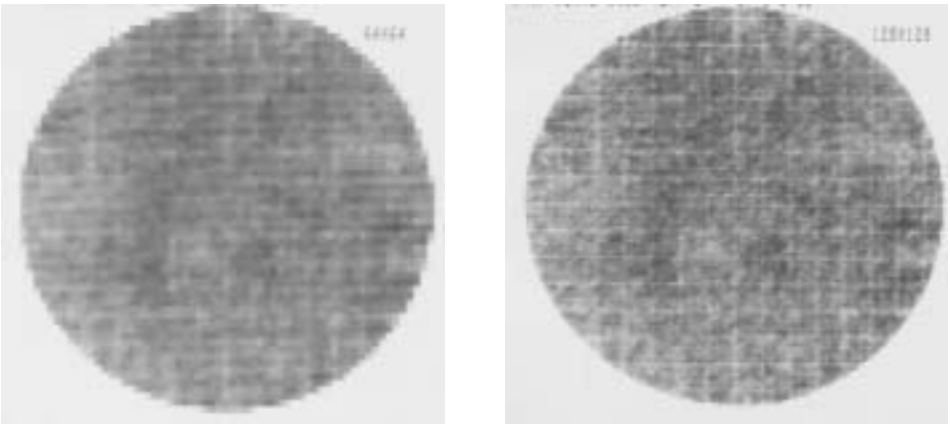

Digital flood field images, ^{99m}Tc.

L: 64 × 64 matrix.
R: 128 × 128 matrix.

Both images have contrast enhancement with a lower threshold of 50%.

Results: The classic stripes in *x* and *y* are seen in both images, but they are clearer in the 128 × 128 matrix image. When checking for ADC artefacts using a flood field uniformity image, it is useful to perform data acquisition with a large matrix size (small pixel size).

5.1.5. Example: Stripes in planar gated blood pool image

One image from a clinical planar gated blood pool study showing horizontal stripes due to non-linearity problems in the ADC of the computer interface.

5.1.6. Example: Stripes in flood image and bone scan

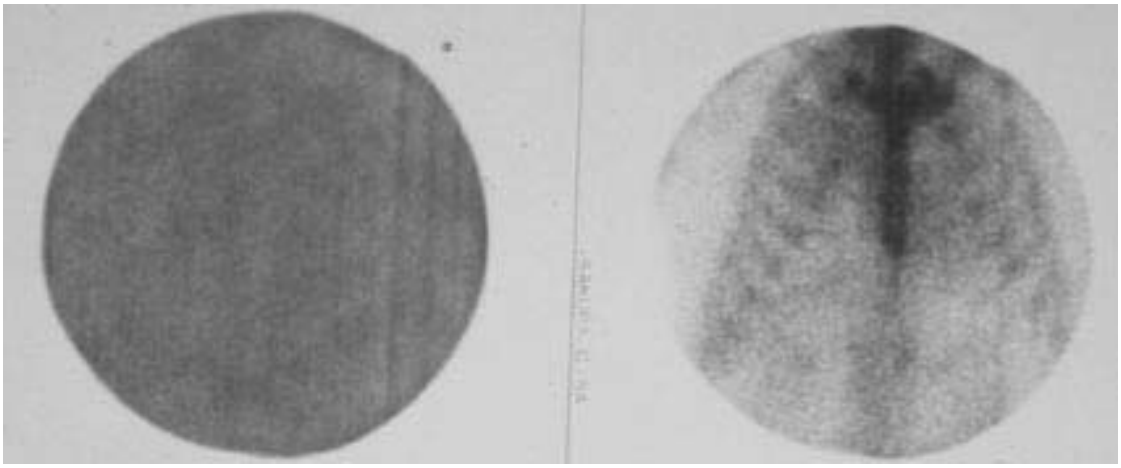

Two images obtained with the same scintillation camera/computer system. Uniformity QC image (L) and clinical static bone scan in the anterior view (R), ^{99m}Tc.

Results: Both images show vertical stripes, which are particularly obvious in the right half of each image. The vertical stripes in the bone scan are very subtle but are nevertheless present in the image of the ribs on the left side of the patient. Comparison of the left and right half of the bone scan shows that the image of the ribs on the left side of the patient is blurred and distorted compared with the ribs on the right side of the patient. The vertical stripes were due to non-linearity in the computer interface.

5.2. DIGITAL IMAGE GAIN AND OFFSET

5.2.1. Example: Gain and offset misadjustment

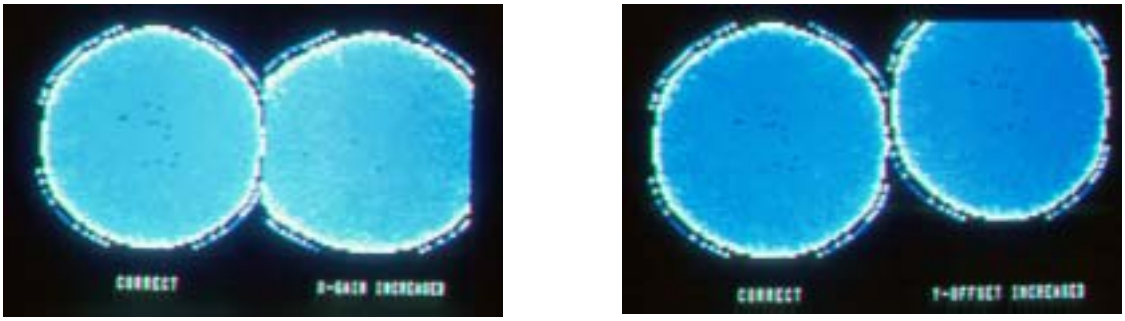

A: gain B: offset

$\rightarrow x \quad \uparrow y$

Intrinsic flood field uniformity images obtained from a circular FOV camera to demonstrate the effect of digital gain and offset.

A: L: No gain error.
R: Gain error in *x*.
B: L: No offset error.
R: Offset error in *y*.

Results:

A: The left digital image shows that the circular FOV fits symmetrically within the matrix, whereas the right image shows the circular FOV elongated in *x*, indicating a gain error (too large) in the *x* direction.

B: The left digital image shows that the circular FOV fits symmetrically within the matrix. The right image is shifted upwards in *y*, and part of the image falls outside of the digital matrix, because of a *y* offset error.

Comments: Gain and offset errors are easily seen for circular FOV cameras. With a rectangular FOV, however, an offset error should be easy to recognize in the long axis but not in the short axis direction. A gain error that enlarges the image is not easy to recognize. Care is therefore needed to check pixel size and the image location within the matrix. Correct gain and offset are crucial for SPECT studies, in particular the matching of images from multiple head scintillation cameras.

5.2.2. Example: ADC non-linearity — offset and gain misadjustment

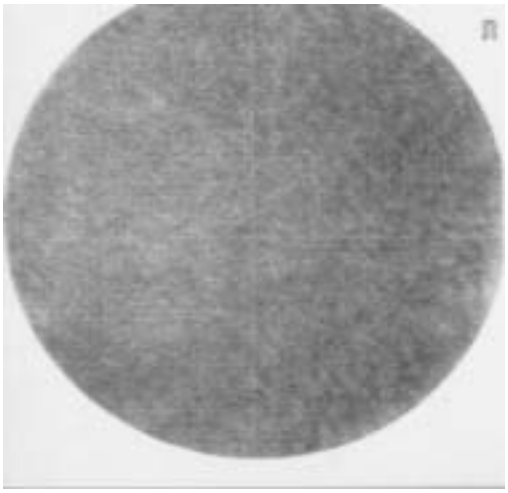

$\rightarrow x$ $\uparrow y$

The analogue scintillation camera had just been connected to a computer with an external digital interface. The flood field image (^{99m}Tc, 3 million counts) shows an offset in both x and y, and a small gain error in x. There are cold stripes passing through the centre of the matrix in both x and y directions. There are also diffuse stripes from differential non-linearity.

5.3. CAMERA TO COMPUTER CONNECTION

5.3.1. Example: Loss of digital spatial resolution (analogue versus digital)

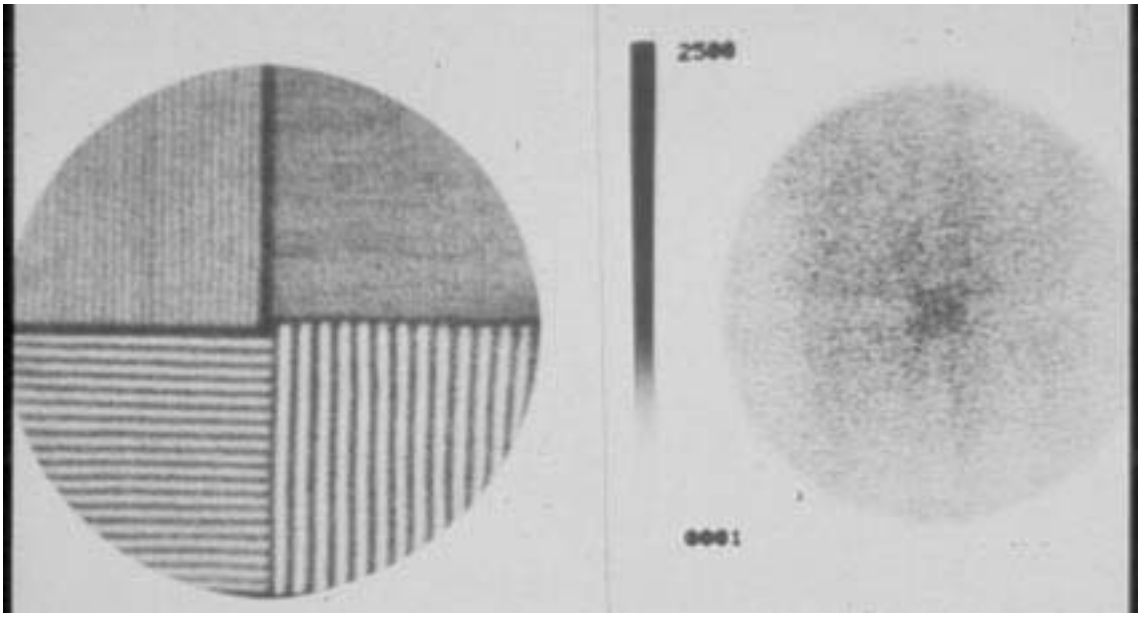

Extrinsic spatial resolution with four quadrant bar pattern, LEHR collimator, ^{99m}Tc flood source, 15% energy window, 5 million counts each image. The images were made with an analogue scintillation camera that was interfaced with a computer.

L: Analogue image.
R: Digital image.

Results: The analogue image on the left shows reasonable spatial resolution (although the linearity is not very good). The digital image on the right shows a complete loss of spatial resolution, indicating that the digitization process was malfunctioning.

Comments: A modern scintillation camera is directly interfaced to a computer and does not produce analogue images. However, older cameras have analogue output signals that require an external analogue to digital interface. This interface may be from the same manufacturer as the camera or from another manufacturer.

When both analogue and digital images are made, the images must be comparable, and the digitization process must not degrade the image. When checking spatial resolution, the maximum matrix size, and if necessary a zoom factor, should be applied in order to assess the spatial resolution adequately.

5.3.2. Example: Incorrect connection between scintillation camera and computer interface

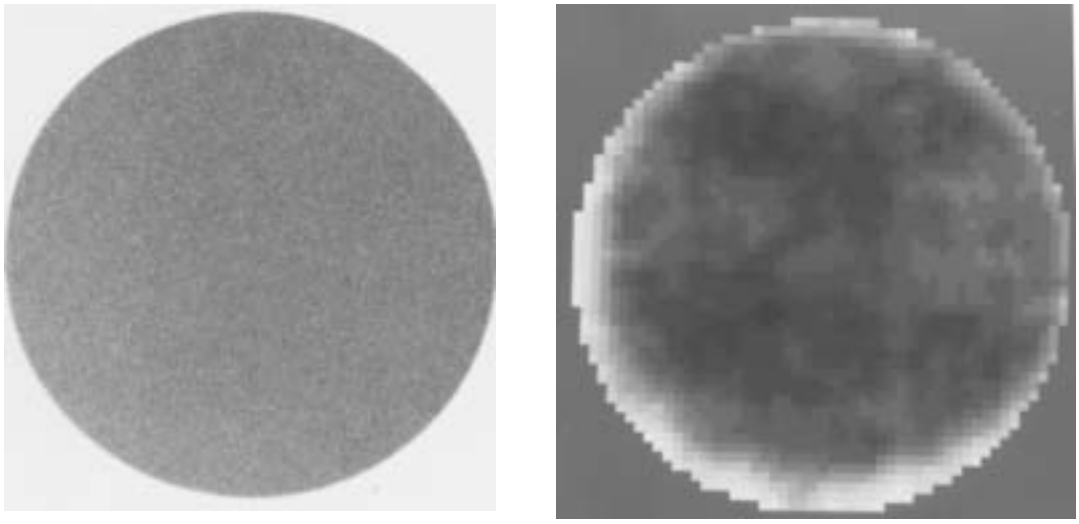

Intrinsic flood field image, ^{99m}Tc, 20% energy window, 3 million counts each image.

L: Analogue image.

R: Digital image (64 × 64 matrix). This is a parametric image to portray visually those pixels which have count values within incremental steps of 2% higher and lower than the mean pixel count. Each incremental step is displayed as a different grey level, relative to the mean pixel count, the background grey level. Higher counts have darker grey levels, and lower counts have lighter grey levels.

Results: The analogue image shows acceptable uniformity up to the edge of the FOV. The digital image shows loss of uniformity towards the edge of the FOV, where the counts drop sharply. This was due to an incorrect interface between the camera and the computer.

The digital image was also quantified using the NEMA uniformity parameters. The NEMA integral uniformity in the UFOV measured 13% with incorrect interfacing and returned to the expected value of 6.8% after the interfacing had been corrected. The NEMA integral uniformity in the CFOV remained at 6% for both incorrect and correct interfacing.

5.4. ECG GATE

5.4.1. Example: Timing of ECG trigger gate — gated blood pool study

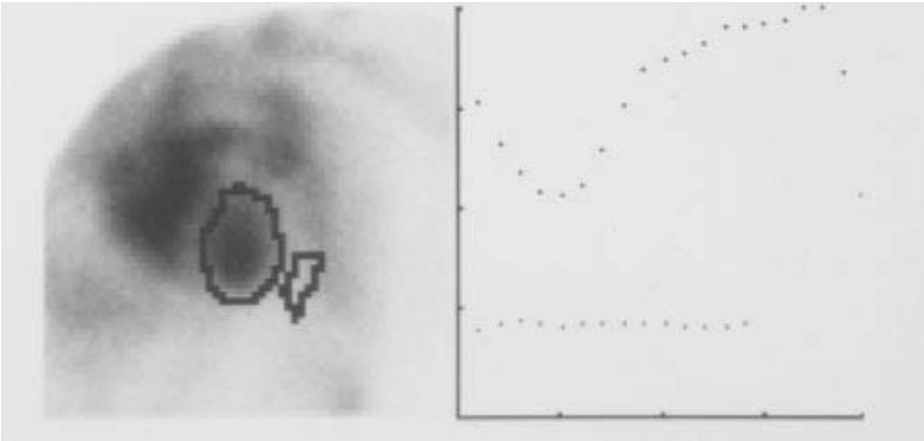

Clinical planar gated blood pool study using ^{99m}Tc labelled erythrocytes, 20 frames per heartbeat.

L: One image from the study with the left ventricular region and background regions of interest.
R: Time activity curves from the two regions of interest. The upper curve is the stroke volume curve from the left ventricular region of interest; the lower curve is from the background region of interest (only the first 14 frames are shown).

Results: The counts at the beginning of the stroke volume curve are lower than at the end of the stroke volume curve. This means that the trigger signal to the computer is not correct. The trigger pulse supplied by the ECG monitor was a negative transistor–transistor logic (TTL) signal, whereas the computer anticipated a positive TTL signal. There was therefore a delay in the response of the computer to the signal, and a response only to the positive-going part of the TTL signal. As a result, the first part of the heart cycle was lost. This was corrected by changing the settings of the ECG monitor.

5.4.2. Example: Gated SPECT data acquisition — arrhythmia problems

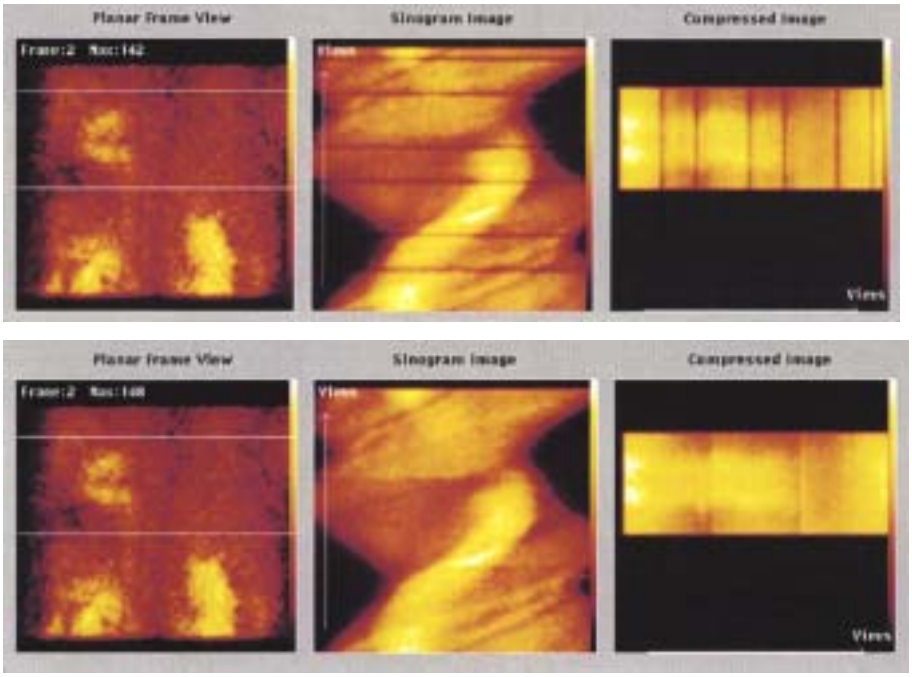

Gated SPECT data acquisition of myocardial perfusion (from a three head SPECT system) using: a fixed acquisition time per projection of 45 s and fixed time bins for the gating; a beat acceptance window of ±25% of the average beat length (determined just prior to data acquisition); a 64 × 64 matrix and 60 projections.

This method of data acquisition implies that, owing to arrhythmia, the projections will not have an identical number of beats, especially if there is considerable arrhythmia and if beats are rejected. Since, in addition, each gated time bin is a fixed time, each projection will show variations in acquired time and thus give different overall count densities. Before data reconstruction, a correction has to be made for this variation.

Top row: An example of SPECT acquisition data when no correction has been made for arrhythmia. The data are from the summed bins of the gated study.

L: One projection image (summed bins).
M: Sinogram from the profile limits shown on the left.
R: Compressed image from the same profile limits.

Notice the six projections with decreased count density.

Bottom row: The projection data corrected for the variations in number of beats.

Comments: Gated SPECT requires considerable care in order to ensure that the acquired data are correct. It is imperative to check the raw projection data before reconstruction and processing, especially if corrections are applied.

5.5. DATA TRANSFER BETWEEN COMPUTERS

5.5.1. Example: Data transfer — byte reversal (big endian/little endian reversal)

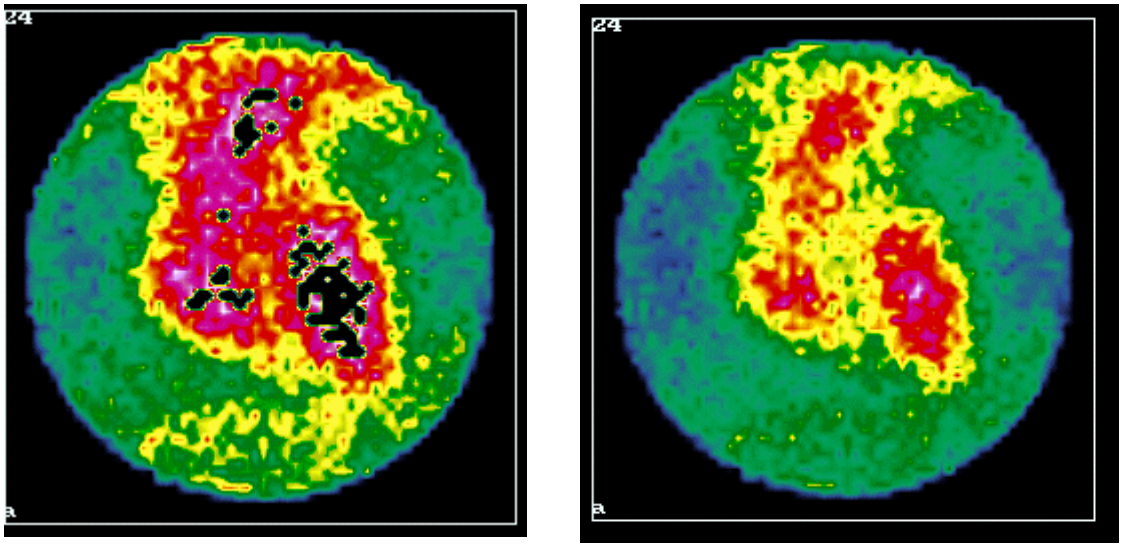

Planar gated blood pool images showing (L) the effect of incorrect data transfer due to byte reversal and (R) correct data transfer.

Results: The left image shows a large number of pixels in black, indicating count overflow. Also, the maximum number of counts in the image is about 32 000. The right image is correct after byte reversal and shows the correct maximum number of counts of 168.

Note that the maximum number of pixel counts in the correct image is only 168, whereas in the incorrect image it is about 32 000. This phenomenon is typical of a byte reversal problem: counts will be 2^{31} or about 32 000 counts, which gives word or byte overflow.

Comments: The order of bytes in multiple byte binary values is encoded as ‘big endian’ and ‘little endian’ (i.e. the value is stored either ‘big end first’ or ‘little end first’). Byte reversal is a consequence of address invariance and occurs when data in one endian format are read by a system that uses the other endian format.

Little endian data: The least significant byte has the lowest memory address.
Big endian data: The most significant byte has the lowest memory address.

5.5.2. Example: Data transfer between vendors — timing errors

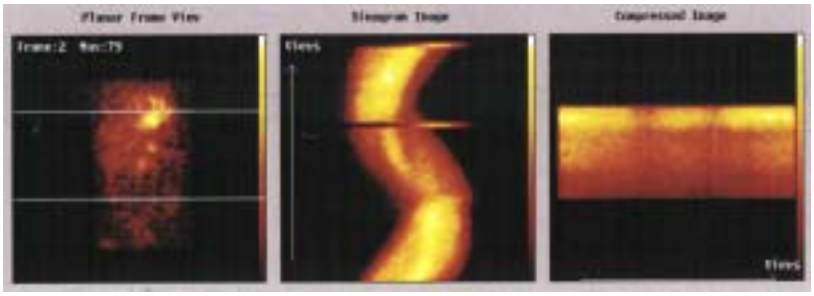

Situation A: data after transfer (computer 2)

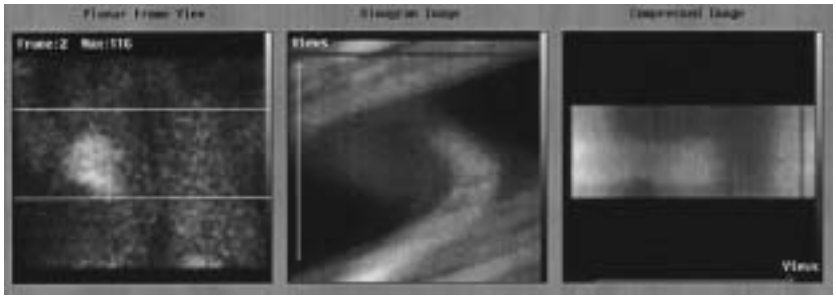

Situation B: data after transfer (computer 2)

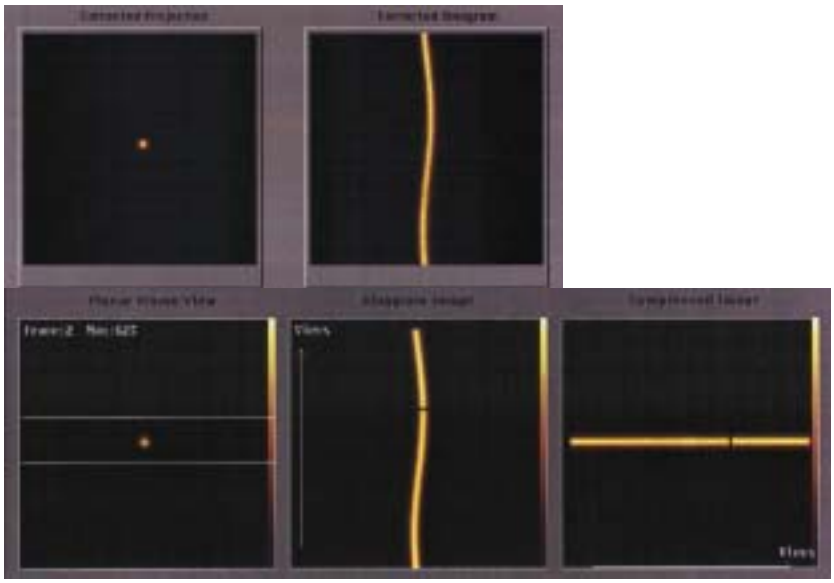

Situation C: above: acquired data (computer 1)
below: data after transfer (computer 2)

Three situations are shown to demonstrate incorrect data transfer of SPECT acquisition data from one computer to another. Computer 1 (origin) was from one manufacturer and was integrated with the scintillation camera. Computer 2 (destination) was from another manufacturer. The two had different patient file formats, so that data transfer required translating the patient file header data. Also, the acquired data were from a three head SPECT system, so that the images needed to be correctly ordered in the destination computer, computer 2. Each image set shows:

L: One projection image.
M: Sinogram from the profile shown on the left image.
R: Compressed image from the profile shown on the left image.

Results: All three situations show incorrect data transfer from computer 1 to computer 2, but each is different.

Situation A: SPECT results of data transferred to computer 2 (^{123}I MIBG SPECT study). The image co-ordinates of two images of the SPECT data are incorrect, giving an offset of data in two projections, as seen on the sinogram.

Situation B: A second set of results from data transferred to computer 2 (^{99m}Tc myocardial perfusion study). One of the projections is missing data (seen on both sinogram and compressed images).

Situation C: A third set of results from data transferred to computer 2 (^{99m}Tc point source test study). The top images are the original data on computer 1 (L: projection image; R: sinogram). The bottom images are the transferred SPECT results on computer 2.

In situation C, one projection (a different projection from situation B) is missing in the transferred data, as seen in both sinogram and compressed image. A check of the data on the original acquisition computer, computer 1, shows that the data are complete.

These situations occurred intermittently and each time produced a slightly different result. The cause was a timing conflict during data transfer. Computer 2 started to translate the incoming data while computer 1 was still transmitting data. The problem was resolved by completing data transfer before data translation was started.

Comments: The three situations are shown to illustrate the fact that data transfer can produce different results. A check of the integrity of data transfer is always essential. It is essential for data transferred between two different computers, but should also be carried out for computers from the same manufacturer.

6. ENVIRONMENT/RADIOACTIVITY

6.1. ELECTRICAL PROBLEMS

6.1.1A. Example: Power failure — flood field non-uniformity

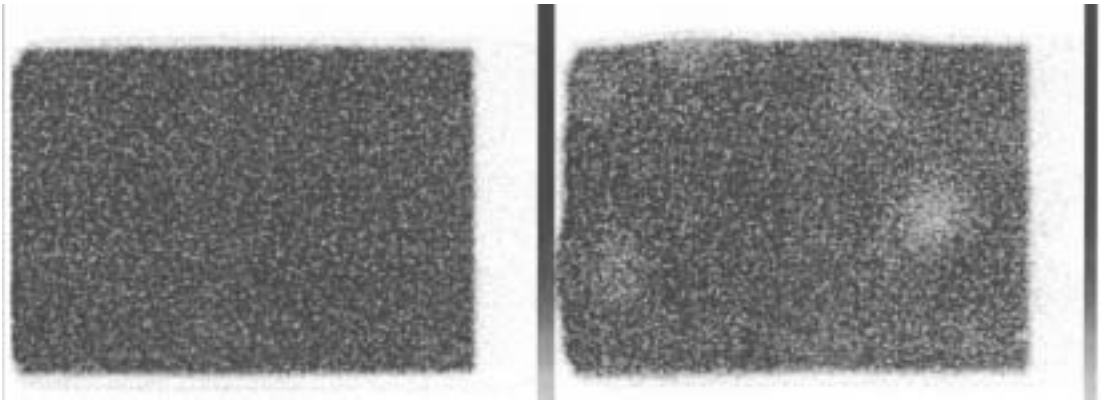

Dual head scintillation camera, extrinsic flood image obtained with a ^{57}Co sheet source, LEHR collimators.

L: Image from detector head 1.
R: Image from detector head 2.

Results: The image from detector 1 is uniform, whereas the image from detector 2 shows multiple cold areas corresponding to PM tubes. This detector had lost its PM tube tune values owing to a power failure. Retuning the camera solved the problem.

Note: The flood source was smaller than the FOV of the camera.

Comments: The power failure had occurred during the night. The uniformity images were obtained the following morning prior to patient imaging.

A minimum basic operational check of energy window setting and uniformity should always be made each morning prior to clinical operation. Although an unexpected failure may occur during the day, the check gives assurance that at the outset of the day's clinical programme the instrumentation is working.

6.1.1B. Example: Power failure — lung perfusion study — non-uniformity

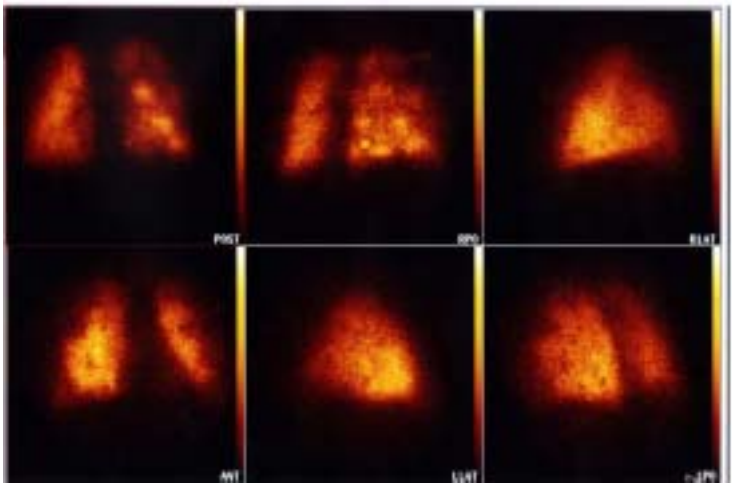

A: Camera 1: bad uniformity — after power failure

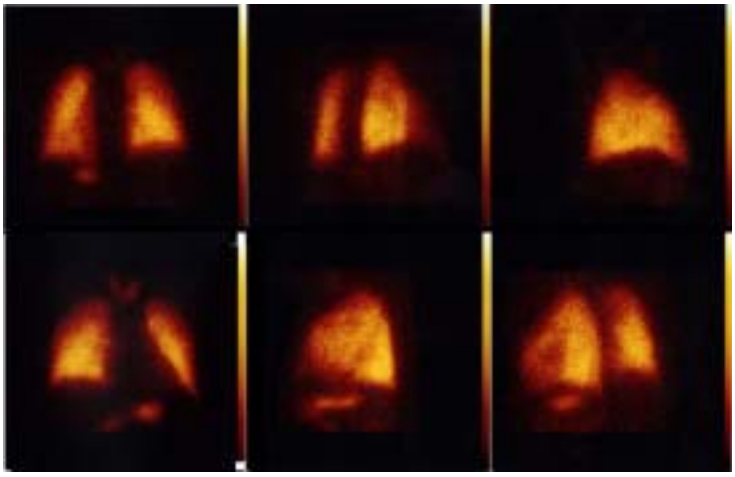

B: Camera 2: good uniformity — unaffected by power failure

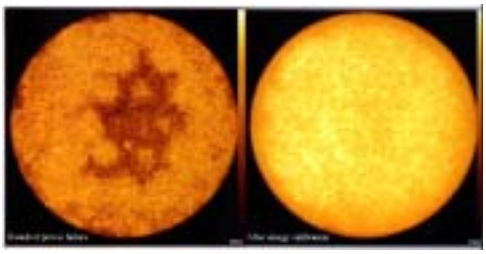

C: Camera 1: uniformity after power failure after retuning

Clinical lung perfusion study using ^{99m}Tc MAA, LEHR collimator, 20% energy window. Images were first obtained with camera 1. The poor quality was not at first recognized as a camera problem. After two subsequent patients demonstrated the same patchy pattern in their lung perfusion images, the problem was investigated by obtaining a flood image, which revealed the gross non-uniformity (left image of C). All patients were recalled and reimaged on camera 2.

A: Lung perfusion images obtained on camera 1.
Top row: Posterior, right posterior oblique, right lateral.
Bottom row: Anterior, left lateral, left posterior oblique.
B: Lung perfusion images obtained on camera 2. Same image order as in A.
C: Flood field images on camera 1 (^{99m}Tc, 20% energy window, 3 million counts each image).
L: Before retuning.
R: After retuning.

Results: The lung perfusion images taken with camera 1 are patchy images with multiple hot and cold areas. When taken with camera 2 (several hours later), the images appear smooth. The flood field image obtained on camera 1 (obtained only after the lung perfusion imaging) was indeed grossly non-uniform. This was rectified by retuning the camera.

On investigation it was found that there had been a power failure during the night. Because the routine QC had not been done prior to patient imaging, the problem was only discovered after several patients had already been imaged.

Comments: The images obtained in A could have been the result of poor labelling of the ^{99m}Tc MAA, or could indeed have been due to clinical pathology of the patient. However, the subsequent lung perfusion studies done with the same scintillation camera all showed a similar irregular pattern. These images had been made in the morning without the daily operational check of the flood field uniformity having first been performed. Only later (at the end of the morning), when the scintillation camera was suspected to be the cause of the patchy images, was a flood field check made (a procedure that routinely took a maximum of 15 minutes). The result is shown as the left image of C, a flood field image indicating extreme non-uniformity due to a loss of tune values.

On that same morning, the situation within the department was such that some of the nuclear medicine computers also had problems. Either they were malfunctioning or they had rebooted automatically during the night. The computers at that time were not connected to uninterrupted power supplies to ensure continuous operation regardless of fluctuations in or failure of the mains power supply.

Various other instruments in the department showed abnormal behaviour. This should have alerted personnel to the fact that something unusual had happened since the previous day. On enquiry it was found that there had been a power failure during the night.

On that particular morning, two of the four scintillation cameras of the department had uniformity problems which were resolved after recalibrating or retuning the camera. This cost extra time that had not been planned for. However, a QC check and recalibration at the start of the day would ultimately have saved time and, more importantly, inconvenience and discomfort to several patients, because all patients who had been imaged before the problems were discovered and corrected required repeat imaging later during the day (without extra administered radioactivity) (see images B).

This example emphasizes the importance of checking camera performance each morning prior to the start of clinical imaging and prior to the administration of radioactivity to patients. If a fault is found that can be rectified, then the programme can continue, but if a fault is found that cannot be rectified, then the patient will not receive unnecessary radiation.

6.1.1C. Example: Power failure — flood field non-uniformity and energy window shift

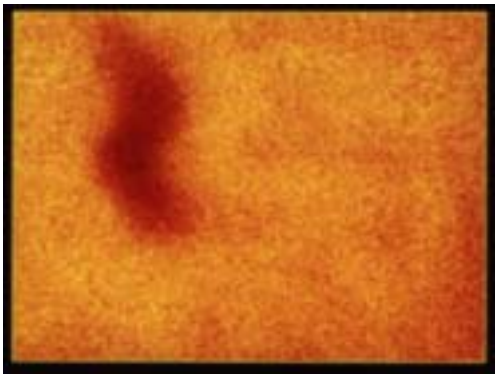

Flood field uniformity, ^{99m}Tc, 15% energy window, 10 million counts. A check of the energy window position prior to data acquisition showed a considerable negative shift to below the photopeak position.

Results: The flood field uniformity image shows overall non-uniformity and a cold area in the shape of an inverse S. The power supply to the camera had unexpectedly failed. On investigation, the PM tube tune values were found to be incorrect. Retuning the PM tubes of the camera rectified the situation.

6.1.2. Example: Electrical power shutdown — shift in image offset

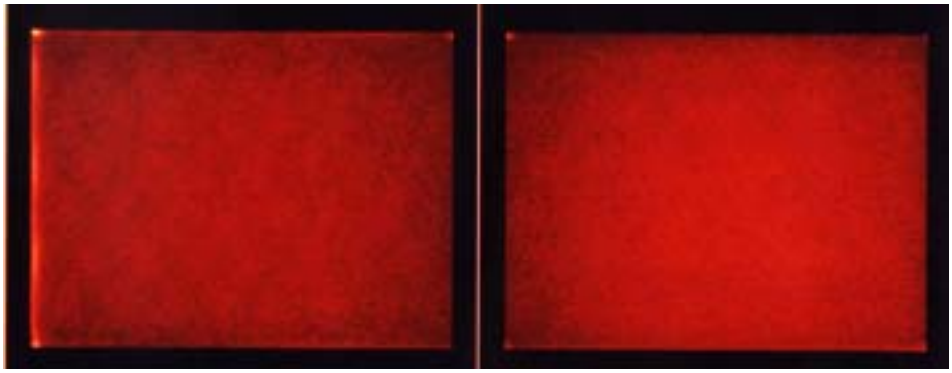

Simultaneous intrinsic flood images using a ^{99m}Tc point source positioned between two detectors (15% energy window, 10 million counts each image) of a multiple head SPECT system. These images were obtained after the scintillation camera system had been shut down completely for a short period (about 30 min) during a hospital-wide electrical power supply check.

L: Image from detector 1.
R: Image from detector 2.

Results: The image from detector 1 shows an accumulation of counts on the left hand edge of the FOV (the bright line at the left edge of the FOV), and a faint pattern of PM tubes over the whole FOV. This was caused by an offset error in the image from detector 1 after shutdown. The image from detector 2 shows satisfactory uniformity. Both images demonstrate the 'dome' response resulting from the point source being only at about 1 FOV distance from each detector. Service was required to readjust the image offset of detector 1, which resulted in uniform response again.

Comments: In this particular camera type, the gain and offset of the image are matched to the linearity corrections. Only a slight deviation in gain and/or offset causes non-uniformities in the form of visible PM tubes.

6.1.3. Example: High voltage junction spark — PM tube malfunction

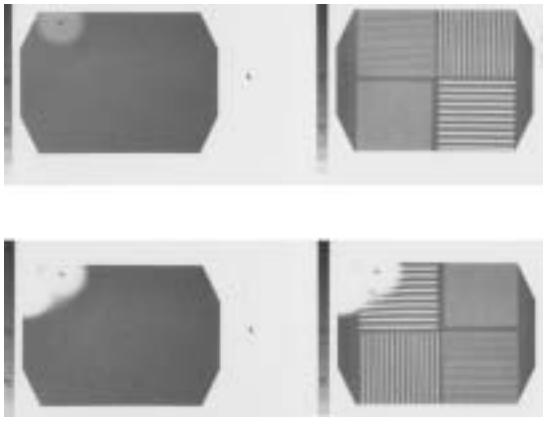

A: QC test images

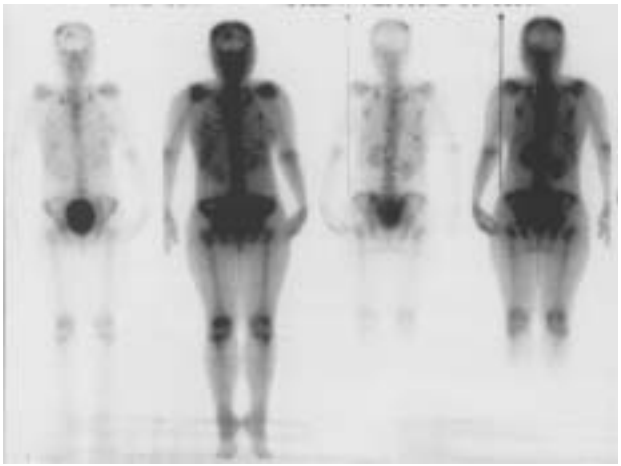

B: clinical bone scans

Images obtained with a single head scintillation camera with whole body scan option.

A: QC of uniformity (^{99m}Tc flood source) and spatial resolution using a four quadrant bar pattern (20% energy window, 3 million counts each image). The images were obtained in the following sequence:
- TL: Uniformity image, detector facing up.
- TR: Spatial resolution after rotating and moving the camera head, detector facing down.
- BL: Uniformity image after again rotating and moving the camera head, detector facing up.
- BR: Spatial resolution image, detector facing up.

B: Analogue whole body images of the skeleton using ^{99m}Tc MDP.
- Left two images: Anterior view (camera facing down), two images made with different intensities.
- Right two images: Posterior view (camera facing up), two images made with different intensities.

Results: The uniformity image (TL) shows a diffuse circular cool area, from one PM tube, with a small central hot spot. After the camera head was moved and rotated through 180º, this disappeared (TR). Rotating the camera back again not only produced the central hot spot but a larger surrounding completely cold area, indicative of two malfunctioning PM tubes.

The posterior view of the whole body images (B), obtained with the camera facing up, shows the effect of the hot spot, which disappears halfway through the whole body scan. It became apparent that the problem only manifested itself when the camera head was facing up.

The problem was a high voltage junction spark, which caused intermittent malfunctioning of the PM tubes. This was corrected by service.

6.1.4A. Example: Power interruption — image orientation change

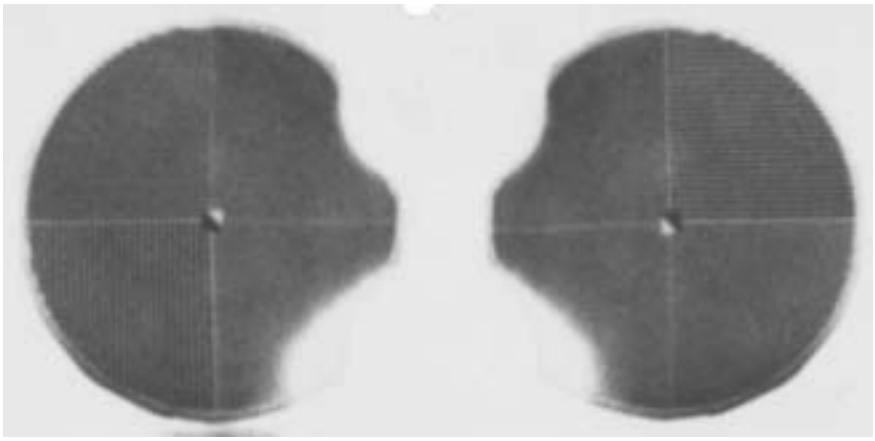

Before After

Intrinsic spatial resolution images of a four quadrant bar pattern, ^{99m}Tc, 20% energy window, 2 million counts each image.

L: Image obtained before a power interruption.
R: Bar pattern rotated 90º clockwise, and imaging started after a power interruption of a few seconds.

Results: The left image shows 3–4 malfunctioning PM tubes on the right hand side of the image. The right image, obtained after the power interruption, shows the PM tubes on the left hand side of the image. The image orientation had flipped horizontally. Note also this flip in image orientation in the bars of the bar pattern, which had been rotated through 90º.

This image orientation problem recurred in this scintillation camera. The image orientation needed to be reset after any power interruption.

6.1.4B. Example: Power interruption — image orientation error

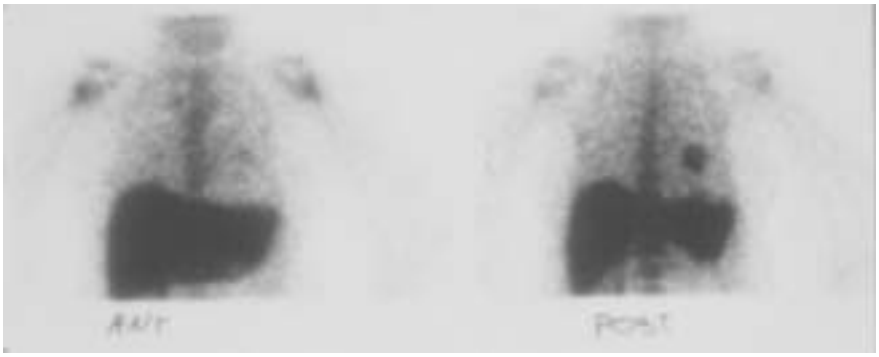

Dual head scintillation camera with detectors in a 180° configuration, clinical study of the upper abdomen obtained with both camera heads simultaneously after switching off and on the electrical power supply to the camera gantry.

L: Anterior view.
R: Posterior view.

Results: The left image in the anterior view shows correct orientation of the image: the liver is on the left hand side of the image. The right image in the posterior view, however, also shows the liver on the left hand side of the image. The power interruption caused a flip in the image orientation for detector 2 whereby right and left were interchanged.

Comments: This phenomenon was typical for this camera. The image orientation reset to an incorrect default setting each time the power was interrupted. Manually activating all the image orientation switches corrected the settings.

In this example, the liver formed an anatomical landmark that helped to identify the problem. However, for symmetrical organs, this situation could lead to erroneous image interpretation. A marker placed at the right (or left) side of the body can assist in unequivocal identification of image orientation.

6.1.5. Example: Effect of high varying ambient temperature

A: camera 1

B: camera 2

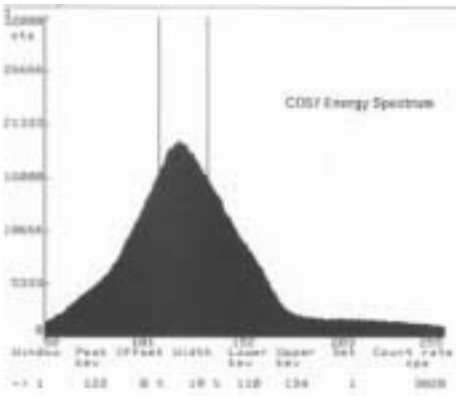

C: camera 1: energy spectrum and window

D: uniformity spatial resolution

^{99m}Tc nanocolloid scintigraphy of the wrists, 20% energy window.

A Image obtained on scintillation camera 1 located in room 1 (128 × 128 matrix, 22 000 counts).
B: Because of the poor spatial resolution of image A, scintigraphy was repeated on another camera, camera 2, located in room 2 (128 × 128 matrix, 11 000 counts).

QC was subsequently carried out, using a ^{57}Co sheet source, in order to investigate the possible cause of the poor resolution of image A.

C: ^{57}Co energy spectrum display, 20% energy window limits displayed between the vertical lines.
D: Uniformity (L) and four quadrant bar pattern spatial resolution (R) images (256 × 256 matrix, 7 million counts each image).

Results: The quality of the spatial resolution image of the wrists obtained with camera 1 was exceedingly poor but was as expected on camera 2. The problem on camera 1 was investigated by performing the regular QC tests using a sheet source of ^{57}Co. The energy spectrum was excessively broad. The uniformity image showed non-uniformity in the form of a pattern of PM tubes. The spatial resolution image of the four quadrant bar pattern showed complete loss of spatial resolution.

The problem in room 1 was caused by variations in temperature up to about 27°C, which caused the *x* and *y* camera signals to fluctuate, resulting in the broad energy spectrum and deterioration of uniformity and spatial resolution. The problem of the varying high temperature was solved by installation of an air-conditioning unit, which maintained the room temperature at about 20°C.

Comments: Stable environmental conditions are essential for the correct functioning of scintillation cameras. A stable ambient temperature within the range 20–22°C is acceptable.

See also example 3.1.8.

6.2. RADIOACTIVE CONTAMINATION AND EXTRANEOUS RADIATION

6.2.1. Example: System uniformity — collimator contaminated with radioactivity

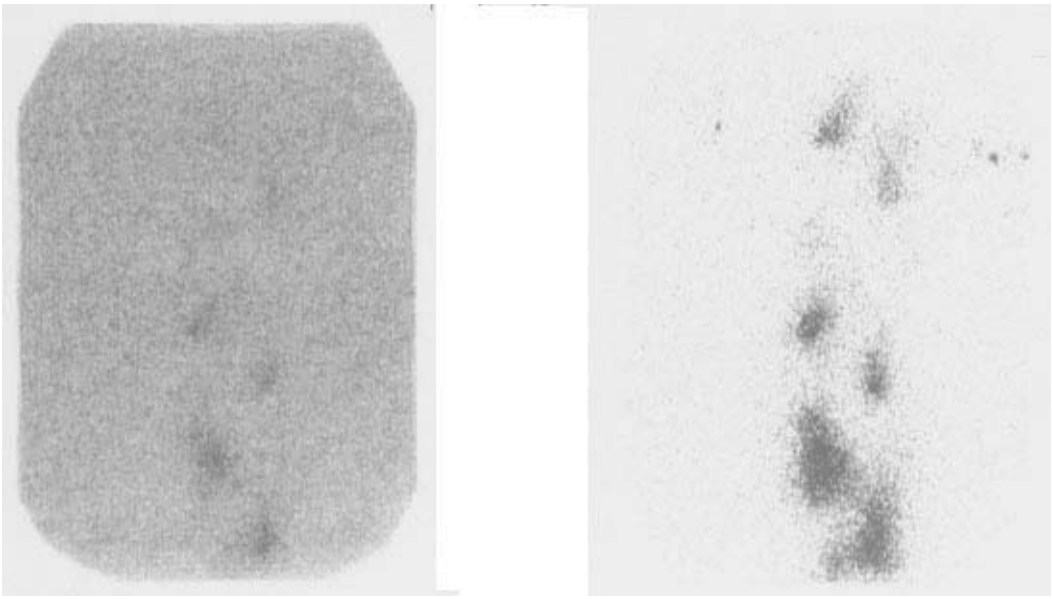

L: Uniformity image, 15% window, ^{99m}Tc, LEAP collimator, 5 million counts.
R: Background image taken immediately after the uniformity image with the same acquisition time.

Results: The dark patches seen in the uniformity image are due to radioactive contamination, as shown in the background image.

Comments: The collimator was inadvertently extensively contaminated with ^{99m}Tc. It was unusable clinically until the collimator had been cleaned, contamination had been removed and any remaining ^{99m}Tc had decayed.

6.2.2. Example: Clinical static study — collimator contaminated with radioactivity

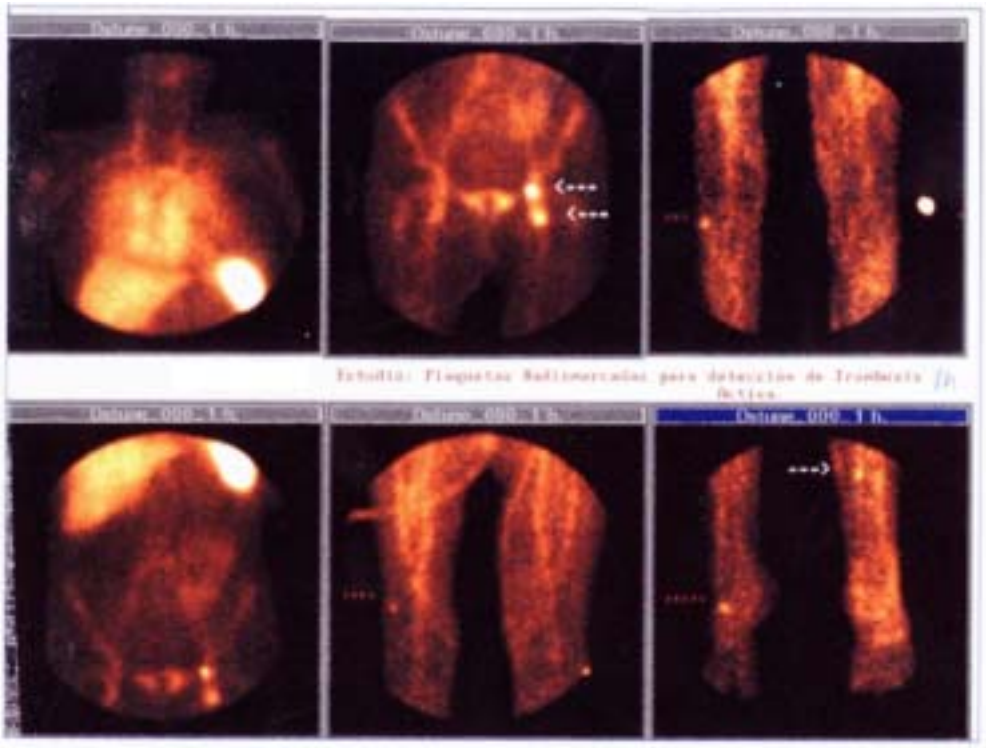

A: patient images in various views taken at 1 h post-injection

B: background images

Patient suspected of having active deep vein thrombosis. Scintigraphy was performed with homologous thrombocytes labelled with ^{99m}Tc HMPAO.

A: Patient images were obtained at 1, 3 and 24 h after administration. The images shown here are from 1 h.
B: Background images obtained without the patient.
L: Camera orientation the same as for the patient studies in A.
R: Camera rotated to another orientation, in order to ascertain whether the hot spot measured was on the collimator or not.

Results: At 1 h there are two hot spots indicating pathological uptake in the left thigh (femoral vein), and a less obvious hot spot indicating abnormal uptake in the proximal left leg (indicated by the white dotted lines and arrows). However, there is also another hot spot (indicated by the red dotted line). On inspection, this other hot spot was seen to be in the same location in each image, regardless of patient position.

After the study, a background image was obtained (without the patient) in the same image orientation as the patient images and showed this hot spot. When the image orientation was changed, the spot changed with it, confirming that this was radioactive contamination on the collimator. On the later, 24 h images, the contamination was absent.

Comments: In this study, the aim was to identify small pathological uptake sites, so that a small discrete collimator contamination was misleading and could have resulted in erroneous reporting, except for the critical evaluation of the initial 1 h images and the fast action taken.

Abnormal patterns that repeat themselves in the same location in the FOV in different clinical images should always be regarded with suspicion and action should be taken before the patient leaves the department. It is essential to assess whether the patterns are due to the patient or to the camera system. One could shift the position of the patient to see if the abnormality also shifts, or as in this case, where a small focal hot spot was suspicious, one could make a blank background image and superimpose the blank image with the previous patient image(s).

In order to ascertain whether the problem is indeed due to radioactive contamination of the collimator, a background image could be made without the collimator, or if possible (if the camera has a round FOV) by rotating the collimator.

6.2.3A. Example: Intrinsic uniformity — interference from an external radioactive source

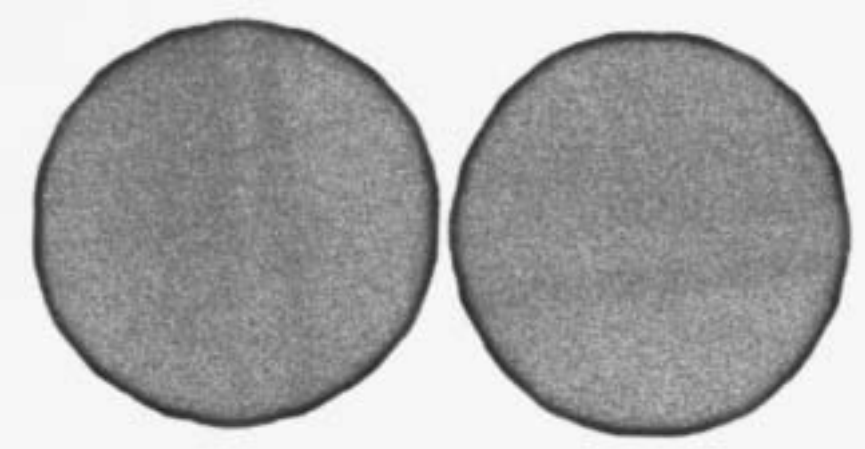

Intrinsic uniformity, ^{99m}Tc point source at 5 FOV distance, 20% energy window, 3 million counts each image. The right image was obtained with an image orientation rotated by 90° with respect to the left image.

Results: The dark lines in the image changed with a change in image orientation of the camera head. The dark lines were due to stray radiation from an extraneous radioactive source.

Comments: When making intrinsic measurements, it is imperative to eliminate stray radiation from other sources. One must therefore be aware of any radioactive sources in the vicinity, such as injected patients in surrounding areas and 'radioactive' patients passing by. It may be necessary to shield the camera detectors.

6.2.3B. Example: Intrinsic uniformity — interference from a radioactive source in the same room

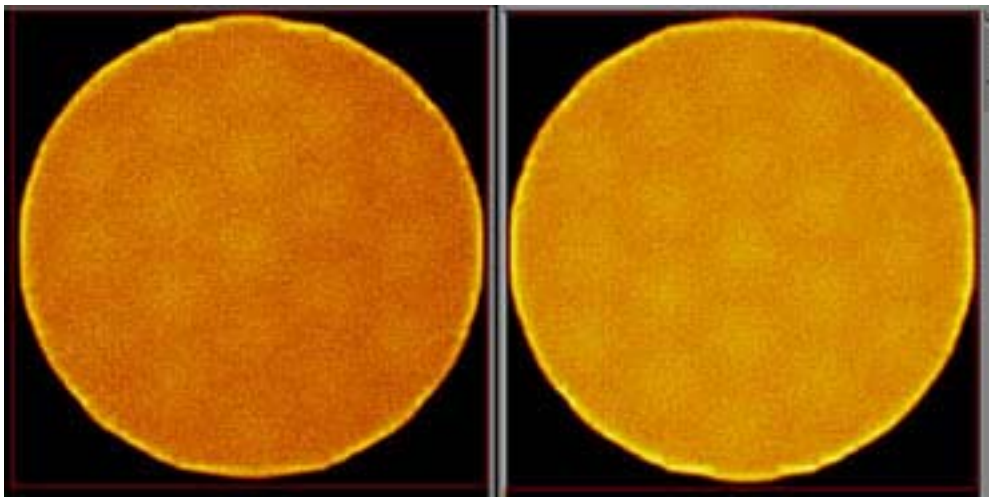

Intrinsic flood field uniformity, ^{99m}Tc point source at 5 FOV distance from the detector, 15% energy window. Images were obtained when tuning the camera.

L: A source of radioactivity (a ^{81m}Kr generator) was in the same room adjacent to the camera.
R: No radioactive source in the vicinity.

Results: The left image was obtained prior to tuning the detector. It was noticed that there was an increase in counts towards the upper right hand part of the image. On investigation it was found that there was a source of radioactivity in the room. Upon removal of the source, the uniformity image returned to that expected. Failure to deal with the interference would have invalidated the tuning.

Note: The regularly spaced hot areas are due to linearity and energy calibrations that require to be redone.

7. DISPLAY/HARD COPY

7.1. FILM ELECTRONIC FORMATTER

7.1.1. Example: Burn on formatter CRT

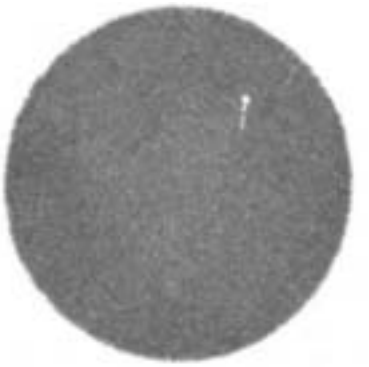

Extrinsic uniformity image, medium energy collimator, ^{99m}Tc flood source, hard copy on film using an electronic formatter.

Results: The image shows a white vertical fleck in the upper right quadrant. This was due to a burn on the CRT of the formatter, so that when the beam hit the phosphor at that point, no light was produced. The CRT required replacement.

7.1.2. Example: Defective electronic formatter CRT

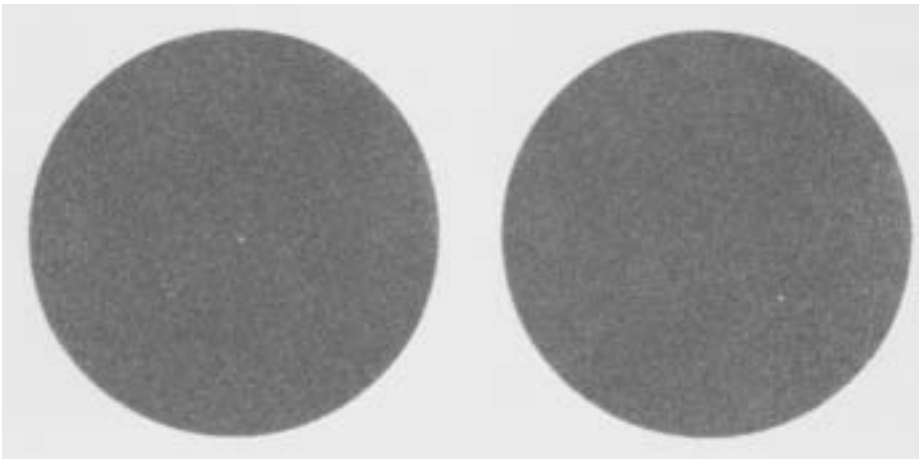

A

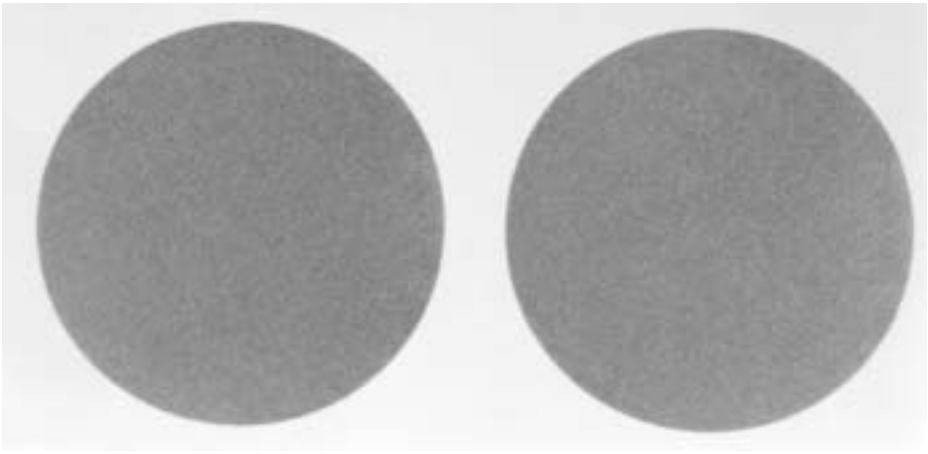

B

Flood field images obtained at service to test an electronic formatter, before and after changing the CRT.

A: Two images taken with the malfunctioning formatter.
B: Two images taken with the replacement CRT.

Results: With the malfunctioning formatter, multiple tiny blank spots were seen in different images. In addition, the spots over the rest of the image were defocused (difficult to show here). The focus was a matter of an electrical contact, but eliminating the blank spots required replacement of the formatter tube. The images taken with the new tube were satisfactory.

Note: In this case the blank spots were not due to dirt on the CRT.

7.1.3. Example: Dirt on electronic formatter CRT and poor film processing

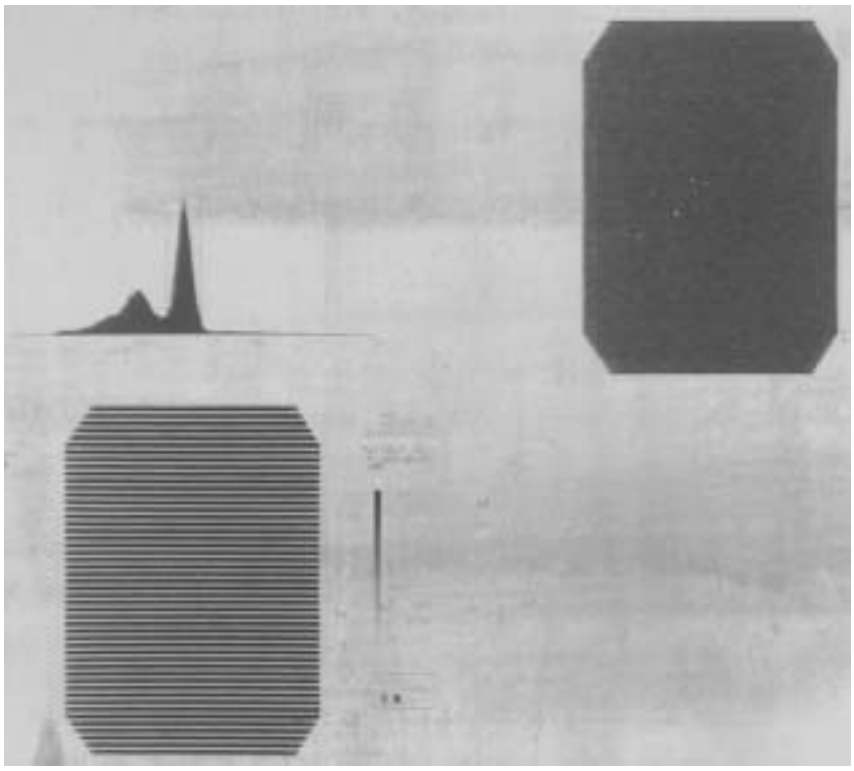

Various QC images documented on film with an electronic formatter.

TL: Energy spectrum.
TR: Flood field uniformity.
BL: Linearity image of a PLES phantom.

Results: The TR and BL images show white spots that were due to dirt on the CRT of the formatter. The grey smeared background is from poor film processing. Both the CRT and the film processor were cleaned, and subsequent results were satisfactory.

7.1.4. Example: Electronic formatter — defocused spots and dirt

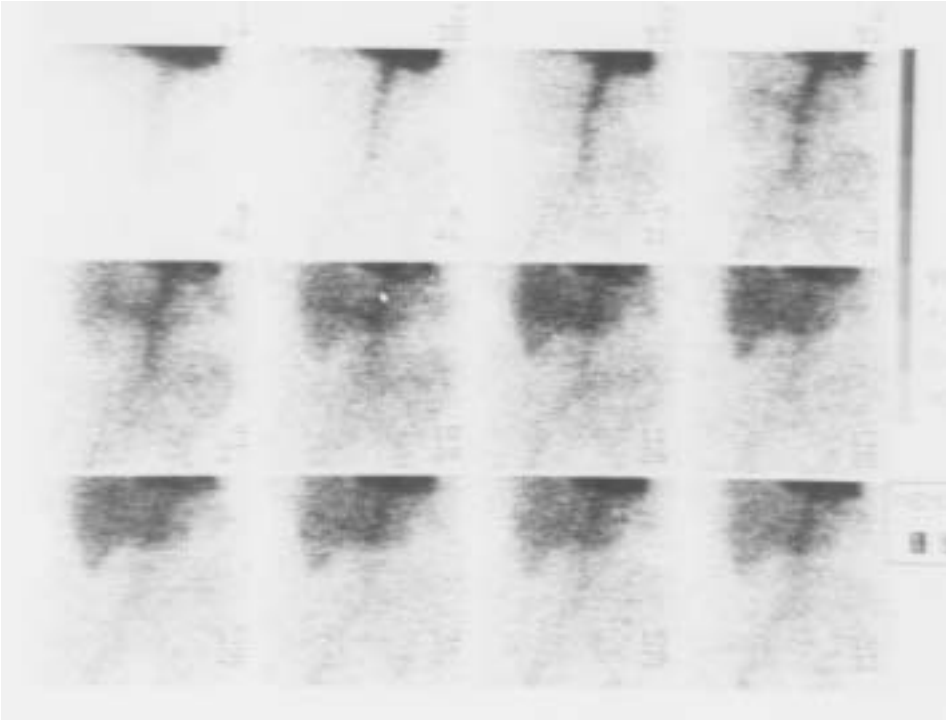

Twelve sequential images from a dynamic flow study of the lower abdomen documented on film using an electronic formatter.

Results: Each image shows defocused spots. There are also blank spots (sixth image from the top left) due to dirt on the formatter. Service was required and solved both problems.

7.1.5. Example: Ball of dust on electronic formatter CRT

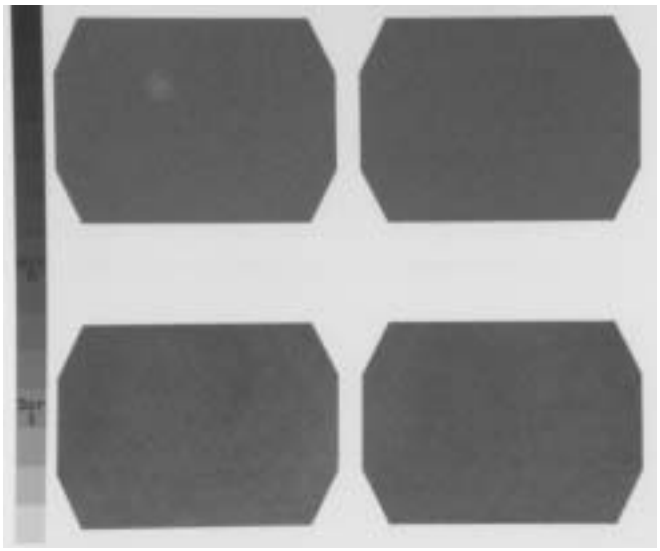

A

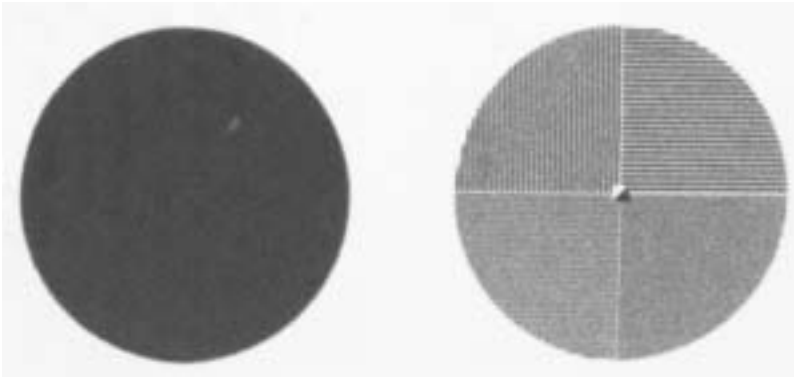

B

Two different examples of the effects of a ball of dust on the surface of the CRT of an electronic formatter.

A: Four flood field uniformity images made with different energy window settings.
B: Uniformity and resolution images.

Results: In each example, A and B, there is a small cool spot in one image only. In A, the cool spot is in the upper left quadrant of the image. In B, the cool spot is in the upper right quadrant. In both situations, this was caused by a ball of dust on that specific part of the CRT surface, and therefore only the image made at that location on the CRT FOV was affected.

Cleaning the CRT surface solved the problems.

Comments: The quality of a CRT can be assessed, in all available image settings, by making a series of identical images.

7.1.6. Example: Dirt on an electronic formatter CRT

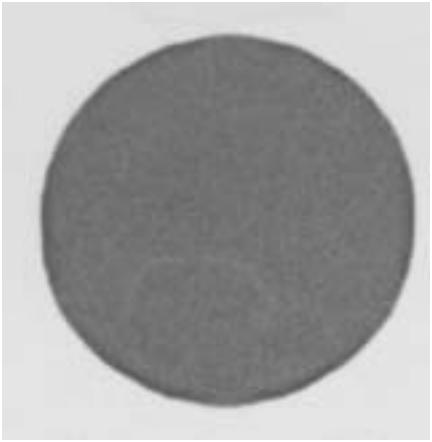

Intrinsic uniformity, ^{99m}Tc, 2.5 million count image documented on an electronic formatter.

Results: The image is uniform except for a faint partial ring of decreased intensity in the lower half of the image. This was due to dirt or lint on the CRT. The dirt had to be removed.

7.1.7. Example: Electronic formatter — loss of spatial resolution — variation in position of events in the *y* direction

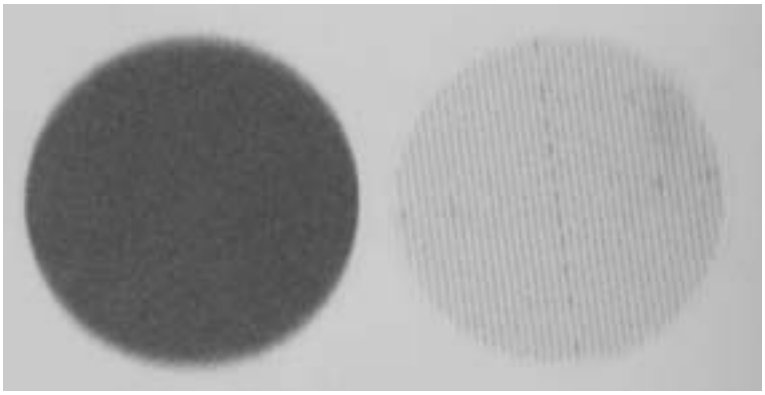

A

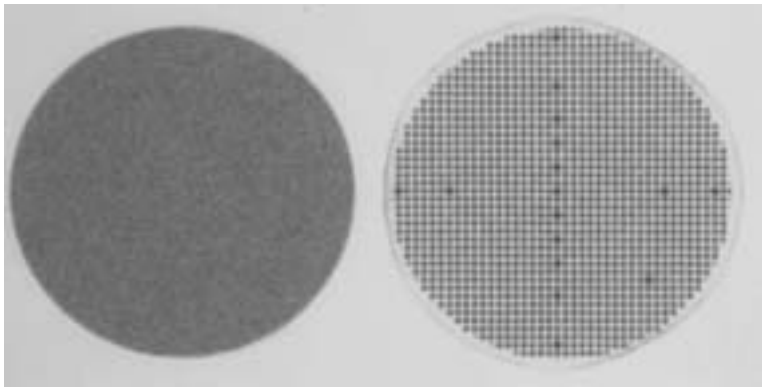

B

Routine QC images of flood field uniformity (L) and spatial resolution and linearity using an orthogonal hole pattern (R).

A: Images obtained with a malfunctioning electronic formatter before service.
B: Images with the same formatter after service.

Results: In A, the flood field uniformity image has a fuzzy border at both the top and the bottom of the image. The transmission image of the orthogonal hole pattern looks more like an image of a PLES or slit pattern. The appearance of these images was caused by an improperly operating relay in the electronic formatter. The individual events were not reliably positioned in the *y* direction.

The problem was corrected by service personnel, after which the formatter produced satisfactory images (B).

7.1.8. Example: Burnt-out electronic formatter CRT — power failure

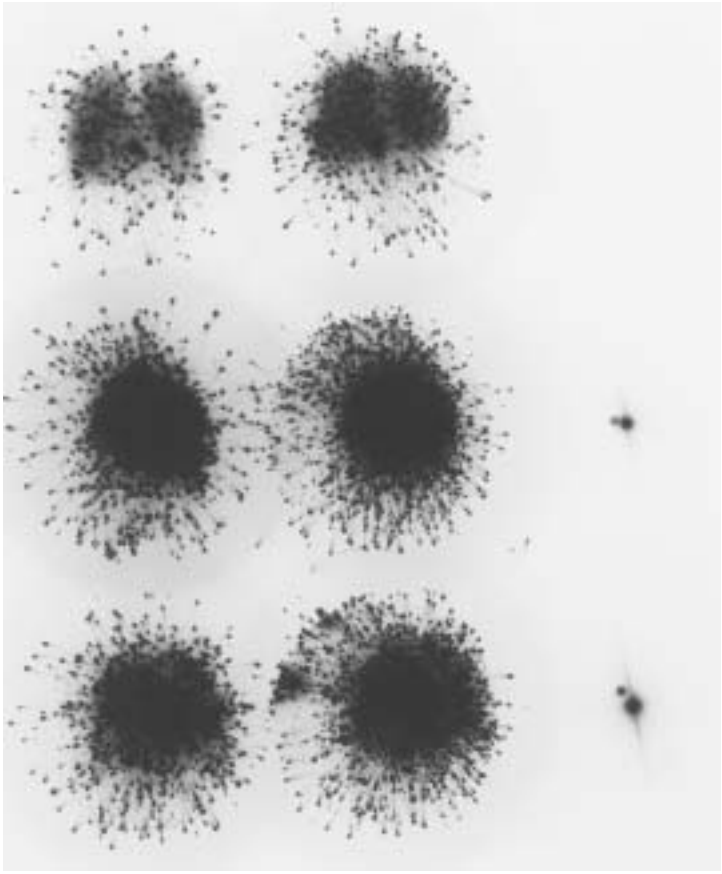

A lung study using ^{99m}Tc MAA was obtained in various views. There had been a power failure just prior to the study.

Results: The images show a bizarre pattern from the burnt-out CRT. The problem was only discovered after all the images had been made. Fortunately, the images could be repeated on another camera. The CRT required replacement.

Comments: The formatter was not connected to a circuit breaker. Instead, the formatter remained switched on, so that when power resumed, the formatter continued to appear to function. CRTs are very susceptible to electrical switching, and in this case possibly one or more power surges had occurred.

If power failure is suspected, the formatter should be checked before clinical studies are resumed.

7.2. FILM PROCESSING

See also example 7.1.3.

7.2.1. Example: Dirt on the film processing rollers

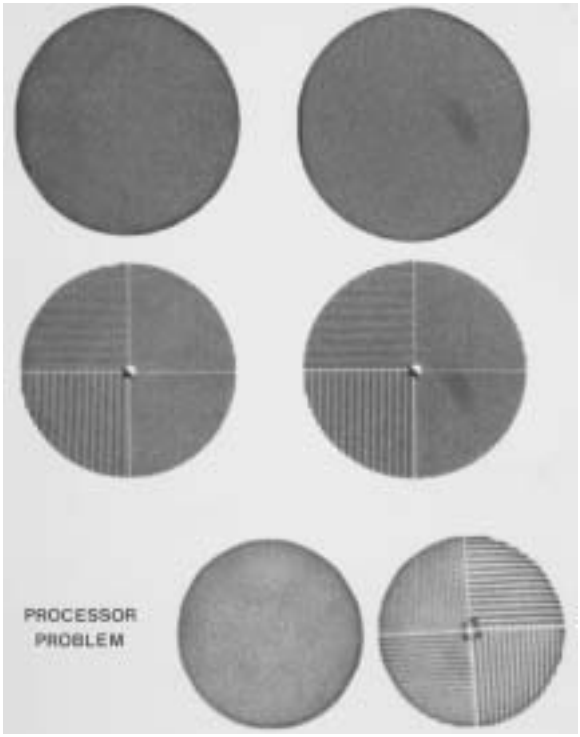

Various QC images were documented on film.

Results: The images in the right hand row all show smudges at regular intervals. These smudges were due to dirt on the rollers of the film processor. After cleaning, the problem was solved.

7.2.2. Example: Poor film processor maintenance

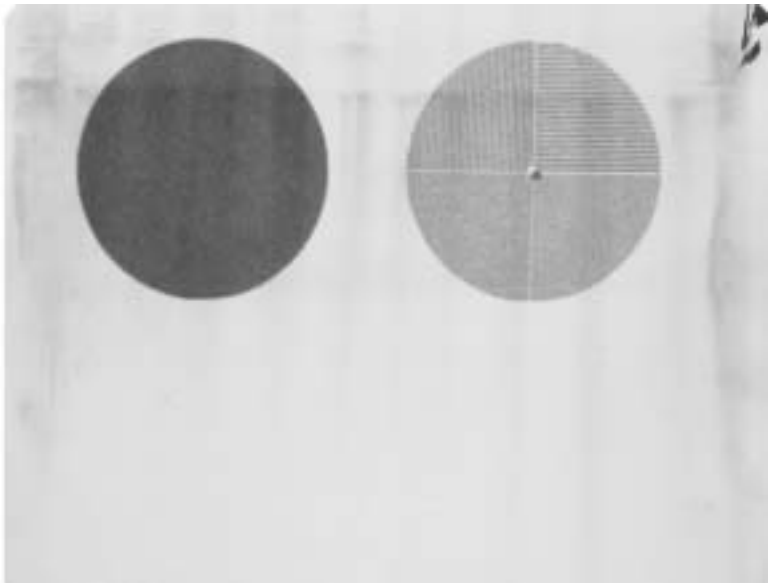

Flood field and spatial resolution images documented on X ray film.

Results: The streaky appearance of the images and film was due to poor film processor maintenance. Such poor quality film processing could lead to errors in clinical image reporting.

7.3. GENERAL

7.3.1. Example: SMPTE test pattern

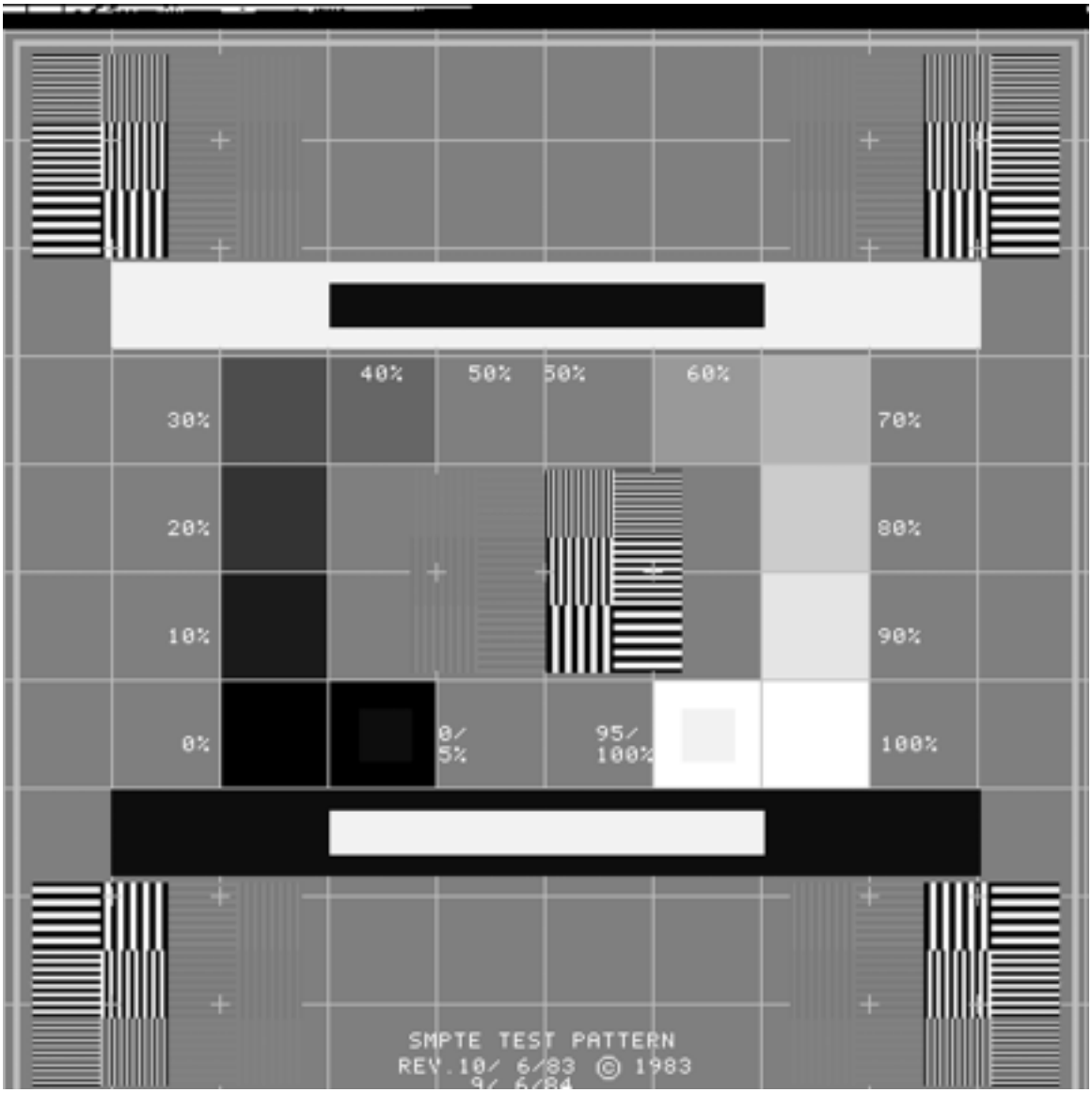

Example of the SMPTE test pattern to check the spatial resolution and image contrast of a formatter or printer.